THE UNIVERSITY OF CHICAGO

NANOSCALE METAL-ORGANIC FRAMEWORKS FOR CANCER IMMUNOTHERAPY

A DISSERTATION SUBMITTED TO

THE FACULTY OF THE DIVISION OF THE PHYSICAL SCIENCES

IN CANDIDACY FOR THE DEGREE OF

DOCTOR OF PHILOSOPHY

DEPARTMENT OF CHEMISTRY

BY

KAIYUAN NI

CHICAGO, ILLINOIS

JUNE 2020

To my family

TABLE OF CONTENTS

LIST OF SCHEMES

LIST OF TABLES

LIST OF FIGURES

LIST OF ABBREVIATIONS

α-CTLA-4	anti-CTLA-4 antibody
α-PD-1	anti-PD-L1 antibody
α-PD-L1	anti-PD-L1 antibody
AcOH	acetic acid
APF	aminophenyl fluorescein
ATP	adenosine triphosphate
BMPO	5-tert-butoxycarbonyl 5-methyl-1-pyrroline N-oxide
bpy	2,2'-bipyridine
CCD	charge-coupled device
CD	cluster of differentiation
CDT	chemodynamic therapy
CLSM	confocal laser scanning microscopy
CpG ODN	CpG oligodeoxynucleotides
CRT	calreticulin
CTL	cytotoxic T-lymphocyte
CTLA-4	cytotoxic T-lymphocyte-associated protein 4
DAPI	4',6-diamidino-2-phenylindole
DAMPs	danger-associated molecular patterns
DBB-Ru	bis(2,2'-bipyridine)(5,5'-di(4-benzoato)-2,2'-bipyridine)ruthenium(II) chloride

DC	dendritic cell
DEF	N,N-diethylformamide
DLS	dynamic light scattering
DMEM	Dulbecco's Modified Eagle's Medium
DMF	N,N-dimethylformamide
DSBs	double strand breaks
DNA	deoxynucleic acid
E2	estradiol
EGTA	ethylene glycol-bis(β-aminoethyl ether)-N,N,N',N'-tetraacetic acid
ELISA	enzyme-linked immunosorbent assay
ELISpot	enzyme-linked immunospot
EMT	epithelial–mesenchymal transition
EPR	enhanced permeability and retention
FFT	fast Fourier transform
FDA	Food and Drug Administration
FITC	fluorescein isothiocyanate
gMDSC	granulocytic myeloid-derived suppressor cell
H_2DBA	2,5-di(*p*-benzoato)aniline
H_2DBAn	9,10-di(*p*-benzoato)anthracene
H_2DBP	5,15-di(*p*-benzoato)porphyrin
H&E	haemotoxylin and eosin

HEPES	2-[4-(2-hydroxyethyl)piperazin-1-yl]ethanesulfonic acid
HMGB-1	high mobility group box protein 1
H_4TBP	5,10,15,20-tetra(p-benzoato)porphyrin
HRTEM	high-resolution transmission electron microscopy
IACUC	Institutional Animal Care and Use Committee
ICD	immunogenic cell death
IC_{50}	inhibitory concentration 50%
ICP-MS	inductively coupled plasma-mass spectrometry
IFN-α	interferon-alpha
IFN-γ	interferon-gamma
Ig	immunoglobulin
IL-6	interleukin-6
i.p. injection	intraperitoneal injection
i.t. injection	intratumoral injection
i.v. injection	intravenous injection
JC-1	5,5',6,6'-tetrachloro-1,1',3,3'-tetraethylbenzimidazolylcarbocyanine iodide
LED	light-emitting diode
MDSC	myeloid-derived suppressor cell
MET	mesenchymal-epithelial transition
MFI	mean fluorescence intensity
MHC-II	major histocompatibility complex class II

mMDSC	monocytic myeloid-derived suppressor cell
MOF	metal-organic framework
MTS	(3-(4,5-dimethylthiazol-2-yl)-5-(3-carboxymethoxyphenyl)-2-(4-sulfophenyl)-2H-tetrazolium)
MTT	(3-(4,5-Dimethylthiazol-2-yl)-2,5-di-phenyltetrazolium bromide
NADH	nicotinamide adenine dinucleotide
nMOF	nanoscale metal-organic framework
4-OHE2	4-hydroxy estradiol
oxa	oxalate
PAMPs	pathogen-associated molecular patterns
PBS	phosphate buffered saline
PDI	polydispersity index
PD-1	programmed cell death protein 1
PD-L1	programmed death-ligand 1
PDT	photodynamic therapy
PI	propidium iodide
PRRs	pattern recognition receptors
PS	photosensitizer
PXRD	powder X-ray diffraction
qPCR	quantitative polymerase chain reaction
ROS	reactive oxygen species

RPMI	Roswell Park Memorial Institute 1640
r.t.	room temperature
RT	radiotherapy
RT-RDT	radiotherapy-radiodynamic therapy
SBU	secondary building unit
SFC	spot forming cells
SOD	superoxide dismutase
SOSG	single oxygen sensor green
STING	stimulator of interferon gene
TAs	tumor antigens
TEM	transmission electron microscopy
TEA	triethylamine
TFA	trifluoroacetic acid
TGI	tumor growth inhibition
TLR	toll-like receptor
TNF-α	tumor necrosis factor-alpha
TPDC	triphenyldicarboxylic acid (*p*-terphenyl-4,4"-dicarboxylic acid)
Treg	regulatory T cell
TUNEL	terminal-deoxynucleoitidyl transferase-mediated dUTP nick end labeling
UiO	University of Oslo (Universitetet i Oslo)
UV-vis	ultraviolet-visible spectroscopy

ABSTRACT

Kaiyuan Ni: Nanoscale Metal-Organic Frameworks for Cancer Immunotherapy

Under Direction of Professor Wenbin Lin

Immunotherapy has revolutionized cancer treatment by reactivating anti-tumor immunity of hosts with durable efficacy and limited toxicity. However, only a small portion of patients with immunostimulatory tumor microenvironments respond to cancer immunotherapy. Various methods have been explored to turn "cold" tumors "hot". Chapter 1 broadly discusses current immunoadjuvant therapies to synergize with cancer immunotherapy, particularly checkpoint blockade immunotherapy, and a brief overview of nanoscale metal-organic frameworks (nMOFs), a new class of porous molecular nanomaterials with potential for biomedical applications. The introduction to the fundamental principle of design and application of nMOFs to generate reactive oxygen species (ROS) for cancer treatment, including radiotherapy (RT), photodynamic therapy (PDT), and chemodynamic therapy (CDT), serve as a foundation for Chapters 2-6.

Chapter 2 discusses the rational design of two Hf-oxo based nMOFs, Hf_6-DBA and Hf_{12}-DBA, as highly effective radiosensitizers that significantly outperform HfO_2, a clinically investigated radiosensitizer *in vitro* and *in vivo*. The enhanced RT effect of Hf-based nMOFs may be attributed to large specific surface areas of Hf-oxo clusters, porous framework structures and enhanced energy deposition. Intratumorally injected Hf-based nMOFs induce immunogenic cell death upon low-dose X-ray irradiation to enhance local inflammation. Importantly, the combination of nMOF-mediated low-dose RT with an anti-programmed death-ligand 1 antibody (αPD-L1) effectively extends the local therapeutic effects of RT to distant tumors *via* abscopal effects.

Chapter 3 describes the design of Hf-DBB-Ru as a mitochondria-targeted nMOF for RT-RDT to further enhance local radiosensitization. Constructed from Ru-based photosensitizers, the cationic framework exhibits strong mitochondria-targeting property. Upon X-ray irradiation, Hf-DBB-Ru efficiently generates hydroxyl radicals from the Hf_6 SBUs and singlet oxygen from the DBB-Ru photosensitizers in a unique RT-RDT mode of action. Mitochondria-targeted RT-RDT depolarizes the mitochondrial membrane to initiate apoptosis of cancer cells, leading to significant regression of colorectal tumors in mouse models and outperforming Hf_6-DBA reported in Chapter 2.

Chapter 4 reports the design of an ultrathin version of nMOFs, Hf-MOL, with reduced dimensionality to facilitate the diffusion of ROS generated by RT-RDT to kill cancer cells upon low-dose X-rays. MOL-enabled RT-RDT in conjunction with various checkpoint blockade inhibitors eradicated local tumors and rejected or regressed distant tumors on several syngeneic bilateral tumor models, and eliminated lung metastases by reactivating anti-tumor immunity and inhibiting myeloid-derived suppressor cells.

Chapter 5 describes the design of cationic nMOF, Hf-DBB^F-Ir as locally injected X-ray activable immunotherapeutics to release danger associated molecular patterns (DAMPs) and tumor antigens (TAs) *via* RT-RDT and deliver pathogen-associated molecular patterns (PAMPs), anionic CpG oligodeoxynucleotides, to facilitate the maturation of antigen presentation cells. Together, DAMPs, TAs, and PAMPs expand cytotoxic T cells in tumor-draining lymph nodes to reinvigorate the adaptive immune system for local tumor regression. When combined with αPD-L1, this immune activation is extended to distant tumors *via* attenuating T cell exhaustion.

Chapter 6 illustrates the use of a Cu-porphyrin nMOF, Cu-TBP, to mediate synergistic hormone-triggered chemodynamic therapy (CDT) and light-triggered photodynamic therapy (PDT) as radical therapy to boost local inflammation. By hijacking dysregulated hormone production, Cu^{2+} catalytically consumes estradiol for ROS generation. The combination of CDT- and PDT-based radical therapy with a checkpoint blockade inhibitor effectively extends the local therapeutic effects of CDT and PDT to distant tumors *via* abscopal effects on mouse tumor models with high levels of estradiol. Combination of nMOF-mediated radical therapy with CBI elicits systemic antitumor immunity in hormonally dysregulated tumor phenotypes.

ACKNOWLEDGEMENTS

The five-year journey finally brings me here to write my dissertation. At this moment, I would like to acknowledge many people helping me on my way to make this dissertation possible.

First I would like to acknowledge my advisor, Prof. Wenbin Lin. I still remember the day when he assigned me the first project and asked me to focus on cancer biology. Even working in a chemical biology lab for three years when I was an undergraduate, it was still pretty challenging for me at that time to take over the duty of a postdoc trained as a biologist. The challenging but significant projects he provided and inspired made this dissertation possible. As a scientist, he is always tireless, vigorous, and rigorous to discuss idea and provide guidance. As a mentor, he is encouraging and supportive for the exploration of unknowns. His mentorship and philosophy on scientific research helped me in past five years and will continue to help in my future career.

I would like to thank my committee members, Prof. Chuan He and Prof. Steve Kron, for their valuable time to review my dissertation and provide constructive advices on my defense and dissertation.

Then I would like to thank to Dr. Kuangda Lu, “KD”, the first lab member I met and talked to. As a senior lab member, he is not only profound in knowledge but also solicitous to young generation. He is always choosing to see the beauty in this world and ready to discover unknown part. I really appreciate his constructive discussion on my lab work and help in daily life.

And special thanks to Dr. Christina Chan, Dr. Xiaopin Duan and Dr. Nining Guo, senior group members leading projects in nanomedicine subgroup in our lab. With the education background in chemical biology, pharmacology and immunology, respectively, they not only passed on

fundamental knowledge and methodologies but also imparted technical skills in biology and immunology. They have always been enormously helpful and considerate before I could do things properly and independently.

It is my luck to have Guangxu Lan, same-grade school mate and closest colleague on all my thesis work. He is a genius in materials chemistry and a reliable collaborator. His productivity and management made our collaboration very effective.

Thanks to all the core facility staff members in the University of Chicago in no particular order — Ms. Yimei Chen from the Electron Microscopy Facility, Ms. Shirley Bond and Dr. Christine Labno from Microscopy Facility, Dr. David Leclerc from Cytometry Antibody Technologies Facility, Dr. Qiti Guo from the Materials Research Science and Engineering Center, Mr. Jim Marsicek from Office of Radiation Safety, Dr. Ming Cheng from Human Tissue Resource Center, Dr. Jin Qin from Mass Spectroscopy Facility, Mr. Philip Griffin from the Soft Matter Characterization Facility, who gave me detailed guidance and enormous help in troubleshooting and data analysis on my experiments.

There are many other people to be acknowledged in the lab: in no particular order — Wenbo Han, Tong Wu, Yang Song, Xuanyu Feng, Taokun Luo, Xiaomin Jiang, Ziwan Xu, Geoffrey Nash, August Culbert, Samuel Veroneau, Dr. Pengfei Ji, Dr. Zekai Lin, Dr. Kui Yang, Dr. Wenxin Zheng, Dr. Shuyi Li, Dr. Youfu Wang, Dr. Ruoyu Xu, Dr. Yangjian Quan, Dr. Nathan Thacker, Dr. Cheng (Wave) Wang, Dr. Xiangjian Kong, Dr. Xin Zhou, Dr. Yuan-Yuan Zhu, Dr. Dan Micheroni and anyone I forgot to acknowledge here. Thank you all for inspiring discussion, useful suggestions and experimental helps on my study and research.

Finally, I would like to thank my family. It is extremely difficult for me to be away from them for such a long time. It is their endless love and strong support that make me sincere, fearless and patient. The dissertation is for my parents, who have been dedicated to science and technology and dreaming of this milestone for me. This dissertation is dedicated to the memory of my grandma, a loved and respected obstetrician, Dr. Jinghuang Yao, who passed away on 2 December 2019.

CHAPTER 1. Introduction

1.1 Cancer and cancer immunotherapy

Cancer, the dysregulatory metabolism and aberrant growth of cells,[1] is currently the second leading cause of death in the United States, with 1.8 million new cases diagnosed and 0.6 million cancer-related deaths in 2019.[2-3] Therapeutic effects of various regimens such as surgery,[4-6] chemotherapy,[7-8] and radiotherapy[9-10] have shown considerable 5-year survival rates, yet are still unsuccessful in achieving long-term remission for many cancer patients. The reasons behind cancer's evasiveness in treatment are multifaceted. First, the recurrence of many cancer types are untreatable and lethal.[11-13] Second, treatments including surgery, chemotherapuetics or local radiation frequently promote tumor metastasis, which fails to respond to further treatments.[14-15] Third, the quality of life of cancer patients suffering from side effects of chemotherapeutics[16-17] or tumor ablation[18-19] is undesirable. Alongside conventional cancer therapies, cancer immunotherapies – in particular, checkpoint blockade immunotherapy (CBI) – have received intense interest in the past decade due to their ability to elicit durable therapeutic responses with manageable side effects by awakening patient's own immune system to fight cancer.[20-21]

The immune system functions as the first line defense against cancer *via* immune surveillance to identify and eliminate nascent tumor cells.[22] Generally, there are three aspects of the immune system that function as the primary defense in the prevention of tumors. First, immune systems can eliminate pathogen-induced inflammation and prevent the establishment of an inflammatory environment, which promotes tumor growth and invasion.[23-24] Second, many cancers have been found to be associated with viruses, such as human papillomavirus (HPV)-positive head and neck

cancer[25] and hepatitis virus-associated liver cancer,[26] among others. The immune system prevents (*via* skin, mucosa), suppresses, and eliminates (*via* leukocytes) viral infections to protect the host from viral-induced tumors. Third, the immune system can specifically discriminate tumor cells from normal cells based on the expression of tumor antigens (TAs), including tumor-associated antigens, tumor-specific antigens, and other molecules induced by cellular stress. Identified nascent tumor cells are then cleaned up by the immune system to maintain host homeostasis.

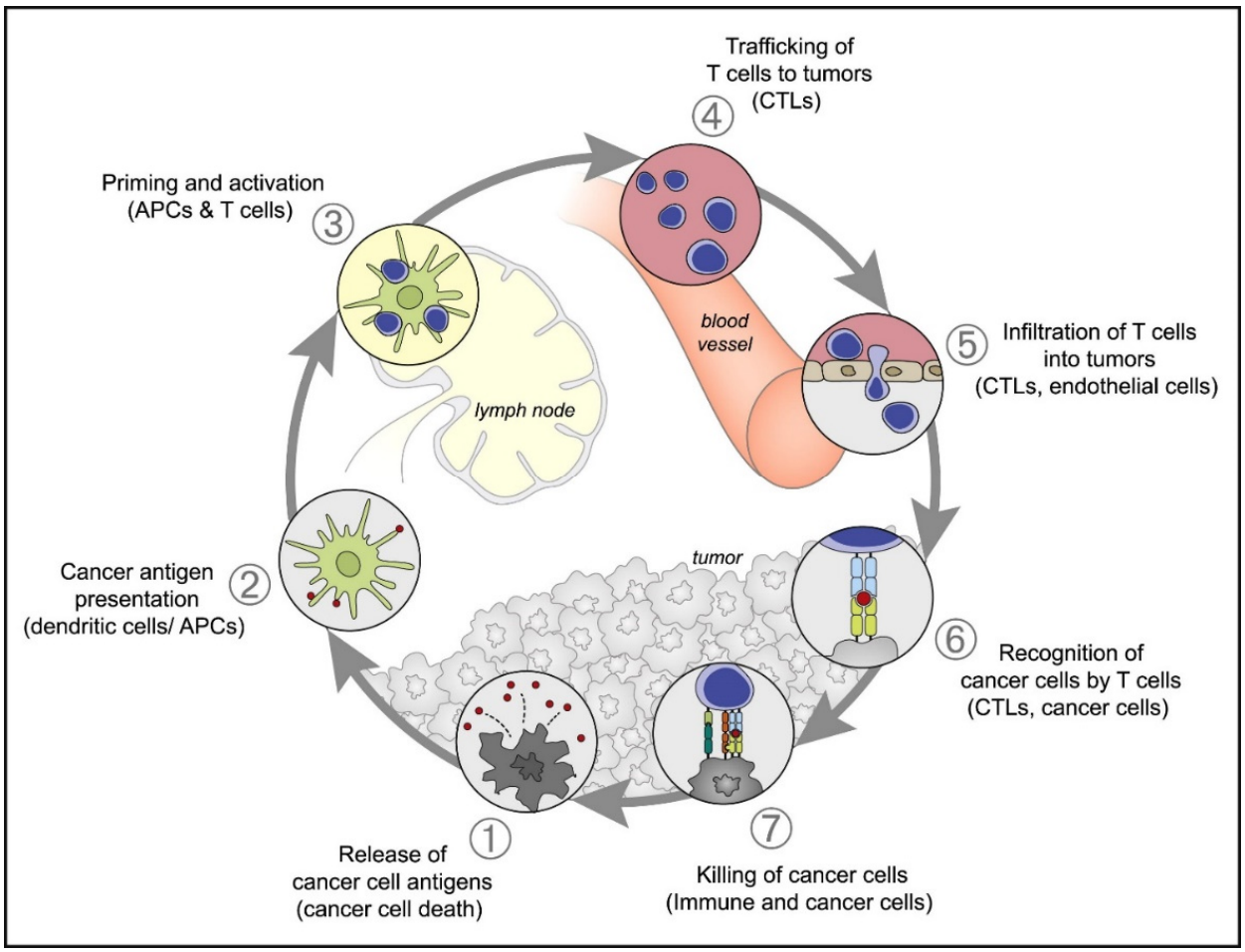

Figure 1-1 The immune-oncology cycle. This cycle starts with the release of antigens by cancer cells, antigen presentation by APCs, T cell activation in lymph node, T cell trafficking and tumor infiltration, and ends with the killing of cancer cells by immune cells. Reprinted with permission from *Immunity*, **2013**, *39*, 1–10. Copyright 2013 Elsevier Inc.

As shown in **Figure 1-1**, the process of activation of anti-tumor immunity is presented as an immune-oncology cycle.[27] The cycle is initiated with immunogenic cell death to release TAs. Then, danger associated molecular patterns (DAMPs), such as pro-inflammatory cytokines and chemokines, are released by the dying tumor cells and recruit antigen presenting cells (APCs) such as macrophages and dendritic cells (DCs) to capture and process TAs. Matured APCs travel to the tumor-draining lymph nodes (TDLNs) with antigens captured on major histocompatibility complex (MHC) molecules and present TAs to T cell receptors (TCR) on T cells in the TDLNs, leading to the priming and activation of effector T cell responses against TAs. Finally, the activated effector T cells traffic to the tumor site, infiltrate the tumor bed, and bind specifically to tumor cells through the interaction between TCR and TAs on tumor cell surface leading to apoptosis and the release of more TAs. The whole cycle functions as an established anti-tumor immune response with great breadth and depth.

Unfortunately, in cancer patients immune-oncology cycles appear abnormally in one or more steps. First, tumors exhibit less mutation burden,[28] express fewer TAs,[29] or release fewer TAs for the immune system to recognize due to non-immunogenic tumor microenvironments.[30] Second, advanced tumors develop mechanisms to escape from immune surveillance and avoid elimination by immune cells.[31] These so-called tumor immunoediting processes include dysregulating normal signaling pathways, hijacking immune suppressive cells/cytokines, and depleting effector cells/molecules.[32] For example, tumor cells frequently upregulate immune checkpoint cytotoxic T-lymphocyte-associated protein 4 (CTLA-4) to interact with co-stimulatory ligands CD80/CD86 on APCs.[33] The hijack of the CD80/86-CD28 axis by tumor cells suppresses APCs, which in turn dampens antigen presentation and results in fewer activated effector T cells.[34] Another immune checkpoint, programmed cell death protein 1 (PD-1) and its two ligands (PD-L1 and PD-L2) is a

critical negative regulatory pathway frequently exploited for immunosuppression. The interaction of PD-1 with either of its ligands inhibits kinase signaling pathways that are responsible for T cell activation, stunting effector T cell activity in tumors.[35-36] The upregulated PD-L1 on tumor cells not only negates recognition by effector T cells[37] but also expands regulatory T cells (Tregs), a subset of immunosuppressive T cell,[38] leading to a more immunosuppressive tumor microenvironment.

Cancer immunotherapy, the strategy focusing on inhibition of immunosuppressive pathways and activation of immunostimulatory pathways, is becoming an important treatment modality alongside surgery, radiotherapy, and chemotherapy for certain cancers.[21, 39] The history of cancer immunotherapy traces back to the late nineteenth century, where William Coley, an American bone surgeon, found that intratumoral injections of killed bacteria presented anti-tumor therapeutic effects.[40] The so-called "Coley's Toxin" was a promising outcome as monotherapy with 50% of total 104 patients with soft-tissue sarcoma showing complete tumor regression and more than 5-year survival.[41] Approximately 20% of patients were cured and survived over 20 years due to Coley's pioneering work in cancer immunotherapy.[42]

The aim of cancer immunotherapy, then, is to activate or recover the immune-oncology cycle with self-sustainability to induce and propagate anti-tumor immunity in a restrained manner.[27] For example, small molecule oral drug NLG919 inhibits immunoregulatory enzyme indoleamine 2,3-dioxygenase (IDO),[43] which establishes immune tolerance by inducing T cell anergy and apoptosis, leading to attenuation of T cell inhibition.[44] Toll-like receptor agonists such as CpG oligodeoxynucleotides (CpG ODNs)[45] and imiquimod[46] signal DC maturation to promote antigen presentation, stimulating the adaptive immune response. One potent immunotherapy, checkpoint

blockade immunotherapy, blocks the aforementioned immunosuppressive T cell regulating pathways to enhance systemic anti-tumor immune responses.[47]

Monoclonal checkpoint inhibitors targeting CTLA-4, PD-1, and PD-L1 have restored systemic anti-tumor immunity in a certain portion of patients, leading to the US Food and Drug Administration (FDA) approval of several antibody therapeutics, including anti-CTLA-4 antibody Ipilimumab[48], anti-PD-1 antibodies Pembrolizumab[49], Nivolumab[50] and Cemiplimab[51], and anti-PD-L1 antibodies Atezolizumab[52], Avelumab[53] and Durvalumab[54] as effective therapies for clinical use. Clinical success has primarily been found in a subset of immunogenic tumors, including melanomas, non-small cell lung cancer, and genitourinary cancers.[55-58] However, targeting regulatory immune checkpoints alone does not elicit sufficient or effective responses for most solid tumors, partly due to the low expression of PD-L1 on tumor cells[59] and/or inadequate T cell infiltration into the cancerous tissues[60] in non-immunogenic tumors. As a result, discovering alternate therapies to turn these so-called "cold" tumors "hot" has emerged as a promising direction for cancer immunotherapy research in the past few years.[61]

The combination of CBI with conventional cancer therapies has been under intense investigation, since cell death caused by other therapies may potentiate release of TAs and DAMPs to initiate T cell activation.[58] For example, there are over a hundred clinical trials on the combination of radiation therapy with anti-CTLA-4 or anti-PD-1/PD-L1 antibodies[62-63], while studies of chemotherapy in combination with immunotherapeutics are also ongoing.[64] Immunomodulatory adjuvant treatments are thus being actively pursued to synergize with CBI to break immune tolerance and potentiate host anti-tumor immunity in a broader population of patients (**Figure 1-2**).

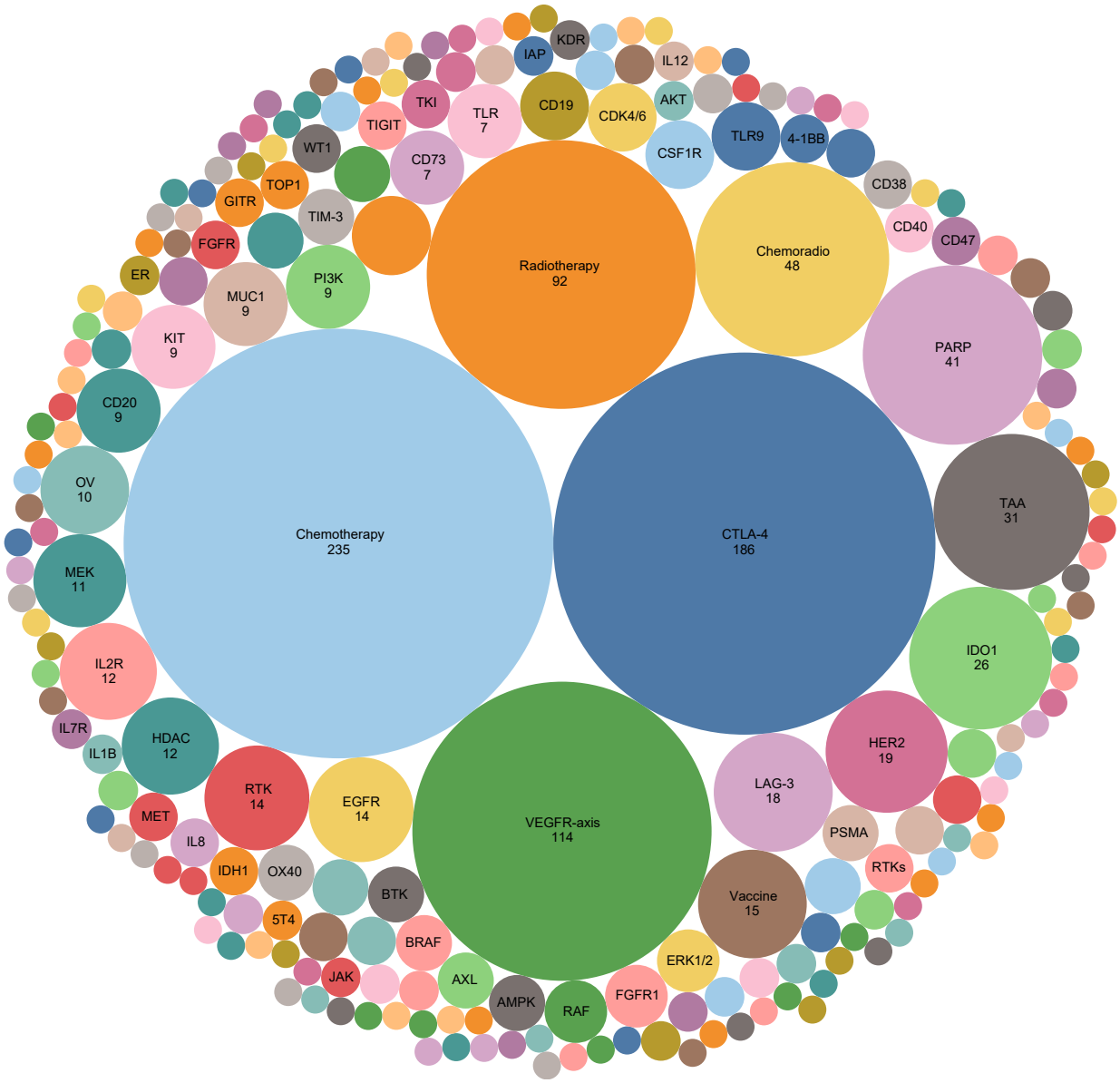

Figure 1-2 The landscape analysis of immunostimulatory adjuvant therapies to combine with anti-PD-1/L1 CBI in clinical trials. The size of the bubble correlates to the number of trials. Data from https://cancerresearch.org/scientists/clinical-accelerator/landscape-of-immuno-oncology-drug-development. Copyright Cancer Research Institute.

1.2 Immunoadjuvant therapy

In immunology, adjuvants refer to any substance that can potentiate or regulate the immune responses to an antigen.[65] The word "adjuvant" comes from the Latin word *adiuvare*, meaning to help.[66] Immune adjuvants have a long history in vaccine manufacturing. As the first clinical use of immunotherapeutics, Coley's toxin, a mixture of killed bacteria, essentially initiates local inflammation and releases pro-inflammatory molecules such as tumor necrosis factor-α (TNF-α) to awaken host immunity to tumorigenesis.[67] Therefore, immunoadjuvant therapy, or immunostimulatory adjuvant therapy, focuses on stimulating inflammatory responses to synergize with CBI to revigorate self-sustained anti-tumor immunity.

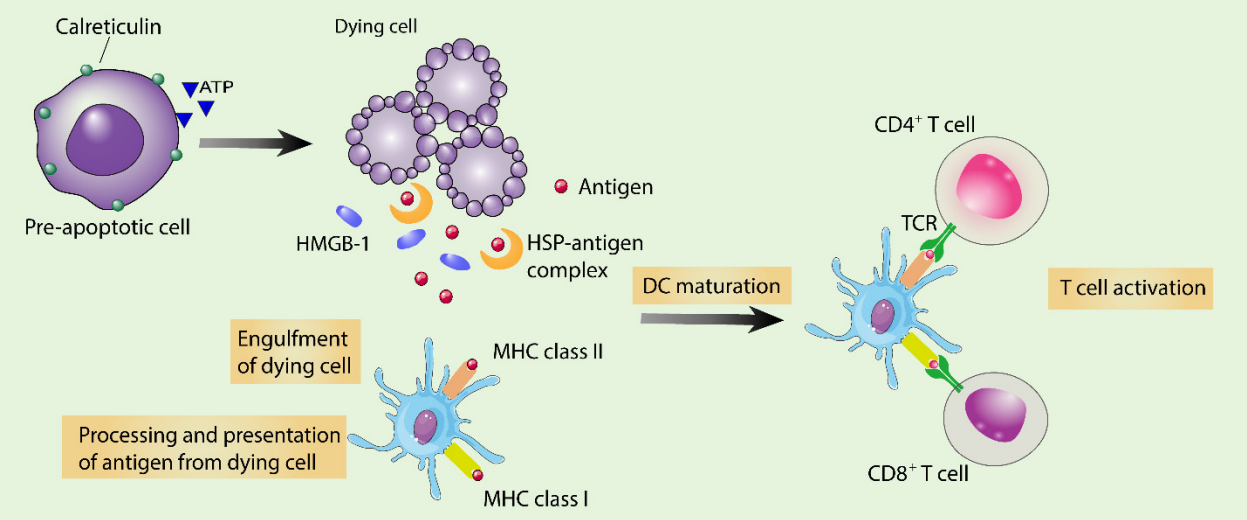

Figure 1-3 In ICD, exposure of CRT, release of HMGB-1, secretion of ATP, TAs and HSP induce the engulfment of cell corpses and debris by APCs (mainly DCs) to stimulate DC maturation. Activated DCs can then prime T cells and adaptive immune responses. Adapted with permission from *Angewandte Chemie International Edition*, **2019**, 58, 670-680. Copyright 2019 John Wiley & Sons, Inc.

Immunoadjuvant therapies are mainly categorized into two subgroups: cancer vaccines and ablative cancer treatments. The former directly immunizes the host with TAs and immune adjuvants, while the later, utilizing ROS *via* radiation, photodynamic process or Fenton-like

reaction, converts tumor to an immunogenic hotbed as *in situ* cancer vaccination by causing tumor cell death in an immunogenic way.[68-69] The immunogenic cell death (ICD) process is characterized by the release of TAs and DAMPs, while local inflammation promotes immunostimulation or subverts immunosuppression for APC maturation, antigen presentation, T cell expansion and tumor infiltration of effector T cells to synergize with CBI. During the ICD process, calreticulin (CRT), a chaperone protein abundant in the endoplasmic reticulum (ER), transposes to the cell surface in response to ER stress. CRT exposure on the cell membrane serves as an "eat-me" signal for macrophages and immature DCs to engulf dying tumor cells and their apoptotic debris.[70] In addition, high mobility group box-1 (HMGB-1), a nucleosome-associated chromatin binding protein, is also released from dead cells to interact with toll-like receptor-4 on DCs for DC maturation and TA presentation.[71] Adenosine triphosphate (ATP), an essential biomolecule for energy storage and conversion, is a third component secreted from dying tumor cells to activate inflammasomes and DCs.[72] Higher levels of CRT exposure, HMGB-1 release and ATP secretion as well as heat shock proteins (HSPs)[73] as DAMPs provide indicators for ICD (**Figure 1-3**).[74]

1.2.1 Cancer vaccine

The principle and methodology of using vaccines for immunization lasts over centuries in the human history of fighting against infectious disease and pandemics.[75-76] Recently, the success of cancer vaccines to prevent cancers associated with exposure to viruses encouraged a more straightforward way to immunize hosts with tumor antigens (TAs) for both prevention and treatment.[77] Ideally, the deliberate vaccination of host immunity with TAs can overcome the insufficient exposure of immune cells to tumor antigens. DAMPs[78] or PAMPs[79] are usually packed

with TAs as immune adjuvants to facilitate immune response. For several decades, cancer vaccines have been explored to amplify tumor-specific T cell responses.[80] In particular, tumor antigen-based cancer vaccines have been widely investigated in the clinic, leading to the approval of the prostatic acid phosphatase based prostate cancer vaccine Sipuleucel T by FDA.[81]

However, traditional approaches to cancer vaccine development face several significant hurdles, including tumor heterogeneity with various somatic mutations and hence varied tumor antigens among patients,[82-83] ineffective delivery of peptide-based tumor antigens to lymph nodes due to rapid renal clearance and enzymatic degradation,[84] inefficient internalization of tumor antigens by APCs,[85] and the ability of tumors to escape from immune surveillance *via* mechanisms such as the PD-1/PD-L1 axis.[86]

Personalized vaccines with neo-antigens or autologous whole tumor lysates as patient-specific cancer immunotherapies can overcome tumor heterogeneity,[87] but their production processes are lengthy, complicated, and expensive.[88] One promising strategy to improve personalized cancer vaccination uses immunostimulatory treatments to generate tumor antigens *in situ*, which can afford systemic antitumor immune responses in a personalized fashion and modulate local tumor microenvironments to relieve immunosuppression.[89] For instance, intratumoral injection of oncolytic viruses such as talimogene laherparepvec (T-VEC) inflicts direct cytotoxic effects on cancer cells and recruits DCs for antigen presentation, acting as *in situ* cancer vaccines with limited side effects[90]. Due to potential bio-safety concerns, non-viral treatments with potent anti-tumor effects, such as phototherapy, radiotherapy, chemotherapy and other treatment releasing TAs, generating DAMPs, or delivering PAMPs are also actively pursued to induce immunogenic cell death.[91]

1.2.2 Radiotherapy

Radiotherapy (RT) is an effective local treatment prevalently used across many cancer types in the clinic. This powerful therapeutic modality kills cancer cells by generating hydroxyl radicals *via* radiolysis and causing DNA double strand breaks upon ionizing energy,[92] which is highly tissue penetrating. Nearly half of all patients will benefit from radiotherapy, with approximately half receiving treatment with curative intents and half for palliation. However, the radiation dose has to be precisely controlled to balance therapeutic benefit and toxic side effects.[93-94]

For years, RT was regarded as immunosuppressive because of the higher sensitivity of T lymphocytes to ionization radiation compared to tumor cells.[95] The local treatment was demonstrated to not only directly kill tumor resident T cells[96] but also promote a more immunosuppressive tumor microenvironment.[97-98] For example, the standard of care for patients receiving organ transplants is to first treat individuals with radiation to weaken the immune system to avoid graft-versus-host disease, the rejection of the donated organ to hosts after transplantation.[99] Recently, however, high-dose, hypofractionated RT has been studied as an immunomodulatory adjuvant treatment with abscopal effect. To date, over a hundred of clinical trials are ongoing to exploit the synergy between hypofractionated RT and immune checkpoint blockade.[100-102]

As a local therapy, RT inflicts ionization damage to tumor tissues in an X-ray dose-dependent manner, with efficacy usually limited by the maximum radiation dose that can be given to a tumor mass without incurring significant injuries to neighboring tissues or organs.[10] Hypofractionated RT with relatively high daily doses of 5–10 Gy and a shortened treatment duration can also trigger a local immune response by releasing immunostimulatory signals to increase T cell infiltration to

the tumor.[103-106] The reported RT-induced upregulation of PD-L1 in tumors further supports the combination of anti-PD-L1 checkpoint blockade with hypofractionated RT.[107-108] However, the immunostimulatory effects of hypofractionated RT are achieved at the expense of damaging side effects on surrounding tissues.[109] Furthermore, the dosing schedule of hypofractionated RT is not synchronous with checkpoint blockade immunotherapy.[110] Toxicity from high doses of X-ray radiation and non-synchronous dosing regimens between RT and CBI thus present major hurdles for optimizing the synergy between these two treatment modalities.

To solve this problem, different strategies have been explored. Medical physicists developed conformation and/or intensity modulated radiotherapies over the past few decades to provide greater spatial control of X-ray energy deposition, thus alleviating normal tissue toxicity.[9] Reducing X-ray doses while maintaining sufficient ionization damage to tumors by using tumor-targeted radiosensitizers can further minimize side effects to the surrounding tissues and also make RT a more compatible and effective adjuvant treatment to enhance checkpoint blockade immunotherapy.[111-112]

Heavy metal-based nanoparticles (NPs) such as Au and HfO_2 NPs have been shown as promising radiosensitizers.[113-116] NPs of high atomic (Z) number elements have high X-ray absorption coefficients and, when selectively deposited in tumors, can significantly increase the radiosensitivity difference between healthy and tumor tissues, effectively reducing radiation dosage without impacting anticancer activity. NP radiosensitizers can generate reactive oxygen species (ROS), typically hydroxyl radicals ($^{\bullet}OH$), to potentially increase the therapeutic index of RT by sparing healthy tissues of high-dose radiation (**Figure 1-4**). HfO_2 NPs as radiosensitizers are actively under clinical investigation.[117] Despite these improvements, radiosensitizers with

stronger radioenhancing effects are still needed to locally sensitize tumors and elicit immunomodulatory effects to enhance cancer immunotherapy.[118-122]

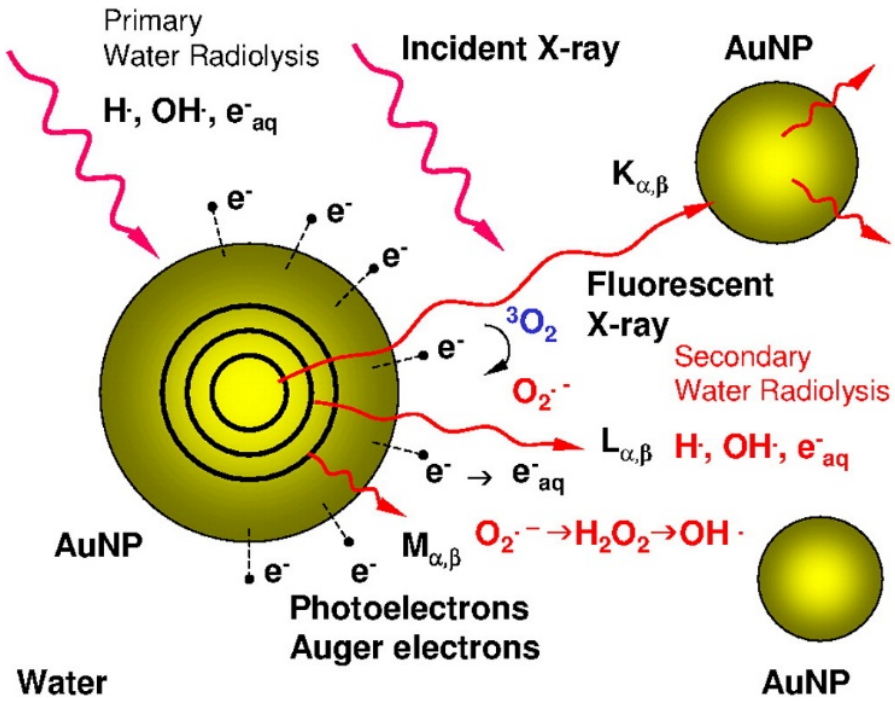

Figure 1-4 Schematic showing several physical processes occurring when incident X-rays interact with high-Z NPs as radiosensitizers for ROS generation and radiosensitization. Reprinted with permission from *Nanomedicine: Nanotechnolology, Biology and Medicine*, **2011**, *7*, 604-614. Copyright 2011 Elsevier Inc.

1.2.3 Photodynamic therapy

In addition to RT, photodynamic therapy (PDT) is another a clinical therapeutic modality with minimal invasiveness and side effects. PDT combines three nontoxic components, photosensitizers (PSs), light, and tissue oxygen ($^3O_2$), to kill cancer cells and induce local inflammation.[123-124] PSs are a class of molecules/materials that can be activated from ground state to excited state by light and further react with other molecules upon light irradiation. Excited state PSs can further couple with $^3O_2$ to generate ROS, including singlet oxygen ($^1O_2$) *via* energy transfer as type II PDT and/or

superoxide anion (O_2^-) *via* electron transfer as type I PDT. Highly cytotoxic ROS further causes oxidative stress to induce apoptosis, necrosis and tumor vasculature rupture.[125-126] However, poor solubility and inefficient cellular internalization of molecular PSs, shallow penetration depth of light through tissue, and insufficient tumor oxygen levels limit the anti-tumor efficacy of PDT.[127]

For better performance in PDT, improvements are need in three aspects. First, light sources with better tissue penetration should be utilized. Second, PSs with intrinsically high extinction coefficients at excitation wavelengths and higher quantum yields of ROS are needed to generate more ROS. In addition, better aqueous stability and efficient cellular enrichment should be expected for an excellent PS. Third, strategies to overcome tumor hypoxia should be coupled and integrated to local PDT treatment. Current commercial PSs have their own strengths and weaknesses. For example, porphyrin and its derivatives feature ideal optical absorption properties but lose energy *via* fluorescence emission; Ir- and Ru-based metal-complexes present high $^1O_2$ conversion but need short wavelength light excitation due to large Stokes shifts. Thus, better PSs are urgently needed for both fundamental research and clinical applications.

As a local therapy, PDT is highly inflammatory, making it an ideal candidate to synergize with cancer immunotherapy. PDT induces acute tumor cell death *via* both apoptosis and necrosis to release DAMPs. Innate immune cells including neutrophils and DCs are recruited *via* chemotaxis and DAMPs, respectively, to generate a strong inflammatory local environment for antigen presentation to the lymph nodes (**Figure 1-5**).[128-129] Subsequent T cell maturation and proliferation not only enhances local tumor destruction but also potentiates systemic antitumor vaccination.

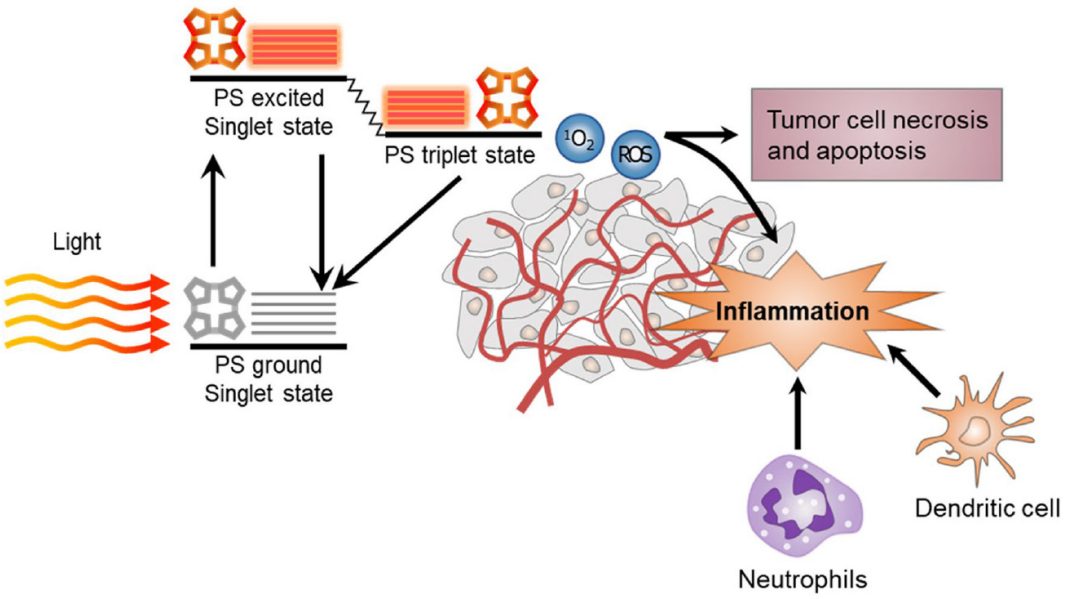

Figure 1-5 Mechanism of PDT and consequent local inflammatory response. Reprinted from *Journal of Pharmaceutical Investigation,* **2012**, *48*, 143-151.

1.2.4 Chemodynamic therapy

Local ablative therapies including RT, PDT and sonodynamic therapy (SDT)[130] kill tumor cells with ROS generated with external stimuli. Recently, another kind of radical therapy, chemodynamic therapy, which generates ROS from endogenous chemical triggers, such as hydrogen peroxide (H_2O_2), hormonal metabolites, and glutathione, has attracted significant attention.[131] In CDT, redox-active metal elements such as Mn,[132] Fe,[133-134] and Cu[135] in tumors decompose intratumoral H_2O_2 to generate cytotoxic $^{\bullet}OH$ and other ROS through Fenton-like reactions. ROS-mediated dynamic therapies are known to be strongly immunogenic by inducing acute local inflammation.[128] However, the efficacy of radical therapies is diminished by many factors in the TME, such as high intracellular concentrations of reducing thiol species,[136] hypoxia,[137] and insufficient endogenous H_2O_2.[138] It is thus of both fundamental and clinical interest to develop new strategies to counteract these adverse factors to enhance the efficacy of CDT.

1.3 Nanoscale Metal-organic frameworks for cancer immunotherapy

Metal-organic frameworks (MOFs), are a class of porous, crystalline hybrid materials constructed from metal-based nodes, also known as secondary building units (SBUs), and organic bridging linkers. Prussian blue, the prototypical MOF constructed from Fe(II)-CN-Fe(III) coordination units, was generated in early eighteenth century as a dark blue pigment.[139] The idea of MOFs was reinvented in early 1990s by Richard Robson[140] and the field of MOF research has since witnessed exponential growth in the past three decades. As a class of inorganic-organic hybrid molecular materials, MOFs have several unique properties, including high porosity, structural stability, synthetic modularity and multifunctionality.[141-142] The applications of MOFs are versatile and diverse, from catalysis,[143-148] energy conversion,[149-152] gas storage/separation,[153-157] conductivity,[158-162] ferroelectricity,[163-164] magnetism,[165] to non-linear optics.[166-167] In biomedical fields, MOFs have also played important roles in biomedical sensing/imaging, [168-173] and drug delivery.[174-176]

The ability for orthogonal design and controllable synthesis *via* coordination chemistry of SBUs and organic linkers allows for the synthesis of a variety of MOF topologies and structures (**Figure 1-6**).[177] So-called reticular chemistry enables versatile design and precise synthesis by selecting metals with the desired coordination chemistry and ligands with the desired geometry.[178-181] Functionalities can thus be intentionally incorporated into MOFs and further integrated with post-synthetic modification on its components: organic linkers,[179, 182-183] inorganic SBUs,[145, 177, 182-185] pores,[186-189] and MOF surfaces.[176]

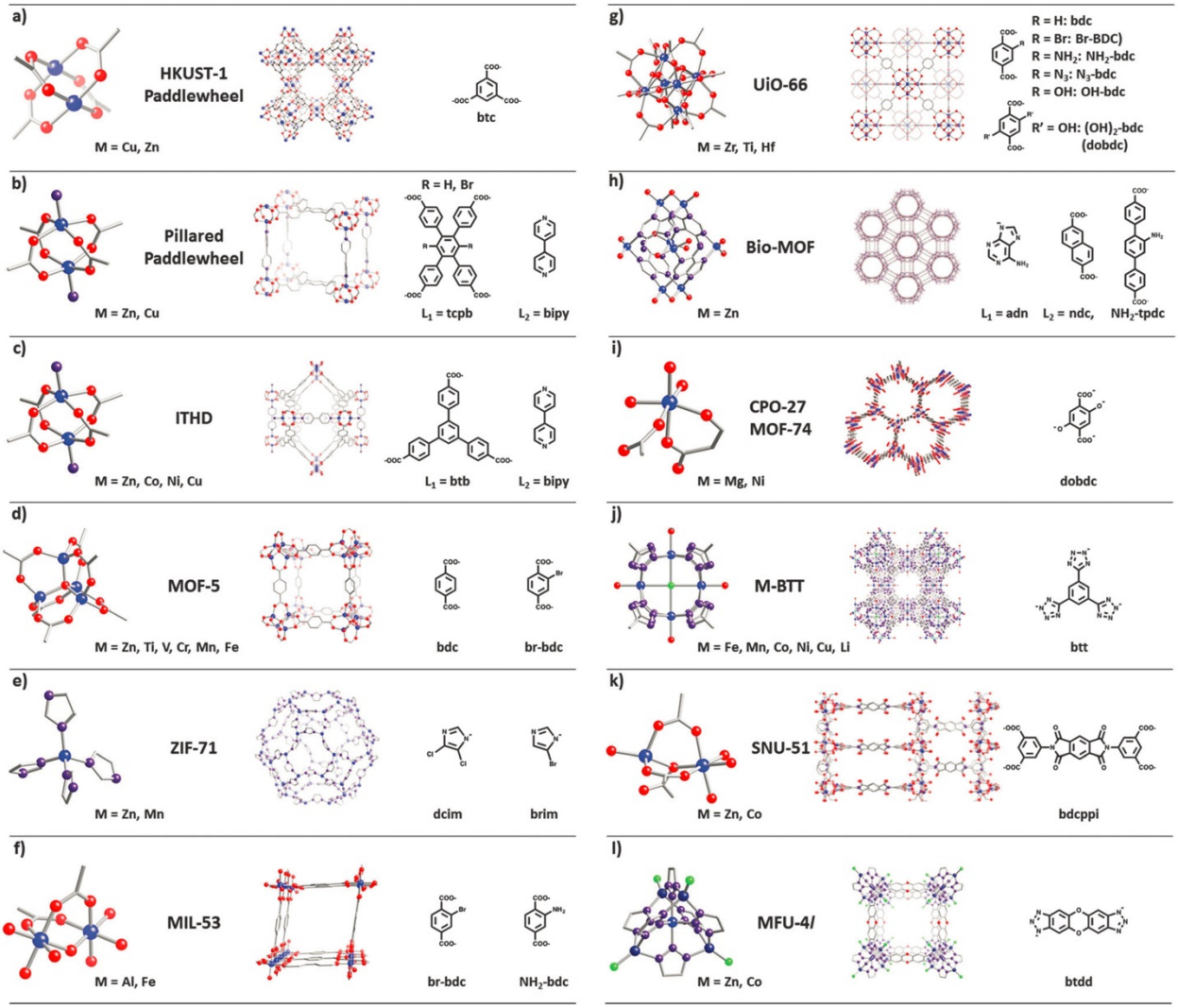

Figure 1-6 SBUs (left), coordination topology (middle), and organic bridging linkers (right) of various MOFs. Atoms are as follows: blue - metal; red - oxygen; purple - nitrogen; grey - carbon; green - chlorine. Adapted with permission from *Chemical Society Review*, **2014**, 43, 5896-5912. Copyright 2014 The Royal Society of Chemistry.

The merging of synthetic chemistry and materials science led to the development of nanotechnology for biomedical applications.[190-199] In the context of MOFs and nanotechnology, a new class of nanomaterials, nanoscale metal-organic frameworks (nMOFs) epitomize the merging of nanotechnology and reticular chemistry. When MOFs are scaled down to the nano-regime,

nMOFs have many advantages compared to purely inorganic or organic nanomaterials: (1) As a type of crystalline frameworks, nMOFs integrate both high porosity and crystallinity, which greatly benefit the development of nMOFs for ROS-mediated inflammatory local treatment. (2) As a class of molecular materials, nMOFs possess compositional tunability and synthetic flexibility for precise material design. (3) Composed of metal-based SBUs and organic bridging linkers, nMOFs can be multi-functionalized and modified post-synthetically. (4) Relatively labile coordination bond connections make nMOFs intrinsically biodegradable in physiological environments for biocompatibility. As a result, nMOFs have been successfully applied to the delivery of chemotherapeutic agents,[200-202] imaging contrast agents,[172, 203] photosensitizers,[204-213] proteins[214-215] and gene therapy drugs.[216-218]

In this dissertation, I report the progress on the design of nMOFs as nanosensitizers to enhance RT,[219] mediate radiotherapy-radiodynamic therapy (RT-RDT),[220-221] and enable PDT and CDT[222] with the advantages of high payload, crystalline order, and porous structures for ROS generation. These therapies augment innate immunity *via* nMOF-mediated local inflammation to synergize with systemic immunotherapy, reinvigorating host anti-tumor immunity for systemic tumor rejection (Scheme 1-1).[223]

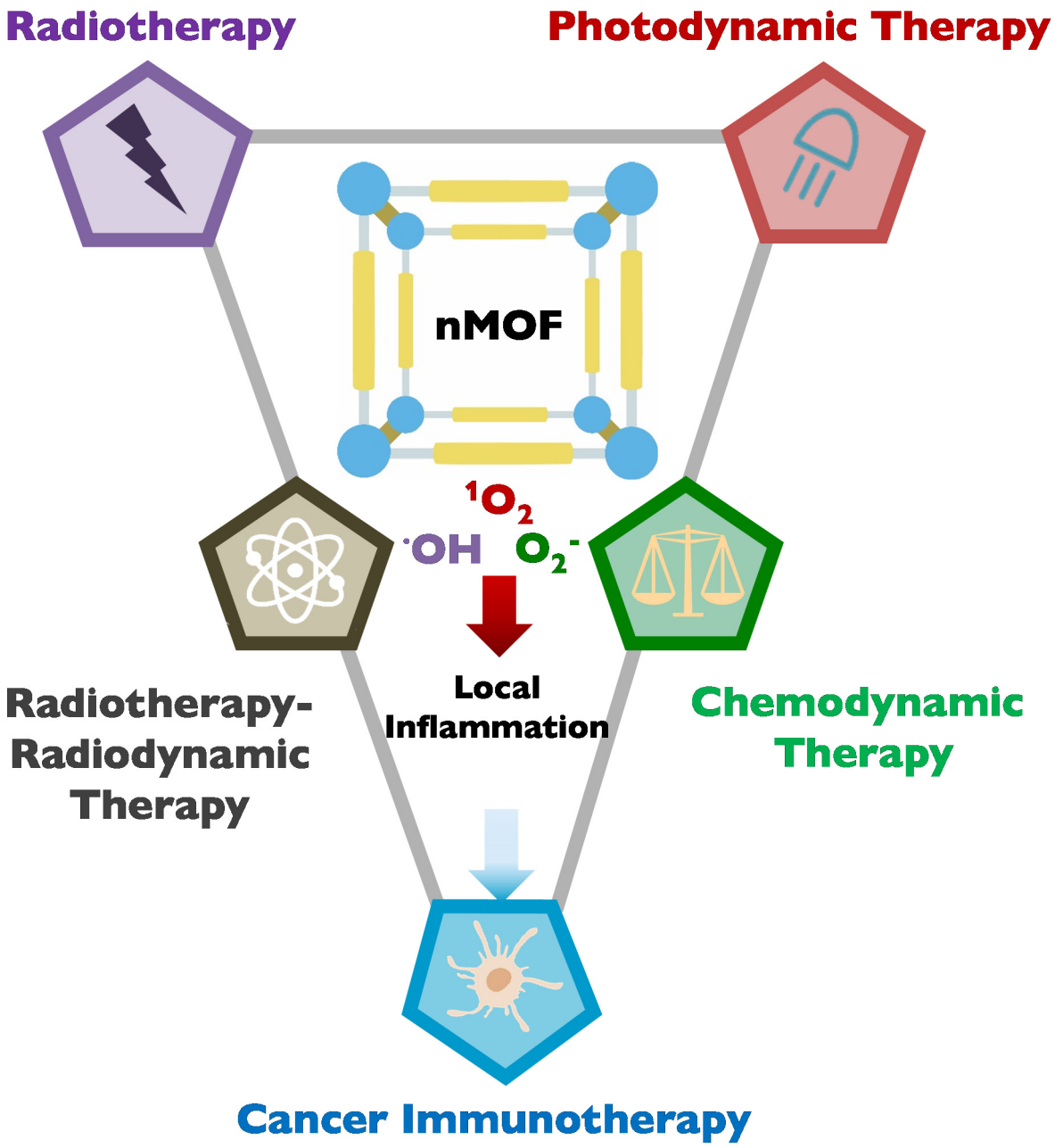

Scheme 1-1 Schematic showing local nMOF-mediated ROS generation *via* PDT, RT, RT-RDT, and CDT to kill tumor cells in an immunogenic way to augment immune response for the synergistic effect with CBI. Adapted with permission from *ACS Central Science* **2020**, DOI: 10.1021/acscentsci.0c00397.

1.4 References

1. Cooper, G. M., The development and causes of cancer. In *The Cell: A Molecular Approach. 2nd edition*, Sinauer Associates: Sunderland, MA, 2000.

2. Miller, K. D.; Nogueira, L.; Mariotto, A. B.; Rowland, J. H.; Yabroff, K. R.; Alfano, C. M.; Jemal, A.; Kramer, J. L.; Siegel, R. L., Cancer treatment and survivorship statistics, 2019. *CA: A Cancer Journal for Clinicians* **2019**. *69* (5), 363-385.

3. Siegel, R. L.; Miller, K. D.; Jemal, A., Cancer statistics, 2019. *CA: A Cancer Journal for Clinicians* **2019,** *69* (1), 7-34.

4. Chen, Q.; Wang, C.; Zhang, X.; Chen, G.; Hu, Q.; Li, H.; Wang, J.; Wen, D.; Zhang, Y.; Lu, Y., *In situ* sprayed bioresponsive immunotherapeutic gel for post-surgical cancer treatment. *Nature Nanotechnology* **2019,** *14* (1), 89-97.

5. Hamdy, F. C.; Donovan, J. L.; Lane, J.; Mason, M.; Metcalfe, C.; Holding, P.; Davis, M.; Peters, T. J.; Turner, E. L.; Martin, R. M., 10-year outcomes after monitoring, surgery, or radiotherapy for localized prostate cancer. *New England Journal of Medicine* **2016,** *375*, 1415-1424.

6. Loughney, L.; West, M.; Kemp, G.; Grocott, M.; Jack, S., Exercise intervention in people with cancer undergoing neoadjuvant cancer treatment and surgery: a systematic review. *European Journal of Surgical Oncology* **2016,** *42* (1), 28-38.

7. Bouwman, P.; Jonkers, J., The effects of deregulated DNA damage signalling on cancer chemotherapy response and resistance. *Nature Reviews Cancer* **2012,** *12* (9), 587-598.

8. André, N.; Carré, M.; Pasquier, E., Metronomics: towards personalized chemotherapy? *Nature Reviews Clinical oncology* **2014,** *11* (7), 413.

9. Schaue, D.; McBride, W. H., Opportunities and challenges of radiotherapy for treating cancer. *Nature Reviews Clinical Oncology* **2015,** *12* (9), 527.

10. Thariat, J.; Hannoun-Levi, J.-M.; Myint, A. S.; Vuong, T.; Gérard, J.-P., Past, present, and future of radiotherapy for the benefit of patients. *Nature Reviews Clinical Oncology* **2013,** *10* (1), 52.

11. Flintoft, L., Recurrence. *Nature Reviews Cancer* **2003,** *3* (10), 718-718.

12. Barker, H. E.; Paget, J. T.; Khan, A. A.; Harrington, K. J., The tumour microenvironment after radiotherapy: mechanisms of resistance and recurrence. *Nature reviews Cancer* **2015,** *15* (7), 409-425.

13. Lee-Jones, C.; Humphris, G.; Dixon, R.; Bebbington Hatcher, M., Fear of cancer recurrence—a literature review and proposed cognitive formulation to explain exacerbation of

recurrence fears. *Psycho-Oncology: Journal of the Psychological, Social and Behavioral Dimensions of Cancer* **1997,** *6* (2), 95-105.

14. Ben-Eliyahu, S., The promotion of tumor metastasis by surgery and stress: immunological basis and implications for psychoneuroimmunology. *Brain, behavior, and immunity* **2003,** *17* (1), 27-36.

15. Martin, O. A.; Anderson, R. L.; Narayan, K.; MacManus, M. P., Does the mobilization of circulating tumour cells during cancer therapy cause metastasis? *Nature Reviews Clinical Oncology* **2017,** *14* (1), 32.

16. Prigerson, H. G.; Bao, Y.; Shah, M. A.; Paulk, M. E.; LeBlanc, T. W.; Schneider, B. J.; Garrido, M. M.; Reid, M. C.; Berlin, D. A.; Adelson, K. B., Chemotherapy use, performance status, and quality of life at the end of life. *JAMA Oncology* **2015,** *1* (6), 778-784.

17. Coates, A.; Gebski, V.; Bishop, J. F.; Jeal, P. N.; Woods, R. L.; Snyder, R.; Tattersall, M. H.; Byrne, M.; Harvey, V.; Gill, G., Improving the quality of life during chemotherapy for advanced breast cancer. *New England Journal of Medicine* **1987,** *317* (24), 1490-1495.

18. Baracos, V. E.; Martin, L.; Korc, M.; Guttridge, D. C.; Fearon, K. C., Cancer-associated cachexia. *Nature Reviews Disease Primers* **2018,** *4* (1), 1-18.

19. Husson, O.; Zebrack, B. J.; Block, R.; Embry, L.; Aguilar, C.; Hayes-Lattin, B.; Cole, S., Health-related quality of life in adolescent and young adult patients with cancer: a longitudinal study. *Journal of Clinical Oncology* **2017,** *35* (6), 652-659.

20. Mellman, I.; Coukos, G.; Dranoff, G., Cancer immunotherapy comes of age. *Nature* **2011,** *480* (7378), 480-489.

21. Couzin-Frankel, J., Cancer immunotherapy. *Science* **2013,** *342* (6165), 1432-1433

22. Swann, J. B.; Smyth, M. J., Immune surveillance of tumors. *The Journal of Clinical Investigation* **2007,** *117* (5), 1137-1146.

23. Akira, S.; Uematsu, S.; Takeuchi, O., Pathogen recognition and innate immunity. *Cell* **2006,** *124* (4), 783-801.

24. Ben-Neriah, Y.; Karin, M., Inflammation meets cancer, with NF-κB as the matchmaker. *Nature Immunology* **2011,** *12* (8), 715.

25. Marur, S.; D'Souza, G.; Westra, W. H.; Forastiere, A. A., HPV-associated head and neck cancer: a virus-related cancer epidemic. *The Lancet Oncology* **2010,** *11* (8), 781-789.

26. Perz, J. F.; Armstrong, G. L.; Farrington, L. A.; Hutin, Y. J. F.; Bell, B. P., The contributions of hepatitis B virus and hepatitis C virus infections to cirrhosis and primary liver cancer worldwide. *Journal of Hepatology* **2006,** *45* (4), 529-538.

27. Chen, D. S.; Mellman, I., Oncology meets immunology: the cancer-immunity cycle. *Immunity* **2013,** *39* (1), 1-10.

28. Chan, T. A.; Yarchoan, M.; Jaffee, E.; Swanton, C.; Quezada, S. A.; Stenzinger, A.; Peters, S., Development of tumor mutation burden as an immunotherapy biomarker: utility for the oncology clinic. *Annals of Oncology* **2019,** *30* (1), 44-56.

29. Whiteside, T. L.; Stanson, J.; Shurin, M. R.; Ferrone, S., Antigen-processing machinery in human dendritic cells: up-regulation by maturation and down-regulation by tumor cells. *The Journal of Immunology* **2004,** *173* (3), 1526-1534.

30. Blankenstein, T.; Coulie, P. G.; Gilboa, E.; Jaffee, E. M., The determinants of tumour immunogenicity. *Nature Reviews Cancer* **2012,** *12* (4), 307-313.

31. Kim, R.; Emi, M.; Tanabe, K., Cancer immunoediting from immune surveillance to immune escape. *Immunology* **2007,** *121* (1), 1-14.

32. Dunn, G. P.; Bruce, A. T.; Ikeda, H.; Old, L. J.; Schreiber, R. D., Cancer immunoediting: from immunosurveillance to tumor escape. *Nature Immunology* **2002,** *3* (11), 991-998.

33. Slavik, J. M.; Hutchcroft, J. E.; Bierer, B. E., CD28/CTLA-4 and CD80/CD86 families. *Immunologic Research* **1999,** *19* (1), 1-24.

34. Linsley, P. S.; Greene, J. L.; Brady, W.; Bajorath, J.; Ledbetter, J. A.; Peach, R., Human B7-1 (CD80) and B7-2 (CD86) bind with similar avidities but distinct kinetics to CD28 and CTLA-4 receptors. *Immunity* **1994,** *1* (9), 793-801.

35. Liang, S. C.; Latchman, Y. E.; Buhlmann, J. E.; Tomczak, M. F.; Horwitz, B. H.; Freeman, G. J.; Sharpe, A. H., Regulation of PD-1, PD-L1, and PD-L2 expression during normal and autoimmune responses. *European Journal of Immunology* **2003,** *33* (10), 2706-2716.

36. Ohigashi, Y.; Sho, M.; Yamada, Y.; Tsurui, Y.; Hamada, K.; Ikeda, N.; Mizuno, T.; Yoriki, R.; Kashizuka, H.; Yane, K., Clinical significance of programmed death-1 ligand-1 and programmed death-1 ligand-2 expression in human esophageal cancer. *Clinical Cancer Research* **2005,** *11* (8), 2947-2953.

37. Blank, C.; Brown, I.; Peterson, A. C.; Spiotto, M.; Iwai, Y.; Honjo, T.; Gajewski, T. F., PD-L1/B7H-1 inhibits the effector phase of tumor rejection by T cell receptor (TCR) transgenic $CD8^+$ T cells. *Cancer research* **2004,** *64* (3), 1140-1145.

38. Li, Z.; Dong, P.; Ren, M.; Song, Y.; Qian, X.; Yang, Y.; Li, S.; Zhang, X.; Liu, F., PD-L1 expression is associated with tumor FOXP3+ regulatory T-cell infiltration of breast cancer and poor prognosis of patient. *Journal of Cancer* **2016,** *7* (7), 784.

39. Shi, Y.; Zheng, W.; Yang, K.; Harris, K. G.; Ni, K.; Xue, L.; Lin, W.; Chang, E. B.; Weichselbaum, R. R.; Fu, Y.-X., Intratumoral accumulation of gut microbiota facilitates CD47-based immunotherapy *via* STING signaling. *Journal of Experimental Medicine* **2020,** *217* (5).

40. Coley, W. B., Contribution to the knowledge of sarcoma. *Annals of Surgery* **1891,** *14*, 199-220.

41. Starnes, C. O., Coley's toxins in perspective. *Nature* **1992,** *357* (6373), 11-12.

42. Coley, W. B., The Treatment of Sarcoma of the Long Bones. *Annals of Surgery* **1933,** *97* (3), 434-60.

43. Mautino, M. R.; Jaipuri, F. A.; Waldo, J.; Kumar, S.; Adams, J.; Van Allen, C.; Marcinowicz-Flick, A.; Munn, D.; Vahanian, N.; Link, C. J., NLG919, a novel indoleamine-2, 3-dioxygenase (IDO)-pathway inhibitor drug candidate for cancer therapy. *Cancer Research* **2013** *73* (8), 491-491 .

44. Löb, S.; Königsrainer, A.; Rammensee, H.-G.; Opelz, G.; Terness, P., Inhibitors of indoleamine-2, 3-dioxygenase for cancer therapy: can we see the wood for the trees? *Nature Reviews Cancer* **2009,** *9* (6), 445-452.

45. Weiner, G. J.; Liu, H.-M.; Wooldridge, J. E.; Dahle, C. E.; Krieg, A. M., Immunostimulatory oligodeoxynucleotides containing the CpG motif are effective as immune adjuvants in tumor antigen immunization. *Proceedings of the National Academy of Sciences* **1997,** *94* (20), 10833-10837.

46. Sauder, D. N., Immunomodulatory and pharmacologic properties of imiquimod. *Journal of the American Academy of Dermatology* **2000,** *43* (1), 6-11.

47. Pardoll, D. M., The blockade of immune checkpoints in cancer immunotherapy. *Nature Reviews Cancer* **2012,** *12* (4), 252-264.

48. Lipson, E. J.; Drake, C. G., Ipilimumab: an anti-CTLA-4 antibody for metastatic melanoma. *Clinical Cancer Research* **2011,** *17* (22), 6958-6962.

49. Robert, C.; Schachter, J.; Long, G. V.; Arance, A.; Grob, J. J.; Mortier, L.; Daud, A.; Carlino, M. S.; McNeil, C.; Lotem, M., Pembrolizumab versus ipilimumab in advanced melanoma. *New England Journal of Medicine* **2015,** *372* (26), 2521-2532.

50. Wolchok, J. D.; Kluger, H.; Callahan, M. K.; Postow, M. A.; Rizvi, N. A.; Lesokhin, A. M.; Segal, N. H.; Ariyan, C. E.; Gordon, R.-A.; Reed, K., Nivolumab plus ipilimumab in advanced melanoma. *New England Journal of Medicine* **2013,** *369*, 122-133.

51. Migden, M. R.; Rischin, D.; Schmults, C. D.; Guminski, A.; Hauschild, A.; Lewis, K. D.; Chung, C. H.; Hernandez-Aya, L.; Lim, A. M.; Chang, A. L. S., PD-1 blockade with cemiplimab

in advanced cutaneous squamous-cell carcinoma. *New England Journal of Medicine* **2018,** *379* (4), 341-351.

52. Socinski, M. A.; Jotte, R. M.; Cappuzzo, F.; Orlandi, F.; Stroyakovskiy, D.; Nogami, N.; Rodríguez-Abreu, D.; Moro-Sibilot, D.; Thomas, C. A.; Barlesi, F., Atezolizumab for first-line treatment of metastatic nonsquamous NSCLC. *New England Journal of Medicine* **2018,** *378* (24), 2288-2301.

53. Motzer, R. J.; Penkov, K.; Haanen, J.; Rini, B.; Albiges, L.; Campbell, M. T.; Venugopal, B.; Kollmannsberger, C.; Negrier, S.; Uemura, M., Avelumab plus axitinib versus sunitinib for advanced renal-cell carcinoma. *New England Journal of Medicine* **2019,** *380* (12), 1103-1115.

54. Antonia, S. J.; Villegas, A.; Daniel, D.; Vicente, D.; Murakami, S.; Hui, R.; Kurata, T.; Chiappori, A.; Lee, K. H.; de Wit, M., Overall survival with durvalumab after chemoradiotherapy in stage III NSCLC. *New England Journal of Medicine* **2018,** *379* (24), 2342-2350.

55. Le, D. T.; Uram, J. N.; Wang, H.; Bartlett, B. R.; Kemberling, H.; Eyring, A. D.; Skora, A. D.; Luber, B. S.; Azad, N. S.; Laheru, D., PD-1 blockade in tumors with mismatch-repair deficiency. *New England Journal of Medicine* **2015,** *372* (26), 2509-2520.

56. Errico, A., Immunotherapy: PD-1–PD-L1 axis: efficient checkpoint blockade against cancer. *Nature Reviews Clinical Oncology* **2014,** *12* (2), 63.

57. Francisco, L. M.; Sage, P. T.; Sharpe, A. H., The PD-1 pathway in tolerance and autoimmunity. *Immunological Reviews* **2010,** *236* (1), 219-242.

58. Sharma, P.; Allison, J. P., The future of immune checkpoint therapy. *Science* **2015,** *348* (6230), 56-61.

59. Patel, S. P.; Kurzrock, R., PD-L1 expression as a predictive biomarker in cancer immunotherapy. *Molecular Cancer Therapeutics* **2015,** *14* (4), 847-856.

60. Tang, H.; Wang, Y.; Chlewicki, L. K.; Zhang, Y.; Guo, J.; Liang, W.; Wang, J.; Wang, X.; Fu, Y.-X., Facilitating T cell infiltration in tumor microenvironment overcomes resistance to PD-L1 blockade. *Cancer Cell* **2016,** *29* (3), 285-296.

61. Xin, Y. J.; Hodge, J.; Oliva, C.; Neftelinov, S.; Hubbard-Lucey, V.; Tang, J., Trends in clinical development for PD-1/PD-L1 inhibitors. *Nature Reviews Drug Discovery* **2020,** *19* (3), 163.

62. Tang, C.; Wang, X.; Soh, H.; Seyedin, S.; Cortez, M. A.; Krishnan, S.; Massarelli, E.; Hong, D.; Naing, A.; Diab, A., Combining radiation and immunotherapy: a new systemic therapy for solid tumors? *Cancer Immunology Research* **2014,** *2* (9), 831-838.

63. Crittenden, M.; Kohrt, H.; Levy, R.; Jones, J.; Camphausen, K.; Dicker, A.; Demaria, S.; Formenti, S. Current clinical trials testing combinations of immunotherapy and radiation, *Seminars in Radiation Oncology*, **2015,** *25* (1), 54-64.

64. Cook, A. M.; Lesterhuis, W. J.; Nowak, A. K.; Lake, R. A., Chemotherapy and immunotherapy: mapping the road ahead. *Current opinion in immunology* **2016,** *39*, 23-29.

65. Guy, B., The perfect mix: recent progress in adjuvant research. *Nature Reviews Microbiology* **2007,** *5* (7), 396-397.

66. Kool, M.; Fierens, K.; Lambrecht, B. N., Alum adjuvant: some of the tricks of the oldest adjuvant. *Journal of Medical Microbiology* **2012,** *61* (7), 927-934.

67. Tsung, K.; Norton, J. A., Lessons from Coley's Toxin. *Surgical Oncology* **2006,** *15* (1), 25-28.

68. Zitvogel, L.; Kepp, O.; Senovilla, L.; Menger, L.; Chaput, N.; Kroemer, G., Immunogenic tumor cell death for optimal anticancer therapy: the calreticulin exposure pathway. *Clincal Cancer Research* **2010,** *16* (12), 3100-3104.

69. Gotwals, P.; Cameron, S.; Cipolletta, D.; Cremasco, V.; Crystal, A.; Hewes, B.; Mueller, B.; Quaratino, S.; Sabatos-Peyton, C.; Petruzzelli, L.; Engelman, J. A.; Dranoff, G., Prospects for combining targeted and conventional cancer therapy with immunotherapy. *Nature Review Cancer* **2017,** *17* (5), 286-301.

70. Grimsley, C.; Ravichandran, K. S., Cues for apoptotic cell engulfment: eat-me, don't eat-me and come-get-me signals. *Trends in Cell Biology* **2003,** *13* (12), 648-656.

71. Sims, G. P.; Rowe, D. C.; Rietdijk, S. T.; Herbst, R.; Coyle, A. J., HMGB1 and RAGE in Inflammation and Cancer. *Annual Review of Immunology* **2010,** *28* (1), 367-388.

72. Aymeric, L.; Apetoh, L.; Ghiringhelli, F.; Tesniere, A.; Martins, I.; Kroemer, G.; Smyth, M. J.; Zitvogel, L., Tumor cell death and ATP release prime dendritic cells and efficient anticancer immunity. *Cancer Research* **2010,** *70* (3), 855-858.

73. Duan, X.; Chan, C.; Lin, W., Nanoparticle-Mediated Immunogenic Cell Death Enables and Potentiates Cancer Immunotherapy. *Angewandte Chemie International Edition* **2019,** *58* (3), 670-680.

74. Duan, X.; Chan, C.; Lin, W., Nanoparticle-mediated Immunogenic Cell Death Enables and Potentiates Cancer Immunotherapy. *Angewandte Chemie International Edition* **2019,** *58* (3), 670-680.

75. Omer, S. B.; Salmon, D. A.; Orenstein, W. A.; Dehart, M. P.; Halsey, N., Vaccine refusal, mandatory immunization, and the risks of vaccine-preventable diseases. *New England Journal of Medicine* **2009,** *360* (19), 1981-1988.

76. Plotkin, S. A.; Plotkin, S. L., The development of vaccines: how the past led to the future. *Nature Reviews Microbiology* **2011,** *9* (12), 889-893.

77. Palefsky, J. M.; Giuliano, A. R.; Goldstone, S.; Moreira Jr, E. D.; Aranda, C.; Jessen, H.; Hillman, R.; Ferris, D.; Coutlee, F.; Stoler, M. H., HPV vaccine against anal HPV infection and anal intraepithelial neoplasia. *New England Journal of Medicine* **2011,** *365* (17), 1576-1585.

78. Wang, J.; Gao, Z. P.; Qin, S.; Liu, C. B.; Zou, L. L., Calreticulin is an effective immunologic adjuvant to tumor-associated antigens. *Experimental and Therapeutic Medicine* **2017,** *14* (4), 3399-3406.

79. Morishita, M.; Takahashi, Y.; Matsumoto, A.; Nishikawa, M.; Takakura, Y., Exosome-based tumor antigens–adjuvant co-delivery utilizing genetically engineered tumor cell-derived exosomes with immunostimulatory CpG DNA. *Biomaterials* **2016,** *111*, 55-65.

80. Goldman, B.; DeFrancesco, L., The cancer vaccine roller coaster. *Nature Biotechnology* **2009,** *27* (2), 129.

81. Hu, Z.; Ott, P. A.; Wu, C. J., Towards personalized, tumour-specific, therapeutic vaccines for cancer. *Nature Reviews Immunology* **2018,** *18* (3), 168.

82. Sahin, U.; Türeci, Ö., Personalized vaccines for cancer immunotherapy. *Science* **2018,** *359* (6382), 1355-1360.

83. Tanyi, J. L.; Bobisse, S.; Ophir, E.; Tuyaerts, S.; Roberti, A.; Genolet, R.; Baumgartner, P.; Stevenson, B. J.; Iseli, C.; Dangaj, D., Personalized cancer vaccine effectively mobilizes antitumor T cell immunity in ovarian cancer. *Science Translational Medicine* **2018,** *10* (436), 5931.

84. Purcell, A. W.; McCluskey, J.; Rossjohn, J., More than one reason to rethink the use of peptides in vaccine design. *Nature Reviews Drug discovery* **2007,** *6* (5), 404.

85. Liu, H.; Moynihan, K. D.; Zheng, Y.; Szeto, G. L.; Li, A. V.; Huang, B.; Van Egeren, D. S.; Park, C.; Irvine, D. J., Structure-based programming of lymph-node targeting in molecular vaccines. *Nature* **2014,** *507* (7493), 519.

86. Joyce, J. A.; Fearon, D. T., T cell exclusion, immune privilege, and the tumor microenvironment. *Science* **2015,** *348* (6230), 74-80.

87. Kuai, R.; Ochyl, L. J.; Bahjat, K. S.; Schwendeman, A.; Moon, J. J., Designer vaccine nanodiscs for personalized cancer immunotherapy. *Nature Materials* **2017,** *16* (4), 489.

88. Scheetz, L.; Park, K. S.; Li, Q.; Lowenstein, P. R.; Castro, M. G.; Schwendeman, A.; Moon, J. J., Engineering patient-specific cancer immunotherapies. *Nature Biomedical Engineering* **2019,** *3* (10), 768-782.

89. Wang, H.; Mooney, D. J., Biomaterial-assisted targeted modulation of immune cells in cancer treatment. *Nature Materials* **2018,** *17* (9), 761-772.

90. Liu, C.; Lou, Y.; Lizée, G.; Qin, H.; Liu, S.; Rabinovich, B.; Kim, G. J.; Wang, Y.-H.; Ye, Y.; Sikora, A. G., Plasmacytoid dendritic cells induce NK cell–dependent, tumor antigen–specific T cell cross-priming and tumor regression in mice. *The Journal of Clinical Investigation* **2008,** *118* (3), 1165-1175.

91. Kepp, O.; Marabelle, A.; Zitvogel, L.; Kroemer, G., Oncolysis without viruses—inducing systemic anticancer immune responses with local therapies. *Nature Reviews Clinical Oncology* **2019**, 1-16.

92. Lomax, M.; Folkes, L.; O'neill, P., Biological consequences of radiation-induced DNA damage: relevance to radiotherapy. *Clinical Oncology* **2013,** *25* (10), 578-585.

93. Jaffray, D. A.; Gospodarowicz, M. K., Radiation therapy for cancer. In *Cancer: Disease Control Priorities, Third Edition (Volume 3)*, Gelband, H.; Jha, P.; Sankaranarayanan, R.; Horton, S., Eds. Washington (DC), **2015**.

94. De Ruysscher, D.; Niedermann, G.; Burnet, N. G.; Siva, S.; Lee, A. W.; Hegi-Johnson, F., Radiotherapy toxicity. *Nature Reviews Disease Primers* **2019,** *5* (1), 1-20.

95. Schaue, D.; McBride, W. H., T lymphocytes and normal tissue responses to radiation. *Frontiers in Oncology* **2012,** *2*, 119.

96. Wara, W. M., Immunosuppression associated with radiation therapy. *International Journal of Radiation Oncology • Biology • Physics* **1977,** *2* (5), 593-596.

97. Trott, K.-R.; Kamprad, F., Radiobiological mechanisms of anti-inflammatory radiotherapy. *Radiotherapy and Oncology* **1999,** *51* (3), 197-203.

98. Kachikwu, E. L.; Iwamoto, K. S.; Liao, Y.-P.; DeMarco, J. J.; Agazaryan, N.; Economou, J. S.; McBride, W. H.; Schaue, D., Radiation enhances regulatory T cell representation. *International Journal of Radiation Oncology • Biology • Physics* **2011,** *81* (4), 1128-1135.

99. Slavin, S.; Fuks, Z.; Kaplan, H.; Strober, S., Transplantation of allogeneic bone marrow without graft-versus-host disease using total lymphoid irradiation. *The Journal of Experimental Medicine* **1978,** *147* (4), 963-972.

100. Gajewski, T. F.; Schreiber, H.; Fu, Y.-X., Innate and adaptive immune cells in the tumor microenvironment. *Nature Immunology* **2013,** *14* (10), 1014.

101. Schaue, D., A century of radiation therapy and adaptive immunity. *Frontiers in Immunology* **2017,** *8*, 431.

102. Apetoh, L.; Ghiringhelli, F.; Tesniere, A.; Obeid, M.; Ortiz, C.; Criollo, A.; Mignot, G.; Maiuri, M. C.; Ullrich, E.; Saulnier, P., Toll-like receptor 4–dependent contribution of the immune system to anticancer chemotherapy and radiotherapy. *Nature Medicine* **2007,** *13* (9), 1050-1059.

103. Reynders, K.; Illidge, T.; Siva, S.; Chang, J. Y.; De Ruysscher, D., The abscopal effect of local radiotherapy: using immunotherapy to make a rare event clinically relevant. *Cancer Treatment Reviews* **2015,** *41* (6), 503-510.

104. Lugade, A. A.; Moran, J. P.; Gerber, S. A.; Rose, R. C.; Frelinger, J. G.; Lord, E. M., Local radiation therapy of B16 melanoma tumors increases the generation of tumor antigen-specific effector cells that traffic to the tumor. *The Journal of Immunology* **2005,** *174* (12), 7516-7523.

105. Lee, Y.; Auh, S. L.; Wang, Y.; Burnette, B.; Wang, Y.; Meng, Y.; Beckett, M.; Sharma, R.; Chin, R.; Tu, T., Therapeutic effects of ablative radiation on local tumor require CD8+ T cells: changing strategies for cancer treatment. *Blood, The Journal of the American Society of Hematology* **2009,** *114* (3), 589-595.

106. Dovedi, S. J.; Adlard, A. L.; Lipowska-Bhalla, G.; McKenna, C.; Jones, S.; Cheadle, E. J.; Stratford, I. J.; Poon, E.; Morrow, M.; Stewart, R., Acquired resistance to fractionated radiotherapy can be overcome by concurrent PD-L1 blockade. *Cancer Research* **2014,** *74* (19), 5458-5468.

107. Deng, L.; Liang, H.; Burnette, B.; Beckett, M.; Darga, T.; Weichselbaum, R. R.; Fu, Y.-X., Irradiation and anti–PD-L1 treatment synergistically promote antitumor immunity in mice. *The Journal of Clinical Investigation* **2014,** *124* (2), 687-695.

108. Deng, L.; Liang, H.; Xu, M.; Yang, X.; Burnette, B.; Arina, A.; Li, X.-D.; Mauceri, H.; Beckett, M.; Darga, T., STING-dependent cytosolic DNA sensing promotes radiation-induced type I interferon-dependent antitumor immunity in immunogenic tumors. *Immunity* **2014,** *41* (5), 843-852.

109. Formenti, S. C.; Demaria, S., Systemic effects of local radiotherapy. *The Lancet Oncology* **2009,** *10* (7), 718-726.

110. Schaue, D.; Ratikan, J. A.; Iwamoto, K. S.; McBride, W. H., Maximizing tumor immunity with fractionated radiation. *International Journal of Radiation Oncology • Biology • Physics* **2012,** *83* (4), 1306-1310.

111. Wardman, P., Chemical radiosensitizers for use in radiotherapy. *Clinical Oncology* **2007,** *19* (6), 397-417.

112. Kwatra, D.; Venugopal, A.; Anant, S., Nanoparticles in radiation therapy: a summary of various approaches to enhance radiosensitization in cancer. *Translational Cancer Research* **2013,** *2* (4), 330-342.

113. Chen, W.; Zhang, J., Using nanoparticles to enable simultaneous radiation and photodynamic therapies for cancer treatment. *Journal of Nanoscience and Nanotechnology* **2006,** *6* (4), 1159-1166.

114. Hainfeld, J. F.; Dilmanian, F. A.; Slatkin, D. N.; Smilowitz, H. M., Radiotherapy enhancement with gold nanoparticles. *Journal of Pharmacy and Pharmacology* **2008,** *60* (8), 977-985.

115. Mirjolet, C.; Papa, A.; Créhange, G.; Raguin, O.; Seignez, C.; Paul, C.; Truc, G.; Maingon, P.; Millot, N., The radiosensitization effect of titanate nanotubes as a new tool in radiation therapy for glioblastoma: a proof-of-concept. *Radiotherapy and Oncology* **2013,** *108* (1), 136-142.

116. Retif, P.; Pinel, S.; Toussaint, M.; Frochot, C.; Chouikrat, R.; Bastogne, T.; Barberi-Heyob, M., Nanoparticles for radiation therapy enhancement: the key parameters. *Theranostics* **2015,** *5* (9), 1030.

117. Bonvalot, S.; Rutkowski, P. L.; Thariat, J.; Carrère, S.; Ducassou, A.; Sunyach, M.-P.; Agoston, P.; Hong, A.; Mervoyer, A.; Rastrelli, M., NBTXR3, a first-in-class radioenhancer hafnium oxide nanoparticle, plus radiotherapy versus radiotherapy alone in patients with locally advanced soft-tissue sarcoma (Act. In. Sarc): a multicentre, phase 2–3, randomised, controlled trial. *The Lancet Oncology* **2019,** *20* (8), 1148-1159.

118. Formenti, S. C.; Demaria, S., Combining radiotherapy and cancer immunotherapy: a paradigm shift. *JNCI: Journal of the National Cancer Institute* **2013,** *105* (4), 256-265.

119. Postow, M. A.; Callahan, M. K.; Barker, C. A.; Yamada, Y.; Yuan, J.; Kitano, S.; Mu, Z.; Rasalan, T.; Adamow, M.; Ritter, E., Immunologic correlates of the abscopal effect in a patient with melanoma. *New England Journal of Medicine* **2012,** *366* (10), 925-931.

120. Lan, G.; Ni, K.; Veroneau, S. S.; Song, Y.; Lin, W., Nanoscale metal–organic layers for radiotherapy–radiodynamic therapy. *Journal of the American Chemical Society* **2018,** *140* (49), 16971-16975.

121. Lin, W.; He, C.; Kuangda, L.; Ni, K.; Lan, G., Nanoparticles for photodynamic therapy, x-ray induced photodynamic therapy, radiotherapy, radiodynamic therapy, chemotherapy, immunotherapy, and any combination thereof. Google Patents: 2018.

122. Lan, G.; Ni, K.; Xu, R.; Lu, K.; Lin, Z.; Chan, C.; Lin, W., Nanoscale metal–organic layers for deeply penetrating X-ray-induced photodynamic therapy. *Angewandte Chemie International Edition* **2017,** *129* (40), 12270-12274.

123. Dolmans, D. E.; Fukumura, D.; Jain, R. K., Photodynamic therapy for cancer. *Nature Reviews Cancer* **2003,** *3* (5), 380-387.

124. Dolmans, D. E. J. G. J.; Fukumura, D.; Jain, R. K., Photodynamic therapy for cancer. *Nature Reviews Cancer* **2003,** *3* (5), 380-387.

125. Castano, A. P.; Mroz, P.; Hamblin, M. R., Photodynamic therapy and anti-tumour immunity. *Nature Reviews Cancer* **2006,** *6* (7), 535-45.

126. Agostinis, P.; Berg, K.; Cengel, K. A.; Foster, T. H.; Girotti, A. W.; Gollnick, S. O.; Hahn, S. M.; Hamblin, M. R.; Juzeniene, A.; Kessel, D.; Korbelik, M.; Moan, J.; Mroz, P.; Nowis, D.; Piette, J.; Wilson, B. C.; Golab, J., Photodynamic therapy of cancer: an update. *CA: A Cancer Journal for Clinicians* **2011,** *61* (4), 250-81.

127. Lan, G.; Ni, K.; Xu, R.; Lu, K.; Lin, Z.; Chan, C.; Lin, W., Nanoscale Metal-Organic Layers for Deeply Penetrating X-ray-Induced Photodynamic Therapy. *Angewandte Chemie International Edition* **2017,** *56* (40), 12102-12106.

128. Castano, A. P.; Mroz, P.; Hamblin, M. R., Photodynamic therapy and anti-tumour immunity. *Nature Reviews Cancer* **2006,** *6* (7), 535-545.

129. Hwang, H. S.; Shin, H.; Han, J.; Na, K., Combination of photodynamic therapy (PDT) and anti-tumor immunity in cancer therapy. *Journal of Pharmaceutical Investigation* **2018,** *48* (2), 143-151.

130. MIŠÍK, V.; Riesz, P., Free radical intermediates in sonodynamic therapy. *Annals of the New York Academy of Sciences* **2000,** *899* (1), 335-348.

131. Tang, Z.; Liu, Y.; He, M.; Bu, W., Chemodynamic therapy: tumour microenvironment-mediated Fenton and Fenton-like reactions. *Angewandte Chemie International Edition* **2019,** *58* (4), 946-956.

132. Lin, L. S.; Song, J.; Song, L.; Ke, K.; Liu, Y.; Zhou, Z.; Shen, Z.; Li, J.; Yang, Z.; Tang, W., Simultaneous Fenton-like ion delivery and glutathione depletion by MnO_2-based nanoagent to enhance chemodynamic therapy. *Angewandte Chemie International Edition* **2018,** *57* (18), 4902-4906.

133. Zhou, Z.; Song, J.; Tian, R.; Yang, Z.; Yu, G.; Lin, L.; Zhang, G.; Fan, W.; Zhang, F.; Niu, G., Activatable singlet oxygen generation from lipid hydroperoxide nanoparticles for cancer therapy. *Angewandte Chemie International Edition* **2017,** *56* (23), 6492-6496.

134. Ni, K.; Lan, G.; Song, Y.; Hao, Z.; Lin, W., Biomimetic nanoscale metal–organic framework harnesses hypoxia for effective cancer radiotherapy and immunotherapy. *Chemical Science* **2020,** DOI: 10.1039/D0SC01949F.

135. Ma, B.; Wang, S.; Liu, F.; Zhang, S.; Duan, J.; Li, Z.; Kong, Y.; Sang, Y.; Liu, H.; Bu, W., Self-assembled copper–amino acid nanoparticles for in situ glutathione "AND" H2O2 sequentially triggered chemodynamic therapy. *Journal of the American Chemical Society* **2018,** *141* (2), 849-857.

136. Zheng, Z.-B.; Zhu, G.; Tak, H.; Joseph, E.; Eiseman, J. L.; Creighton, D. J., N-(2-Hydroxypropyl)methacrylamide copolymers of a glutathione (GSH)-activated glyoxalase

inhibitor and DNA alkylating agent: synthesis, reaction kinetics with GSH, and *in vitro* antitumor activities. *Bioconjugate Chemistry* **2005,** *16* (3), 598-607.

137. Kim, J.; Cho, H. R.; Jeon, H.; Kim, D.; Song, C.; Lee, N.; Choi, S. H.; Hyeon, T., Continuous O_2-evolving $MnFe_2O_4$ nanoparticle-anchored mesoporous silica nanoparticles for efficient photodynamic therapy in hypoxic cancer. *Journal of the American Chemical Society* **2017,** *139* (32), 10992-10995.

138. Fan, W.; Lu, N.; Huang, P.; Liu, Y.; Yang, Z.; Wang, S.; Yu, G.; Liu, Y.; Hu, J.; He, Q.; Qu, J.; Wang, T.; Chen, X., Glucose-responsive sequential generation of hydrogen peroxide and nitric oxide for synergistic cancer starving-like/gas therapy. *Angewandte Chemie International Edition* **2017,** *56* (5), 1229-1233.

139. Itaya, K.; Uchida, I.; Neff, V. D., Electrochemistry of polynuclear transition metal cyanides: Prussian blue and its analogues. *Accounts of Chemical Research* **1986,** *19* (6), 162-168.

140. Hoskins, B. F.; Robson, R., Infinite polymeric frameworks consisting of three dimensionally linked rod-like segments. *Journal of the American Chemical Society* **1989,** *111* (15), 5962-5964.

141. Furukawa, H.; Cordova, K. E.; O'Keeffe, M.; Yaghi, O. M., The chemistry and applications of metal-organic frameworks. *Science* **2013,** *341* (6149), 1230444.

142. Long, J. R.; Yaghi, O. M., The pervasive chemistry of metal–organic frameworks. *Chemical Society Reviews* **2009,** *38* (5), 1213-1214.

143. Liu, J.; Chen, L.; Cui, H.; Zhang, J.; Zhang, L.; Su, C.-Y., Applications of metal–organic frameworks in heterogeneous supramolecular catalysis. *Chemical Society Reviews* **2014,** *43* (16), 6011-6061.

144. Seo, J. S.; Whang, D.; Lee, H.; Im Jun, S.; Oh, J.; Jeon, Y. J.; Kim, K., A homochiral metal–organic porous material for enantioselective separation and catalysis. *Nature* **2000,** *404* (6781), 982-986.

145. Lee, J.; Farha, O. K.; Roberts, J.; Scheidt, K. A.; Nguyen, S. T.; Hupp, J. T., Metal–organic framework materials as catalysts. *Chemical Society Reviews* **2009,** *38* (5), 1450-1459.

146. Ma, L.; Falkowski, J. M.; Abney, C.; Lin, W., A series of isoreticular chiral metal–organic frameworks as a tunable platform for asymmetric catalysis. *Nature Chemistry* **2010,** *2* (10), 838-846.

147. Zhao, M.; Ou, S.; Wu, C.-D., Porous metal–organic frameworks for heterogeneous biomimetic catalysis. *Accounts of Chemical Research* **2014,** *47* (4), 1199-1207.

148. Corma, A.; García, H.; Llabrés i Xamena, F., Engineering metal organic frameworks for heterogeneous catalysis. *Chemical Reviews.* **2010,** *110* (8), 4606-4655.

149. Zhang, T.; Lin, W., Metal–organic frameworks for artificial photosynthesis and photocatalysis. *Chemical Society Reviews* **2014,** *43* (16), 5982-5993.

150. Kent, C. A.; Mehl, B. P.; Ma, L.; Papanikolas, J. M.; Meyer, T. J.; Lin, W., Energy transfer dynamics in metal− organic frameworks. *Journal of the American Chemical Society* **2010,** *132* (37), 12767-12769.

151. Wang, J.-L.; Wang, C.; Lin, W., Metal–organic frameworks for light harvesting and photocatalysis. *ACS Catalysis* **2012,** *2* (12), 2630-2640.

152. Song, Y.; PI, Y.; Feng, X.; Ni, K.; Xu, Z.; Chen, J. S.; Li, Z.; Lin, W., Cerium-based Metal-Organic Layers Catalyze Hydrogen Evolution Reaction through Dual Photoexcitation. *Journal of the American Chemical Society* **2020**.

153. Eddaoudi, M.; Kim, J.; Rosi, N.; Vodak, D.; Wachter, J.; O'Keeffe, M.; Yaghi, O. M., Systematic design of pore size and functionality in isoreticular MOFs and their application in methane storage. *Science* **2002,** *295* (5554), 469-472.

154. He, Y.; Zhou, W.; Qian, G.; Chen, B., Methane storage in metal–organic frameworks. *Chemical Society Reviews* **2014,** *43* (16), 5657-5678.

155. Suh, M. P.; Park, H. J.; Prasad, T. K.; Lim, D.-W., Hydrogen storage in metal–organic frameworks. *Chemical Reviews* **2011,** *112* (2), 782-835.

156. Li, J.-R.; Sculley, J.; Zhou, H.-C., Metal–organic frameworks for separations. *Chemical Reviews* **2011,** *112* (2), 869-932.

157. Sumida, K.; Rogow, D. L.; Mason, J. A.; McDonald, T. M.; Bloch, E. D.; Herm, Z. R.; Bae, T.-H.; Long, J. R., Carbon dioxide capture in metal–organic frameworks. *Chemical Reviews* **2011,** *112* (2), 724-781.

158. Ramaswamy, P.; Wong, N. E.; Shimizu, G. K., MOFs as proton conductors–challenges and opportunities. *Chemical Society Reviews* **2014,** *43* (16), 5913-5932.

159. Kobayashi, Y.; Jacobs, B.; Allendorf, M. D.; Long, J. R., Conductivity, doping, and redox chemistry of a microporous dithiolene-based metal− organic framework. *Chemistry of Materials* **2010,** *22* (14), 4120-4122.

160. Silva, C. G.; Corma, A.; García, H., Metal–organic frameworks as semiconductors. *Journal of Materials Chemistry* **2010,** *20* (16), 3141-3156.

161. Narayan, T. C.; Miyakai, T.; Seki, S.; Dincă, M., High charge mobility in a tetrathiafulvalene-based microporous metal–organic framework. *Journal of the American Chemical Society* **2012,** *134* (31), 12932-12935.

162. Talin, A. A.; Centrone, A.; Ford, A. C.; Foster, M. E.; Stavila, V.; Haney, P.; Kinney, R. A.; Szalai, V.; El Gabaly, F.; Yoon, H. P., Tunable electrical conductivity in metal-organic framework thin-film devices. *Science* **2014,** *343* (6166), 66-69.

163. Jain, P.; Ramachandran, V.; Clark, R. J.; Zhou, H. D.; Toby, B. H.; Dalal, N. S.; Kroto, H. W.; Cheetham, A. K., Multiferroic behavior associated with an order− disorder hydrogen bonding transition in metal− organic frameworks (MOFs) with the perovskite ABX3 architecture. *Journal of the American Chemical Society* **2009,** *131* (38), 13625-13627.

164. Zhang, W.; Xiong, R.-G., Ferroelectric metal–organic frameworks. *Chemical Reviews* **2011,** *112* (2), 1163-1195.

165. Kurmoo, M., Magnetic metal–organic frameworks. *Chem Soc Rev* **2009,** *38* (5), 1353-1379.

166. Evans, O. R.; Lin, W., Crystal engineering of NLO materials based on metal-organic coordination networks. *Accounts of Chemical Research* **2002,** *35* (7), 511-522.

167. Wang, C.; Zhang, T.; Lin, W., Rational synthesis of noncentrosymmetric metal–organic frameworks for second-order nonlinear optics. *Chemical Reviews* **2011,** *112* (2), 1084-1104.

168. Hu, X.; Wang, Z.; Su, Y.; Chen, P.; Chen, J.; Zhang, C.; Wang, C., Nanoscale metal–organic frameworks and metal–organic layers with two-photon-excited fluorescence. *Inorganic Chemistry* **2020,** *59* (7), 4181-4185.

169. He, C.; Lu, K.; Lin, W., Nanoscale metal–organic frameworks for real-time intracellular pH sensing in live cells. *Journal of the American Chemical Society* **2014,** *136* (35), 12253-12256.

170. Xu, R.; Wang, Y.; Duan, X.; Lu, K.; Micheroni, D.; Hu, A.; Lin, W., Nanoscale metal–organic frameworks for ratiometric oxygen sensing in live cells. *Journal of the American Chemical Society* **2016,** *138* (7), 2158-2161.

171. Rieter, W. J.; Taylor, K. M.; An, H.; Lin, W.; Lin, W., Nanoscale metal− organic frameworks as potential multimodal contrast enhancing agents. *Journal of the American Chemical Society* **2006,** *128* (28), 9024-9025.

172. Taylor, K. M.; Rieter, W. J.; Lin, W., Manganese-based nanoscale metal-organic frameworks for magnetic resonance imaging. *Journal of the American Chemical Society* **2008,** *130* (44), 14358-14359.

173. deKrafft, K. E.; Boyle, W. S.; Burk, L. M.; Zhou, O. Z.; Lin, W., Zr-and Hf-based nanoscale metal–organic frameworks as contrast agents for computed tomography. *Journal of materials chemistry* **2012,** *22* (35), 18139-18144.

174. Taylor-Pashow, K. M.; Della Rocca, J.; Xie, Z.; Tran, S.; Lin, W., Postsynthetic modifications of iron-carboxylate nanoscale metal− organic frameworks for imaging and drug delivery. *Journal of the American Chemical Society* **2009,** *131* (40), 14261-14263.

175. Della Rocca, J.; Liu, D.; Lin, W., Nanoscale metal-organic frameworks for biomedical imaging and drug delivery. *Accounts of Chemical Research* **2011,** *44* (10), 957-968.

176. Rieter, W. J.; Taylor, K. M.; Lin, W., Surface modification and functionalization of nanoscale metal-organic frameworks for controlled release and luminescence sensing. *Journal of the American Chemical Society* **2007,** *129* (32), 9852-9853.

177. Deria, P.; Mondloch, J. E.; Karagiaridi, O.; Bury, W.; Hupp, J. T.; Farha, O. K., Beyond post-synthesis modification: evolution of metal-organic frameworks *via* building block replacement. *Chemical Society Reviews* **2014,** *43* (16), 5896-5912.

178. Stock, N.; Biswas, S., Synthesis of metal-organic frameworks (MOFs): routes to various MOF topologies, morphologies, and composites. *Chemical Reviews* **2011,** *112* (2), 933-969.

179. Lu, W.; Wei, Z.; Gu, Z.-Y.; Liu, T.-F.; Park, J.; Park, J.; Tian, J.; Zhang, M.; Zhang, Q.; Gentle III, T., Tuning the structure and function of metal–organic frameworks *via* linker design. *Chemical Society Reviews* **2014,** *43* (16), 5561-5593.

180. Eddaoudi, M.; Moler, D. B.; Li, H.; Chen, B.; Reineke, T. M.; O'keeffe, M.; Yaghi, O. M., Modular chemistry: secondary building units as a basis for the design of highly porous and robust metal-organic carboxylate frameworks. *Accounts of Chemical Research* **2001,** *34* (4), 319-330.

181. Tranchemontagne, D. J.; Mendoza-Cortes, J. L.; O'Keeffe, M.; Yaghi, O. M., Secondary building units, nets and bonding in the chemistry of metal-organic frameworks. *Chemical Society Reviews* **2009,** *38* (5), 1257-1283.

182. Ma, L.; Abney, C.; Lin, W., Enantioselective catalysis with homochiral metal–organic frameworks. *Chemical Society Reviews* **2009,** *38* (5), 1248-1256.

183. Cohen, S. M., Postsynthetic methods for the functionalization of metal–organic frameworks. *Chemical Reviews* **2011,** *112* (2), 970-1000.

184. Brozek, C.; Dincă, M., Cation exchange at the secondary building units of metal–organic frameworks. *Chemical Society Reviews* **2014,** *43* (16), 5456-5467.

185. Chen, B.; Wang, L.; Zapata, F.; Qian, G.; Lobkovsky, E. B., A luminescent microporous metal− organic framework for the recognition and sensing of anions. *Journal of the American Chemical Society* **2008,** *130* (21), 6718-6719.

186. Wang, C.; deKrafft, K. E.; Lin, W., Pt nanoparticles@photoactive metal–organic frameworks: efficient hydrogen evolution via synergistic photoexcitation and electron injection. *Journal of the American Chemical Society* **2012,** *134* (17), 7211-7214.

187. Lu, G.; Li, S.; Guo, Z.; Farha, O. K.; Hauser, B. G.; Qi, X.; Wang, Y.; Wang, X.; Han, S.; Liu, X., Imparting functionality to a metal–organic framework material by controlled nanoparticle encapsulation. *Nature Chemistry* **2012,** *4* (4), 310-316.

188. Zhu, Q.-L.; Xu, Q., Metal–organic framework composites. *Chemical Society Reviews* **2014,** *43* (16), 5468-5512.

189. Yaghi, O. M.; Li, G.; Li, H., Selective binding and removal of guests in a microporous metal–organic framework. *Nature* **1995,** *378* (6558), 703-706.

190. He, C.; Liu, D.; Lin, W., Nanomedicine applications of hybrid nanomaterials built from metal–ligand coordination bonds: nanoscale metal–organic frameworks and nanoscale coordination polymers. *Chemical Reviews* **2015,** *115* (19), 11079-11108.

191. Peer, D.; Karp, J. M.; Hong, S.; Farokhzad, O. C.; Margalit, R.; Langer, R., Nanocarriers as an emerging platform for cancer therapy. *Nature Nanotechnology* **2007,** *2* (12), 751-760.

192. Kim, J.; Piao, Y.; Hyeon, T., Multifunctional nanostructured materials for multimodal imaging, and simultaneous imaging and therapy. *Chemical Society Reviews* **2009,** *38* (2), 372-390.

193. Gu, F. X.; Karnik, R.; Wang, A. Z.; Alexis, F.; Levy-Nissenbaum, E.; Hong, S.; Langer, R. S.; Farokhzad, O. C., Targeted nanoparticles for cancer therapy. *Nano Today* **2007,** *2* (3), 14-21.

194. Mura, S.; Nicolas, J.; Couvreur, P., Stimuli-responsive nanocarriers for drug delivery. *Nature Materials* **2013,** *12* (11), 991-1003.

195. Sapsford, K. E.; Algar, W. R.; Berti, L.; Gemmill, K. B.; Casey, B. J.; Oh, E.; Stewart, M. H.; Medintz, I. L., Functionalizing nanoparticles with biological molecules: developing chemistries that facilitate nanotechnology. *Chemical Reviews* **2013,** *113* (3), 1904-2074.

196. Chou, L. Y.; Ming, K.; Chan, W. C., Strategies for the intracellular delivery of nanoparticles. *Chemical Society Reviews* **2011,** *40* (1), 233-245.

197. Zhao, Z.; Zhou, Z.; Bao, J.; Wang, Z.; Hu, J.; Chi, X.; Ni, K.; Wang, R.; Chen, X.; Chen, Z., Octapod iron oxide nanoparticles as high-performance T_2 contrast agents for magnetic resonance imaging. *Nature Communications* **2013,** *4* (1), 1-7.

198. Zhou, Z.; Zhu, X.; Wu, D.; Chen, Q.; Huang, D.; Sun, C.; Xin, J.; Ni, K.; Gao, J., Anisotropic shaped iron oxide nanostructures: controlled synthesis and proton relaxation shortening effects. *Chemistry of Materials* **2015,** *27* (9), 3505-3515.

199. Ni, K.; Zhao, Z.; Zhang, Z.; Zhou, Z.; Yang, L.; Wang, L.; Ai, H.; Gao, J., Geometrically confined ultrasmall gadolinium oxide nanoparticles boost the T 1 contrast ability. *Nanoscale* **2016,** *8* (6), 3768-3774.

200. Horcajada, P.; Chalati, T.; Serre, C.; Gillet, B.; Sebrie, C.; Baati, T.; Eubank, J. F.; Heurtaux, D.; Clayette, P.; Kreuz, C.; Chang, J.-S.; Hwang, Y. K.; Marsaud, V.; Bories, P.-N.; Cynober, L.; Gil, S.; Ferey, G.; Couvreur, P.; Gref, R., Porous metal-organic-framework nanoscale carriers as a potential platform for drug delivery and imaging. *Nature Materials* **2010,** *9* (2), 172-178.

201. Horcajada, P.; Serre, C.; Vallet-Regí, M.; Sebban, M.; Taulelle, F.; Férey, G., Metal–organic frameworks as efficient materials for drug delivery. *Angewandte Chemie International Edition* **2006,** *118* (36), 6120-6124.

202. Taylor-Pashow, K. M. L.; Della Rocca, J.; Xie, Z.; Tran, S.; Lin, W., Postsynthetic modifications of iron-carboxylate nanoscale metal-organic frameworks for imaging and drug delivery. *Journal of the American Chemical Society.* **2009,** *131* (40), 14261-14263.

203. He, C.; Lu, K.; Lin, W., Nanoscale metal-organic frameworks for real-time intracellular pH sensing in live cells. *Journal of the American Chemical Society* **2014,** *136* (35), 12253-6.

204. Lu, K.; He, C.; Lin, W., Nanoscale metal–organic framework for highly effective photodynamic therapy of resistant head and neck cancer. *Journal of the American Chemical Society* **2014,** *136* (48), 16712-16715.

205. Lu, K.; He, C.; Lin, W., A chlorin-based nanoscale metal–organic framework for photodynamic therapy of colon cancers. *Journal of the American Chemical Society* **2015,** *137* (24), 7600-7603.

206. Liu, J.; Yang, Y.; Zhu, W.; Yi, X.; Dong, Z.; Xu, X.; Chen, M.; Yang, K.; Lu, G.; Jiang, L., Nanoscale metal− organic frameworks for combined photodynamic & radiation therapy in cancer treatment. *Biomaterials* **2016,** *97*, 1-9.

207. Park, J.; Jiang, Q.; Feng, D.; Mao, L.; Zhou, H.-C., Size-Controlled Synthesis of Porphyrinic Metal–Organic Framework and Functionalization for Targeted Photodynamic Therapy. *Journal of the American Chemical Society* **2016,** *138* (10), 3518-3525.

208. Lu, K.; He, C.; Guo, N.; Chan, C.; Ni, K.; Weichselbaum, R. R.; Lin, W., Chlorin-based nanoscale metal–organic framework systemically rejects colorectal cancers via synergistic photodynamic therapy and checkpoint blockade immunotherapy. *Journal of the American Chemical Society* **2016,** *138* (38), 12502-12510.

209. Lan, G.; Ni, K.; Xu, Z.; Veroneau, S. S.; Song, Y.; Lin, W., Nanoscale metal–organic framework overcomes hypoxia for photodynamic therapy primed cancer immunotherapy. *Journal of the American Chemical Society* **2018,** *140* (17), 5670-5673.

210. Lan, G.; Ni, K.; Lin, W., Nanoscale metal–organic frameworks for phototherapy of cancer. *Coordination Chemistry Reviews* **2019,** *379*, 65-81.

211. Lan, G.; Ni, K.; Veroneau, S. S.; Feng, X.; Nash, G. T.; Luo, T.; Xu, Z.; Lin, W., Titanium-Based Nanoscale Metal–Organic Framework for Type I Photodynamic Therapy. *Journal of the American Chemical Society* **2019,** *141* (10), 4204-4208.

212. Luo, T.; Ni, K.; Culbert, A.; Lan, G.; Li, Z.; Jiang, X.; Kaufmann, M.; Lin, W., Nanoscale Metal-Organic Frameworks Stabilize Bacteriochlorins for Type I and Type II Photodynamic Therapy. *Journal of the American Chemical Society* **2020,** *142* (16), 7334-7339

213. Ni, K.; Luo, T.; Lan, G.; Culbert, A.; Song, Y.; Wu, T.; Jiang, X.; Lin, W., Nanoscale metal-organic frameworks mediate photodynamic therapy and deliver CpG oligodeoxynucleotides to enhance antigen presentation and cancer immunotherapy. *Angewandte Chemie International Edition* **2020** 132 (3), 1124-1128

214. Sontz, P. A.; Bailey, J. B.; Ahn, S.; Tezcan, F. A., A metal-organic framework with spherical protein nodes: rational chemical design of 3D protein crystals. *Journal of the American Chemical Society* **2015,** *137* (36), 11598-11601.

215. Li, P.; Moon, S.-Y.; Guelta, M. A.; Harvey, S. P.; Hupp, J. T.; Farha, O. K., Encapsulation of a nerve agent detoxifying enzyme by a mesoporous zirconium metal-organic framework engenders thermal and long-term stability. *Journal of the American Chemical Society* **2016,** *138* (26), 8052-8055.

216. Morris, W.; Briley, W. E.; Auyeung, E.; Cabezas, M. D.; Mirkin, C. A., Nucleic acid–metal organic framework (MOF) nanoparticle conjugates. *Journal of the American Chemical Society* **2014,** *136* (20), 7261-7264.

217. Liang, K.; Ricco, R.; Doherty, C. M.; Styles, M. J.; Bell, S.; Kirby, N.; Mudie, S.; Haylock, D.; Hill, A. J.; Doonan, C. J., Biomimetic mineralization of metal-organic frameworks as protective coatings for biomacromolecules. *Nature Communications* **2015,** *6*.

218. He, C.; Lu, K.; Liu, D.; Lin, W., Nanoscale metal–organic frameworks for the co-delivery of cisplatin and pooled siRNAs to enhance therapeutic efficacy in drug-resistant ovarian cancer cells. *Journal of the American Chemical Society* **2014,** *136* (14), 5181-5184.

219. Ni, K.; Lan, G.; Chan, C.; Quigley, B.; Lu, K.; Aung, T.; Guo, N.; La Riviere, P.; Weichselbaum, R. R.; Lin, W., Nanoscale metal-organic frameworks enhance radiotherapy to potentiate checkpoint blockade immunotherapy. *Nature Communications* **2018,** *9* (1), 1-12.

220. Ni, K.; Lan, G.; Veroneau, S. S.; Duan, X.; Song, Y.; Lin, W., Nanoscale metal-organic frameworks for mitochondria-targeted radiotherapy-radiodynamic therapy. *Nature Communications* **2018,** *9* (1), 4321.

221. Ni, K.; Lan, G.; Chan, C.; Duan, X.; Guo, N.; Veroneau, S. S.; Weichselbaum, R. R.; Lin, W., Ultrathin metal-organic-layer mediated radiotherapy-radiodynamic therapy. *Matter* **2019,** *1* (5), 1331-1353.

222. Ni, K.; Aung, T.; Li, S.; Fatuzzo, N.; Liang, X.; Lin, W., Nanoscale metal-Organic framework mediates radical therapy to enhance cancer immunotherapy. *Chem* **2019,** *5* (7), 1892-1913.

223. Ni, K.; Lan, G.; Lin, W., Nanoscale metal-Organic frameworks generate reactive oxygen species for cancer therapy. *ACS Central Science* **2020**, DOI: 10.1021/acscentsci.0c00397.

CHAPTER 2. Nanoscale Metal-Organic Frameworks Enhance Radiotherapy to Potentiate Checkpoint Blockade Immunotherapy

2.1 Rationale for the project design

As a local immunogenic treatment, radiotherapy (RT) is prevalently used for treating many cancers.[1] A major challenge in RT is to maximize the therapeutic effect while minimizing deleterious effects on the surrounding healthy tissues.[2] The therapeutic ratio of RT can be enlarged with radiosensitizers that can effectively increase differential radiation absorption between healthy and tumor tissues. Heavy metal-based nanoparticles (NPs) such as Au and HfO_2 NPs have been shown as promising radiosensitizers *via* enhanced radiolysis.[3-6] NPs of high atomic number (Z) elements have high X-ray absorption coefficients and, when selectively deposited in tumors, can significantly increase radiosensitivity difference between healthy and tumor tissues, thus reducing radiation dose without impacting anticancer activity. For instance, HfO_2 NPs have been tested as radiosensitizers in several clinical trials actively for the treatment of soft tissue sarcomas, head and neck cancer, and other cancers.[7-8]

In the study of Au NP radiosensitization, it was found that reactive oxygen species (ROS) generation is inversely proportional to the particle diameter, indicating that larger specific surface areas may be an important design parameter for the efficiency of radiolysis.[9] Considering that nanoscale metal-organic frameworks (nMOFs) are assembled from ultrasmall metal-containing clusters with ultra large specific surface areas, we hypothesized that Hf-based nMOFs with both high-Z elements and high specific surface areas could be ideal candidates for radiosensitization.

Moreover, the porous structure of MOFs may facilitate fast diffusion of ROS, which have very short lifetimes typically on the order of 10^{-7} to 10^{-4} s.

Enhanced X-ray energy deposition in nMOFs presents another advantage for radiosensitization. Compared to incident X-rays, secondary photons generated from the enhanced photoelectric and/or Compton effects have lower energies and are more likely to interact with the radiosensitizers. In the case of solid NPs, the secondary photons are only generated on the surface of NPs and cannot be effectively used since the photons are randomly scattered in all directions and have low probability to encounter other NPs.[10] In contrast, the periodic structure of nMOFs may allow for effective use of secondary photons and electrons. For example, in the Hf-based nMOFs, each Hf SBU is surrounded by other Hf clusters extended in all directions with inter-cluster distance typically shorter than 2 nm. As a result, there is a higher probability for the secondary photons generated inside the MOFs to interact with other metal clusters, setting off a chain reaction to enhance the overall efficacy of RT.

In this chapter, we synthesized two Hf-based nMOFs, Hf_6-DBA and Hf_{12}-DBA with different Hf-oxo clusters, to study the radiosensitization effect of nMOFs. Upon low-dose X-ray irradiation, both nMOFs outperformed ultrasmall solid HfO_2 NPs in radioenhancement based on the same amount of Hf, evidenced by hydroxyl radical (•OH) generation as well as *in vitro* and *in vivo* efficacy results. The enhanced RT effect of Hf_6-DBA and Hf_{12}-DBA may be attributed to their large specific surface areas of Hf-oxo clusters and porous framework structures. Interestingly, Hf_{12}-DBA is a better radiosensitizer than Hf_6-DBA, likely due to more efficient X-ray energy absorption of Hf_{12} clusters over Hf_6 clusters, demonstrated by stronger radioluminscence intensity of anthracene-based analog, Hf_{12}-DBAn, compared against Hf_6-DBAn. On a bilateral tumor model, we further proved that Hf_{12}-DBA not only exhibited superior localized therapeutic effects upon

low-dose X-ray irradiation to eradicate primary, irradiated tumors, but also regressed distant, un-irradiated tumors when used in combination with an anti-PD-L1 checkpoint blockade inhibitor (CBI, **Figure 2-1**).

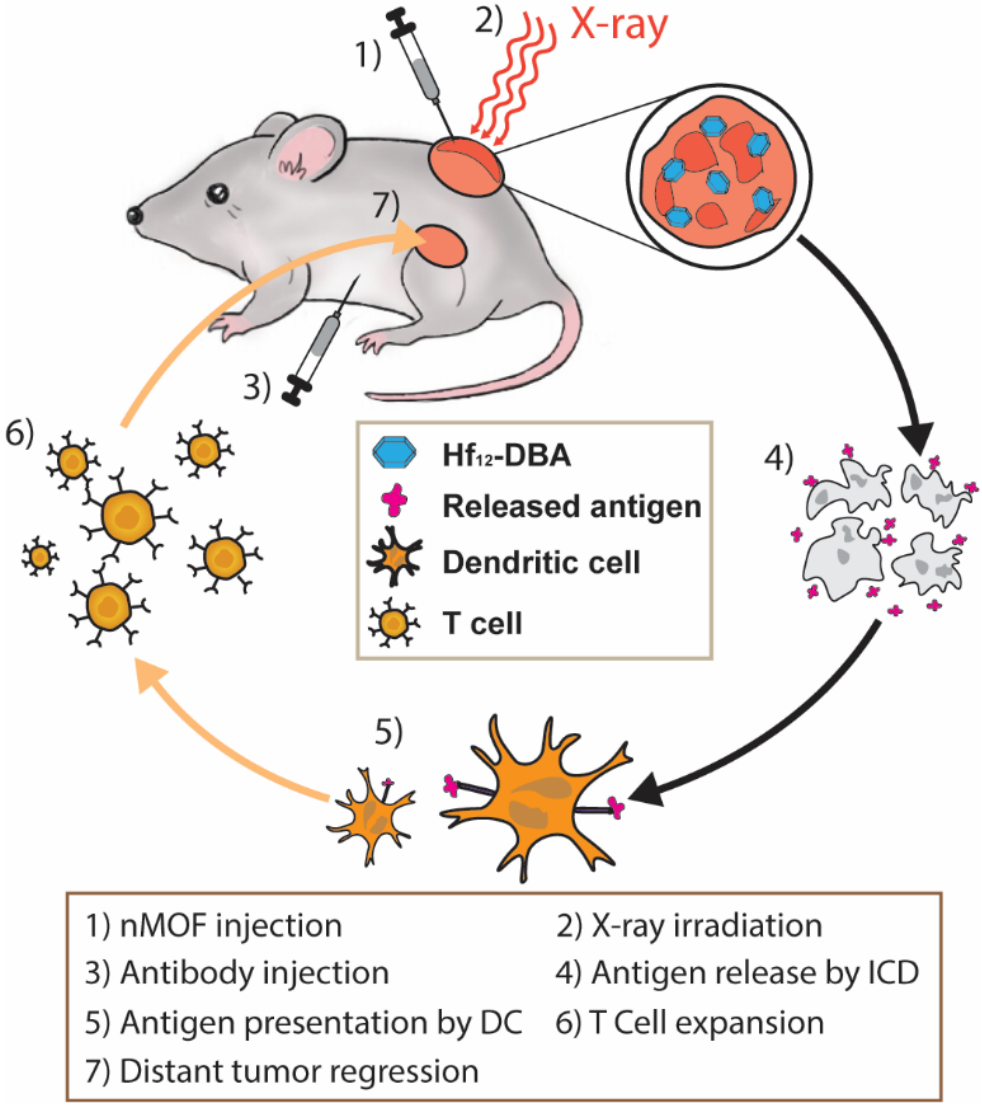

Figure 2-1. Abscopal effect of nMOFs-mediated RT and immune checkpoint blockade with low-dose X-rays. nMOF was intratumorally injected into the primary tumors of mice bearing bilateral subcutaneous tumors. nMOF-mediated RT destroyed the irradiated tumors, caused immunogenic cell death and released tumor antigens. Injected anti-PD-L1 antibody overcame the suppressive tumor microenvironment by targeting PD-1/PD-L1 axis. The combination of nMOF-mediated RT and anti-PD-L1 checkpoint blockade led to the effective T cell expansion and tumor-infiltration, which effectively suppressed/eradicated the distant tumors. Reprinted with permission from *Nature Communications* **2018**, *9*, 2351–2363. Copyright 2018 Nature Publishing Group.

2.2 Results and Discussion

2.2.1 Synthesis and characterization of Hf_6-DBA and Hf_{12}-DBA nMOFs

By tuning the temperature and modulators, two Hf-based nMOFs with different SBUs, Hf_6-DBA [DBA=2,5-di(*p*-benzoato)aniline] with a formula of $Hf_6(\mu_3\text{-}O)_4(\mu_3\text{-}OH)_4(DBA)_6$ and Hf_{12}-DBA with a formula of $Hf_{12}(\mu_3\text{-}O)_8(\mu_3\text{-}OH)_8(\mu_2\text{-}OH)_6(DBA)_9$, were synthesized *via* solvothermal reactions (**Scheme 2-1**).

Scheme 2-1 Synthesis of Hf_6 or Hf_{12} cluster and their nMOFs, Hf_6/Hf_{12}-DBA or Hf_6/Hf_{12}-DBAn. Reprinted with permission from *Nature Communications* **2018**, *9*, 2351–2363. Copyright 2018 Nature Publishing Group.

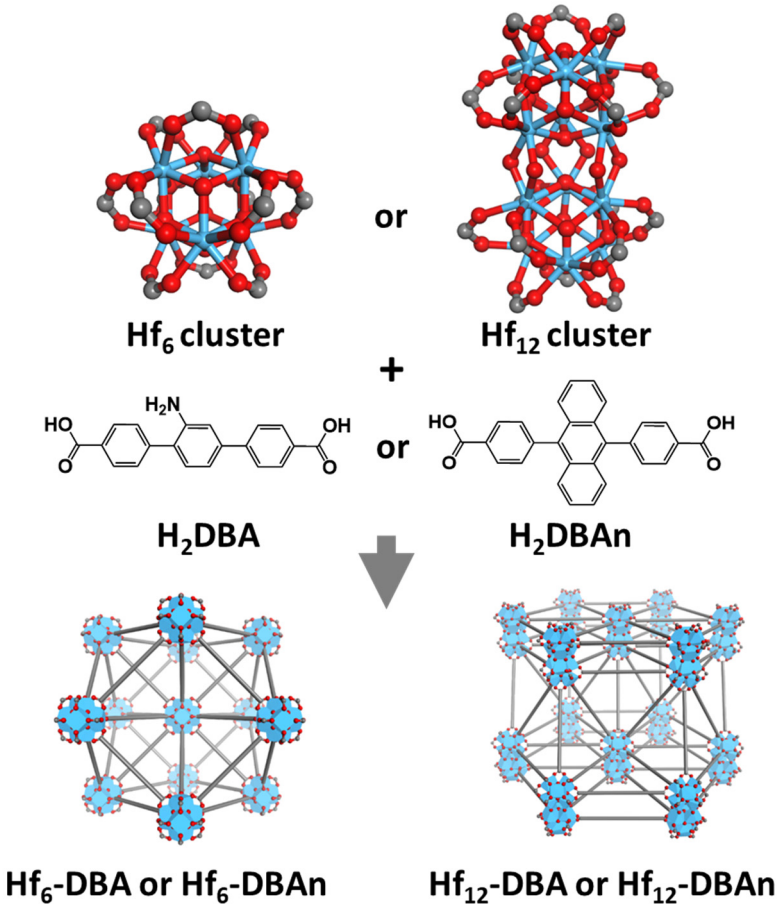

Transmission electron microscopy (TEM) images showed that Hf_6-DBA exhibited spherical morphology with a diameter of ~98 nm (**Figure 2-2a,b**), while Hf_{12}-DBA possessed a plate-like morphology of ~68 nm in diameter and ~30 nm in thickness (**Figure 2-2c,d**). Dynamic light scattering (DLS) measurements showed both nMOFs had good dispersity in ethanol with number-averaged diameter and polydispersity index of 116.0 ± 0.9 nm and 0.07 ± 0.01, respectively, for Hf_6-DBA and 102.1 ± 4.1 nm and 0.08 ± 0.02, respectively, for Hf_{12}-DBA (**Figure 2-2e**). The powder X-ray diffraction (PXRD) pattern of Hf_6-DBA was identical to that of UiO-68[11] while the PXRD pattern of Hf_{12}-DBA was identical to that of Zr_{12}-TPDC[12], indicative of their crystalline nature and different topological structures (**Figure 2-2f**).

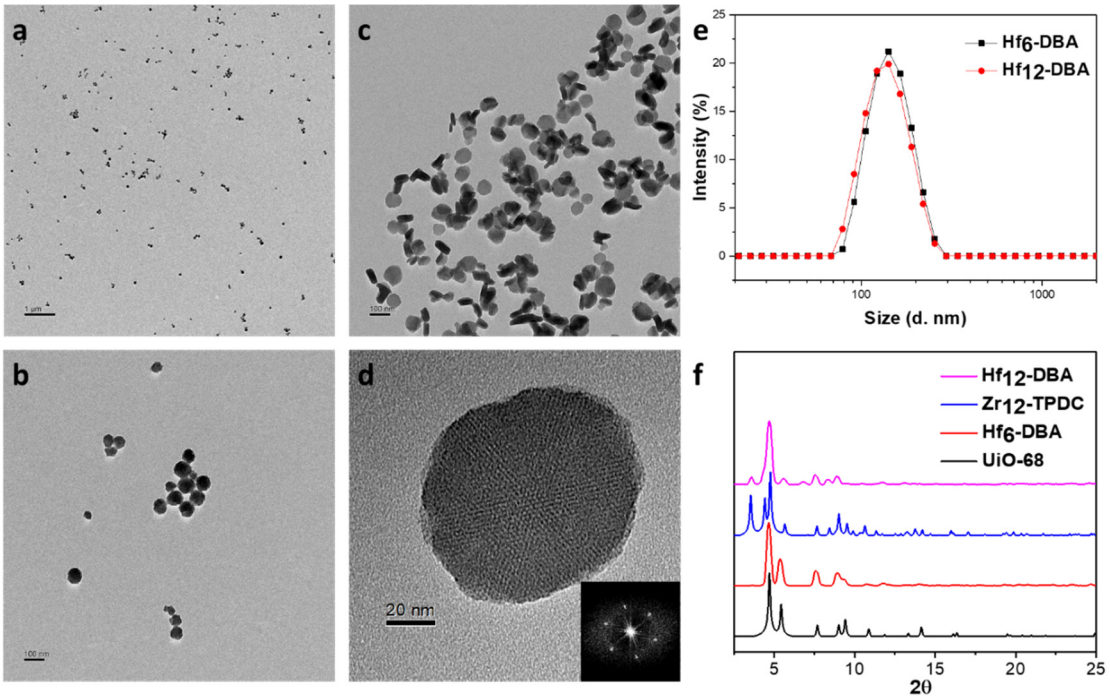

Figure 2-2 TEM images of Hf_6-DBA (a, b) and Hf_{12}-DBA (c-d) with its fast Fourier transform (FFT) pattern shown in inset of (d). Scale bar = 1000 nm (a), 100 nm (b&c) or 20 nm (d). (e) Hydrodynamic sizes of nMOFs in water by DLS measurements, n = 3. (f) PXRD patterns of nMOFs in comparison to those of UiO-68 and Zr_{12}-TPDC. Reprinted with permission from *Nature Communications* **2018**, *9*, 2351–2363. Copyright 2018 Nature Publishing Group.

Thermogravimetric analysis (TGA) results of Hf_6-DBA and Hf_{12}-DBA matched the weight losses expected for their decomposition to HfO_2 (**Figure 2-3a,b**). Nitrogen sorption measurements demonstrated porous structures of Hf_6-DBA and Hf_{12}-DBA, possessing BET surface areas of 804.4 m^2/g and 463.9 m^2/g, respectively (**Figure 2-3c,d**). Due to strong coordination between Hf^{4+} ions and carboxylate groups, both nMOFs were stable in aqueous suspensions. After incubation in RPMI 1640 cell culture medium for 240 hours or upon X-ray irradiation at a dose of 16 Gy, the TEM image (**Figure 2-3e**) and PXRD pattern (**Figure 2-3f**) of Hf_{12}-DBA were identical to that of the pristine sample, indicating the structural stability of Hf_{12}-DBA under physiological conditions and upon X-ray irradiation.

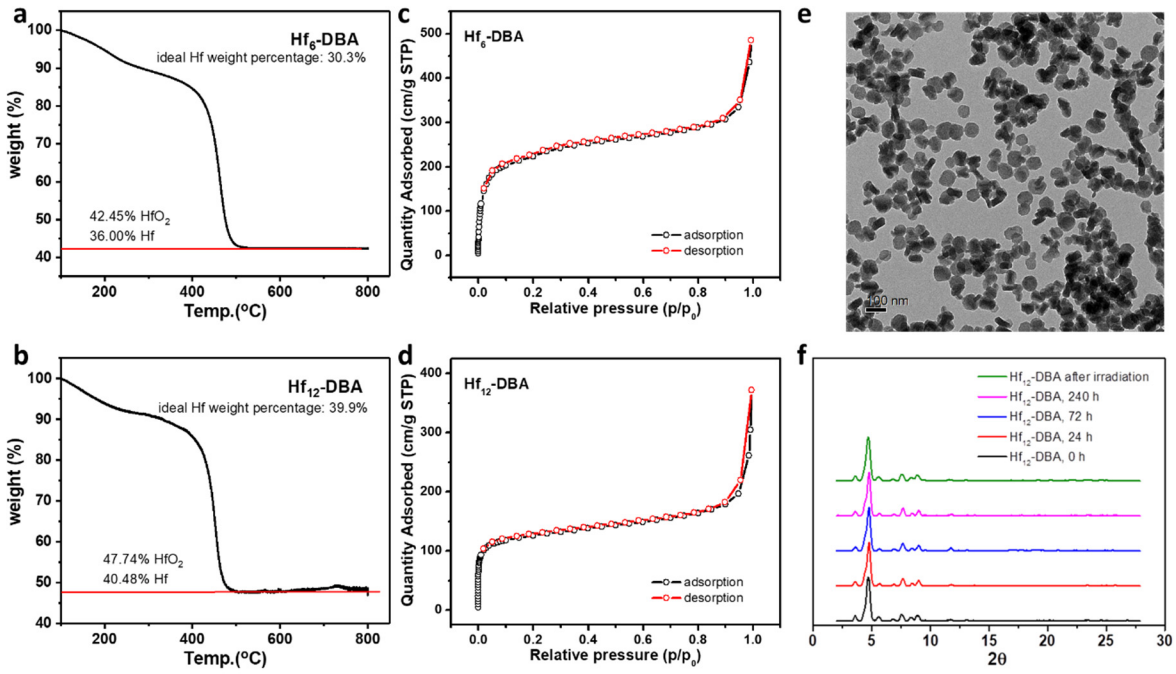

Figure 2-3 TGA curves of freshly prepared Hf_6-DBA (a) and Hf_{12}-DBA (b) in the 100 ~ 800 ºC range. The weight loss of Hf_6-DBA is 58.5%, consistent with a calculated result of 60.4% based on the conversion of $Hf_6(\mu_3\text{-}O)_4(\mu_3\text{-}OH)_4(DBA)_6$ to $(HfO_2)_6$. The weight loss of Hf_{12}-DBA is 52.3%, consistent with a calculated result of 53.9% based on the conversion of $Hf_{12}(\mu_3\text{-}O)_8(\mu_3\text{-}OH)_8(\mu_2\text{-}OH)_6(DBA)_9$ to $(HfO_2)_{12}$. Nitrogen sorption isotherms (77 K) of Hf_6-DBA (c) and Hf_{12}-

Figure 2-3, continued DBA (d). TEM (e) and PXRD pattern (f) of Hf_{12}-DBA after incubation in medium or X-ray irradiation. Reprinted with permission from *Nature Communications* **2018**, *9*, 2351–2363. Copyright 2018 Nature Publishing Group.

2.2.2 Hydroxyl radical formation

•OH, the major cytotoxic radical species from ionizing radiation, was detected *via* aminofluorescein (APF) assay, in which APF reacts with •OH to give bright green fluorescence (excitation/emission maxima 490/515 nm). Ultrasmall solid HfO_2 NPs with a diameter of ~10 nm (**Figure 2-4a,b**) were synthesized and used as a control. As designed, Hf-based SBUs effectively absorb energy to generate •OH *via* radiolysis when encountering incident X-rays (**Figure 2-4c**). The fluorescence signal might be possibly weakened due to trapped APF inside the pores of nMOFs. Thus we first determined the percentage of APF trapped in Hf_6-DBA or Hf_{12}-DBA *via* detecting chemically produced •OH from Fenton's reaction by APF with and without the nMOF: the percentage of APF trapped in Hf_6-DBA or Hf_{12}-DBA equals to one minus the fluorescence intensity ratio of APF with nMOF over that of APF without nMOF (**Figure 2-4d**). We then irradiated 5μM APF in aqueous solution or in aqueous dispersion of HfO_2, Hf_6-DBA, or Hf_{12}-DBA at equivalent Hf concentration of 20 μM with X-ray in the dose range of 0 to 10 Gy and determined their fluorescence signals. After correcting for the percentage of APF trapped in the nMOF, we deduced the fluorescence intensity corresponding to the amounts of •OH generated by H_2O, HfO_2, Hf_6-DBA, or Hf_{12}-DBA as shown in **Figure 2-4e**. All four groups showed linear increases of hydroxyl radical generation with increasing X-ray dose. The relative enhancement of hydroxyl radical generation compared with H_2O was obtained by subtracting the APF fluorescence intensity from H_2O group as shown in **Figure 2-4f**. HfO_2, Hf_6-DBA, or Hf_{12}-DBA enhanced hydroxyl generation over water by 14.3%, 33.6%, or 55.3%, respectively.

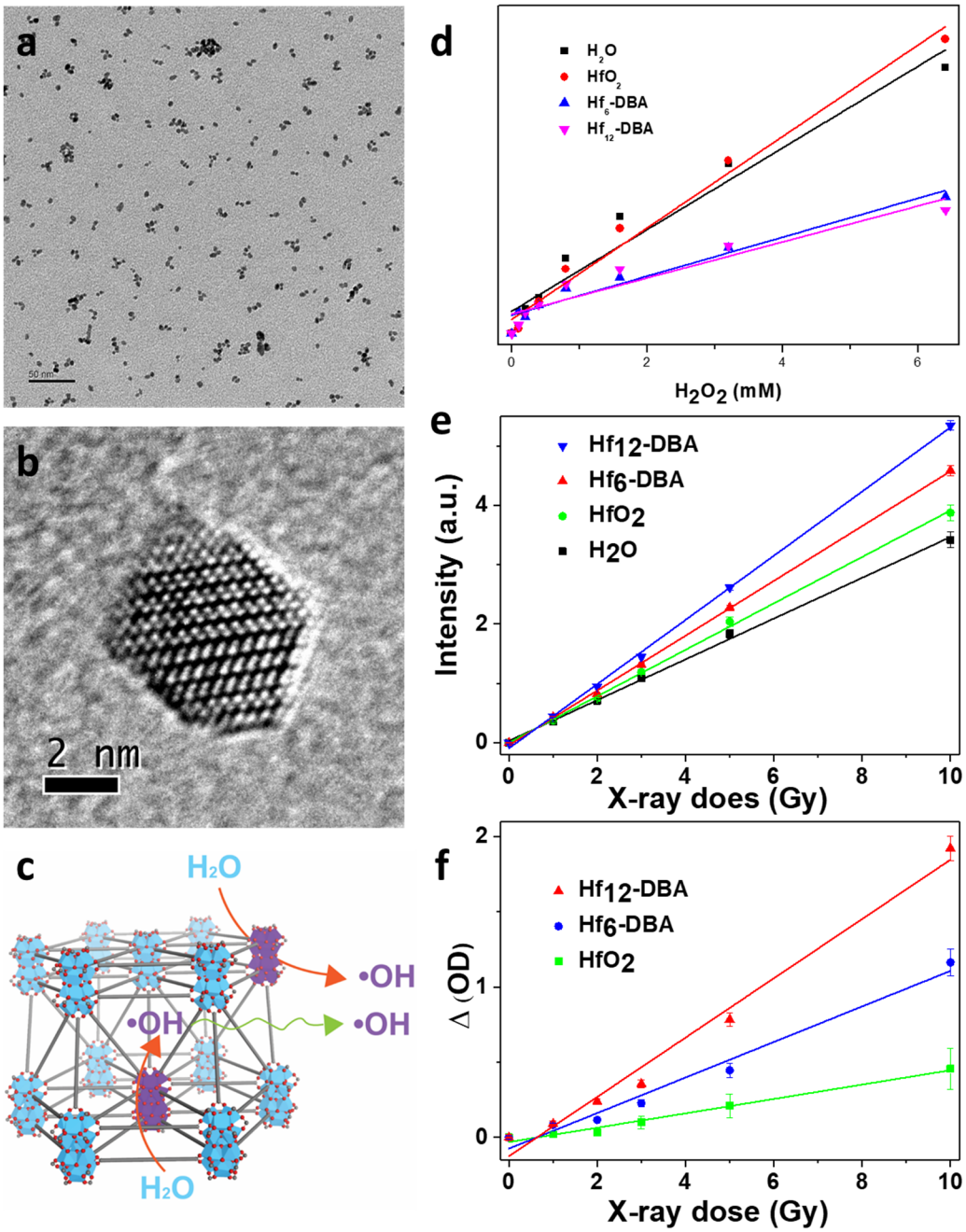

Figure 2-4 TEM image (a) and high-resolution TEM image (b) of HfO_2. Scale bar = 50 nm (a) or 2 nm (b). (c) Illustration of nMOF-mediated radiosensitization. (d) APF fluorescence of H_2O, HfO_2, Hf_6-DBA, or Hf_{12}-DBA with Fenton reaction at equivalent Hf concentrations of 20 μM. The ratio of fitting slope of HfO_2, Hf_6-DBA, or Hf_{12}-DBA is 1.12, 0.48, or 0.44, respectively. (e) APF fluorescence of H_2O, HfO_2, Hf_6-DBA, and Hf_{12}-DBA upon X-ray irradiation at equivalent Hf concentrations of 20 μM. (f) Enhanced APF fluorescence of HfO_2, Hf_6-DBA, and Hf_{12}-DBA over H_2O at equivalent Hf concentrations of 20 μM, n = 6. Reprinted with permission from *Nature Communications* **2018**, *9*, 2351–2363. Copyright 2018 Nature Publishing Group.

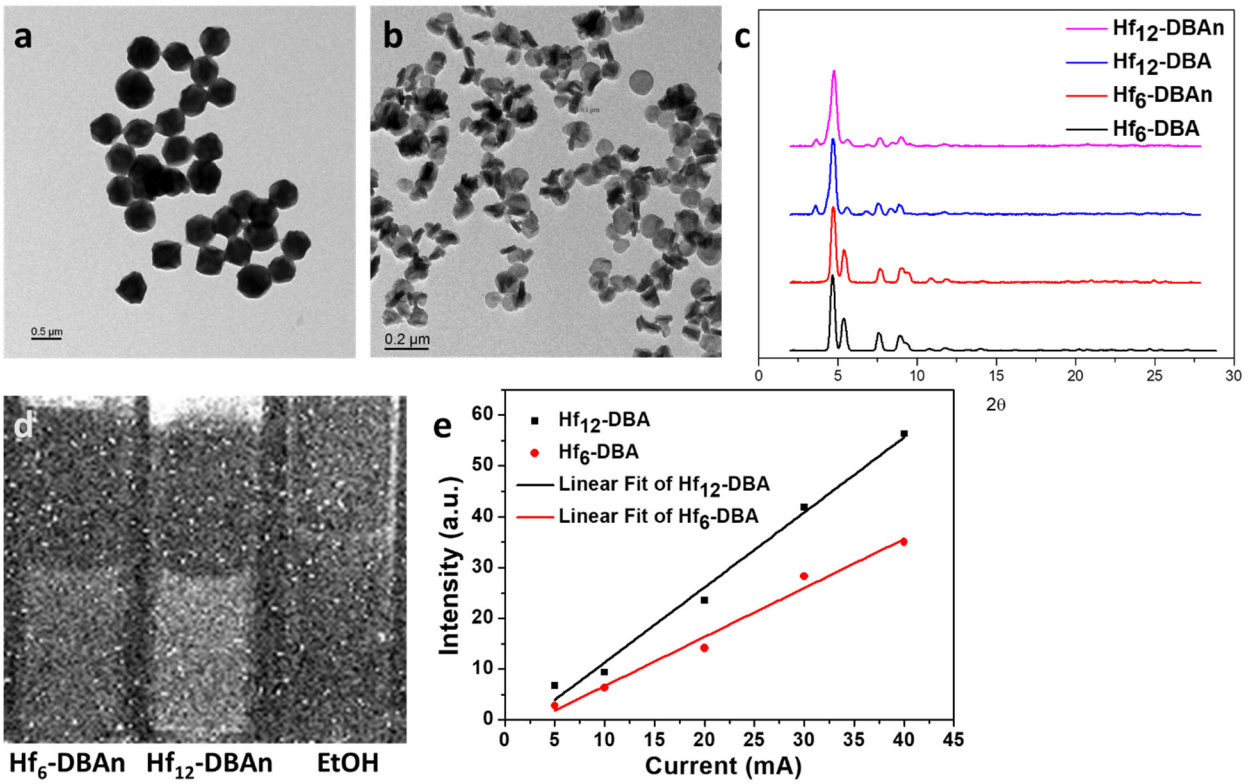

Figure 2-5 TEM images of Hf_6-DBAn (a) and Hf_{12}-DBAn (b). Scale bar = 500 nm (a) or 200 nm. (c) PXRD patterns of Hf_6-BDA, Hf_6-DBAn, Hf_{12}-DBA and Hf_{12}-DBAn. (d) Optical images of radioluminescence from Hf_6-DBAn (1 mM in ethanol), Hf_{12}-DBAn (1 mM in ethanol), and pure ethanol at an X-ray dose rate of 2.93 Gy/min. (e) Linear fits of radioluminescence intensities with respect to X-ray tube currents of Hf_6-DBA and Hf_{12}-DBA after subtraction of pure ethanol background. Reprinted with permission from *Nature Communications* **2018**, *9*, 2351–2363. Copyright 2018 Nature Publishing Group.

2.2.3 Radioluminescence

Upon X-ray irradiation, Hf-based MOFs were previously shown to transfer energy to anthracene-based bridging ligands, DBAn [DBAn = 9,10-di(*p*-benzoato)antheracene], to emit radioluminescence in the visible spectrum.[13] Radioluminescence of Hf-DBAn-based MOFs can thus be used to probe their X-ray absorption efficiency. We synthesized Hf_6-DBAn and Hf_{12}-DBAn, two DBAn MOFs with Hf_6 and Hf_{12} SBUs for radioluminescence measurements to investigate the relationship between SBU structure and X-ray absorption efficiency. TEM images

and PXRD patterns showed Hf_6-DBAn and Hf_{12}-DBAn displayed the same morphology and topology as Hf_6-DBA and Hf_{12}-DBA, respectively (**Figure 2-5a-c**). After degassing, 4 mL vials of Hf_{12}-DBAn and Hf_6-DBAn at an equivalentt Hf concentration of 1 mM in ethanol along with the ethanol control were irradiated with X-rays at a maximum dose rate of 2.93 Gy/min and their radioluminescence images were acquired using a CCD camera. As shown in **Figure 2-5d**, Hf_{12}-DBAn gave a much brighter radioluminescence signal compared to Hf_6-DBAn and EtOH. ImageJ was then used to calculate radioluminescence intensities by sampling the average pixel value of the vials and subtracting the average pixel value of pure ethanol background. The measured intensities were fit linearly as a function of X-ray tube current, which is proportional to the radiation dose (**Figure 2-5e**). Hf_{12}-DBAn had radioluminescence slope of 1.36 ± 0.05, 1.58-fold higher than that of Hf_6-DBAn (0.86 ± 0.04). This result indicated that Hf_{12}-DBAn exhibited approximately 1.5 times higher X-ray absorption efficiency than Hf_6-DBAn. Both hydroxyl radical generation and radioluminescence measurements demonstrated that Hf_{12}-DBA is an excellent radiosensitizer for RT.

2.2.4 Clonogenic assay

We then evaluated nMOF-mediated radiosensitization *in vitro*. First, time-dependent cellular uptake of HfO_2, Hf_6-DBA, and Hf_{12}-DBA in CT26 cells from 1 to 8 h demonstrated efficient cellular uptake of nMOFs as quantified by inductively coupled plasma-mass spectrometry (ICP-MS) analysis and 4 h incubation was chosen as the time point for further *in vitro* studies (**Figure 2-6a**). Facile nMOF endocytosis was also confirmed by confocal imaging; nMOFs labeled with Rhodamine B (Hf_6-DBA-R and Hf_{12}-DBA-R) co-localized with Lysotracker Green that labeled endo/lysosomes in both Hf_6-DBA and Hf_{12}-DBA treated cells (**Figure 2-6b**).

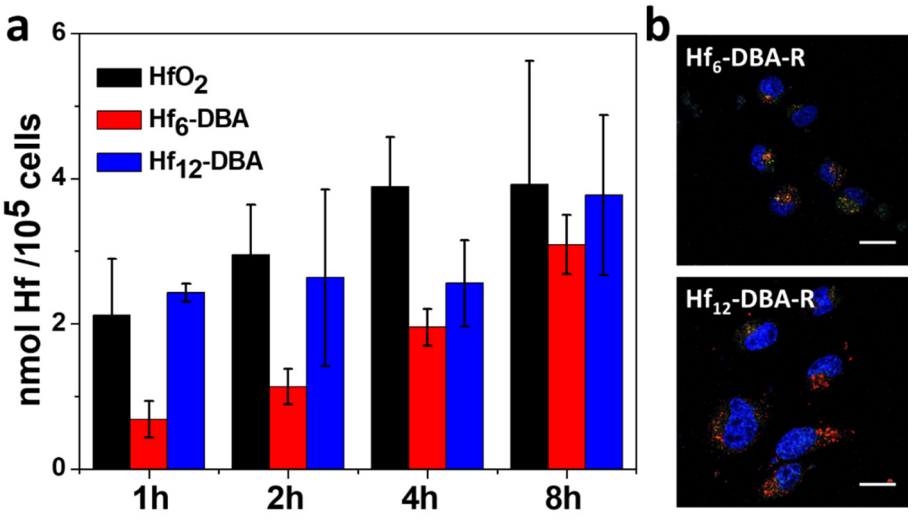

Figure 2-6 (a) Cellular uptake of three Hf-based nanoparticles after 1, 2, 4 or 8 hour incubation with equivalent Hf concentrations of 20 μM. The Hf concentrations were determined by ICP-MS.n = 3. (b) Endocytosis of Hf-based nMOFs. Cells were treated with Hf_6-DBA or Hf_{12}-DBA preloaded with Rhodamine B for 4 hours. Endosome/lysosome and nuclei were stained with Lysotracker Green and DAPI, respectively. Scale bar = 10 μm. Reprinted with permission from *Nature Communications* **2018**, *9*, 2351–2363. Copyright 2018 Nature Publishing Group.

Clonogenic assays were performed to assess the colony-forming potential of cells treated with nMOFs at a Hf concentration of 20 μM for 4 h followed by irradiation with either X-ray or ^{60}Co isotope γ-ray source at 0-16 Gy. Treated cells were trypsinized, re-seeded and cultured for 10-20 days and the clones were counted and plotted with the survival fraction as shown in **Figure 2-7** and **2-8**. Radiation enhancement factor at 10% survival dose (REF_{10}) was calculated as the ratio of equivalent irradiation doses needed to give 10% survival rate for the PBS control group over that for the experimental group. As shown in **Table 2-1**, 20 μM HfO_2 showed only moderate radiosensitization effect compared to PBS and exhibited much smaller REF_{10} values than Hf_6-DBA and Hf_{12}-DBA in all cell lines examined, which is consistent with the APF assay results. At the same Hf concentration, Hf_{12}-DBA outperformed Hf_6-DBA, with REF_{10} values from 1.45 to 1.73 compared to those from 1.10 to 1.31 for Hf_6-DBA. Hf_{12}-DBA thus exhibited superior radiosensitization over Hf_6-DBA, likely due to enhanced X-ray absorption by the electron-dense

Hf_{12} clusters and hydroxyl radical diffusion through the porous nanoplates. Upon irradiation with γ-rays from a ^{60}Co source, Hf_{12}-DBA also exhibited higher radiosensitization (REF_{10}=1.10-1.47) than HfO_2 and Hf_6-DBA, suggesting that Hf_{12}-DBA is compatible with linear accelerators commonly used in the clinic.

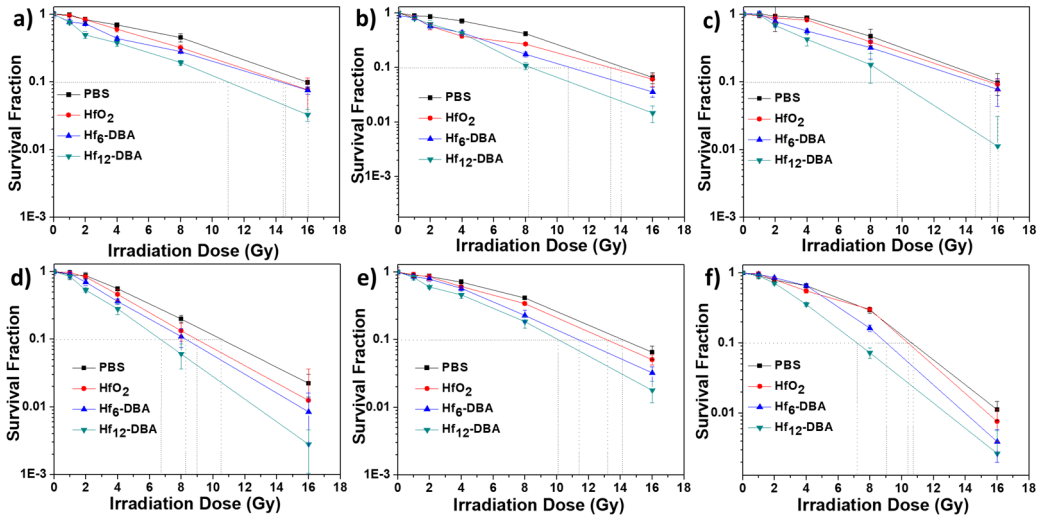

Figure 2-7 Clonogenic assay for evaluating radioenhancement upon X-ray irradiation on (a) 4T1, (b) TUBO, (c) SQ20B, (d) JSQ3, (e) CT26, (f) Hela cancer cell lines, n = 6. Reprinted with permission from *Nature Communications* **2018**, *9*, 2351–2363. Copyright 2018 Nature Publishing Group.

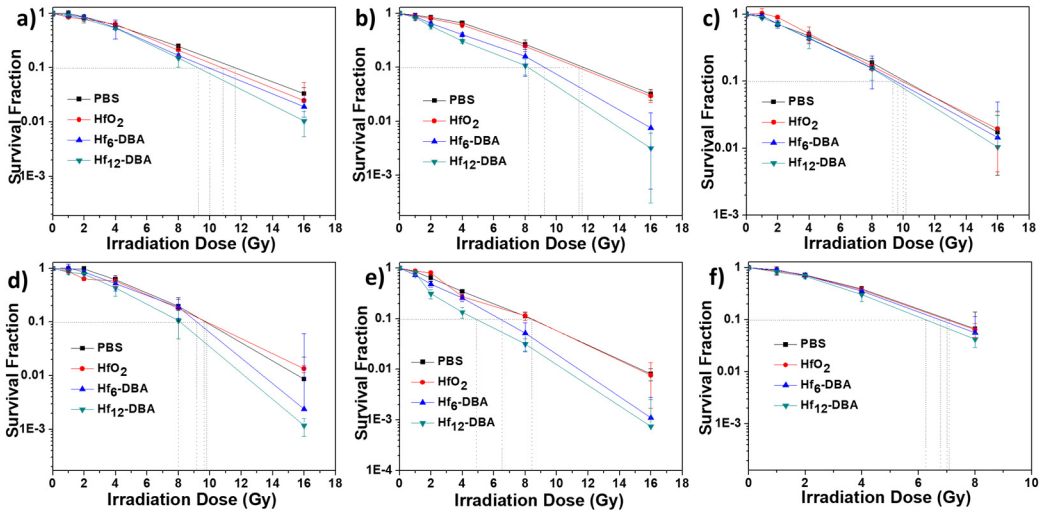

Figure 2-8 Clonogenic assay for evaluating radioenhancement upon γ-ray irradiation with ^{60}Co source on (a) 4T1, (b) TUBO, (c) SQ20B, (d) JSQ3, (e) CT26, (f) Hela cancer cell lines, n = 6.

Figure 2-8, continued Reprinted with permission from *Nature Communications* **2018**, *9*, 2351–2363. Copyright 2018 Nature Publishing Group.

Table 2-1. REF_{10} values by clonogenic assays in a panel of cell lines upon X-ray irradiation or γ-ray irradiation from a ^{60}Co source.

	REF_{10}	4T1	TUBO	HeLa	CT26	JSQ3	SQ20B
X-ray	HfO_2	1.09	1.13	1.10	1.03	1.00	1.16
	Hf_6-DBA	1.11	1.31	1.25	1.19	1.10	1.29
	Hf_{12}-DBA	1.45	1.73	1.43	1.49	1.65	1.56
γ-ray	HfO_2	1.06	1.03	1.11	1.01	1.00	1.00
	Hf_6-DBA	1.15	1.27	1.31	1.06	1.06	1.08
	Hf_{12}-DBA	1.26	1.44	1.47	1.14	1.10	1.23

2.2.5 DNA double-strand break (DSB) and apoptosis analysis

To elucidate the anti-tumor mechanism of nMOF-based RT, we investigated DNA double-strand break (DSB) and cell death pathways caused by nMOFs upon X-ray irradiation on CT26 cells. γ-H2AX, a phosphorylated protein resulted from direct ionizing radiation or generated •OH to induce DNA damage repair, has been used as a sensitive biomarker for probing DSBs.[14-15] 24 h after irradiation, significant red γ-H2AX fluorescence indicating DSBs was observed in the groups treated with Hf-based nanoparticles while no fluorescence was observed in groups either without X-ray irradiation or without Hf-based nanoparticle (**Figure 2-9a**). Quantitative flow cytometric analyses showed that cells treated with Hf_{12}-DBA exhibited stronger red fluorescence than cells treated with Hf_6-DBA or HfO_2, confirming that Hf_{12}-DBA induced stronger DNA DSBs (**Figure 2-9b**).

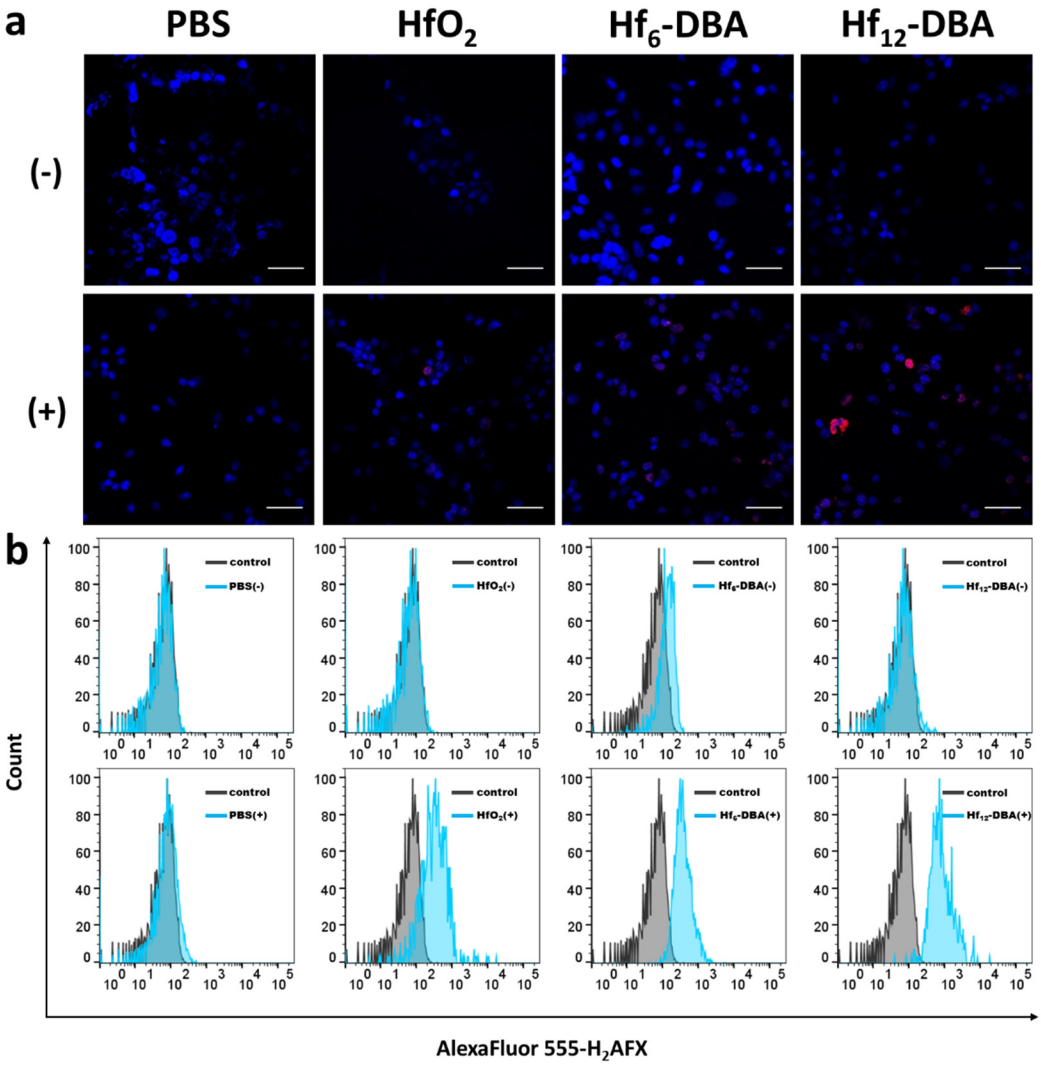

Figure 2-9 γ-H2AX showing DNA DSBs in CT26 cells observed under CLSM (a) and quantified with flow cytometry (b). Cells were treated with PBS, HfO_2, Hf_6-DBA or Hf_{12}-DBA, with (+) or without (-) X-ray irradiation. (a) Blue and red fluorescence show DAPI-stained nucleus and antibody-labeled γ-H2AX in the cells, respectively. Scale bar = 20 μm. (b) Red histogram (control) and blue histogram show the difference of γ-H2AX level in the cells. From left to right: PBS control, HfO_2, Hf_6-DBA or Hf_{12}-DBA, respectively. Reprinted with permission from *Nature Communications* **2018**, *9*, 2351–2363. Copyright 2018 Nature Publishing Group.

Hf_{12}-DBA not only showed significant increases in the percentage of cells with DSB foci quantitatively compared with the PBS control, but induced more foci per cell as shown in **Figure 2-10a**, with 45.0 ± 2.2, 21.8 ± 1.5, 12.4 ± 2.7, and 2.4 ± 1.1 foci per nucleus in Hf_{12}-DBA, Hf_6-

DBA, HfO_2, and PBS treated cells, respectively (**Figure 2-10b**). These results support potent radiosensitization efficiency of the unique Hf_{12} structure.

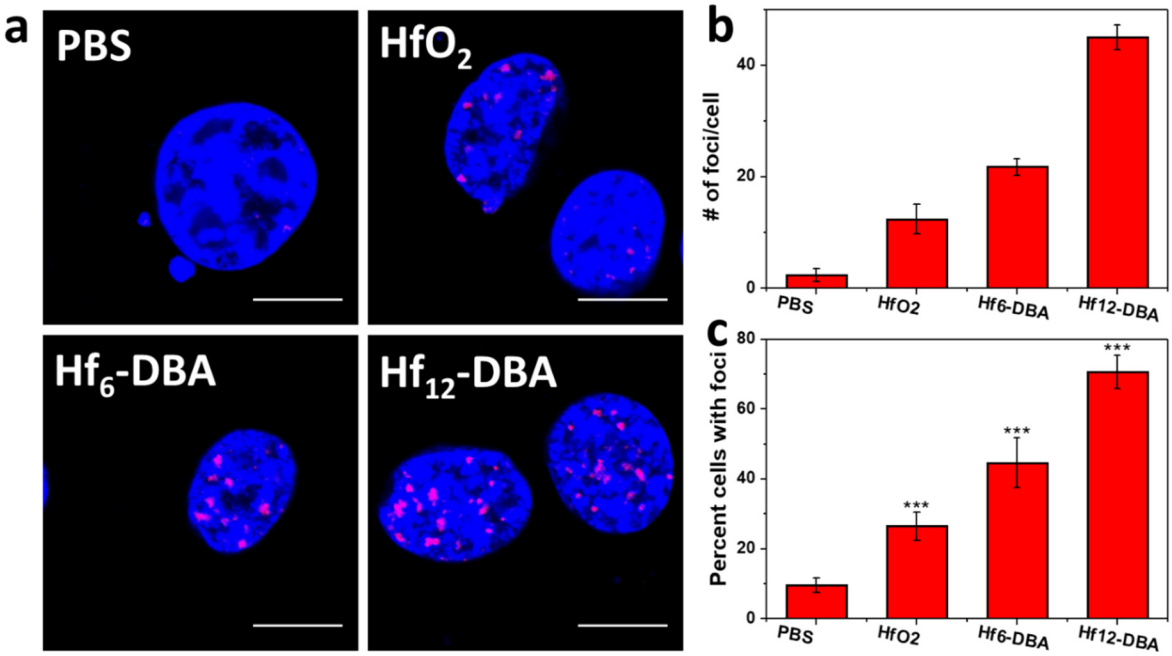

Figure 2-10 γ-H2AX assays showing the DSBs in CT26 cells treated with nMOFs and X-ray irradiation. Blue and red fluorescences show DAPI-stained nucleus and antibody-labeled γ-H2AX in the cells, respectively. Scale bar = 10 μm**.** Quantitative analysis of number of DBS foci per nucleus (b) and the percentage of cells with nuclear foci (c), n = 5. Reprinted with permission from *Nature Communications* **2018**, *9*, 2351–2363. Copyright 2018 Nature Publishing Group.

The cell death pathways were then evaluated with Annexin V/Cell death kit. Significant amounts of cells underwent apoptosis/necrosis when treated with Hf_{12}-DBA and X-ray irradiation with only 71.6% healthy cells, compared to 92.8% and 88.0% healthy cells for HfO_2 or Hf_6-DBA plus X-ray irradiation (**Figure 2-11**). 90%+ cells remained healthy in dark controls or the PBS group with irradiation, indicating that NP radioenhancers are not intrinsically cytotoxic and the low dose X-ray showed negligible cytotoxicity without a NP radiosensitizer. Taken together, Hf_{12}-DBA is a significantly more efficient radiosensitizer than both HfO_2 and Hf_6-DBA at equivalent Hf and X-ray doses.

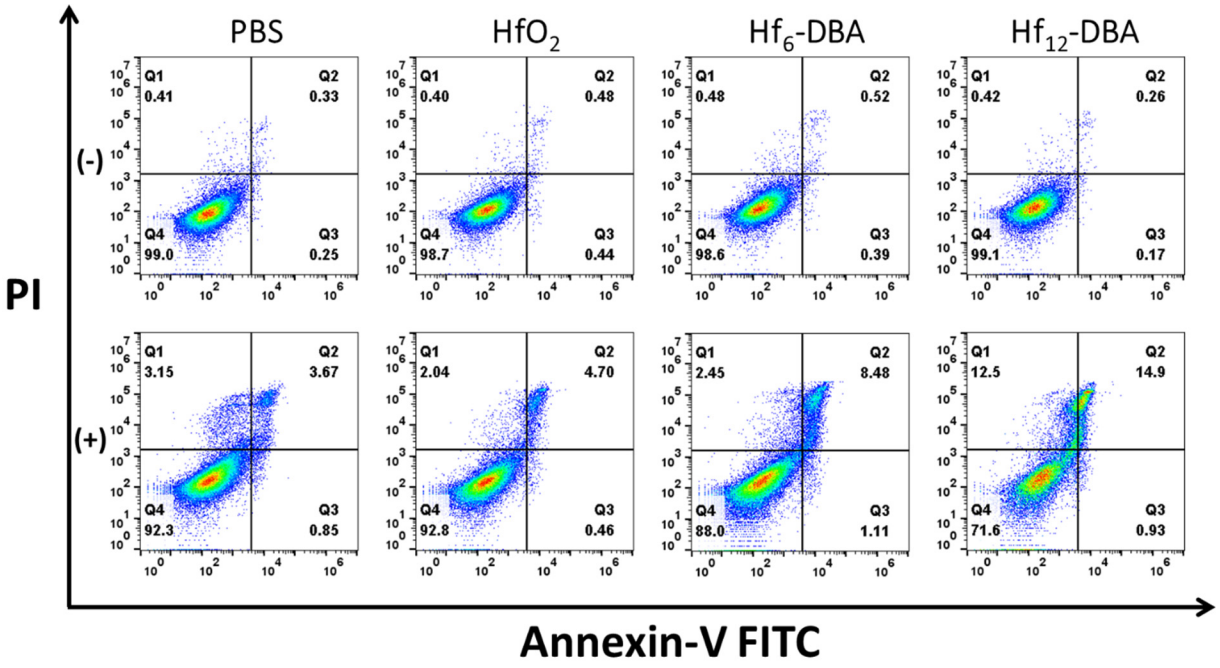

Figure 2-11 Annexin V/PI analysis of CT26 cells. Cells were incubated with PBS, HfO_2, Hf_6-DBA, or Hf_{12}-DBA with or without X-ray irradiation at a dose of 4 Gy. The quadrants from lower left to upper left (counter clockwise) represent healthy, early apoptotic, late apoptotic, and necrotic cells, respectively. The percentage of cells in each quadrant was shown on the graphs. (+) and (-) refer to with and without irradiation, respectively. Reprinted with permission from *Nature Communications* **2018**, *9*, 2351–2363. Copyright 2018 Nature Publishing Group.

2.2.6 *In vivo* anti-tumor efficacy

After demonstrating that Balb/c mice dosed subcutaneously with 10μmol Hf_{12}-DBA (based on Hf) showed no difference in body weight evolution compared with PBS control (**Figure 2-12a**), we carried out *in vivo* efficacy studies with mice receiving a single nMOF injection followed by X-ray irradiation. A colorectal adenocarcinoma mouse model of single CT26-tumor bearing BALB/c mice was employed to evaluate the radiosensitizing effects and anti-tumor efficacy of HfO_2, Hf_6-DBA, and Hf_{12}-DBA. When the tumors reached 100-150 mm^3 in volume, Hf_6-DBA, Hf_{12}-DBA, or HfO_2 NPs were injected intratumorally at equivalent Hf doses of 1 μmol followed by daily X-ray irradiation at a dose of 1 Gy/fraction (120 kVp, 20 mA, 2 mm Cu filter) for a total

of 10 fractions on consecutive days. An additional high-dose group of HfO_2 at 3.2 μmol was employed to further illustrate the difference between nMOFs and HfO_2.

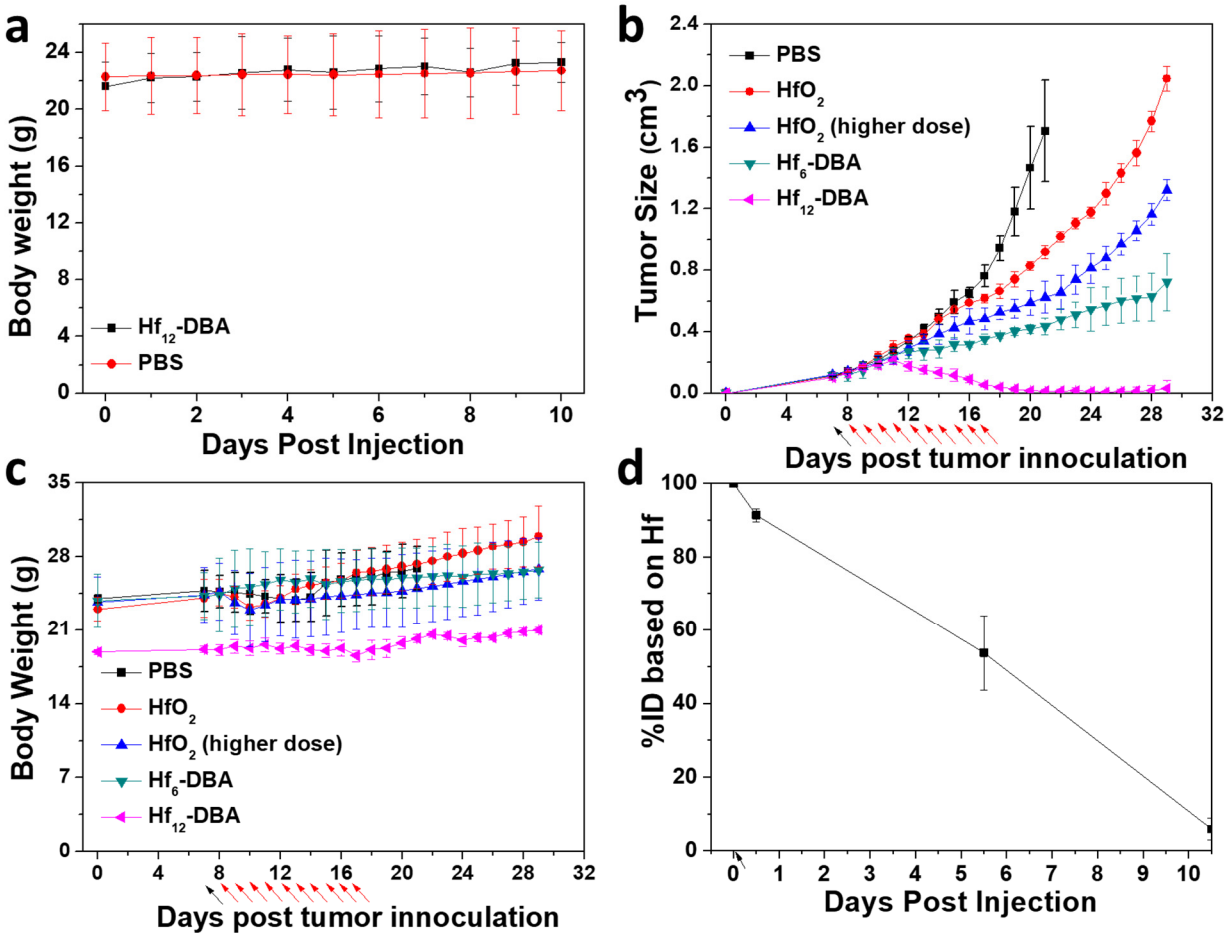

Figure 2-12 (a) Mean body weights of Balb/c mice treated with 10 μmol Hf_{12}-DBA per mouse or PBS, n = 3. Tumor growth inhibition curves (a) and body weights (b) after RT treatment in the single CT26 tumor-bearing mice treated with PBS, HfO_2 (low and high doses), Hf_6-DBA, or Hf_{12}-DBA, n = 6. (d) Tumor retention of Hf_{12}-DBA based on Hf content after intratumoral injection to CT26 tumor-bearing mice, n = 3. Black and red arrows refer to the times of PBS or nanoparticles injections and X-ray irradiation, respectively. Reprinted with permission from *Nature Communications* **2018**, *9*, 2351–2363. Copyright 2018 Nature Publishing Group.

As shown in **Figure 2-12b**, two Hf-based nMOFs afforded better local RT outcomes than HfO_2. Hf_{12}-DBA effectively regressed the locally irradiated tumors after a total of 10 Gy X-ray irradiation. In comparison, Hf_6-DBA and HfO_2 treated groups showed only moderate anti-tumor

efficacy, even after increasing the HfO_2 dose 3.2-fold. The body weights of mice remained consistent regardless of treatment (**Figure 2-12c**), suggesting there was no systemic toxicity. ICP-MS analysis showed that the amounts of Hf_{12}-DBA in tumors slowly decreased following intratumoral injection (**Figure 2-12d**).

2.2.7 Immunogenic cell death

The immunogenic cell death (ICD) induced by Hf NP-mediated radiation treatment was investigated by detecting cell-surface expression of calreticulin (CRT) both *in vitro* and *in vivo*.[16] As shown in **Figure 2-13a**, more green fluorescence was observed in the group treated with nMOFs compared to groups treated with either PBS or HfO_2 under CLSM, suggesting higher immunogenicity of nMOF-mediated RT treatment. Quantitative flow cytometry analyses confirmed that Hf_{12}-DBA showed significantly higher CRT expression on the cell-surface upon irradiation compared to Hf_6-DBA, HfO_2, PBS, or without irradiation, demonstrating that Hf_{12}-DBA-mediated radiation treatment induced stronger ICD over groups treated with either Hf_6-DBA or HfO_2 (**Figure 2-13b**).

We also evaluated CRT expression in CT26 tumor-bearing mice treated with PBS, HfO_2, Hf_6-DBA, or Hf_{12}-DBA and 5 consecutive days of irradiation at 1 Gy/fraction. The tumors were excised and sectioned for immunostaining. Hf_{12}-DBA treated tumors showed more green fluorescence (**Figure 2-13c**), indicating that the superior radioenhancement of Hf_{12}-DBA also led to higher CRT expression *in vivo*.

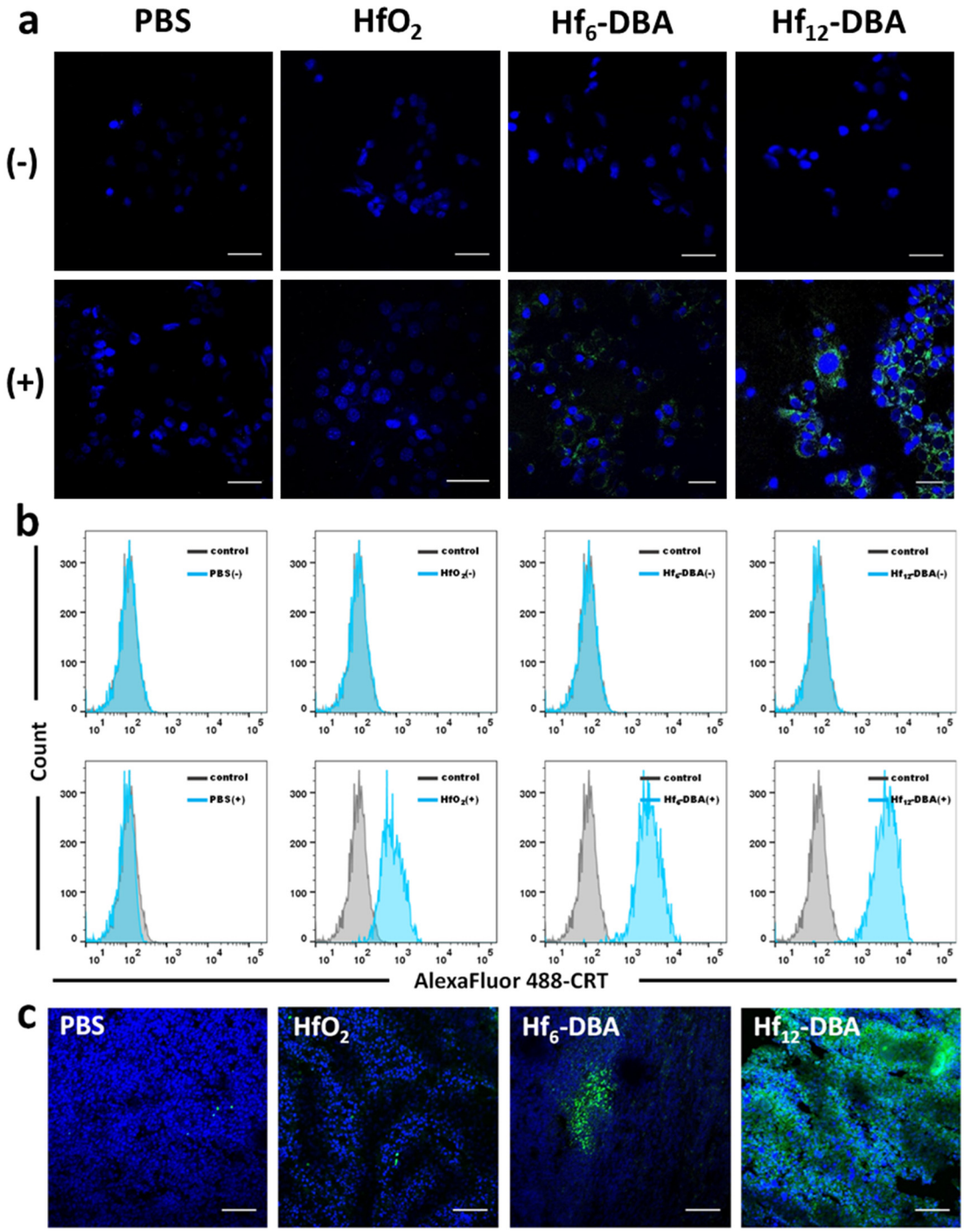

Figure 2-13 *In vitro* CRT exposure on the cell surface of CT26 was assessed after incubation with PBS, HfO_2, Hf_6-DBA, or Hf_{12}-DBA with X-ray irradiation by immunofluorescence microscopy (a) and flow cytometry (b). (+) and (-) refer to with and without irradiation, respectively. (c) *In vivo* CRT exposure was evaluated on sectioned tumor slides of CT26-bearing mice after 5 consecutive days of X-ray irradiation. Scale bar = 50 μm (a) or 100 μm (b). Reprinted with permission from *Nature Communications* **2018**, *9*, 2351–2363. Copyright 2018 Nature Publishing Group.

2.2.8 *In vivo* anti-tumor efficacy of nMOF-mediated RT plus CBI

We then combined nMOF-mediated RT with CBI to extend local treatment to systemic cancer management. A bilateral model of CT26 was established to assess the systemic anticancer efficacy of Hf_6-DBA or Hf_{12}-DBA mediated RT combined with immune checkpoint blockade. When the primary tumors reached 100-150 mm^3 in volume, nMOFs were intratumorally injected to the primary tumors at equivalent doses of 1μmol Hf, followed by daily X-ray irradiation at a dose of 1 Gy/fraction (120 kVp, 20 mA, 2 mm Cu filter) for a total of 10 fractions on consecutive days. 75μg of anti-PD-L1 antibody was given every three days by intraperitoneal injection.

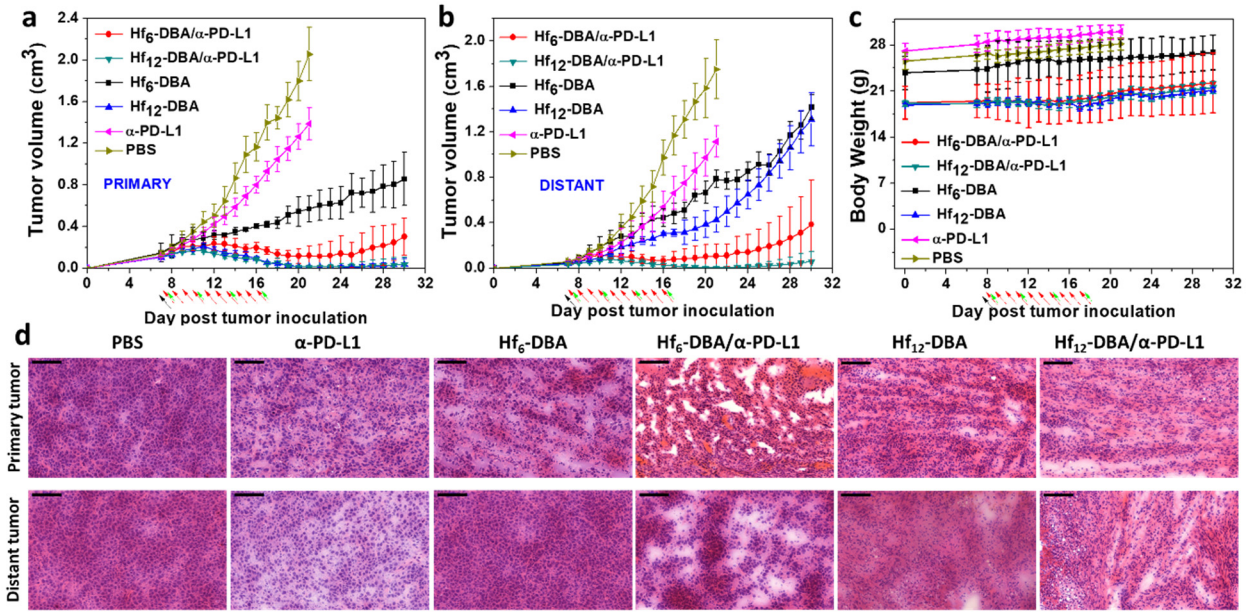

Figure 2-14 Tumor growth curves of primary tumors (a), distant tumors (d), body weights (c) and tumor histologies (d) of CT26 bilateral tumor-bearing mice treated with Hf_6-DBA (with or without anti-PD-L1 antibody), Hf_{12}-DBA (with or without anti-PD-L1 antibody), anti-PD-L1 antibody or PBS with X-rays irradiation. X-ray irradiation was carried out on mice 12 h after the i.t. injection of PBS or NPs on ten consecutive days at a dose of 1 Gy/fraction. Antibody was given intraperitoneally every three days at a dose of 75 μg/mouse. Black, red, and green arrows refer to the times of PBS or nanoparticles injections, X-ray irradiation, and antibody administration, respectively. Scale bar = 100 μm. Reprinted with permission from *Nature Communications* **2018**, *9*, 2351–2363. Copyright 2018 Nature Publishing Group.

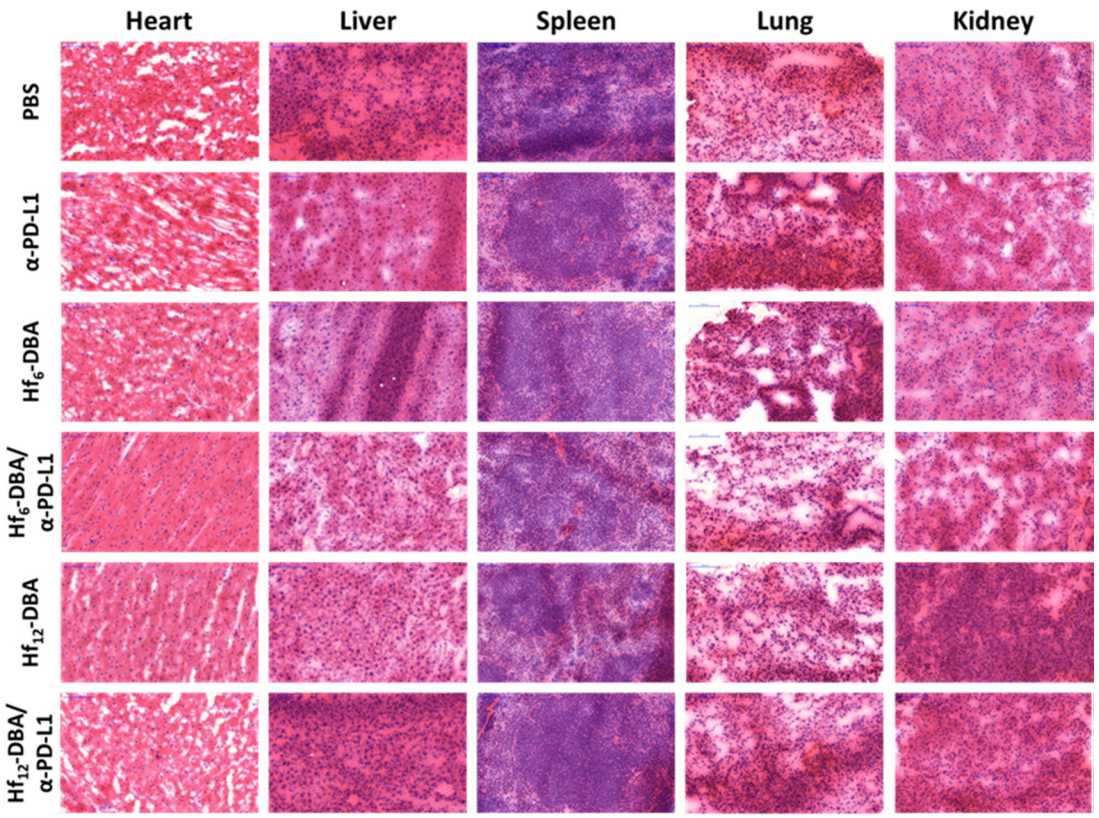

Figure 2-15 Histologies of frozen sections of major organs of CT26 tumor-bearing mice receiving intratumoral injection of Hf-based nMOFs or PBS and X-ray irradiation treatment with or without antibody treatment after H&E staining. From left to right: heart, liver, spleen, lung or kidney. Scale bar = 100 μm. Reprinted with permission from *Nature Communications* **2018**, *9*, 2351–2363. Copyright 2018 Nature Publishing Group.

Combination treatment of nMOFs and anti-PD-L1 antibody regressed the locally irradiated tumors at 10 Gy of total X-ray dose. Again, Hf_{12}-DBA outperformed Hf_6-DBA on primary tumor treatment (**Figure 2-14a**). More significantly, when combined with an anti-PD-L1 antibody, Hf_{12}-DBA not only produced local regression of irradiated tumors but also shrank distant, non-irradiated tumors. The inhibition of distant tumors by Hf_{12}-DBA mediated RT plus CBI indicated effective induction of systemic antitumor immune response (**Figure 2-14b**). Histological analysis of the tumors confirmed nMOF-mediated RT caused apoptosis/necrosis in local tumors, while only Hf_{12}-DBA/anti-PD-L1 antibody treated group showed apoptotic tumor histology with a lower density

of tumor cells in the untreated distant tumor (**Figure 2-14d**). The steady body weights in all treated mice indicated that nMOF-mediated RT with or without checkpoint blockade did not lead to systemic toxicity (**Figure 2-14c**). This was further confirmed by the absence of abnormality in major organs histologies compared against PBS treated mice (**Figure 2-15**).

2.2.9 Anti-tumor immunity

We then tested the anti-tumor immunity of CT26-bearing mice treated with Hf_{12}-DBA plus anti-PD-L1 antibody by Enzyme-Linked ImmunoSpot (ELISpot) and flow cytometry. We first determined the presence of tumor-antigen specific cytotoxic T cells with an IFN-γ ELISpot assay. At day 15 after the first treatment, splenocytes were harvested from CT26-bearing mice and stimulated with SPSYVYHQF, a tumor associated antigen, for 42 hours and the IFN-γ spot forming cells were counted by Immunospot Reader. The number of antigen-specific IFN-γ producing T cells significantly increased in tumor-bearing mice treated with Hf_{12}-DBA plus anti-PD-L1 antibody (100.2 ± 15.7 compared to 5.3 ± 2.7 for PBS or 8.2 ± 6.1 for Hf_{12}-DBA, **Figure 2-16a**), suggesting that Hf_{12}-DBA with X-ray irradiation plus anti-PD-L1 antibody effectively generates tumor-specific T cell response. We further profiled infiltrating leukocytes in both the primary and distant tumors. There was no significant difference between PBS with or without X-ray irradiation, demonstrating that low-dose X-ray irradiation did not influence the immunological environment of tumors. The Hf_{12}-DBA with antibody group showed significant increase of tumor-infiltrating $CD4^+$ T cells (**Figure 2-16c**) and $CD8^+$ T cells (**Figure 2-16d**) in both the primary tumors and the distant tumors. Specifically, for the primary tumor, the percentage of $CD8^+$ T cells in the total tumor cells significantly increased in both Hf_{12}-DBA mediated-RT (2.92 ± 1.58 %) and Hf_{12}-DBA mediated-RT plus anti-PD-L1 treated groups (2.42 ± 1.31%) compared to the PBS control group (0.67 ± 0.40%). For the distant tumor, the percentage of $CD8^+$ T cells in the total

tumor cells increased in Hf_{12}-DBA mediated-RT plus anti-PD-L1 treatment group (2.04 ± 1.24%) compared to Hf_{12}-DBA mediated-RT group (1.21 ± 0.48 %) and PBS control group (1.20 ± 0.20 %). The significant increase of infiltrating $CD8^+$ T cells likely induced the abscopal effect. The Hf_{12}-DBA with antibody group showed significant increase of tumor-infiltrating leukocytes (**Figure 2-16b**) as well as B cells (**Figure 2-16g**) in the primary tumors but not in the distant tumors. Significant increase of $CD8^+$ T cells (**Figure 2-16h**) in the primary tumor-draining lymph nodes and decrease of regulatory T cells in distant sides were observed in the combination treatment groups.

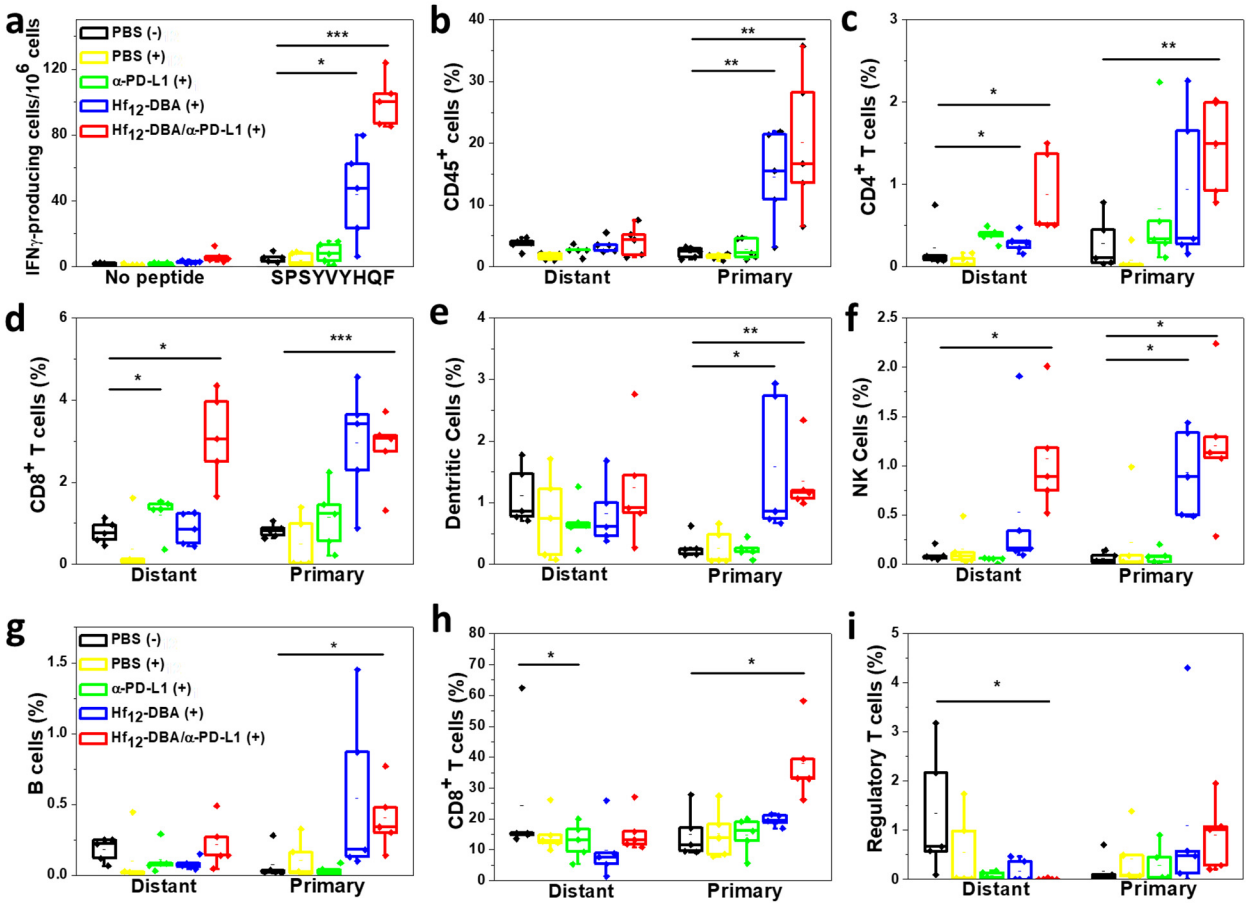

Figure 2-16 (a) ELISpot assay was performed to detect IFN-γ producing T cells. The primary (right) and distant (left) tumors were collected for flow cytometry analysis and the percentage of tumor-infiltrating $CD45^+$ cells (b), $CD4^+$ T cells (c), $CD8^+$ T cells (d), dentritic cells (e), NK cells (f), and B cells (g) with respect to the total tumor of cells treated with PBS dark control, PBS, anti-

Figure 2-16, continued PD-L1 antibody, Hf_{12}-DBA, or Hf_{12}-DBA plus anti-PD-L1 antibody with X-ray irradiation. Percentages of $CD8^+$ T cells (h) and regulatory T cells (i) in lymph nodes of as treated bilateral tumor bearing mice. Data are expressed as means ± s.d., n = 5). *P<0.05 from control, **P<0.01 from control and ***P<0.001 from control by t-test. Central lines, bounds of box and whiskers represent mean values, 25% to 75% of the range of data and 1.5 fold of interquartile range away from outliers, respectively. Reprinted with permission from *Nature Communications* **2018**, *9*, 2351–2363. Copyright 2018 Nature Publishing Group.

In immunotherapy, dendritic cells can be recruited to the tumor sites and then present antigens to T cells after migration to the lymph nodes. Hf_{12}-DBA mediated-RT groups significantly increased the percentages of dendritic cells in primary tumors (**Figure 2-16e**). We also found a significant increase of NK cells in both primary and distant tumors treated with Hf_{12}-DBA mediated-RT and anti-PD-L1 antibody (**Figure 2-16f**). These results suggest that the combination of nMOF-mediated RT and PD-L1 checkpoint blockade therapy not only augments tumor-specific adaptive response, but also induces innate immune response in tumors.

2.2.10 Depletion study and tumor rechallenge

We further investigated how immune cells mediated the therapeutic effects of nMOF-mediated RT. The anticancer efficacy of Hf_{12}-DBA was evaluated in the subcutaneous CT26 model with concurrent $CD4^+$ T or $CD8^+$ T cell depletion. Mice receiving i.p. injections of anti-CD4, anti-CD8, or mouse IgG antibodies were treated with Hf_{12}-DBA and X-ray irradiation combined with an anti-PD-L1 antibody. Mouse IgG did not have any effect on tumor growth, but other antibody-treated groups all showed rapid tumor growth after cessation of X-ray treatment (**Figure 2-17a**) with no difference in body weights (**Figure 2-17b**). These results indicated that T cells played an essential role in the anticancer efficacy of our treatment and support the rationale of using nMOF-mediated RT to augment checkpoint blockade cancer immunotherapy. To confirm the long-term antitumor immune response, we carried out a tumor challenge study. CT26 tumors

were established on the right flanks of mice and treated with Hf_{12}-DBA and X-ray (1 Gy/fraction, 10 fractions in consecutive days). Three out of six mice had their tumors completely eradicated after treatment, affording a cure rate of 50%. Tumors in the other three mice shrank to very small sizes, but regrew beginning days 17, 26 and 32, respectively, post tumor inoculation. On day 50 post tumor inoculation, approximately one month after tumor eradication for the cured mice, the treated mice and naïve control mice were challenged with 2×10^6 CT26 cells on the contralateral, left flank. None of the treated mice developed tumors on the left flank within 21 days (**Figure 2-17c**), but two mice had to be euthanized due to large primary tumor burden. The three cured mice remained tumor-free 60 days after tumor challenge, indicating strong anticancer immune memory effect. In comparison, all mice in the control group consistently developed tumors after injection with 2×10^6 CT26 cells.

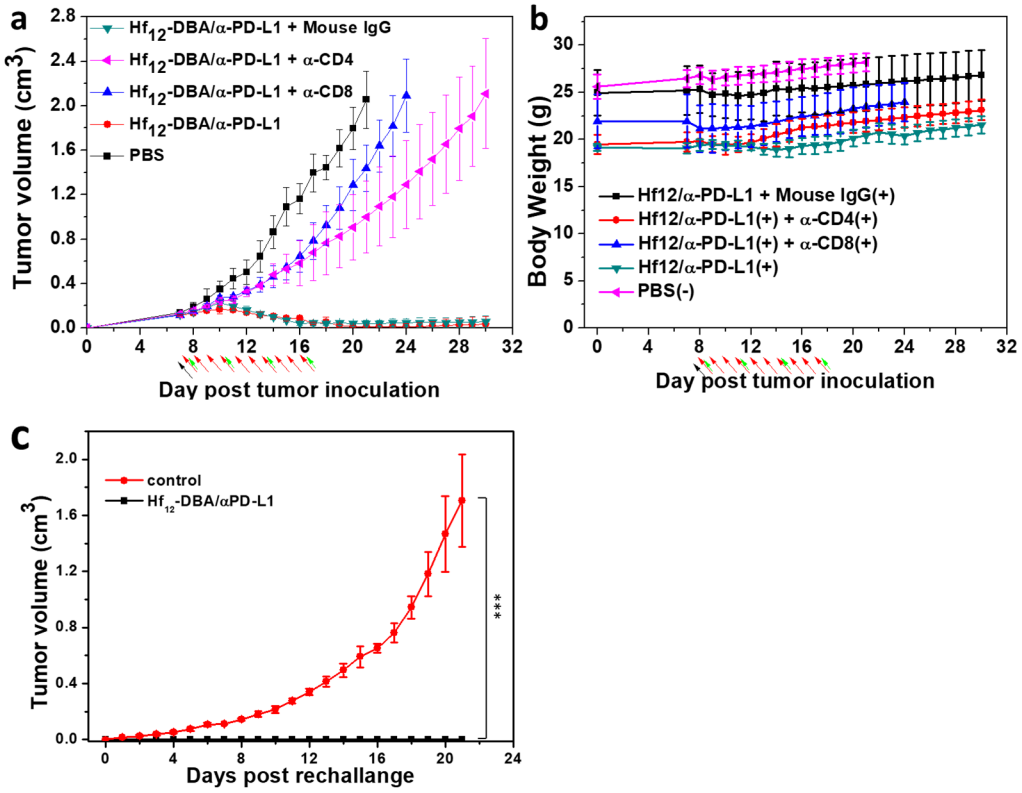

Figure 2-17 Tumor growth curves (a) and body weight (b) of CT26 tumor bearing mice with T cell depletion and treated with Hf_{12}-DBA, anti-PD-L1 antibody and X-ray irradiation. (c) Tumor

Figure 2-17, continued growth curves after the tumor rechallenge with CT26 cells. Treatment began on day 7 after tumor inoculation when the tumor reached a volume of 100-150 mm^3. Black, red, and green arrows refer to the times of PBS or nanoparticles injections, X-ray irradiation, and antibody administration, respectively, n = 6. P values for comparisons with controls by t-test are indicated by three asterisks: *** $P<0.001$. Central data points and error bars represent mean ± s.d. values, respectively. Reprinted with permission from *Nature Communications* **2018**, *9*, 2351–2363. Copyright 2018 Nature Publishing Group.

2.3 Conclusion

In this chapter, we have developed Hf-based nMOFs, Hf_6-DBA and Hf_{12}-DBA, as effective radiosensitizers for low-dose X-ray RT. Compared with solid high-Z NPs, nMOFs assembled from ultrasmall metal clusters in an ordered manner effectively enhance energy deposition by utilizing the secondary radiation, promote radiolysis by maintaining ultra large specific surface area and facilitate ROS diffusion through porous structures to generate much better radiosensitization effect. The combination of nMOF-mediated RT and PD-L1 checkpoint blockade extended the local therapeutic effects of RT to distant tumors *via* systemic anti-tumor immunity. With the ability to rationally design and systematically tune the compositions and structures of nMOFs, we expect that even more powerful nMOF-based radioenhancers will become available to drastically enhance the efficacy of RT without incurring deliberating side effects and to significantly potentiate checkpoint blockade immunotherapy for the treatment of non-immunogenic tumors.

2.4 Methods

Materials, cell lines, and animals: All of the starting chemicals were purchased from Sigma-Aldrich and Fisher (USA), unless otherwise noted, and used without further purification.

Human head and neck cancer cells SQ20B and JSQ3, and murine breast cancer cells TUBO and 4T1 were kindly provided by Dr. Stephen J. Kron at University of Chicago. The murine colon adenocarcinoma cell, CT26, and the human cervical cancer cell, HeLa, were purchased from the American Type Culture Collection (Rockville, MD, USA). TUBO and CT26 cells were cultured in Roswell Park Memorial Institute (RPMI) 1640 medium (GE Healthcare, USA) supplemented with 10% fetal bovine serum (FBS, VWR, USA). 4T1 and HeLa cells were cultured in Dulbecco's Modified Eagle's Medium (DMEM) medium (GE Healthcare, USA) supplemented with 10% FBS. SQ20B and JSQ3 cells were cultured in Dulbecco's Modified Eagle's Medium (DME) and Ham's F-12 Nutrient Mixture (DME/F12) medium (GE Healthcare, USA) supplemented with 20% FBS. All media were supplemented with 10% FBS, 100 U/mL penicillin G sodium and 100 μg/mL streptomycin sulfate. Cells were cultured in a humidified atmosphere containing 5% CO_2 at 37ºC. Mycoplasma was tested before use by MycoAlert detection kit (Lonza Nottingham, Ltd.) BALB/c mice (6-8 weeks) were obtained from Harlan-Envigo Laboratories, Inc (USA). The study protocol was reviewed and approved by the Institutional Animal Care and Use Committee (IACUC) at the University of Chicago.

Synthesis of Hf_6-DBA and Hf_6-DBAn nMOFs: To a 1 dram glass vial was added 0.5 mL of $HfCl_4$ solution (2.0 mg/mL in DMF), 0.5 mL of the 2,5-di(*p*-benzoato)aniline (H_2DBA) solution (2.0 mg/mL in DMF) or 9,10-di(*p*-benzoato)anthracene (H_2DBAn) solution (2.5 mg/mL in DMF) and 0.5 μL of trifluoroacetic acid. The reaction mixture was kept in a 60 °C oven for 72 h. The

white precipitate was collected by centrifugation and washed with DMF, 1% trimethylamine/ethanol solution and ethanol.

Synthesis of Hf_{12}-DBA and Hf_{12}-DBAn nMOFs: To a 1 dram glass vial was added 0.5 mL of $HfCl_4$ solution (1.6 mg/mL in DMF), 0.5 mL of the H_2DBA solution (1.6 mg/mL in DMF) or H_2DBAn solution (2 mg/mL in DMF), 75 μL of acetic acid and 5 μL of water. The reaction mixture was kept in an 80 °C oven for 72 h. The white precipitate was collected by centrifugation and washed with DMF, a 1% trimethylamine/ethanol solution, and ethanol.

Synthesis of HfO_2 nanoparticles: HfO_2 nanoparticles were synthesized according to the reported protocol.[17] To a 20 mL Teflon cup was added 15 mL of $HfCl_4$ solution (10mg/mL in benzyl alcohol), which was sealed in a steel autoclave and heated to 200 °C for 48 h. The white precipitate was collected by centrifugation and washed with ethanol.

Irradiator settings: An RT250 orthovoltage X-ray machine model (Philips, USA) with fixed setting at 250 kVp, 15 mA and a built-in 1 mm Cu filter was used for *in vitro studies*. An X-RAD 225 image-guided biological irradiator (Precision X-ray Inc., USA) was used for both test tubes and *in vivo* studies. The instrument was set at 120 kVp and 20 mA, with a 2 mm flat-board Cu filter installed before a 25 mm collimator. A γ-ray irradiator ($^{Co}60$ source, Atomic Energy Canada Limited, Canada) was used for clonogenic assay. All three irradiators are maintained and calibrated for dosimetry routinely by the Department of Radiation Oncology, The University of Chicago, before all experiments.

Radioluminescence measurements: Hf_{12}-DBAn and Hf_6-DBAn were suspended in ethanol at equivalent Hf concentration of 1 mM, degassed and refilled with nitrogen gas. The solutions were transferred to 1 dram vials for X-ray irradiation with a maximum dose rate of 2.93 Gy/min. X-ray

luminescence measurements were acquired with the X-RAD irradiator through a 2 mm aluminum filter. The radioluminescence was detected using a cooled CoolSNAP HQ2 CCD camera (Photometrics, USA) equipped with a DX Micro-NIKKOR f/2.8 macro lens (Nikon, Japan). Samples were tested at a voltage of 70 kVp and current values ranging from 5, 10, 20, 30 to 40 mA for 30 s. Radioluminescence intensities were processed by ImageJ with background subtraction.

Detection of hydroxyl radical produced by irradiation: HfO_2, Hf_6-DBA and Hf_{12}-DBA were suspended in water at equivalent Hf concentrations of 20 μM in the presence of 5 μM APF. A water solution of 5 μM APF was used as background. 100 μL of each suspension was added to a 96-well plate and then irradiated with 0, 1, 2, 3, 5, or 10 Gy X-ray. The fluorescence signal was immediately collected with a Xenogen IVIS 200 imaging system.

Clonogenic assay: The clonogenic assay was performed according to a modified protocol. CT26 cells were cultured in a 6-well plate overnight and incubated with particles at equivalent Hf concentration of 20 μM for 4 h followed by irradiation with 0, 1, 2, 4, 8 and 16 Gy X-ray. Cells were trypsinized and counted immediately. 200-2000 cells were seeded in a 6-well plate and cultured with 2 mL medium for 15 days. Once colony formation was observed, the culture medium was discarded. The plates were rinsed twice with PBS, then stained with 500 μL of 0.5% w/v crystal violet in 50% methanol/H_2O. The wells were rinsed with water for three times and the colonies were counted manually.

Apoptosis/necrosis: 4T1 cells were cultured in a 6-well plate overnight and incubated with particles at equivalent Hf concentration of 20 μM for 4 h followed by irradiation at 0 and 2 Gy X-

ray. 24 h later, the cells were stained according to the AlexaFluor 488 Annexin V/dead cell apoptosis kit (Life technology, USA) and quantified by flow cytometry (LSRFortessa, BD, USA).

DNA damage: CT26 cells were cultured in a 6-well plate overnight and incubated with particles at equivalent Hf concentration of 20 μM for 4 h followed by irradiation at 0 and 2 Gy X-ray. Cells were stained immediately with the HCS DNA damage kit (Life Technology, USA) for confocal laser scanning microscopy (CLSM, FV1000, Olympus, Japan) and flow cytometry. ImageJ was used to quantify the number of cells with foci and number of intranuclear foci.

Immunogenic cell death: CT26 cells were cultured in a 6-well plate overnight and incubated with particles at equivalent Hf concentration of 20 μM for 4 h followed by irradiation with 0 or 2 Gy X-ray (250 kVp, 15 mA, 1 mm Cu filter). After incubation for 4 h, the cells were washed three times with PBS, fixed with 4% paraformaldehyde, incubated with AlexaFluor 488-CRT (Enzo Life Sciences, USA) with 1: 100 dilution for 2 h, stained with DAPI, and observed by CLSM. Treated cells were incubated for 4 h, collected, incubated with AlexaFluor 488-CRT antibody for 2 h, and then stained with PI for analysis by flow cytometry.

Abscopal Effect: A bilateral model was established by subcutaneously inoculating 2×10^6 and 1×10^6 CT26 cells onto the right and left flanks of BALB/c mice for respective primary and secondary tumors. When the primary tumors reached 100-150 mm^3 in volume, mice were injected intratumorally with nMOFs at a dose of 1 μmol Hf or PBS. 12 h after injection, mice were anaesthetized with 2% (v/v) isoflurane and the primary tumors were irradiated with 0.5 or 1 Gy X-ray/fraction for a total of 10 daily fractions. Antibodies were given every three days by intraperitoneal injection at a dose of 75 μg/mouse. The tumor sizes were measured daily with a caliper where tumor volume equals ($width^2 \times length$)/2. Mice treated with Hf_6-DBA and Hf_{12}-

DBA were sacrificed on Day 30 and mice treated with PBS or anti-PD-L1 antibody alone were sacrificed on Day 21. Each mouse was weighed daily to evaluate toxicity.

ELISpot assay: Tumor-specific immune responses to IFN-γ was measured *ex vitro* by ELISpot assay (Mouse IFN gamma ELISPOT Ready-SET-Go!®; Cat. No. 88-7384-88; eBioscience). Millipore Multiscreen HTS-IP plates was coated overnight at 4°C with anti-Mouse IFN-γ capture antibody. Single-cell suspensions of splenocytes were obtained from CT26 tumor-carrying mice and seeded onto the antibody-coated plate at a concentration of 2×10^5 cells/well. Cells were incubated with or without SPSYVYHQF stimulation (10 mg/ml; in purity >95%; PEPTIDE 2.0) for 42 h at 37 °C and then discarded. The plate was then incubated with biotin-conjugated anti-IFN-γ detection antibody at room temperature (r.t.) for 2 h, followed by incubation with Avidin-HRP for 2 h at r.t. 3-amino-9-ethylcarbazole substrate solution (Sigma, Cat. AEC101) was added for cytokine spot detection. Spots were imaged and quantified with a CTL ImmunoSpot Analyzer (Cellular Technology Ltd, USA).

Lymphocyte profiling: Tumors were harvested, treated with 1 mg/mL collagenase I (Gibco™, USA) for 1 h, and ground by the rubber end of a syringe. Cells were filtered through nylon mesh filters with size of 40 μm and washed with PBS. Tumor-draining lymph nodes were collected and directly ground through the cell strainers. The single-cell suspension was incubated with anti-CD16/32 (clone 93) to reduce nonspecific binding to FcRs. Cells were further stained with the following fluorochrome-conjugated antibodies: CD45 (30-F11), CD3ε (145-2C11), CD4 (GK1.5), CD8α (53-6.7), Foxp3 (FJK-16s), CD25 (PC61.5), Nkp46 (29A1.4), F4/80 (BM8), B220 (RA3-6B2) and PI (all from eBioscience). Antibodies were used with the dilution of 1: 200. Representative gating strategies for different immune cells are shown in **Figure 2-18**. LSR

Fortessa (BD Biosciences) was used for cell acquisition and data analysis was carried out with FlowJo software (Tree Star, Ashland, OR).

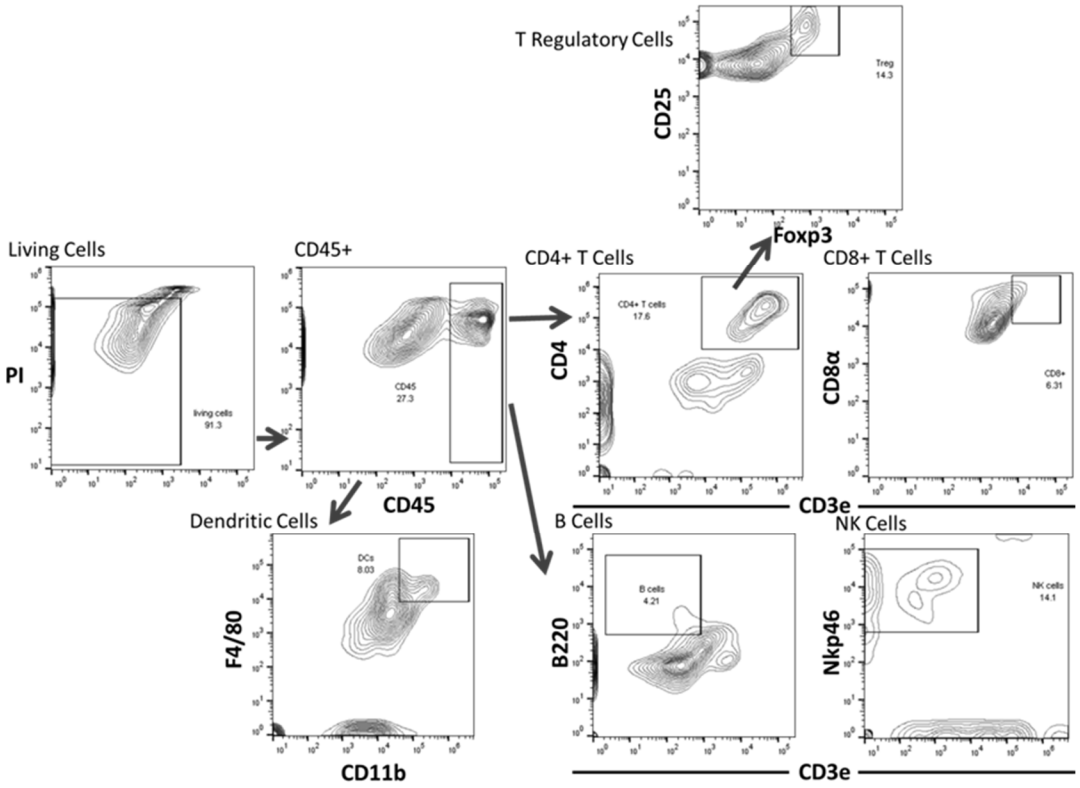

Figure 2-18 Representative gating strategies for $CD4^+$ T cells, $CD8^+$ T cells, T regulatory cells, B cells, NK cells and dendritic cells. Reprinted with permission from *Nature Communications* **2018**, *9*, 2351–2363. Copyright 2018 Nature Publishing Group.

T cell depletion: The bilateral subcutaneous model was established as for the *in vivo* anti-tumor efficacy. When the primary tumors reached 100-150 mm^3 in volume, mice were injected intratumorally with nMOFs at a dose of 0.11 mg/mouse or PBS. Anti-CD4 (GK1.5, BioXCell, USA), anti-CD8 (OKT-8, BioXCell, USA) and mouse IgG (C1.18.4, BioXCell, USA) antibodies were intraperitoneally injected into the mice (200 μg/mouse) on Day 0 and 5 after the first

treatment. Twelve hours post-injection, mice were anesthetized with 2% (v/v) isoflurane, and irradiated.

Tumor challenge studies: On day 50 post tumor inoculation, mice were challenged with 2×10^6 CT26 cells on the contralateral flank. Healthy mice were simultaneously inoculated as control. The mice were sacrificed when the tumors of the control mice reached 2 cm^3.

2.5 References

1. Schaue, D.; McBride, W. H., Opportunities and challenges of radiotherapy for treating cancer. *Nature reviews Clinical oncology* **2015,** *12* (9), 527-540.

2. Thariat, J.; Hannoun-Levi, J.-M.; Myint, A. S.; Vuong, T.; Gérard, J.-P., Past, present, and future of radiotherapy for the benefit of patients. *Nature Reviews Clinical oncology* **2013,** *10* (1), 52-60.

3. Chen, W.; Zhang, J., Using nanoparticles to enable simultaneous radiation and photodynamic therapies for cancer treatment. *Journal of nanoscience and nanotechnology* **2006,** *6* (4), 1159-1166.

4. Hainfeld, J. F.; Dilmanian, F. A.; Slatkin, D. N.; Smilowitz, H. M., Radiotherapy enhancement with gold nanoparticles. *Journal of Pharmacy and Pharmacology* **2008,** *60* (8), 977-985.

5. Mirjolet, C.; Papa, A.; Créhange, G.; Raguin, O.; Seignez, C.; Paul, C.; Truc, G.; Maingon, P.; Millot, N., The radiosensitization effect of titanate nanotubes as a new tool in radiation therapy for glioblastoma: a proof-of-concept. *Radiotherapy and Oncology* **2013,** *108* (1), 136-142.

6. Retif, P.; Pinel, S.; Toussaint, M.; Frochot, C.; Chouikrat, R.; Bastogne, T.; Barberi-Heyob, M., Nanoparticles for radiation therapy enhancement: the key parameters. *Theranostics* **2015,** *5* (9), 1030.

7. Bonvalot, S.; Le Pechoux, C.; De Baere, T.; Kantor, G.; Buy, X.; Stoeckle, E.; Terrier, P.; Sargos, P.; Coindre, J. M.; Lassau, N., First-in-human study testing a new radioenhancer using nanoparticles (NBTXR3) activated by radiation therapy in patients with locally advanced soft tissue sarcomas. *Clinical Cancer Research* **2017,** *23* (4), 908-917.

8. Bonvalot, S.; Rutkowski, P. L.; Thariat, J.; Carrère, S.; Ducassou, A.; Sunyach, M.-P.; Agoston, P.; Hong, A.; Mervoyer, A.; Rastrelli, M., NBTXR3, a first-in-class radioenhancer

hafnium oxide nanoparticle, plus radiotherapy versus radiotherapy alone in patients with locally advanced soft-tissue sarcoma (Act. In. Sarc): a multicentre, phase 2–3, randomised, controlled trial. *The Lancet Oncology* **2019,** *20* (8), 1148-1159.

9. Misawa, M.; Takahashi, J., Generation of reactive oxygen species induced by gold nanoparticles under X-ray and UV Irradiations. *Nanomedicine: Nanotechnology, Biology and Medicine* **2011,** *7* (5), 604-614.

10. Goel, S.; Ni, D.; Cai, W., Harnessing the power of nanotechnology for enhanced radiation therapy. *ACS Nano* **2017,** *11* (6), 5233-5237.

11. Cavka, J. H.; Jakobsen, S.; Olsbye, U.; Guillou, N.; Lamberti, C.; Bordiga, S.; Lillerud, K. P., A new zirconium inorganic building brick forming metal organic frameworks with exceptional stability. *Journal of the American Chemical Society* **2008,** *130* (42), 13850-13851.

12. Dai, R.; Peng, F.; Ji, P.; Lu, K.; Wang, C.; Sun, J.; Lin, W., Electron crystallography reveals atomic structures of metal–organic nanoplates with $M_{12}(\mu_3\text{-O})_8(\mu_3\text{-OH})_8(\mu_2\text{-OH})_6$ (M= Zr, Hf) secondary building units. *Inorganic Chemistry* **2017,** *56* (14), 8128-8134.

13. Wang, C.; Volotskova, O.; Lu, K.; Ahmad, M.; Sun, C.; Xing, L.; Lin, W., Synergistic assembly of heavy Metal clusters and luminescent organic bridging ligands in metal–organic frameworks for highly efficient X-ray scintillation. *Journal of the American Chemical Society* **2014,** *136* (17), 6171-6174.

14. Bonner, W. M.; Redon, C. E.; Dickey, J. S.; Nakamura, A. J.; Sedelnikova, O. A.; Solier, S.; Pommier, Y., γH2AX and cancer. *Nature Reviews Cancer* **2008,** *8* (12), 957-967.

15. Celeste, A.; Fernandez-Capetillo, O.; Kruhlak, M. J.; Pilch, D. R.; Staudt, D. W.; Lee, A.; Bonner, R. F.; Bonner, W. M.; Nussenzweig, A., Histone H2AX phosphorylation is dispensable for the initial recognition of DNA breaks. *Nature Cell Biology* **2003,** *5* (7), 675.

16. Obeid, M.; Panaretakis, T.; Joza, N.; Tufi, R.; Tesniere, A.; Van Endert, P.; Zitvogel, L.; Kroemer, G., Calreticulin exposure is required for the immunogenicity of γ-irradiation and UVC light-induced apoptosis. *Cell Death & Differentiation* **2007,** *14* (10), 1848-1850.

17. Pinna, N.; Garnweitner, G.; Antonietti, M.; Niederberger, M., Non-aqueous synthesis of high-purity metal oxide nanopowders using an ether elimination process. *Advanced Materials* **2004,** *16* (23-24), 2196-2200.

CHAPTER 3. Nanoscale Metal-Organic Frameworks for Mitochondria-Targeted Radiotherapy-Radiodynamic Therapy

3.1 Rationale for the project design

In Chapter 2, we defined the critical parameters for developing nMOFs for radiosensitization. In the radioluminescence experiment of Hf-DBAn, it was demonstrated that Hf-based SBUs effectively deposited X-ray radiation and transferred energy to nearby bridging anthracene-based ligands for luminescence emission. Considering similar energy deposition and energy transfer process, it might be possible to generate other ROS, including singlet oxygen ($^1O_2$) or superoxide (O_2^-), when photosensitizer (PS)-based ligands are integrated into Hf-based nMOFs.

Among various PSs, ruthenium (Ru)-based PSs, , including $Ru(bpy)_3^{2+}$ (bpy=2,2'-bipyridine), possess several favorable properties including long excited state lifetimes, high $^1O_2$ generation efficiencies, and good aqueous solubility.[1] In addition, cationic $Ru(bpy)_3^{2+}$ has recently been reported to target mitochondria, further increasing its potency.[2-3]

In this chapter, we report the synthesis of Hf-DBB-Ru [DBB-Ru = bis(2,2'-bipyridine)(5,5'-di(4-benzoato)-2,2'-bipyridine)ruthenium(II) chloride] as a mitochondria-targeted nMOF for a new therapeutic modality, radiotherapy-radiodynamic therapy (RT-RDT). By integrating $Ru(bpy)_3^{2+}$ PSs into the framework, Hf-DBB-Ru possesses a cationic UiO topology and exhibits strong mitochondria-targeting property as demonstrated by elemental quantification and confocal microscopy. Upon irradiation with low doses of X-rays, the Hf_6 SBUs efficiently absorb energy to not only generate $^{\bullet}OH$ *via* radiolysis but also transfer energy to the DBB-Ru PSs to generate $^1O_2$

in a radiodynamic mode of action. Mitochondria-targeted RT-RDT process depolarizes the mitochondrial membrane potential, releases cytochrome c, and disturbs the respiratory chain to lead to programmable cell death of tumor cells. We further show that nMOF-enabled, mitochondria-targeted RT-RDT significantly regresses colorectal tumors on mouse models at very low X-ray doses and with no side effects (**Figure 3-1**).

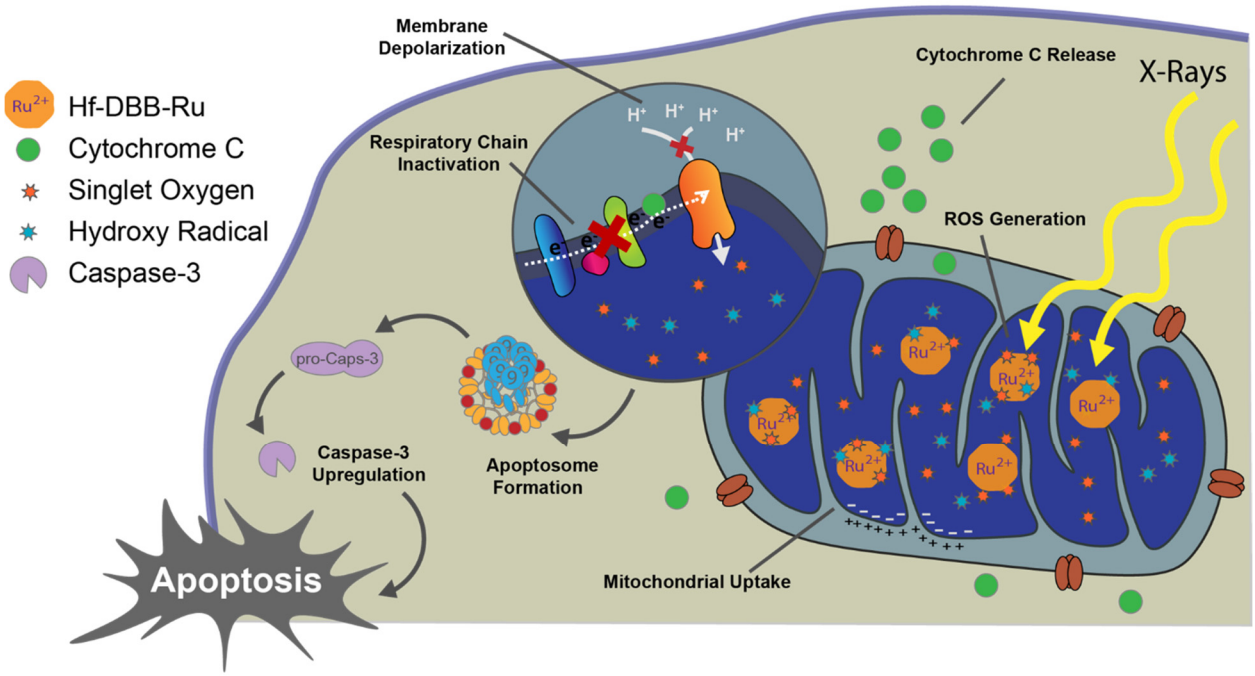

Figure 3-1 Schematic showing the RT and RDT process enabled by Hf-DBB-Ru. Mitochondria-targeted RT-RDT mediated by Hf-DBB-Ru. Hf-DBB-Ru was internalized by tumor cells efficiently and enriched in mitochondria due to dispersed cationic charges in the nMOF framework. Hf_6 SBUs preferentially absorb X-rays over tissues to enhance RT by sensitizing hydroxyl radical generation and enable RDT by transferring energy to $Ru(bpy)_3^{2+}$-based bridging ligands to generate singlet oxygen. The RT-RDT process trigger mitochondrial membrane potential depolarization, membrane integrity loss, respiratory chain inactivation, and cytochrome c release to initiate apoptosis of cancer cells. Reprinted with permission from *Nature Communications*, **2018**, *9*, 4321–4333. Copyright 2018 Nature Publishing Group.

3.2 Results

3.2.1 Synthesis and characterization of Hf-DBB-Ru

Hf-DBB-Ru was synthesized through a solvothermal reaction between $HfCl_4$ and H_2DBB-Ru with TFA as modulator. Transmission electron microscopy (TEM) imaging showed a uniform spherical morphology of <100 nm in diameter for Hf-DBB-Ru (**Figure 3-2a**), whereas dynamic light scattering (DLS) measurements gave a Z-average diameter, number-average diameter, and polydispersity index of 98.1 ± 4.1 nm, 76.0 ± 3.9 nm, and 0.12 ± 0.01, respectively, for Hf-DBB-Ru (**Figure 3-2b**). Hf-DBB-Ru particles exhibited a positive ζ potential of 38.9 ± 3.1 mV due to the cationic $[DBB\text{-}Ru]^{2+}$ bridging ligands.

Powder X-ray diffraction (PXRD) studies showed that Hf-DBB-Ru adopted a UiO-like topological structure (**Figure 3-2c**). Though Hf-DBB-Ru showed the same peak positions as the reported UiO-69, the first peak at $2\theta = 3.96$ °, which corresponds to the (111) reflection, exhibited lower intensity than UiO-69, likely due to out-of-phase destructive interference from Ru centers which are sitting half way between the in-phase Hf clusters. Based on the UiO-69 topological structure, the cationic Hf-DBB-Ru framework was formulated as $[Hf_6(\mu_3\text{-}O)_4(\mu_3\text{-}OH)_4(DBB\text{-}Ru)_6]^{12+}$. PXRD studies also showed that Hf-DBB-Ru was stable in 0.6 mM PBS for 6 days owing to strong carboxylate coordination to the Hf_6 clusters.

As an nMOF-based photosensitizer, Hf-DBB-Ru showed similar absorption peaks (**Figure 3-2d**) and phosphorescence peak (**Figure 3-2e**) to the H_2DBB-Ru ligand. Upon X-ray irradiation, Hf-DBB-Ru efficiently absorbs energy to generate $^{\bullet}OH$ from the Hf_6 SBUs and $^1O_2$ from the DBB-Ru by effective transfer energy (**Figure 3-2f**).

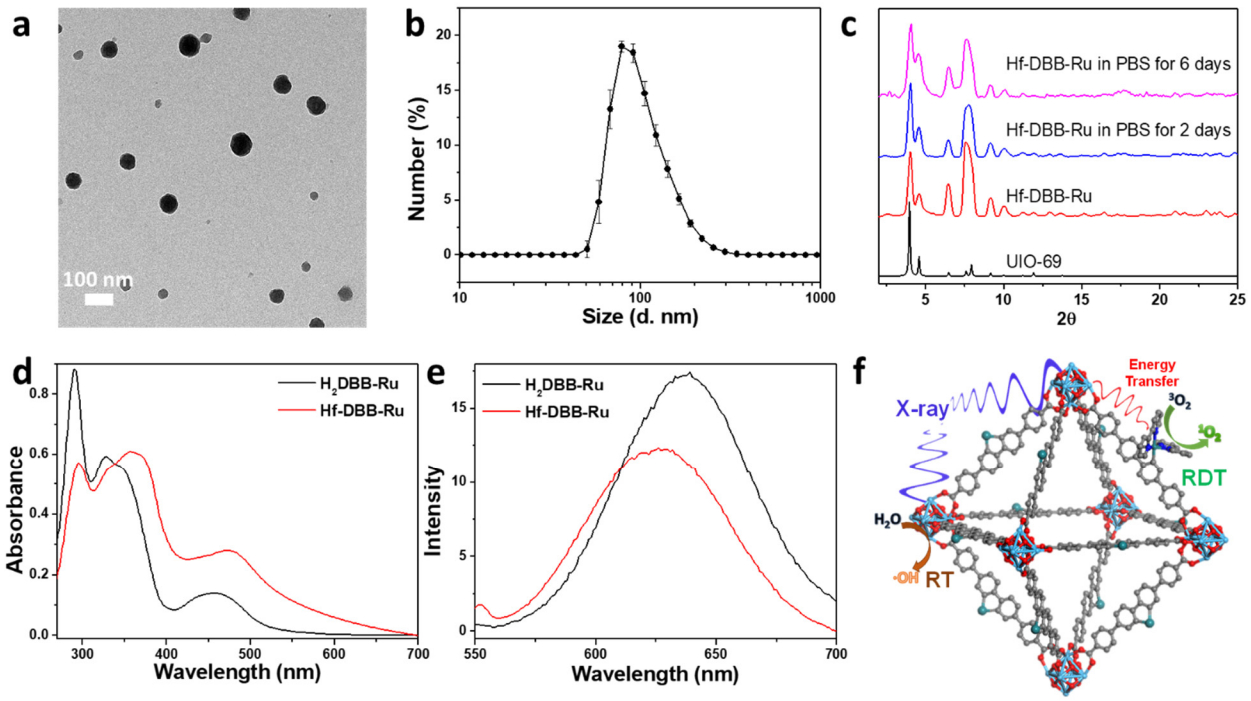

Figure 3-2 TEM image (a) and number-averaged diameter in water by DLS measurements (b) of Hf-DBB-Ru, n = 3. (c) PXRD patterns of Hf-DBB-Ru samples and UiO-69. Hf-DBB-Ru was freshly prepared or incubated in 0.6 mM PBS for 6 days. (d) UV-visible spectra of Hf-DBB-Ru and H_2DBB-Ru. (e) Emission spectra of Hf-DBB-Ru and H_2DBB-Ru with 450 nm excitation. (f) Schematic showing the RT and RDT process enabled by Hf-DBB-Ru. Reprinted with permission from *Nature Communications*, **2018**, *9*, 4321–4333. Copyright 2018 Nature Publishing Group.

3.2.2 ROS generation

We next determined if Hf-DBB-Ru could generate both $^{\bullet}OH$ and $^1O_2$ upon X-ray irradiation. Hydroxyl radicals were detected *via* APF assay. The amount of APF trapped in Hf-DBB-Ru or Hf-DBA was first estimated by detecting chemically produced hydroxyl radicals using APF in the presence of the nMOF. The percentage of APF trapped in the nMOF is approximated to one minus the fluorescence intensity ratio of APF with nMOF over that of APF without nMOF (**Figure 3-3a**). An aqueous solution or an aqueous dispersion of Hf-DBB-Ru or Hf-DBA at an equivalent Hf concentration of 20μM was added 5μM APF and then irradiated with X-ray in the dose range of 0 to 10 Gy. The fluorescence signals at 515 nm were detected. We deduced the fluorescence intensity

corresponding to the amounts of hydroxyl radicals generated by Hf-DBB-Ru, Hf-DBA, and H_2O by correcting for the percentage of APF trapped in the nMOF (**Figure 3-3b**). $^{\bullet}OH$ generation for all groups increased linearly with X-ray dose and the relative enhancement of hydroxyl radical generation compared with water was determined to be 54.2% and 30.5% for Hf-DBB-Ru and Hf-DBA, respectively. We then used SOSG assay to detect $^1O_2$ generation by Hf-DBB-Ru. 12.5 μM SOSG was added to an aqueous solution or an aqueous dispersion of Hf-DBB-Ru or Hf-DBA at an equivalent Hf concentration of 20μM and irradiated with X-ray in the dose range of 0 to 3 Gy. The fluorescence signals at 540 nm were determined and subtracted from that of an aqueous solution. As shown in **Figure 3-4**, Hf-DBB-Ru showed significant SOSG signal while Hf-DBA showed no singlet oxygen generation. APF and SOSG assays thus show that Hf-DBB-Ru generates both $^{\bullet}OH$ by Hf_6 SBUs *via* radiosensitization and $^1O_2$ through energy transfer from Hf_6 SBUs to DBB-Ru ligands upon X-ray irradiation.

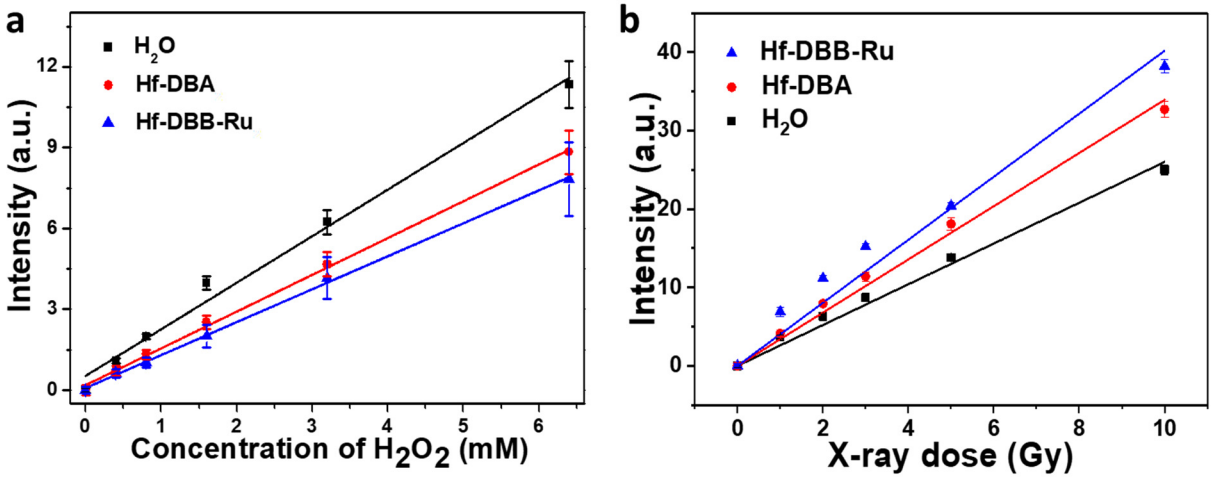

Figure 3-3 APF assay. (a) APF fluorescence of H_2O, Hf-DBA, and Hf-DBB-Ru with Fenton reaction at equivalent Hf concentrations of 20 μM, n = 6. (b) APF fluorescence of Hf-DBB-Ru and Hf-DBA at equivalent Hf concentrations of 20 μM and H_2O upon X-ray irradiation. The error bars represent s.d. values. Reprinted with permission from *Nature Communications*, **2018**, *9*, 4321–4333. Copyright 2018 Nature Publishing Group.

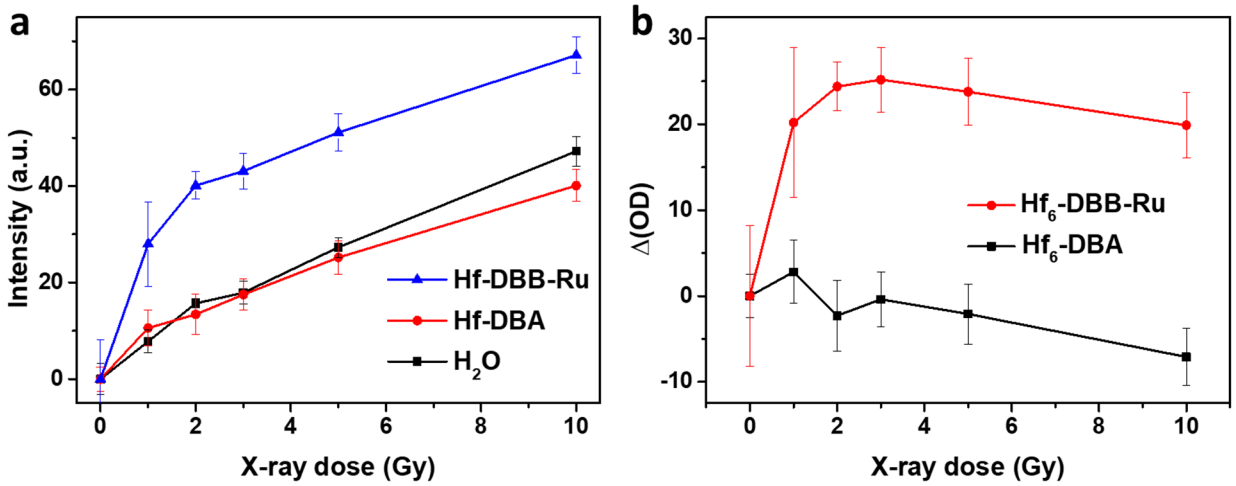

Figure 3-4 SOSG assay. Original data (a) and relative intensity with background subtraction (b) of SOSG fluorescence of Hf-DBB-Ru and Hf-DBA at equivalent Hf concentrations of 20 μM upon X-ray irradiation, n = 6. The error bars represent s.d. values. Reprinted with permission from *Nature Communications*, **2018**, *9*, 4321–4333. Copyright 2018 Nature Publishing Group.

3.2.3 Mitochondria targeting

We hypothesized that small size and cationic nature of Hf-DBB-Ru could lead to efficient uptake by tumor cells and subsequent internalization into mitochondria. We compared mitochondria targeting capability of Hf-DBB-Ru to Hf-DBA, a neutral MOF with a ζ potential of -24.1 ± 5.6 mV in water. Hf-DBA was synthesized as reported Hf_6-DBA in Chapter 2, exhibiting similar size and morphology as Hf-DBB-Ru (**Figure 2-2b**). Meanwhile, we capped Hf-DBB-Ru with excess oxalic acid to generate Hf-DBB-Ru-oxa with a ζ potential of 18.3 ± 0.8 mV in water as a better control. We first used inductively coupled plasma-mass spectrometry (ICP-MS) to determine time-dependent cellular uptake of Hf-DBB-Ru, Hf-DBB-Ru-oxa and Hf-DBA on MC38 cells over 8h (**Figure 3-5a**). Hf-DBB-Ru was rapidly uptaken by MC38 cells, reaching saturation after 2 h incubation. At 1 h incubation, 71.3% Hf-DBB-Ru was already uptaken by MC38 cells. In comparison, only 6.8% Hf-DBA was uptaken by MC38 cells after 1 h incubation. These results indicate that MC38 cells uptake cationic Hf-DBB-Ru more efficiently than Hf-DBA

with a negative ζ potential. Interestingly, no significant difference of cellular uptake between Hf-DBB-Ru-oxa and Hf-DBB-Ru at 8 h.

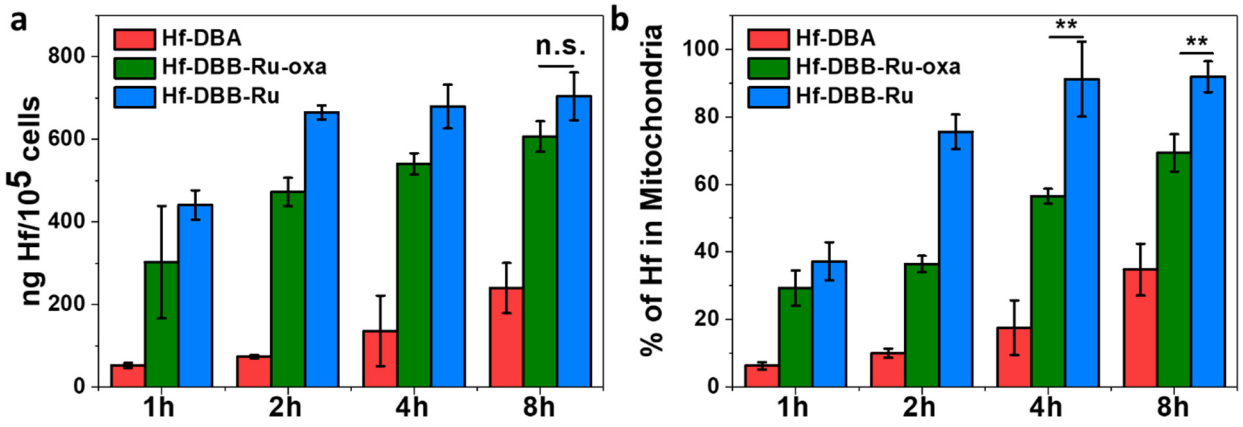

Figure 3-5 (a) Cellular uptake of Hf-DBB-Ru, Hf-DBB-Ru-oxa or Hf-DBA after 1, 2, 4 or 8 hour incubation with equivalent Hf concentrations of 20 μM. (b) Time-dependent enrichment of Hf-DBB-Ru, Hf-DBB-Ru-oxa or Hf-DBA in mitochondria. Mitochondria were isolated from nMOF treated cells and the nMOF amounts quantified by ICP-MS, n = 3. The Hf concentrations were determined by ICP-MS, n = 3. The dots and error bars represent individual data points and s.d. values. Reprinted from Reprinted with permission from *Nature Communications*, **2018**, *9*, 4321–4333. Copyright 2018 Nature Publishing Group.

Mitochondria enrichment of Hf-DBB-Ru, Hf-DBB-Ru-oxa and Hf-DBA in MC38 cells was then quantitatively determined by ICP-MS and directly visualized by confocal laser scanning microscopic (CLSM) imaging. We extracted mitochondria using a modified protocol to quantify the percentage of internalized particles in mitochondria.[4] ICP-MS analyses showed that Hf-DBB-Ru was quickly enriched in mitochondria, reaching saturation after 4h incubation (**Figure 3-5b**). At 4h, over 90% of Hf-DBB-Ru internalized by MC38 cells was found in mitochondria, while only 18% of internalized Hf-DBA was detected in mitochondria. Incorporation of cationic $Ru(bpy)_3^{2+}$ into nMOFs thus not only increases the efficiency of cellular uptake, but also endows mitochondria-targeting property. Capped with oxalate, Hf-DBB-Ru-oxa showed lower enrichment

in mitochondria than Hf-DBB-Ru, indicating that the mitochondria-targeting property of Hf-DBB-Ru is highly surface charge-dependent.

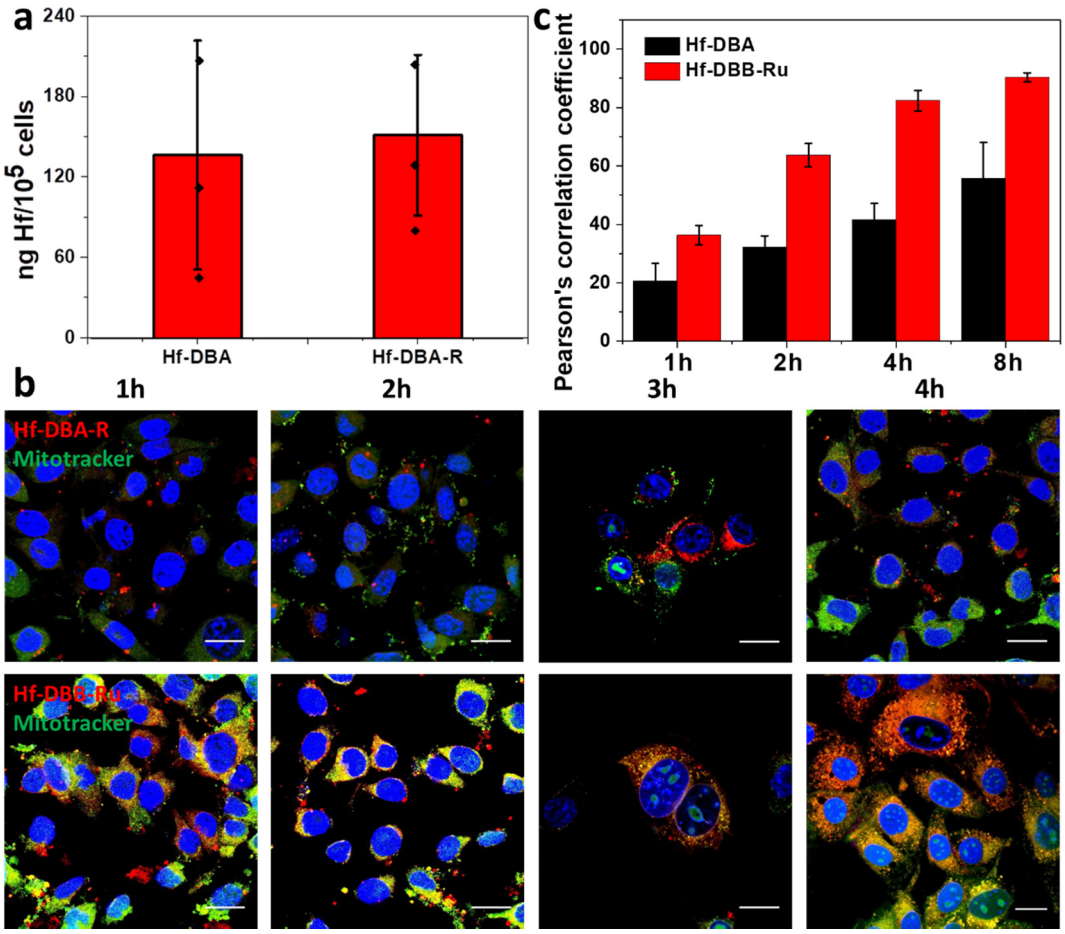

Figure 3-6 (a) Cellular uptake of Hf-DBA and Hf-DBA-R after 4 hour incubation with equivalent Hf concentrations of 20 μM. The Hf concentrations were determined by ICP-MS, n = 3. (b) Co-localization of Hf-DBA-R or Hf-DBB-Ru with mitochondria after different nMOFs incubation time. The cells were first treated with Hf-DBA-R or Hf-DBB-Ru for 1, 2, 4 or 8 hour incubation with equivalent Hf concentrations of 20 μM. After washing with PBS, treated MC38 cells at each time point were then co-stained with commercial organelle trackers for 10 min at room temperature. Blue: Hoechst 33342; Green: Rhodamine 123; Red: Hf-DBA-R or Hf-DBB-Ru. Scale bar = 20 μm. (c) Time-dependent Pearson's correlation coefficients. Co-localization of Hf-DBA-R or Hf-DBB-Ru with mitochondria was analyzed based on fluorescence images captured at 1, 2, 4, and 8 h incubation. The dots and error bars represent individual data points and s.d. values. Reprinted from Reprinted with permission from *Nature Communications*, **2018**, *9*, 4321–4333. Copyright 2018 Nature Publishing Group.

Localization of Hf-DBB-Ru in mitochondria was further visualized by CLSM using its strong red phosphorescence at 628 nm when excited at 450 nm. As a control, Hf-DBA-R, a fluorescent version of Hf-DBA, was synthesized by conjugating Rhodamine B to Hf-DBA *via* a thiourea linkage between the isothiocyanate group on Rhodamine B and the amine group of Hf-DBA.[5] ICP-MS studies indicated that Hf-DBA-R exhibited similar cellular uptake as Hf-DBA (**Figure 3-6a**). After incubating MC38 cells with Hf-DBA-R or Hf-DBB-Ru for 1, 2, 4, and 8 h, CLSM images were captured for co-localization analysis (**Figure 3-6b**). Hf-DBA-R and Hf-DBB-Ru showed red color while mitochondria were labeled with green Rhodamine 123 dye. The co-localization of nMOFs with mitochondria was observed as merged yellow areas. Hf-DBB-Ru treated cells showed significantly more yellow areas than Hf-DBA-R at all time points and gave higher Pearson's correlation coefficients than Hf-DBA-R after detailed analyses of CLSM images using the Co-localization Analysis plugin for ImageJ (**Figure 3-6c**).

To visualize co-localization between nMOFs and mitochondria at higher spatial resolutions, we performed super-resolution confocal imaging and analyzed intensity profiles by ImageJ. Yellow signals come from merging of red signals from nMOFs and green signals from Rhodamine 123-labeled mitochondria. As shown in **Figure 3-7a,c,e**, Hf-DBB-Ru clearly exhibited stronger yellow signals than Hf-DBA-R or Hf-DBB-Ru-oxa due to higher accumulation of Hf-DBB-Ru in mitochondria. The corresponding luminescence intensity profiles for Hf-DBB-Ru, Hf-DBA-R and Hf-DBB-Ru-oxa are shown in **Figure 3-7b,d,f**, respectively. The red luminescence signal from Hf-DBB-Ru traced the green fluorescence from mitochondria, but the red fluorescence of Hf-DBA-R was well separated from the green fluorescence of mitochondria. Hf-DBB-Ru-oxa showed partial mitochondria-targeting property but not as strong as Hf-DBB-Ru. Taken together, Hf-DBB-

Ru was efficiently uptaken by tumor cells and internalized into mitochondria due to its small particle size and highly delocalized positive charges on the particle.

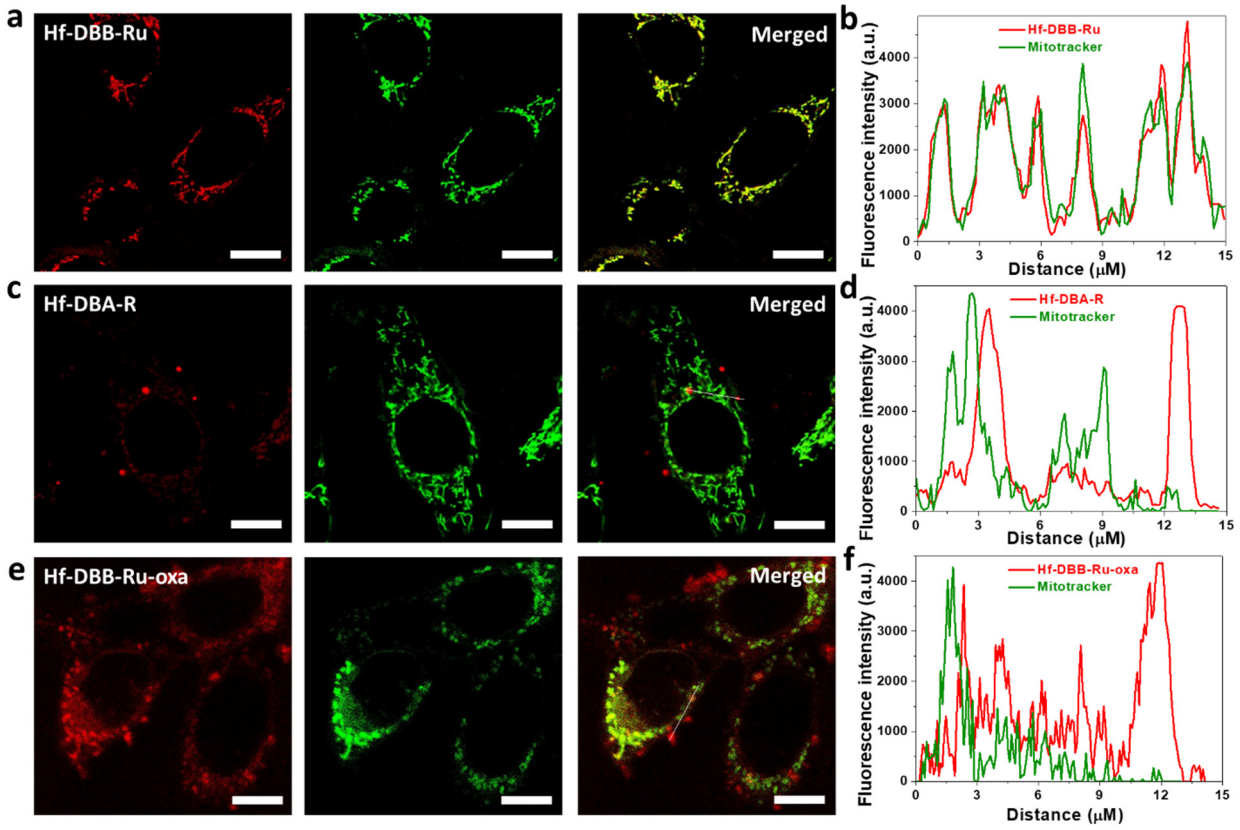

Figure 3-7 Representative mitochondria co-localization images of Hf-DBB-Ru (a), Hf-DBA-R (b) and Hf-DBB-Ru-oxa (c) by CLSM. Scale bar = 5 μm. Mitochondria were labeled with Rhodamine 123 in green (middle column). nMOFs emitted red signal. Yellow areas merged from the red and green signals represent co-localization of Hf-DBB-Ru, Hf-DBA-R or Hf-DBB-Ru-oxa with mitochondria. Fluorescence topographic profiles (b, d and f) display fluorescence intensity curves of straight white lines marked in merged (a), (b) and (c), respectively. Reprinted with permission from *Nature Communications*, **2018**, *9*, 4321–4333. Copyright 2018 Nature Publishing Group.

To confirm the fast cellular internalization and mitochondrial enrichment of Hf-DBB-Ru, time-dependent confocal imaging studies were performed to monitor endocytosis/endosomal escape and mitochondria uptake processes. As shown in **Figure 3-8**, internalized Hf-DBB-Ru escaped from endo/lysosome and was simultaneously enriched in mitochondria within 1 hour.

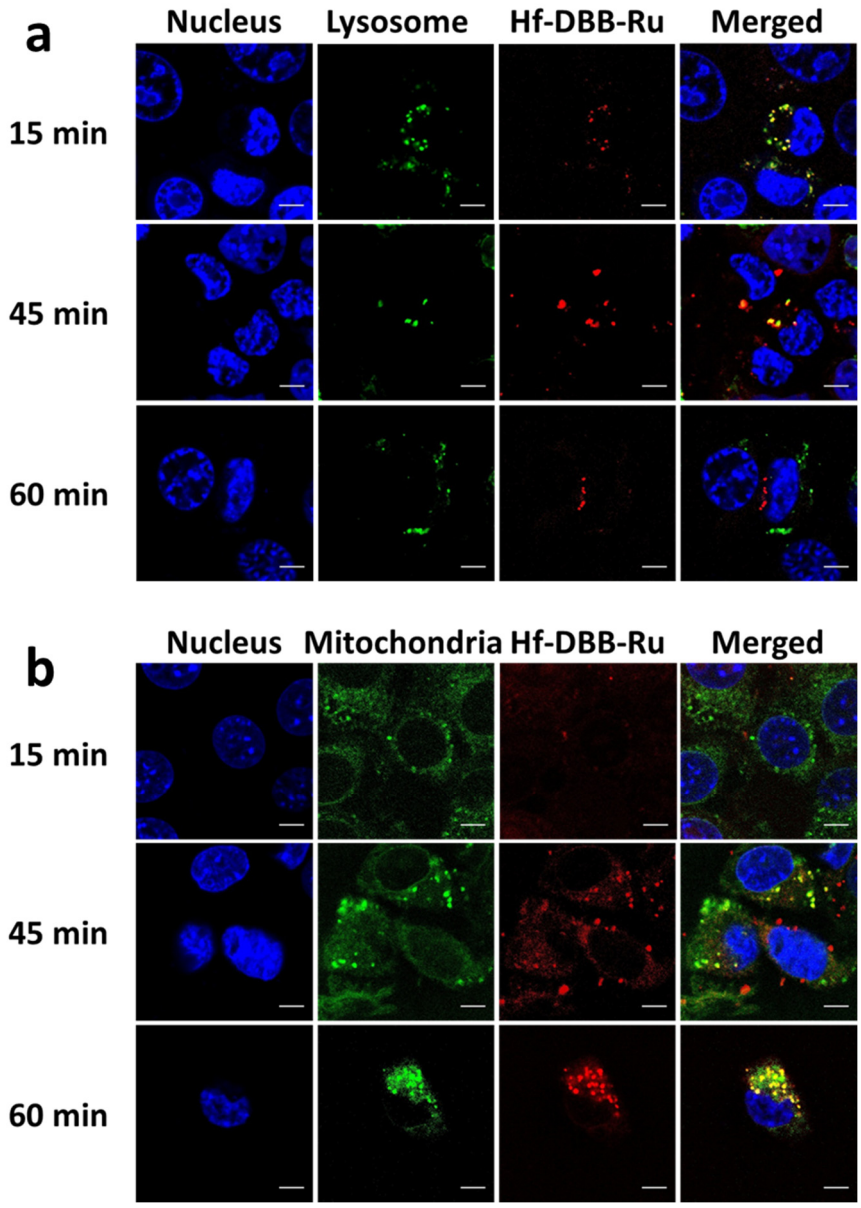

Figure 3-8 Time-dependent endosomal escape (a) and mitochondrial enrichment (b) of Hf-DBB-Ru by confocal microscope imaging. The cells were incubated with Hf-DBB-Ru at equivalent Hf concentrations of 20 μM for 15 to 60 minutes. After washing with PBS, treated MC38 cells at each time point were co-stained with commercial organelle trackers for 10 min at room temperature. Blue: Hoechst 33342 for nuclei; Green: Lysotracker Green (a) or Rhodamine 123 for mitochondria (b); Red: Hf-DBB-Ru. Scale bar = 5 μm. Reprinted with permission from *Nature Communications*, **2018**, *9*, 2351–2363. Copyright 2018 Nature Publishing Group.

3.2.4 *In vitro* anti-tumor efficacy of RT-RDT

Anti-tumor efficacy of Hf-DBA, H_2DBB-Ru, Hf-DBB-Ru-oxa, and Hf-DBB-Ru against MC38 was first investigated by 3-(4,5-dimethylthiazol-2-yl)-5-(3-carboxymethoxyphenyl)-2-(4-sulfophenyl)-2H-tetrazolium (MTS) assay. Particles were incubated with cells at various concentrations for 4 h, followed by irradiation with an X-ray irradiator at a dose of 2 Gy. Hf-DBB-Ru significantly outperformed Hf-DBA, H_2DBB-Ru ligand and Hf-DBB-Ru-oxa in MTS assays (**Figure 3-9a**). The IC_{50} values for Hf-DBB-Ru, Hf-DBA, and H_2DBB-Ru against MC38 cells were calculated to be 20.13 ± 8.58, (14.91 ± 2.2)×10^3, and (3.69 ± 0.31)×10^6 μM, respectively. Stronger cytotoxicity of Hf-DBB-Ru than Hf-DBB-Ru-oxa upon low-dose X-ray validated that mitochondria-targeting contributed to the enhanced RT-RDT. No cytotoxicity was observed in dark control groups (**Figure 3-9b**).

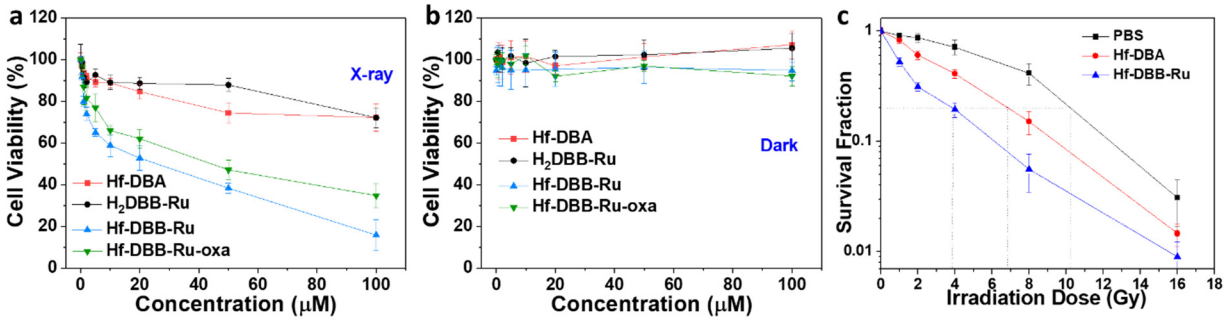

Figure 3-9 Cytotoxicity upon X-ray irradiation at 0 (a) or 2 (b) Gy in MC38 cells. (c) Clonogenic assay on MC38 cells, n = 6. Reprinted with permission from *Nature Communications*, **2018**, *9*, 2351–2363. Copyright 2018 Nature Publishing Group.

Clonogenic assays were then performed to assess the long-term proliferation of cells treated with nMOFs at an equivalent Hf concentration of 20 μM for 4 h followed by irradiation with X-ray from 0 to 16 Gy. At the same Hf concentration, Hf-DBB-Ru outperformed Hf-DBA in radiosensitization, with an REF_{10} value of 2.68 compared to 1.50 for Hf-DBA (**Figure 3-9c**). Interestingly, different from clonogenic curves of conventional radiosensitizers, the concave-

shaped dose-response curves of Hf-DBB-Ru confirmed early response of cells to $^1O_2$ due to the RDT effect.[6]

To confirm the radiosensitization effect of Hf-DBB-Ru, we determined DNA double-strand breaks (DSBs) by detecting phosphorylated γ-H2AX. When incubated with Hf-DBB-Ru and irradiated with X-rays at a dose of 2 Gy, significant γ-H2AX fluorescence indicating DSBs was observed in the nuclei of MC38 cells, similar to the red fluorescence observed for Hf-DBA treated cells upon X-ray irradiation (**Figure 3-10**). No DSB was observed in PBS or H_2DBB-Ru treated cells with irradiation or any particle treated cells without X-ray irradiation. These results indicate that Hf-DBB-Ru exhibits strong radiosensitization effect to cause DNA DSBs.

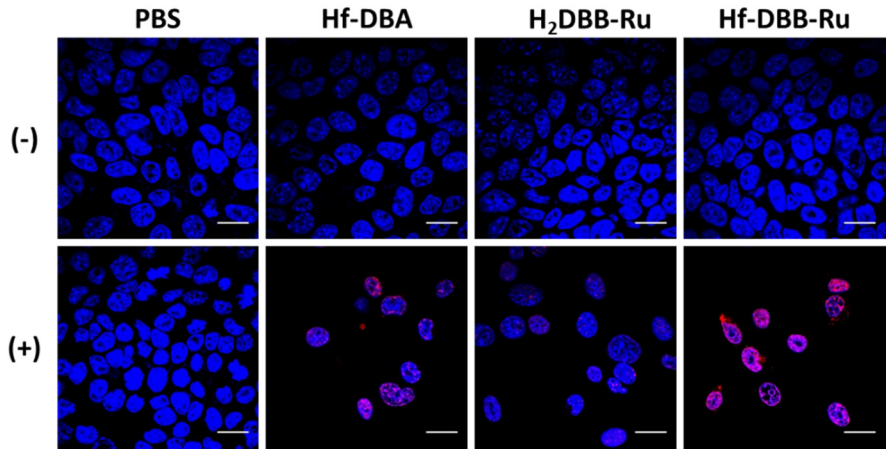

Figure 3-10 Representative γ-H2AX immunostaining assay showing DNA DSBs in MC38 cells. Cells were treated with PBS, Hf-DBA, H_2DBB-Ru or Hf-DBB-Ru with (+) or without (-) X-ray irradiation. Blue and red fluorescence show DAPI-stained nucleus and antibody-labeled γ-H2AX in the cells, respectively. Scale bar = 20 μm. Reprinted with permission from *Nature Communications*, **2018**, *9*, 4321–4333. Copyright 2018 Nature Publishing Group.

MC38 cells treated with Hf-DBB-Ru and X-ray irradiation followed by incubation with SOSG showed strong green fluorescence by CLSM, indicating the generation of $^1O_2$ (**Figure 3-11**). No fluorescence was detected in PBS, Hf-DBA, and H_2DBB-Ru treated group with or without X-ray irradiation or in Hf-DBB-Ru treatment without irradiation. $^1O_2$ was only generated intracellularly

by combining Hf-DBB-Ru and X-ray irradiation, suggesting that heavy metal SBUs, photosensitizers, and X-rays are three indispensable elements for the generation of $^1O_2$ in nMOF-enabled RDT. It is worth noting that the H_2DBB-Ru treated group showed weak green signals, likely due to direct excitation of H_2DBB-Ru from slight absorption of X-rays by Ru atoms.

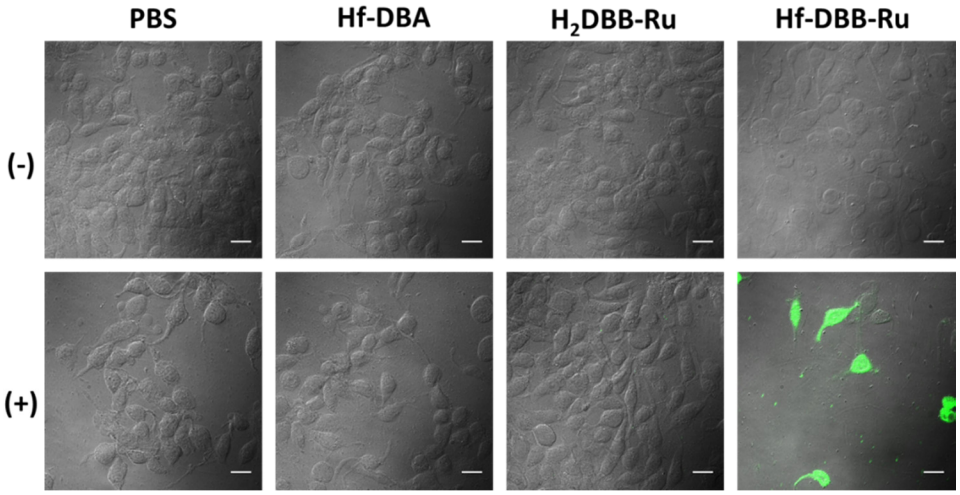

Figure 3-11 Intracellular $^1O_2$ generation detected by SOSG. MC38 cells were preloaded with SOSG, incubated with PBS, Hf-DBA, H_2DBB-Ru, or Hf-DBB-Ru and irradiated at 0 (-) or 2 (+) Gy. Green fluorescence from SOSG captured $^1O_2$. Scale bar = 20 μm. Reprinted with permission from *Nature Communications*, **2018**, *9*, 4321–4333. Copyright 2018 Nature Publishing Group.

COX-2, a cyclooxygenase involved in lipid peroxidation, is up-regulated after $^1O_2$-induced cell membrane damage, which is commonly observed after PDT treatment.[7] We determined the upregulation of COX-2 in MC38 cells after PBS, Hf-DBA, H_2DBB-Ru, or Hf-DBB-Ru incubation with and without X-ray irradiation by quantitative flow cytometric analysis. 24 h after irradiation, treated cells were collected, fixed and stained with biotin-conjugated COX-2 antibody and followed by incubation with Cy5-conjugated streptavidin. The intensity shift of red fluorescence compared to the control indicated COX-2 up-regulation of cells. No COX-2 up-regulation was observed from PBS or Hf-DBA treated group or dark controls (**Figure 3-12**). The mean

fluorescence intensities were 8973, 1356, 231, and 186 for the cells treated with Hf-DBB-Ru, H_2DBB-Ru, Hf-DBA and PBS with X-ray irradiation, respectively. This result is consistent with SOSG assay showing strong RDT effects by Hf-DBB-Ru and low level $^1O_2$ generation by H_2DBB-Ru from slight absorption of X-rays by Ru atoms.

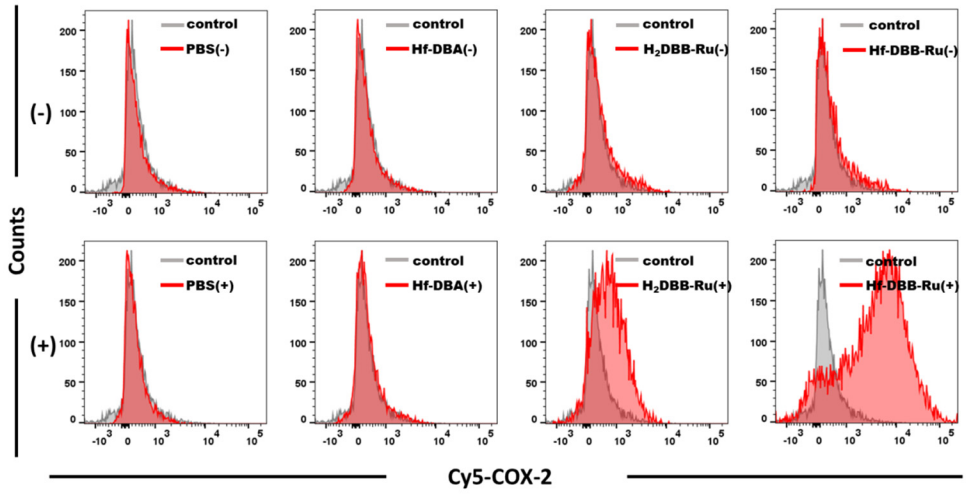

Figure 3-12 Quantification of COX-2 by flow cytometry after cells incubated with PBS, Hf-DBA, H_2DBB-Ru, or Hf-DBB-Ru and irradiated with X-rays at a dose of 0 (-) or 2 (+) Gy. Reprinted with permission from *Nature Communications*, **2018**, *9*, 4321–4333. Copyright 2018 Nature Publishing Group.

The cell death pathways were then evaluated with an Annexin V/Cell death kit (**Figure 3-13a**). Significant amounts of cells underwent apoptosis/necrosis when treated with Hf-DBB-Ru and X-ray irradiation, with only 33.6% healthy cells, compared to 74.8% and 83.1% healthy cells for Hf-DBA or H_2DBB-Ru plus X-ray irradiation, respectively. >90% cells remained healthy in dark controls and in the PBS group with irradiation, indicating that Hf-DBA, H_2DBB-Ru, and Hf-DBB-Ru are not intrinsically cytotoxic and the low dose X-ray elicited negligible cytotoxicity with PBS treatment (**Figure 3-13b,c**). Furthermore, severe morphological changes were observed for cells treated with Hf-DBB-Ru plus X-ray irradiation (**Figure 3-13d**). Taken together, Hf-DBB-Ru

possesses a strong cell killing effect when combined with X-ray irradiation due to the mitochondria-targeted RT-RDT effects.

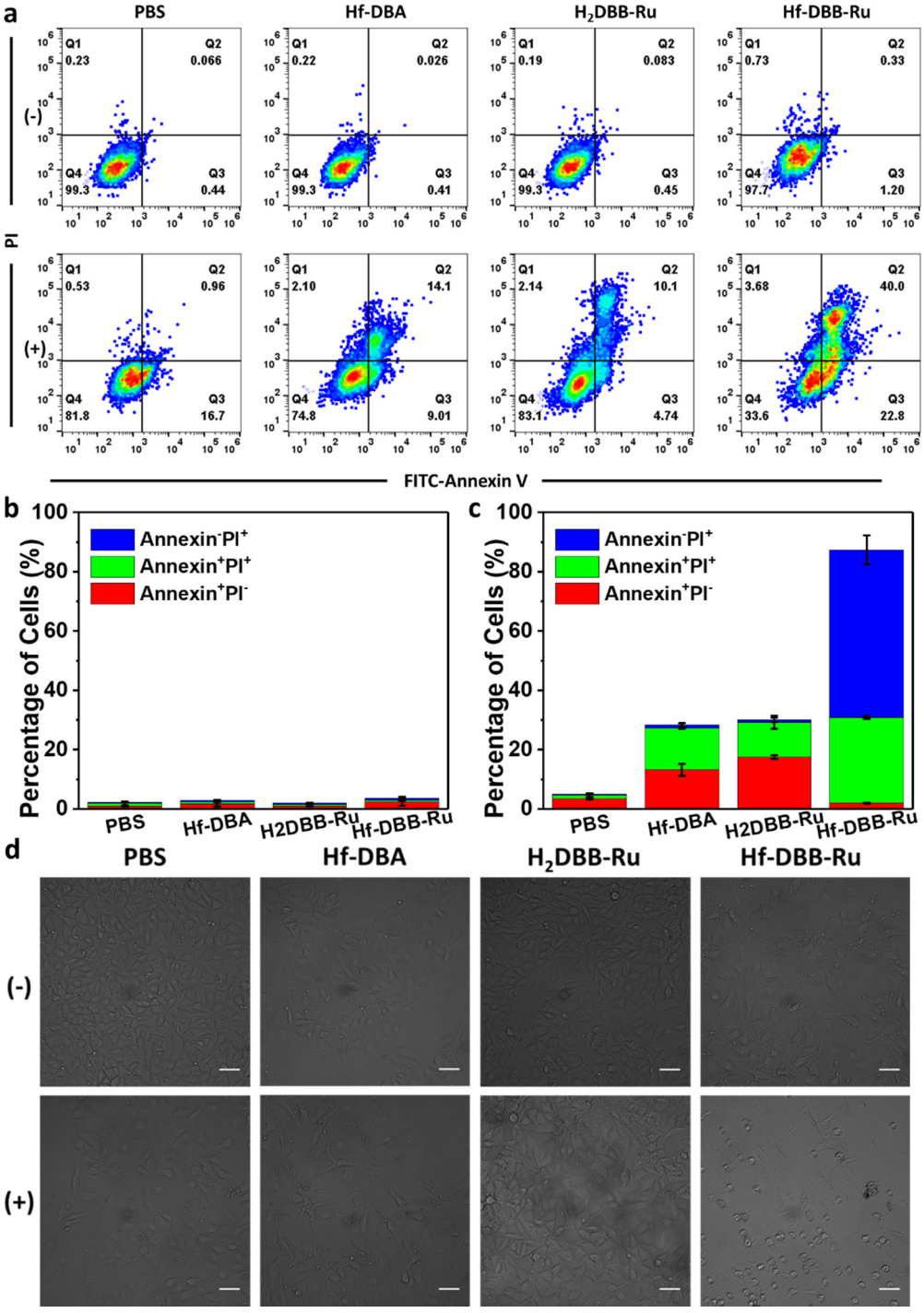

Figure 3-13 (a) Annexin V/PI analysis of MC38 cells treated PBS, Hf-DBA, H_2DBB-Ru, or Hf-DBB-Ru at an equivalent dose of 20 μM and irradiated with X-rays at a dose of 0 (-) or 2 (+) Gy.

Figure 3-13, continued The quadrants from lower left to upper left (counter clockwise) represent healthy, early apoptotic, late apoptotic, and necrotic cells, respectively. The percentage of cells in each quadrant was shown on the graphs. Statistical analysis of the percentages of early apoptotic cell (red brick, Annexin$^+$PI$^-$), late apoptotic cell (green brick, Annexin$^+$PI$^+$), or necrotic cell (blue brick, Annexin$^-$PI$^+$) without (a) or with (b) X-ray irradiation, n = 3. (d) Representative optical images of MC38 cells showing morphological changes 72 hours post treatment. Scale bar = 50 μm. Reprinted with permission from *Nature Communications*, **2018**, *9*, 4321–4333. Copyright 2018 Nature Publishing Group.

3.2.5 *In vitro* mechanistic studies of mitochondria-targeted RT-RDT

In PDT, subcellular localization of a PS determines the initial photodynamic damage and ensuing cellular responses. The results from the proceeding sections suggested the enhanced RT-RDT efficacy of Hf-DBB-Ru due to its mitochondria-targeting property. The generation of $^{\bullet}$OH and $^1O_2$ in mitochondria can cause maximal membrane damage to initiate an efficient apoptotic process. To gain mechanistic insights into mitochondria-targeted RT-RDT, we evaluated depolarization of the mitochondria membrane potential, the release of cytochrome c, and the loss of respiratory chain activity in MC38 cells following Hf-DBB-Ru treatment and X-ray irradiation.

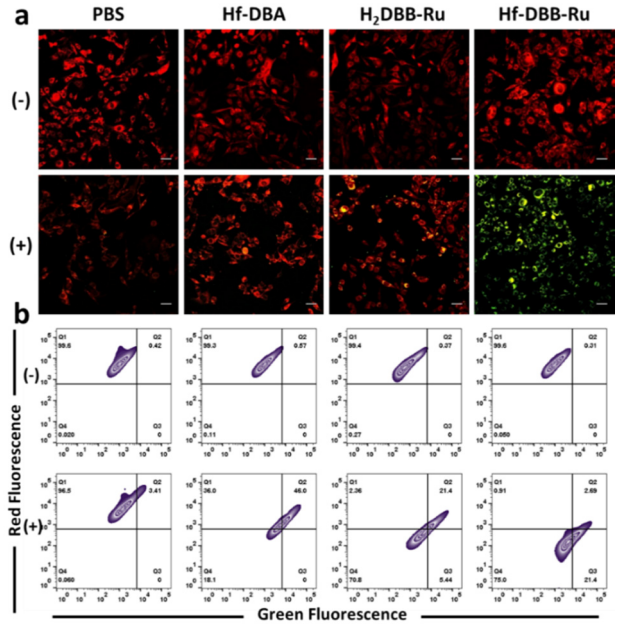

Figure 3-14 JC-1 staining for detecting mitochondria membrane depolarization by CLSM (a) or flow cytometry (b). MC38 cells treated with PBS, Hf-DBA, H_2DBB-Ru, or Hf-DBB-Ru at an

Figure 3-14, continued equivalent dose of 20 μM upon X-ray irradiation at 0 (-) or 2 (+) Gy dose were stained with JC-1 4 h after irradiation. Green fluorescence indicates the monomerization of JC-1, suggesting the decrease of mitochondria membrane potential. Scale bar = 50 μm. Reprinted with permission from *Nature Communications*, **2018**, *9*, 4321–4333. Copyright 2018 Nature Publishing Group.

The depolarization of mitochondrial membrane potential was assayed with the mitochondria permeable dye 5,5',6,6'-tetrachloro-1,1',3,3'-tetraethylbenzimidazolylcarbocyanine iodide (JC-1). With a polarized mitochondrial potential in normal cells, JC-1 emits red fluorescence from the J-aggregate that forms in the mitochondrial matrix. When the mitochondrial membrane potential depolarizes, JC-1 exists as a monomer and emits green fluorescence. The shift from red to green fluorescence is thus an indicator for a decrease in the mitochondrial membrane potential. MC38 cells treated with Hf-DBA, H_2DBB-Ru, or Hf-DBB-Ru at an equivalent dose of 20 μM of Hf upon X-ray irradiation at a dose of 0 or 2 Gy were stained with JC-1 for CLSM analyses. Cells treated with PBS without X-ray irradiation served as control. As shown in **Figure 3-14a**, all four groups showed strong red fluorescence and negligible green fluorescence without X-ray treatment. 4h after X-ray irradiation, obvious green fluorescence was observed in Hf-DBB-Ru treated group, while Hf-DBA and H_2DBB-Ru treated groups only showed a few yellow spots, indicating only weak green fluorescence. Flow cytometry analyses further confirmed these observations. Upon X-ray irradiation, the Hf-DBB-Ru group showed an increased number of mitochondria with green fluorescence and few mitochondria with red fluorescence. In contrast, the groups treated with PBS, Hf-DBA, or DBB-Ru did not show such a distinct change upon X-ray irradiation (**Figure 3-14b**). The depolarization of mitochondria membrane potential is an indicator of mitochondria dysfunction.[8] With an increase in ROS generation and decrease in ATP synthesis, the permeability transition pore complex is primed to release cytochrome c into the cytosol to form a complex with cytoplasmic apoptosis activating factor-1, which activates caspase-9 and caspase-3 to induce apoptosis. Mitochondria and cytochrome c were stained with Mitotracker and FITC-conjugated

cytochrome c antibody, respectively, 6 h after X-ray irradiation for CLSM imaging. Compared with other groups, the Hf-DBB-Ru treated group displayed an obvious separation of green and red fluorescence (**Figure 3-15**), indicating the release of cytochrome c into cytosol.

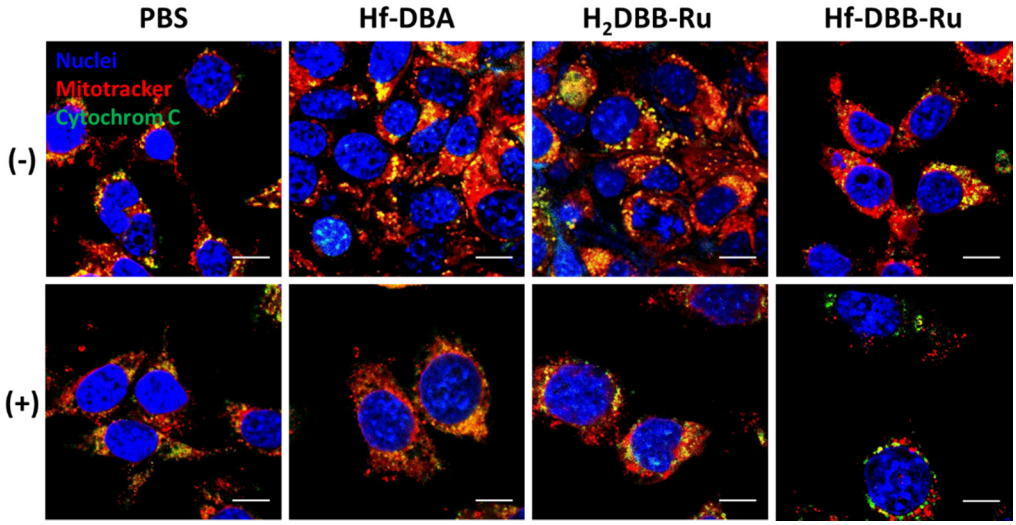

Figure 3-15 Cytochrome c staining for presenting the release of cytochrome c from damaged mitochondria. MC38 cells were treated with PBS, Hf-DBA, H_2DBB-Ru, or Hf-DBB-Ru at an equivalent dose of 20 μM upon X-ray irradiation at 0 (-) or 2 (+) Gy dose. Cells were then stained with Mitotracker Red, fixed and permeabilized 8 h after irradiation. After stained with FITC-conjugated cytochrome c antibody and DAPI, slides were observed under CLSM. The deco-localization of green and red fluorescence indicates the release of cytochrome c from mitochondria. Scale bar = 10 μm. Reprinted with permission from *Nature Communications*, **2018**, *9*, 4321–4333. Copyright 2018 Nature Publishing Group.

To probe if the anticancer effect originates from RT-RDT damage to mitochondria, we detected Bcl-2 and caspase-3 protein expression levels 8 h after X-ray irradiation. PBS, Hf-DBA, H_2DBB-Ru, and Hf-DBB-Ru treated cells all showed similar levels of Bcl-2 protein based on western blots (**Figure 3-16**), indicating no strong downregulation of Bcl-2 protein expression among all groups, likely due to local RT-RDT effects causing mitochondria outer membrane permeabilization. In contrast, Hf-DBB-Ru treated cells showed upregulation of caspase-3 in comparison to PBS, Hf-DBA, or H2DBB-Ru treated groups. Bcl-2 and caspase-3 quantification results thus indicated that the RT-RDT damage was initiated from mitochondria to directly induce

the downstream apoptotic pathways without downregulating Bcl-2 due to the localization of Hf-DBB-Ru in mitochondria.[9]

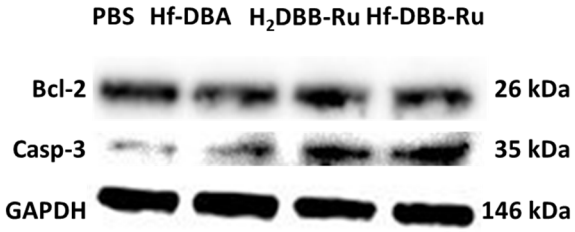

Figure 3-16 Bcl-2 and Caspase-3 protein expression levels of MC38 cells 8 h after treatment of PBS, Hf-DBA, H_2DBB-Ru and Hf-DBB-Ru upon X-ray irradiation (2 Gy). The glyceraldehyde 3-phosphate dehydrogenase (GAPDH) band served as loading control. Reprinted with permission from *Nature Communications*, **2018**, *9*, 4321–4333. Copyright 2018 Nature Publishing Group.

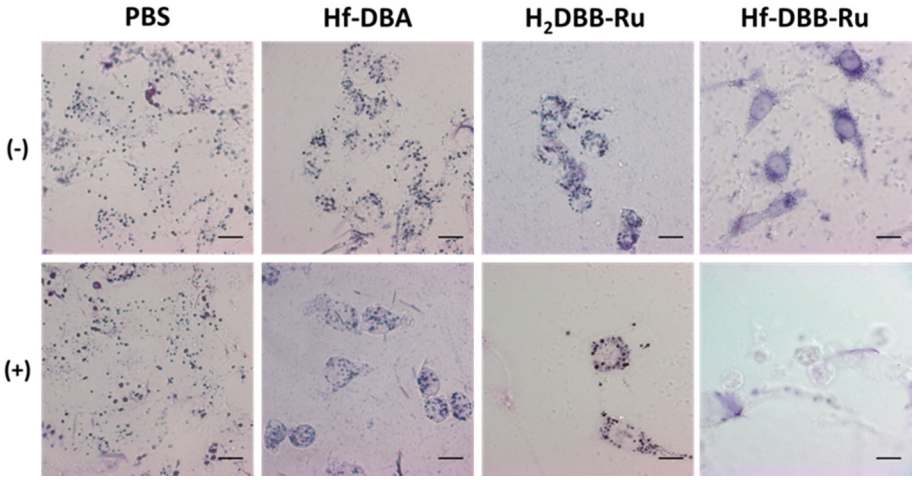

Figure 3-17 Viability test for intact mitochondria and respiratory activity. MC38 cells were treated with after treated with PBS, Hf-DBA, H_2DBB-Ru, or Hf-DBB-Ru at an equivalent dose of 20 μM upon X-ray irradiation at 0 (-) or 2 (+) Gy dose. After incubation for 24 h, MTT was added to the cells for 20 mins to measure respiratory activity as the amount of MTT reduced to formazan. Dark blue "grains" in the image correspond to generated formazan microgranules. Scale bar = 10 μm. Reprinted with permission from *Nature Communications*, **2018**, *9*, 4321–4333. Copyright 2018 Nature Publishing Group.

The dysfunction of mitochondria leads to the loss of respiratory chain activity and increased generation of reduced nicotinamide adenine dinucleotide phosphate (NADPH). We evaluated the respiratory chain activity and viability by (3-(4,5-Dimethylthiazol-2-yl)-2,5-diphenyltetrazolium bromide (MTT) assay. In this assay, MTT is reduced to formazan which appears as dark blue

microgranules[10] in cells with normal respiratory chain activity (**Figure 3-17**). The amount of formazan correlates with the activity of the respiratory chain. Compared with control groups, the Hf-DBB-Ru plus X-ray group showed significantly reduced amount of reduced formazan, suggesting the loss of the respiratory chain activity after mitochondria-targeted RT-RDT treatment.

3.2.6 *In vivo* anti-tumor efficacy of mitochondria-targeted RT-RDT

A colorectal adenocarcinoma mouse model of MC38-tumor bearing C57BL/6 mice was employed to evaluate the anti-tumor efficacy of Hf-DBA and Hf-DBB-Ru *in vivo*. H_2DBB-Ru ligand and PBS served as controls. When the tumors reached 100-150 mm^3 in volume on day 7 post tumor inoculation, Hf-DBB-Ru, Hf-DBA, or H_2DBB-Ru was injected intratumorally at equivalent doses of 0.2 μmol per mouse followed by daily X-ray irradiation at a dose of 1 Gy per fraction for a total of 6 fractions on consecutive days. As shown in **Figure 3-18a**, the H_2DBB-Ru treated group showed slight tumor growth inhibition with a TGI of 34.4% on Day 22, which was likely due to the RT-RDT damage to mitochondria caused by slight X-ray absorption by the Ru compound. The Hf-DBA group showed moderate tumor suppression with a TGI of 57.9%, indicating the radiosensitization effect of Hf-DBA. In stark contrast, Hf-DBB-Ru treatment led to effective tumor regression at a low X-ray dose of 6 Gy. The average tumor volume of the Hf-DBB-Ru treatment group was only 3.0 % of that of the PBS control on Day 22, affording an impressive TGI of 97.0 %.

We also tested the therapeutic efficacy of intravenously injected Hf-DBB-Ru followed by X-ray irradiation. Hf-DBB-Ru was injected intravenously to MC38 tumor-bearing mice at a dose of 2 μmol per mouse twice on day 7 and day 9 followed by daily X-ray irradiation at a dose of 2 Gy per fraction for a total of 4 consecutive fractions on days 8-11. PBS injected intravenously followed

the same X-ray irradiation treatment served as a control. Tumor sizes and body weights were measured daily. PBS group treated with daily X-ray irradiation did not exhibit statistically significant difference from the untreated group, indicating that fractionated X-ray irradiation for a total dose of 8Gy does not have radiotherapeutic effects. In contrast, intravenously injected Hf-DBB-Ru followed by X-ray irradiation led to effective tumor regression with a TGI ratio of 93.9%. There is no statistically significant difference between the tumors of the mice intratumorally or intravenously injected with Hf-DBB-Ru followed by X-ray irradiation.

We confirmed the radiotherapeutic efficacy of intravenously injected Hf-DBB-Ru followed by X-ray irradiation on BALB/c mice bearing CT26 tumors, another commonly used colorectal adenocarcinoma mouse model. Similar tumor regression results were observed on the CT26 with a TGI ratio of 91.5% (**Figure 3-18b**) when the mice were intravenously injected with Hf-DBB-Ru at a dose of 2 μmol per mouse twice on day 7 and day 9 followed by daily X-ray irradiation at a dose of 2 Gy per fraction for a total of 4 consecutive fractions on days 8-11. These results indicate that Hf-DBB-Ru-enabled mitochondria-targeted RT-RDT can be administered to treat many different types of cancers. Statistical analysis of tumor sizes of all groups is listed in **Table 3-1**. Tumors were excised for further analysis (**Figure 3-18c-e**).

The tumor growth inhibition/regression results of MC38 model were confirmed by the weights of excised tumors on Day 22 (**Figure 3-18f**). The weights of tumors treated with i.t. and i.v. injected Hf-DBB-Ru were 0.23 ± 0.16 and 0.25 ± 0.13 g compared to 2.69 ± 0.42 g, 1.15 ± 0.40 g, and 1.80 ± 0.39 g for tumors treated with PBS, Hf-DBA, and H_2DBB-Ru, respectively. For CT26 model, the weights of excised tumors on Day 21 treated with i.v. injected Hf-DBB-Ru was 0.25 ± 0.17 g compared to 1.67 ± 0.30 g and 1.85 ± 0.38 g for tumors treated with PBS with or

without X-ray irradiation, respectively (inset of **Figure 3-18b**). Statistical analysis of tumor weights of all groups is listed in **Table 3-2**.

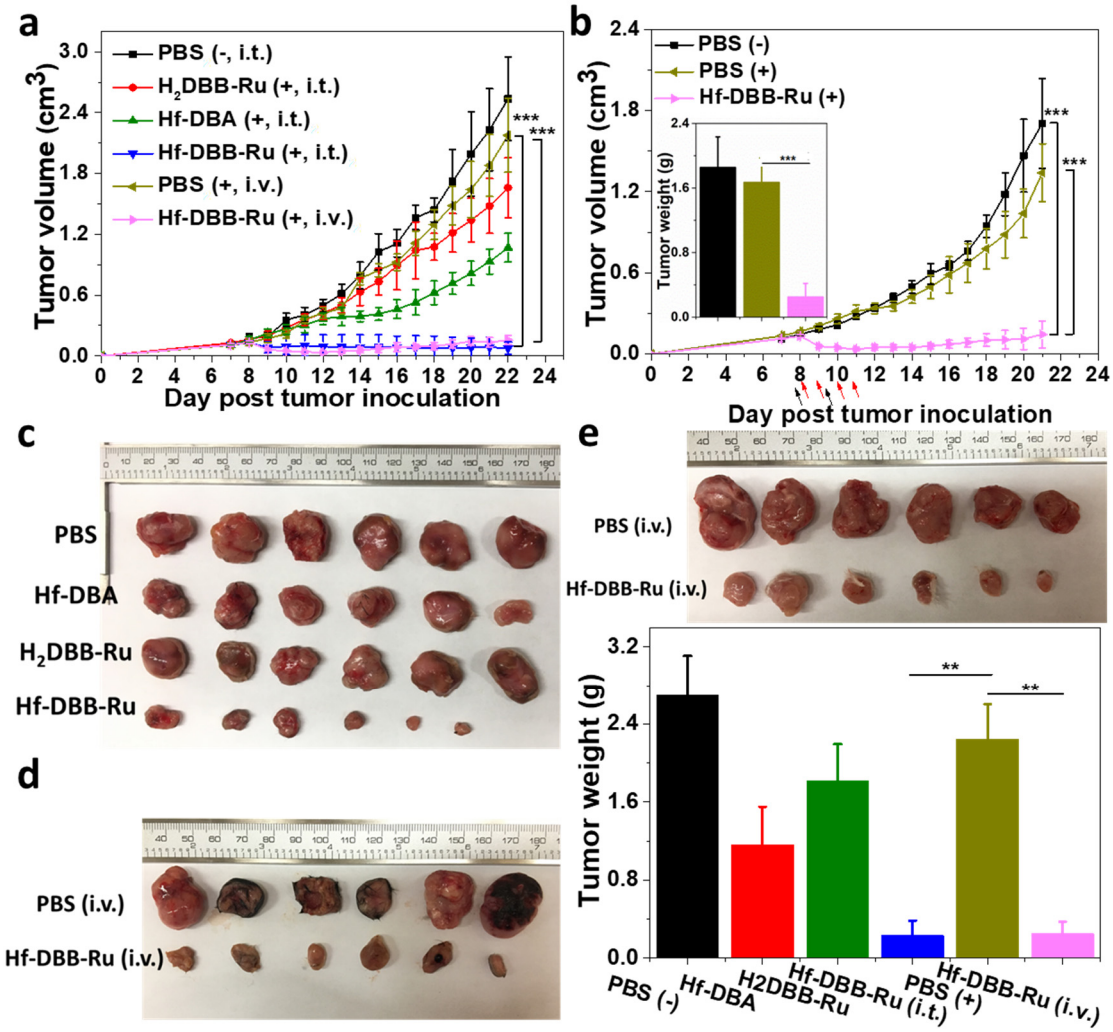

Figure 3-18 (a) Tumor growth inhibition/regression curves in MC38 tumor-bearing mice treated with PBS, Hf-DBA, DBB-Ru, or Hf-DBB-Ru by intratumoral (i.t.) injection with (-) or without (+) X-ray irradiation or Hf-DBB-Ru by intravenous (i.v.) injection followed by X-ray irradiation, n = 6. (b) Tumor growth regression curves in CT26 tumor-bearing mice treated with PBS with (-) or without (+) X-ray irradiation or i.v. injected with Hf-DBB-Ru followed by X-ray irradiation. Black arrows refer to i.v. injection of different treatments and red arrows refer to X-ray irradiation. Excised tumor weights on day 21 shown in the inset, n = 6. Photos of excised tumors of MC38 tumor model with different i.t. injected (c), i.v. injected (d) treatments and CT26 tumor model with i.v. injected treatment (e), n = 6. (f) Excised tumor weights on day 22, n = 6. **P<0.05, ***P<0.001 from control by t-test. Reprinted with permission from *Nature Communications*, **2018**, *9*, 4321–4333. Copyright 2018 Nature Publishing Group.

Table 3-1. Statistical analysis of the tumor sizes at the end of treatment on CT26 or MC38 tumor bearing mice.

	P values	
	CT26	MC38
PBS (+) vs PBS (-)	0.202	0.170
Hf-DBA (+, i.t.) vs PBS (+)		0.002
H_2DBB-Ru (+, i.t.) vs PBS (+)		0.024
Hf-DBB-Ru (+, i.t.) vs PBS (+)		<0.0001
Hf-DBB-Ru (+, i.v.) vs PBS (+)	<0.0001	<0.0001
Hf-DBB-Ru (+, i.t.) vs Hf-DBB-Ru (+, i.v.)		0.109
Hf-DBB-Ru (+, i.t.) vs Hf-DBA (+, i.t.)		<0.0001
Hf-DBB-Ru (+, i.t.) vs H_2DBB-Ru (+, i.t.)		<0.0001

H&E histological staining indicated severe necrosis of tumor slices from Hf-DBB-Ru treatment (**Figure 3-19a**). A TdT-mediated dUTP nick end labeling (TUNEL, Invitrogen, USA) assay was performed to further evaluate the *in vivo* apoptosis. The sectioned tumor slices were fixed with acetone and then stained sequentially according to the product protocol. DAPI was employed to label cell nuclei. As shown in **Figure 3-19b**, strong green fluorescence was observed in Hf-DBB-Ru-treated tumor slice, indicating significant apoptosis after treatment. In comparison, negligible green fluorescence was found in DBB-Ru, Hf-DBA and PBS treated groups. The staining results support the high antitumor efficacy from mitochondria-targeted RT-RDT by Hf-DBB-Ru.

Table 3-2. Statistical analysis of the tumor weights at the end of excised tumors from CT26 or MC38 tumor bearing mice.

	P values	
	CT26	MC38
PBS (+) vs PBS (-)	0.299	0.321
Hf-DBA (+, i.t.) vs PBS (+)		0.012
H_2DBB-Ru (+, i.t.) vs PBS (+)		0.025
Hf-DBB-Ru (+, i.t.) vs PBS (+)		0.003
Hf-DBB-Ru (+, i.v.) vs PBS (+)	<0.001	0.0015
Hf-DBB-Ru (+, i.t.) vs Hf-DBB-Ru (+, i.v.)		0.866
Hf-DBB-Ru (+, i.t.) vs Hf-DBA (+, i.t.)		0.0019
Hf-DBB-Ru (+, i.t.) vs H_2DBB-Ru (+, i.t.)		<0.001

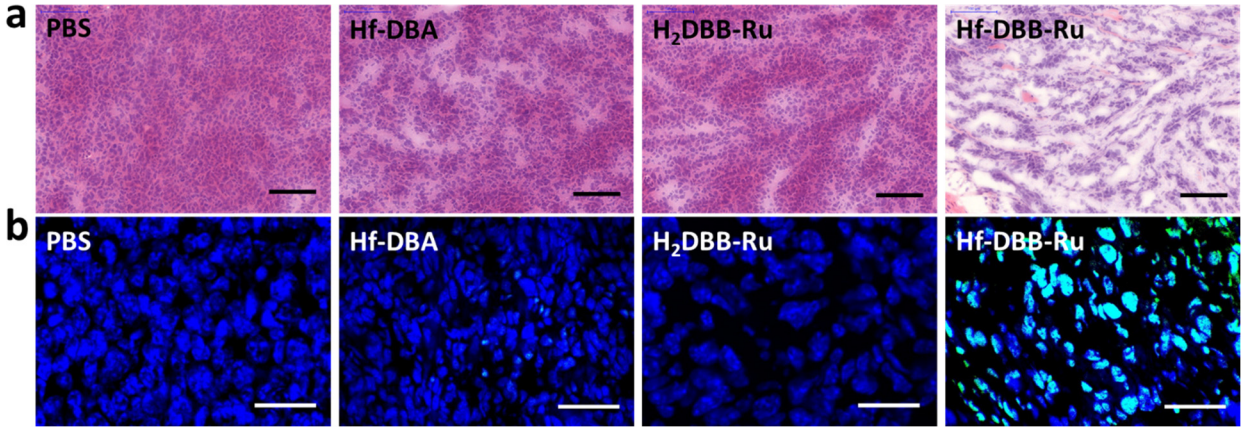

Figure 3-19 Representative (d) H&E histological staining and (e) TUNEL immunofluorescence staining of excised tumor slices for PBS, Hf-DBA, DBB-Ru, and Hf-DBB-Ru (i.t. injection) treatment groups (left to right), respectively. (d) H&E, scale bar = 100 μm. (e) TUNEL, scale bar = 50 μm. Reprinted with permission from *Nature Communications*, **2018**, *9*, 2351–2363. Copyright 2018 Nature Publishing Group.

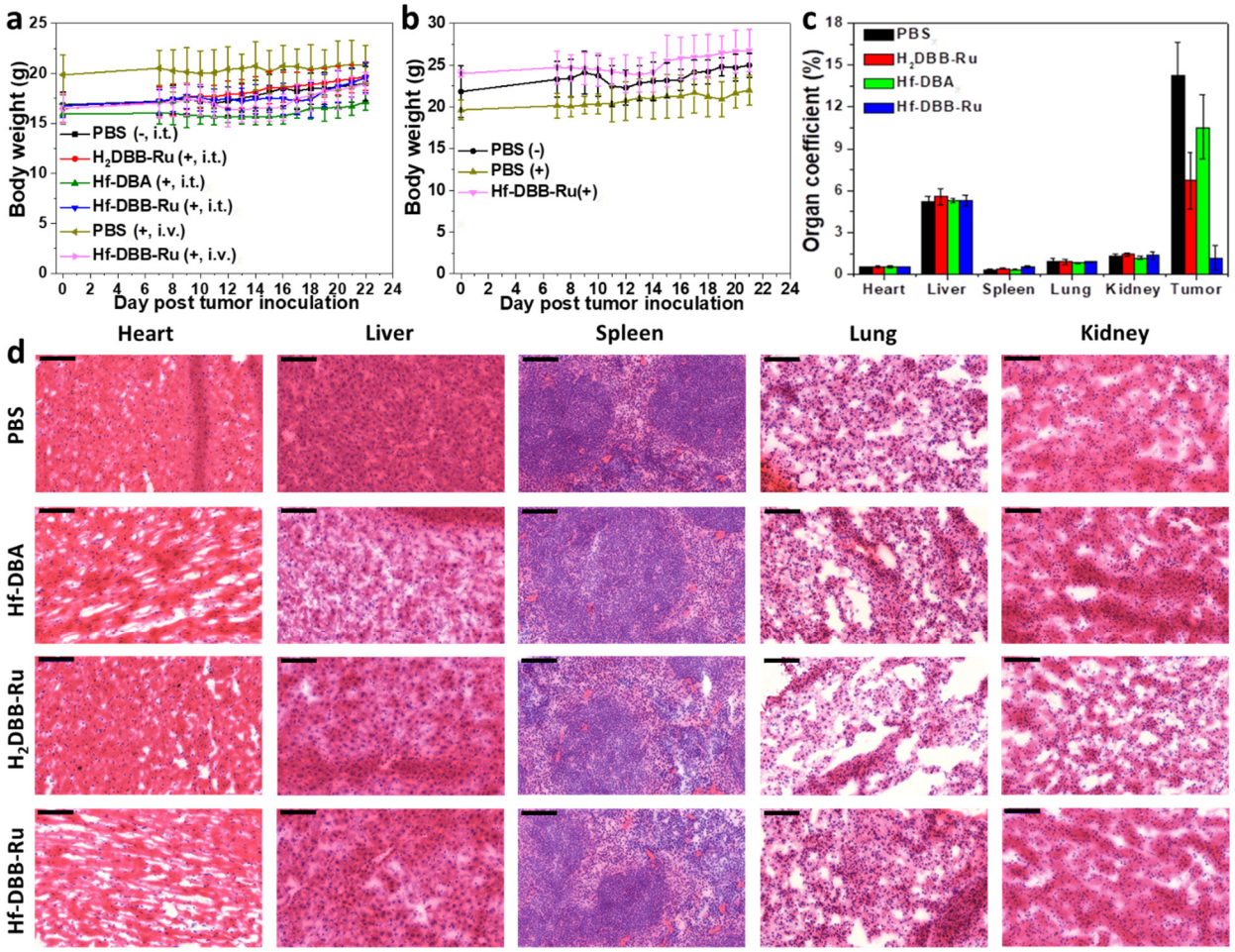

Figure 3-20 Body weights curves of MC38 tumor-bearing mice were treated with PBS, Hf-DBA, DBB-Ru, or Hf-DBB-Ru by intratumoral (i.t.) injection with (-) or without (+) X-ray irradiation or Hf-DBB-Ru by intravenous (i.v.) injection followed by X-ray irradiation (a) or CT26 tumor-bearing mice treated with i.v. injected PBS or Hf-DBB-Ru, n = 6. The error bars represent s.d. values. (c) Comparison of organ coefficients. MC38 tumor-bearing mice treated with i.t. injected PBS, Hf-DBA, DBB-Ru, or Hf-DBB-Ru followed by X-ray irradiation were euthanized and majors organs were harvested and weighted, n = 6. (d) Histologies of frozen sections of major organs of MC38 tumor-bearing mice receiving treatment of Hf-DBA, Hf-DBB-Ru, H_2DBB-Ru or PBS and X-ray irradiation treatment after H&E staining. Scale bar = 100 μm. Reprinted with permission from *Nature Communications*, **2018**, *9*, 2351–2363. Copyright 2018 Nature Publishing Group.

Finally, steady body weights (**Figure 3-20a,b**), and no obvious difference in organ weights and functions (**Figure 3-20c**) were observed in all groups, indicating that intratumoral or intravenous administration of mitochondria-targeted Hf-DBB-Ru was not systemically toxicity.

The lack of abnormalities on histological images of frozen major organ slices further supported non-toxic nature of Hf-DBB-Ru enabled RT-RDT treatment (**Figure 3-20d**).

3.3 Discussion

Due to a short lifetime of $^1O_2$ in biological systems (~40 ns) and limited radius of diffusion from its site of generation (< 30 nm)[11], the therapeutic effect of $^1O_2$ is greatly influenced by localization of $^1O_2$ generator (PSs in PDT and radiosensitizers in RT-RDT) in specific subcellular organelles. Sensitizers that target subcellular organelles, including mitochondria,[12] lysosomes,[13] and plasma membranes,[14] are actively pursued. In particular, mitochondria have been recognized as a novel pharmacological target for cancer treatment due to their central role in mediating cell apoptosis.[15-17] Mitochondria undertake critical functions in various biological processes of cells, including energy production, molecular metabolism, and redox status maintenance. Mitochondrial dysfunction can interrupt energy supply and activate mitochondria-mediated apoptotic pathways.[18] In cancer, mitochondria play key roles on tumor cell proliferation, invasion, and metastasis. Thus, generating $^1O_2$ inside mitochondria can damage them at the early stage of PDT treatment to maximize the cytotoxic effect. Consequently, there is significant interest in developing mitochondria-targeted sensitizers to improve cancer treatment.

Cationic Ru-based PSs can target mitochondria without the need of conjugating extrinsic mitochondria-targeting moieties such as the triphenylphosphonium group.[19-20] Unfortunately, due to large Stoke shifts, Ru-based PSs can only be excited with light at short wavelengths, which has shallow tissue penetration depth (< 0.1 cm).[21] Although two-photon excitation can be used activate Ru-based PSs for mitochondria-targeted PDT, the two-photon process has low photosensitizing efficiency.[22-24] Innovative strategies are thus needed to realize anti-tumor PDT treatment with

mitochondria-targeted Ru-based PSs. Incorporated into Hf-DBB-Ru, $Ru(bpy)_3^{2+}$ can be activated by highly penetrating X-ray while keeping mitochondria-targeting property to realize mitochondria-targeted RT-RDT.

3.4 Conclusion

In this chapter, we have designed the first nMOF for mitochondria-targeted and X-ray activated cancer therapy. The integration of $Ru(bpy)_3^{2+}$ photosensitizers into Hf-DBB-Ru led to a nMOF with strong mitochondria-targeting property. When irradiated with low doses of X-rays, Hf-DBB-Ru enabled RT-RDT by efficiently generating hydroxyl radicals from the Hf_6 SBUs and singlet oxygen from the DBB-Ru PSs. The mitochondria-targeted RT-RDT process depolarized the mitochondrial membrane potential, released cytochrome c, and disturbed the respiratory chain to initiate apoptotic pathways for programmable cell death. The nMOF-enabled, mitochondria-targeted RT-RDT significantly regressed colorectal tumors on mouse models at very low X-ray doses and with no side effects.

3.5 Methods

Materials, cell lines, and animals: All of the starting chemicals were purchased from Sigma-Aldrich and Fisher (USA), unless otherwise noted, and used without further purification.

Murine colon adenocarcinoma cell, MC38, was purchased from the American Type Culture Collection (Rockville, MD, USA). Cells were cultured in Dulbecco's Modified Eagle's Medium (DMEM) medium (GE Healthcare, USA) supplemented with 10% FBS. Medium was further supplemented with 100 U per mL penicillin G sodium and 100 μg per mL streptomycin sulfate. Cells were cultured in a humidified atmosphere containing 5% CO_2 at 37 °C. Mycoplasma was

tested before use by MycoAlert detection kit (Lonza Nottingham, Ltd.). C57Bl/6 mice (6-8 weeks) were obtained from Harlan-Envigo Laboratories, Inc (USA). The study protocol was reviewed and approved by the Institutional Animal Care and Use Committee (IACUC) at the University of Chicago.

Synthesis of Hf-DBB-Ru: To a 1 dram glass vial was added 0.5 mL of $HfCl_4$ solution (2.0 mg per mL in DMF), 0.5 mL of DBB-Ru solution (4.0 mg per mL in DMF), 5 μL of TFA and 2 μL of H_2O. The reaction mixture was kept in an 80 °C oven for 24 h. The orange precipitate was collected by centrifugation and washed with DMF and ethanol.

Irradiator settings: An RT250 orthovoltage X-ray machine model (Philips, USA) with fixed setting at 250 kVp, 15 mA and a built-in 1 mm Cu filter was used for *in vitro* studies. An X-RAD 225 image-guided biological irradiator (Precision X-ray Inc., USA) was used for both test tubes and *in vivo* studies. The instrument was set at 225kVp and 13mA, with a 0.3mm flat-board Cu filter installed before a 25 mm collimator. Irradiators were maintained and calibrated for dosimetry routinely by the Department of Radiation Oncology, The University of Chicago, before all experiments.

Hydroxyl radical detection: Hf-DBA and Hf-DBB-Ru were suspended in water at equivalent Hf concentrations of 20 μM in the presence of 5 μM APF. A water solution of 5 μM APF was used as a control for background subtraction. 100 μL of each suspension was added to a 96-well plate and then irradiated with 0, 1, 2, 3, 5, or 10 Gy X-ray. The fluorescence signal was immediately collected with the Xenogen IVIS 200 imaging system.

Singlet oxygen detection: Hf-DBA and Hf-DBB-Ru were suspended in water at equivalent Hf concentrations of 20 μM in the presence of 12.5 μM SOSG. A water solution of 12.5 μM SOSG

was used as a control for background subtraction. 100 μL of each suspension was added to a 96-well plate and then irradiated with 0, 1, 2, 3, 5, or 10 Gy X-ray. The fluorescence signal was immediately collected with the Xenogen IVIS 200 imaging system.

Synthesis of Hf-DBA-R: The Hf-DBA nMOF was dispersed in DMF (1 mL, 1 mmol per L by DBA concentration). To the dispersion was added 25 μL of rhodamine B isothiocyanate solution (2 μmol per mL in DMF). The mixture was stirred overnight. The resulting Hf-DBA-R nMOF was washed with ethanol and water.

Co-localization of nMOFs and mitochondria: MC38 cells were cultured in 35 mm tissue culture dishes overnight and incubated with Hf-DBA-R or Hf-DBB-Ru at an equivalent dose of 20 μM for 4 h. Cellular nuclei and mitochondria were labeled with Hoechest 33342 and Rhodamine 123, respectively. The slides were then washed with PBS and observed under CLSM. Fluorescence topographic profiles and Pearson's correlation coefficients were obtained using the Co-localization Analysis plugin for ImageJ.[25]

Isolation of mitochondria: Extraction of mitochondria was conducted according to previously reported protocol, with a few modifications.[4] MC38 cells were washed twice in mitochondrial extraction buffer containing mannitol (200 mM), sucrose (70 mM), HEPES (10 mM), and EGTA (1.0 mM) at pH 7.2 and 4 ℃ and then resuspended for homogenization. The homogenate was spun for 10 min at 600 g to recover the supernatant. The supernatant was further spun for 10 min at 11,000 g to recover the mitochondrial fraction for ICP-MS quantification.

Cytotoxicity: 3-(4,5-dimethylthiazol-2-yl)-5-(3-carboxymethoxyphenyl)-2-(4-sulfo-phenyl)-2H-tetrazolium (MTS) assay (Promega, USA) was employed to evaluate cytotoxicity. MC38 cells were seeded on 96-well plates at 1×10^3/well and further cultured for 12 h. Hf-DBA, H_2DBB-Ru

or Hf-DBB-Ru was added to the cells at an equivalent dose of 0, 0.5, 1, 2, 5, 10, 20, 50 μM and incubated for 4 h, followed by X-ray irradiation with 0 or 2 Gy. The cells were further incubated for 72 h before determining the cell viability by MTS assay.

Clonogenic assay: The clonogenic assay was performed according to a previously reported protocol, with a few modifications.[26] MC38 cells were cultured in a 6-well plate overnight and incubated with particles at equivalent Hf concentration of 20 μM for 4 h followed by irradiation with 0, 1, 2, 4, 8 and 16 Gy X-ray. Cells were trypsinized and counted immediately. 100-1000 cells were seeded in a 6-well plate and cultured with 2 mL medium for 10-20 days. Once colony formation was observed, the culture medium was discarded. The plates were rinsed twice with PBS, then stained with 500 μL of 0.5% w/v crystal violet in 50% methanol per H_2O. The wells were rinsed with water and the colonies were counted manually.

***In vitro* singlet oxygen generation:** SOSG reagent (Life Technologies, USA) was employed for the detection of singlet oxygen. MC38 cells were seeded on cover slides in 35 mm tissue culture dishes overnight. Hf-DBA, H_2DBB-Ru or Hf-DBB-Ru was added to the cells at an equivalent dose of 20 μM. Cells incubated with PBS served as a control. After incubation of 4 hours, cells were irradiated with X-rays (250 kVp, 15 mA, 1 mm Cu filter) at a dose of 0 or 2 Gy. The slides were then immediately washed with PBS and observed under CLSM (FV1000, Olympus, Japan).

COX-2 Assay: The cell membrane damage caused by RDT upon X-ray was investigated by COX-2 assay (BD Bioscience, USA). MC38 cells were seeded on cover slides in 35 mm tissue culture dishes and cultured for 12 h then incubated with particles at an equivalent concentration of 20 μM for 4 h followed by X-ray irradiation at 0 and 2 Gy dose. Cells were fixed with 4% paraformaldehyde 24 h after X-ray irradiation. Biotin-conjugated anti-COX-2 antibody

(PerkinElmer, USA) with concentration of 10 μg per mL was incubated with cells at 4 °C overnight then followed by incubation with Cy5-conjugated streptavidin for flow cytometry.

Apoptosis/necrosis: MC38 cells were cultured in 35 mm tissue culture dishes overnight and incubated with Hf-DBA, H_2DBB-Ru or Hf-DBB-Ru at an equivalent dose of 20 μM for 4 h followed by irradiation with 0 or 2 Gy X-ray. 24 h later, the cells were stained according to the AlexaFluor 488 Annexin V/dead cell apoptosis kit (Life technology, USA) and quantified by flow cytometry with three different runs for statistical analysis.

DNA damage: MC38 cells were cultured in 35 mm tissue culture dishes overnight and incubated with particles at an equivalent concentration of 20 μM for 4 h followed by irradiation at 0 and 2 Gy X-ray. Cells were stained immediately with the HCS DNA damage kit (Life Technology, USA) for CLSM.

JC-1 staining: MC38 cells were cultured in 35 mm tissue culture dishes overnight and then treated with PBS, Hf-DBA, H_2DBB-Ru, or Hf-DBB-Ru at an equivalent dose of 20 μM for 4 h followed by irradiation with 0 or 2 Gy X-ray. 4 h later, samples were stained with JC-1 (Abcam, UK) at a concentration of 10 μM at 37°C for 30 min in the dark. Slides were washed with PBS and observed under CLSM or quantified with flow cytometry.

Respiratory chain activity assay: Respiratory chain activity was assayed with (3-(4,5-Dimethylthiazol-2-yl)-2,5-di-phenyltetrazolium bromide (MTT). MC38 cells seeded on cover slides in in 35 mm tissue culture dishes overnight. Hf-DBA, H_2DBB-Ru or Hf-DBB-Ru was added to the cells at an equivalent dose of 20 μM. Cells incubated with PBS served as a control. After incubation of 4 hours, cells were irradiated upon X-ray irradiation at a dose of 0 or 2 Gy. After 24-

hour incubation, MTT was added with concentration of 0.1 mg/mL and stained for 20 min at room temperature. The slides were then washed with PBS and observed under the stereomicroscope.

Cytochorome c release: MC38 cells were cultured in 35 mm tissue culture dishes overnight and then treated with PBS, Hf-DBA, H_2DBB-Ru, or Hf-DBB-Ru at an equivalent dose of 20 μM for 4 h followed by irradiation with 0 or 2 Gy X-ray. Cells were then stained with Mitotracker Red CMXRos (Thermofisher, USA) at a concentration of 1 μg per mL at 37°C for 10 min, fixed and permeabilized 8 h after irradiation. After being stained with FITC-conjugated cytochrome c antibody (Thermofisher, USA) at a concentration of 10 μM at 37°C for 1h and DAPI, slides were observed under CLSM.

Caspase-3 and Bcl-2 western blot: MC38 cells were cultured in 35 mm tissue culture dishes overnight and then treated with PBS, Hf-DBA, H_2DBB-Ru, or Hf-DBB-Ru at an equivalent dose of 20 μM for 4 h followed by irradiation with 2 Gy X-ray. 8 h later, cells were lysed and separated by SDS/polyacrylamide-gel electrophoresis. After membrane transfer, anti-caspase-3 (#9662, Cell Signaling, USA, 1: 2000) and anti-Bcl-2 (Bcl-2-100, Thermofisher, USA, 1: 1000) were separately incubated with the cropped membranes for blotting.

***In vivo* anticancer efficacy:** For the evaluation of RT-RDT efficacy of Hf-DBA, H_2DBB-Ru, and Hf-DBB-Ru, a syngeneic model was established by subcutaneously inoculating 2×10^6 MC38 cells onto the right flanks subcutaneous tissues of C57Bl/6 mice on day 0 as a MC38 model. When the tumors reached 100-150 mm^3 in volume, Hf-DBA, H_2DBB-Ru, or Hf-DBB-Ru at an equivalent dose of 0.2 μmol or PBS was injected intratumorally. 12 h after injection, mice were anaesthetized with 2% (v/v) isoflurane and the primary tumors were irradiated with 1 Gy X-ray per fraction for a total of 6 daily fractions. The tumor sizes were measured with a caliper every day where tumor

volume equals (width^2 × length)/2. Body weight of each group was monitored every day. Mice were sacrificed on Day 22 and the excised tumors were photographed and weighed. Tumors and major organs were sectioned for hematoxylin-eosin staining (H&E) and immunofluorescence analysis. Tumor growth inhibition indices (TGI) was calculated by the formula: TGI=[1-(mean volume of treated tumors/mean volume of control tumors)]×100%

TUNEL assay: TdT-mediated dUTP nick end labeling (TUNEL, Invitrogen, USA) assay was used for evaluating the *in vivo* apoptosis. The sectioned tumor slices were fixed with acetone then stained sequentially according to product protocol. DAPI was employed to label cell nuclei.

3.6 References

1. Zeng, L.; Gupta, P.; Chen, Y.; Wang, E.; Ji, L.; Chao, H.; Chen, Z.-S., The development of anticancer ruthenium (II) complexes: from single molecule compounds to nanomaterials. *Chemical Society Reviews* **2017,** *46* (19), 5771-5804.

2. Poynton, F. E.; Bright, S. A.; Blasco, S.; Williams, D. C.; Kelly, J. M.; Gunnlaugsson, T., The development of ruthenium (ii) polypyridyl complexes and conjugates for in vitro cellular and in vivo applications. *Chemical Society Reviews* **2017,** *46* (24), 7706-7756.

3. Pierroz, V.; Joshi, T.; Leonidova, A.; Mari, C.; Schur, J.; Ott, I.; Spiccia, L.; Ferrari, S.; Gasser, G., Molecular and cellular characterization of the biological effects of ruthenium (II) complexes incorporating 2-pyridyl-2-pyrimidine-4-carboxylic acid. *Journal of the American Chemical Society* **2012,** *134* (50), 20376-20387.

4. Chandel, N. S.; McClintock, D. S.; Feliciano, C. E.; Wood, T. M.; Melendez, J. A.; Rodriguez, A. M.; Schumacker, P. T., Reactive oxygen species generated at mitochondrial complex III stabilize hypoxia-inducible factor-1α during hypoxia a mechanism of O_2 sensing. *Journal of Biological Chemistry* **2000,** *275* (33), 25130-25138.

5. He, C.; Lu, K.; Lin, W., Nanoscale metal–organic frameworks for real-time intracellular pH sensing in live cells. *Journal of the American Chemical Society* **2014,** *136* (35), 12253-12256.

6. Lu, K.; He, C.; Guo, N.; Chan, C.; Ni, K.; Lan, G.; Tang, H.; Pelizzari, C.; Fu, Y.-X.; Spiotto, M. T., Low-dose X-ray radiotherapy–radiodynamic therapy via nanoscale metal–organic frameworks enhances checkpoint blockade immunotherapy. *Nature Biomedical Engineering* **2018,** *2* (8), 600.

7. Ferrario, A.; von Tiehl, K.; Wong, S.; Luna, M.; Gomer, C. J., Cyclooxygenase-2 inhibitor treatment enhances photodynamic therapy-mediated tumor response. *Cancer Research* **2002,** *62* (14), 3956-3961.

8. Kessel, D.; Luo, Y., Photodynamic therapy: a mitochondrial inducer of apoptosis. *Cell Death and Differentiation* **1999,** *6* (1), 28.

9. Moor, A. C., Signaling pathways in cell death and survival after photodynamic therapy. *Journal of Photochemistry and Photobiology B: Biology* **2000,** *57* (1), 1-13.

10. Stockert, J. C.; Blázquez-Castro, A.; Cañete, M.; Horobin, R. W.; Villanueva, Á., MTT assay for cell viability: intracellular localization of the formazan product is in lipid droplets. *Acta histochemica* **2012,** *114* (8), 785-796.

11. Moan, J.; BERG, K., The photodegradation of porphyrins in cells can be used to estimate the lifetime of singlet oxygen. *Photochemistry and Photobiology* **1991,** *53* (4), 549-553.

12. Ji, Z.; Yang, G.; Vasovic, V.; Cunderlikova, B.; Suo, Z.; Nesland, J. M.; Peng, Q., Subcellular localization pattern of protoporphyrin IX is an important determinant for its photodynamic efficiency of human carcinoma and normal cell lines. *Journal of Photochemistry and Photobiology B: Biology* **2006,** *84* (3), 213-220.

13. Castano, A. P.; Demidova, T. N.; Hamblin, M. R., Mechanisms in photodynamic therapy: part one—photosensitizers, photochemistry and cellular localization. *Photodiagnosis and Photodynamic Therapy* **2004,** *1* (4), 279-293.

14. Liu, L. H.; Qiu, W. X.; Zhang, Y. H.; Li, B.; Zhang, C.; Gao, F.; Zhang, L.; Zhang, X. Z., A charge reversible self-delivery chimeric peptide with cell membrane-targeting properties for enhanced photodynamic therapy. *Advanced Functional Materials* **2017,** *27* (25), 1700220.

15. Neupert, W.; Herrmann, J. M., Translocation of proteins into mitochondria. *Annual Review of Biochemistry,* **2007,** *76*, 723-749.

16. Galluzzi, L.; Bravo-San Pedro, J. M.; Kroemer, G., Organelle-specific initiation of cell death. *Nature Cell Biology* **2014,** *16* (8), 728.

17. Deng, J.; Wang, K.; Wang, M.; Yu, P.; Mao, L., Mitochondria targeted nanoscale zeolitic imidazole framework-90 for ATP imaging in live cells. *Journal of the American Chemical Society* **2017,** *139* (16), 5877-5882.

18. Green, D. R.; Reed, J. C., Mitochondria and apoptosis. *Science* **1998**, 1309-1312.

19. Tan, X.; Luo, S.; Long, L.; Wang, Y.; Wang, D.; Fang, S.; Ouyang, Q.; Su, Y.; Cheng, T.; Shi, C., Structure-guided design and synthesis of a mitochondria-targeting near-infrared fluorophore with multimodal therapeutic activities. *Advanced Materials* **2017,** *29* (43).

20. Jung, H. S.; Han, J.; Lee, J.-H.; Lee, J. H.; Choi, J.-M.; Kweon, H.-S.; Han, J. H.; Kim, J.-H.; Byun, K. M.; Jung, J. H., Enhanced NIR radiation-triggered hyperthermia by mitochondrial targeting. *Journal of the American Chemical Society* **2015,** *137* (8), 3017-3023.

21. Smith, A. M.; Mancini, M. C.; Nie, S., Bioimaging: second window for *in vivo* imaging. *Nature Nanotechnology* **2009,** *4* (11), 710.

22. Liu, J.; Chen, Y.; Li, G.; Zhang, P.; Jin, C.; Zeng, L.; Ji, L.; Chao, H., Ruthenium (II) polypyridyl complexes as mitochondria-targeted two-photon photodynamic anticancer agents. *Biomaterials* **2015,** *56*, 140-153.

23. Zhang, P.; Huang, H.; Chen, Y.; Wang, J.; Ji, L.; Chao, H., Ruthenium (II) anthraquinone complexes as two-photon luminescent probes for cycling hypoxia imaging *in vivo*. *Biomaterials* **2015,** *53*, 522-531.

24. Chen, Y.; Guan, R.; Zhang, C.; Huang, J.; Ji, L.; Chao, H., Two-photon luminescent metal complexes for bioimaging and cancer phototherapy. *Coordination Chemistry Reviews* **2016,** *310*, 16-40.

25. Bolte, S.; Cordelières, F. P., A guided tour into subcellular colocalization analysis in light microscopy. *Journal of Microscopy* **2006,** *224* (3), 213-232.

26. Franken, N. A.; Rodermond, H. M.; Stap, J.; Haveman, J.; Van Bree, C., Clonogenic assay of cells in vitro. *Nature Protocols* **2006,** *1* (5), 2315-2319.

CHAPTER 4. Ultrathin Metal-Organic-Layer Mediated Radiotherapy-Radiodynamic Therapy for Checkpoint Blockade Immunotherapy

4.1 Rationale for the project design

We discussed the principle of developing Hf-based nMOF for radiosensitization to potentiate checkpoint blockade immunotherapy (CBI) in Chapter 2 and we demonstrated a novel therapeutic modality, radiotherapy-radiodynamic therapy (RT-RDT), mediated by an nMOF assembled from high-Z SBUs and photosensitizing linkers in Chapter 3. In this chapter, we report the design of a novel Hf-based nanoscale metal-organic layer (nMOL), the 2D version of nMOF, Hf-MOL, for effective treatment of local tumors by enabling RT-RDT upon low-dose X-rays and, when in combination with an immune checkpoint inhibitor, regression of metastatic tumors by re-activating anti-tumor immunity and inhibiting myeloid-derived suppressor cells (MDSCs). The RT-RDT effect of nMOLs can be optimized by facilitating the diffusion of reactive oxygen species (ROS) owing to the reduced dimensionality.[1-2] The synergy of Hf-MOL-enabled RT-RDT immune activation and anti-programming death ligand 1 (anti-PD-L1) CBI led to robust abscopal effects on a series of bilateral models of colon, head and neck, and breast cancers and significant anti-metastatic effects on an orthotopic model of breast cancer (**Figure 4-1**).

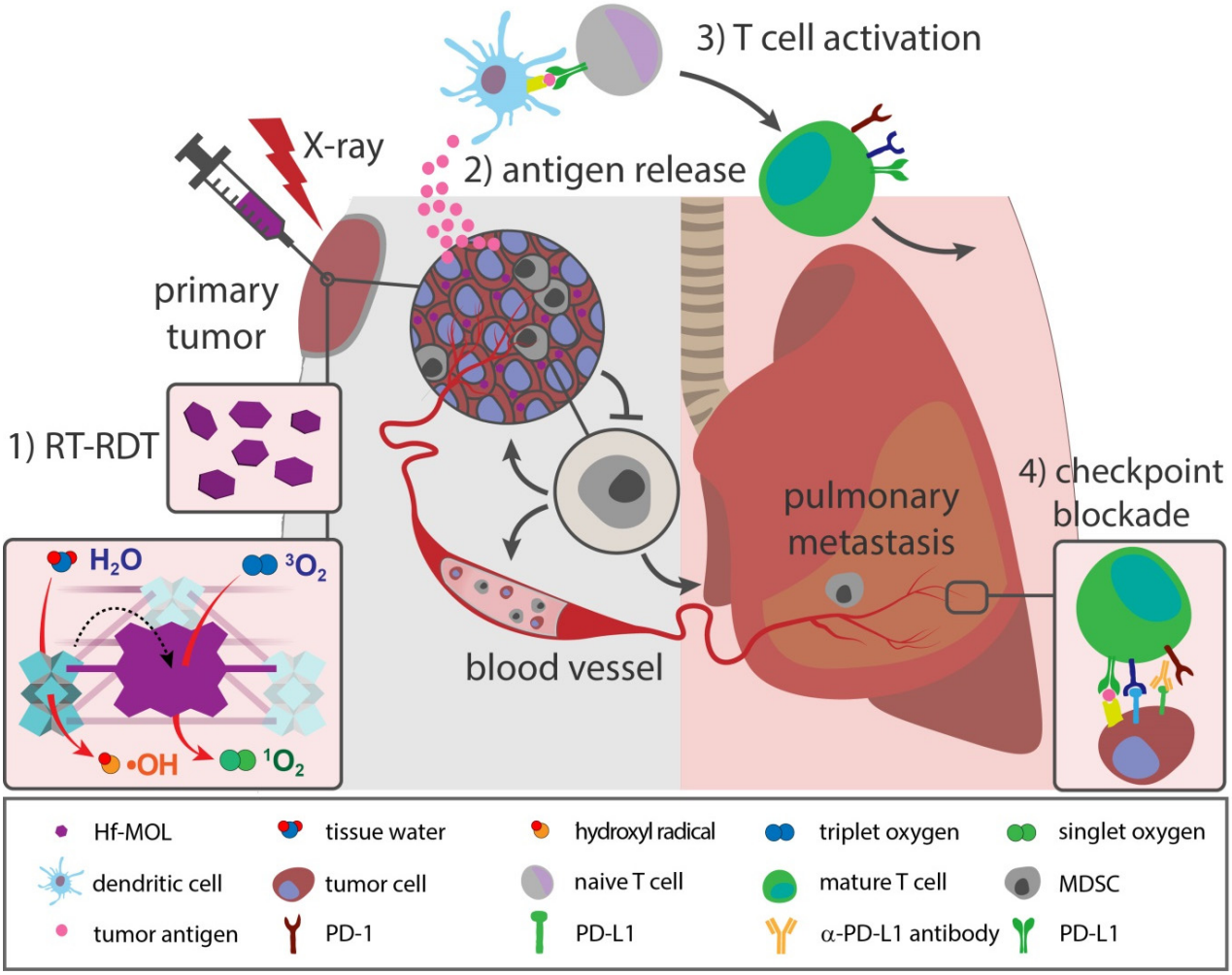

Figure 4-1 Schematic presentation of Hf-MOL-enabled local RT-RDT treatment synergizes with CBI to elicit systemic anti-tumor and anti-metastatic effects. Local injection of Hf-MOL in 4T1 orthotopic tumors enables RT-RDT with fractionated, low-dose X-rays. The RT-RDT effects potentiate CBI to systemically eliminate tumors and prevent metastasis through three mechanisms: regressing local tumors by direct killing effects, stimulating anti-tumor immunity via immunogenic cell death and tumor antigen release, and decreasing pro-metastatic MDSCs in bone marrow, spleen, and lungs. The combination of Hf-MOL-enabled RT-RDT and anti-PD-L1 antibody thus overcomes suppressive tumor microenvironments and activate cytotoxic T cells to eliminate lung metastasis. Reprinted with permission from *Matter*, **2019**, *1*, 1331-1353. Copyright 2019 Elsevier Inc.

4.2 Results

4.2.1 Synthesis and characterization of Hf-MOL

By carefully controlling the synthetic conditions, we synthesized the Hf-DBP nMOL based on Hf-oxo SBUs and photosensitizing porphyrin-based ligands for RT-RDT, reducing the dimensionality of 3D nMOFs to 2D nMOLs to relief the diffusion barrier for ROS (**Scheme 4-1**).

Scheme 4-1 Reduction of dimentionality to nMOL from nMOF. Reprinted with permission from *Matter*, **2019**, *1*, 1331-1353. Copyright 2019 Elsevier Inc.

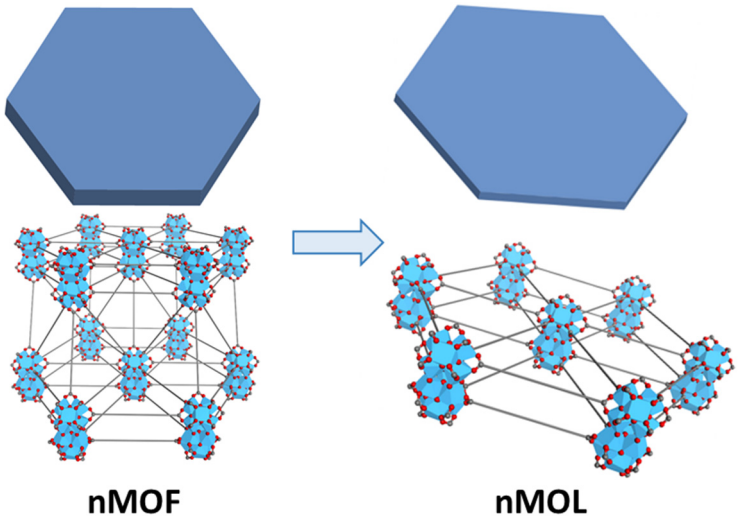

Hf-MOL was synthesized through a solvothermal reaction between $HfCl_4$ and H_2DBP in DMF at 80 °C with AcOH and water as modulators. Hf-MOL is constructed from $Hf_{12}(\mu_3\text{-}O)_8(\mu_3\text{-}OH)_8(\mu_2\text{-}OH)_6$ SBUs and DBP bridging ligands as a monolayer with an infinite 2D network of kagome dual (kgd) topology. Hf-MOL monolayers are vertically capped by acetate groups (*via* coordination to the Hf_{12} SBUs) to afford a molecular formula of $Hf_{12}(\mu_3\text{-}O)_8(\mu_3\text{-}OH)_8(\mu_2\text{-}OH)_6(DBP)_6(AcO)_6$. Transmission electron microscopy (TEM) imaging showed a flat-plate morphology of Hf-MOL with a diameter of ~150 nm (**Figure 4-2a,b**) and a thickness of ~1.6 nm by atomic force microscopy (AFM, **Figure 4-2 e,f**), consistent with the modeled height of Hf_{12}

SBUs capped with acetate groups (**Figure 4-2d**). High resolution TEM (HRTEM) images of Hf-MOL, in which Hf_{12} SBUs appear as black spots, and fast Fourier transform (FFT) patterns of the HRTEM image revealed six-fold symmetry that is consistent with its kgd topology (**Figure 4-2c**).

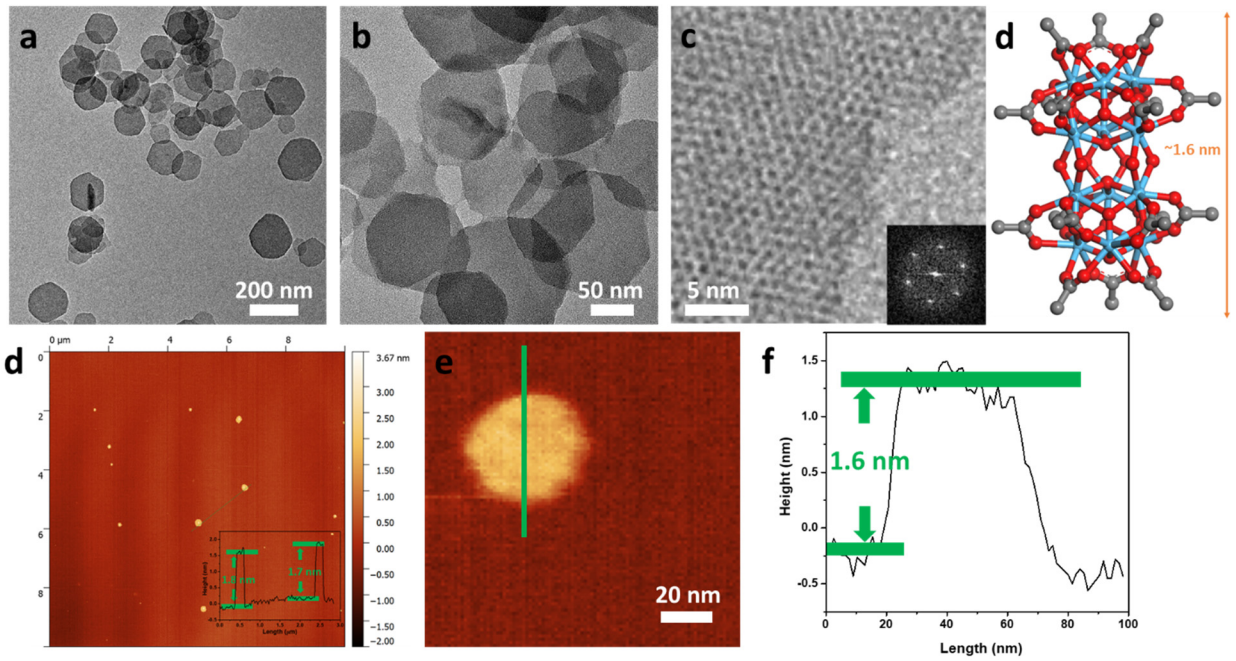

Figure 4-2 TEM image of Hf-MOL in a large (a) and small (b) field. (c) HR-TEM image of Hf-MOL with its fast Fourier transform (FFT) pattern shown in inset of (c). (d) A view of the Hf_{12} cluster capped by acetate with a height measured to be ~1.6 nm. The formulation for the Hf_{12} cluster is $Hf_{12}(\mu_3\text{-}O)_8(\mu_3\text{-}OH)_8(\mu_2\text{-}OH)_6(DBP)_6(AcO)_6(carboxylate)_{12}$. (e) Representative AFM topography of Hf-MOL in a large field. Height profile in inset of straight green line display the heights of marked Hf-MOL. (f) AFM topography and (g) height profile of Hf-MOL. Scale bar = 200 nm (a), 50 nm (b), 5 nm (c) and 20 nm (e). Reprinted with permission from *Matter*, **2019**, *1*, 1331-1353. Copyright 2019 Elsevier Inc.

As a control, the 3D Hf-DBP nMOF (Hf-MOF) was also synthesized through a solvothermal reaction between $HfCl_4$ and H_2DBP as reported previously.[3] Hf-MOF displayed a 3D nanoplate morphology with a diameter of ~100 nm and a thickness of 15-50 nm (**Figure 4-3**). Dynamic light scattering (DLS) measurements gave number-average sizes of 59.2 ± 0.6 nm and 80.6 ± 4.2 nm for Hf-MOL and Hf-MOF, respectively (**Figure 4-4a**). Singlet oxygen sensor green (SOSG) indicated ~1.5 times higher $^1O_2$ presence in solutions of 2D Hf-MOL upon light irradiation over

3D Hf-MOF under identical conditions, likely due to enhanced diffusion of generated $^1O_2$ which facilitates reaction with SOSG (**Figure 4-4b**). The powder X-ray diffraction (PXRD) patterns of Hf-MOL incubated in 6 mM phosphate buffered saline (PBS) solution for 10 days were identical to that of the pristine sample (**Figure 4-4c**), indicating the stability of Hf-MOL in physiological environments. This was further confirmed by the TEM image of Hf-MOL incubated in 6 mM PBS (**Figure 4-4d**).

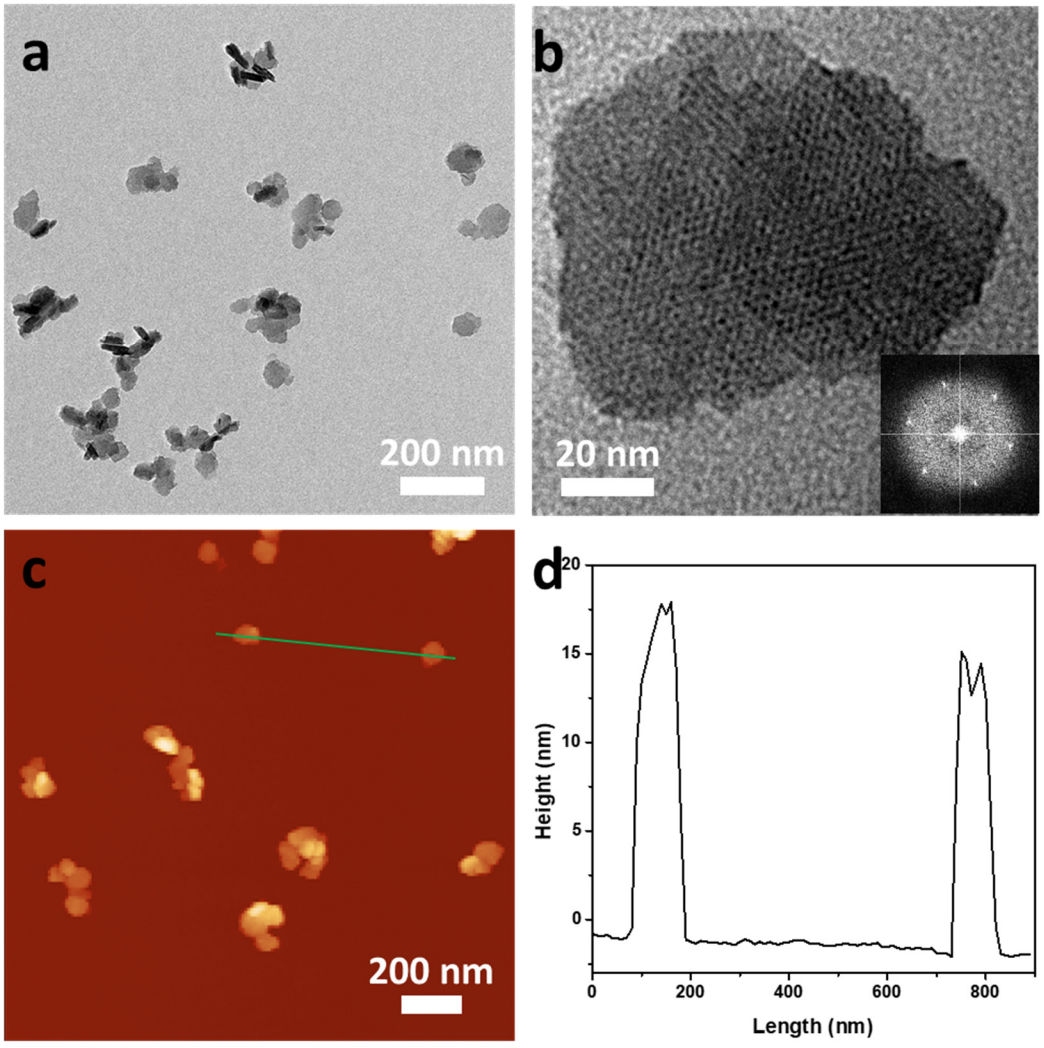

Figure 4-3 TEM (a) and HRTEM (b) images of Hf-MOF. (c) AFM topography and (d) height profile of Hf-MOL. Scale bar = 200 nm (a), 20 nm (b), and 200 nm (c). Reprinted with permission from *Matter*, **2019**, *1*, 1331-1353. Copyright 2019 Elsevier Inc.

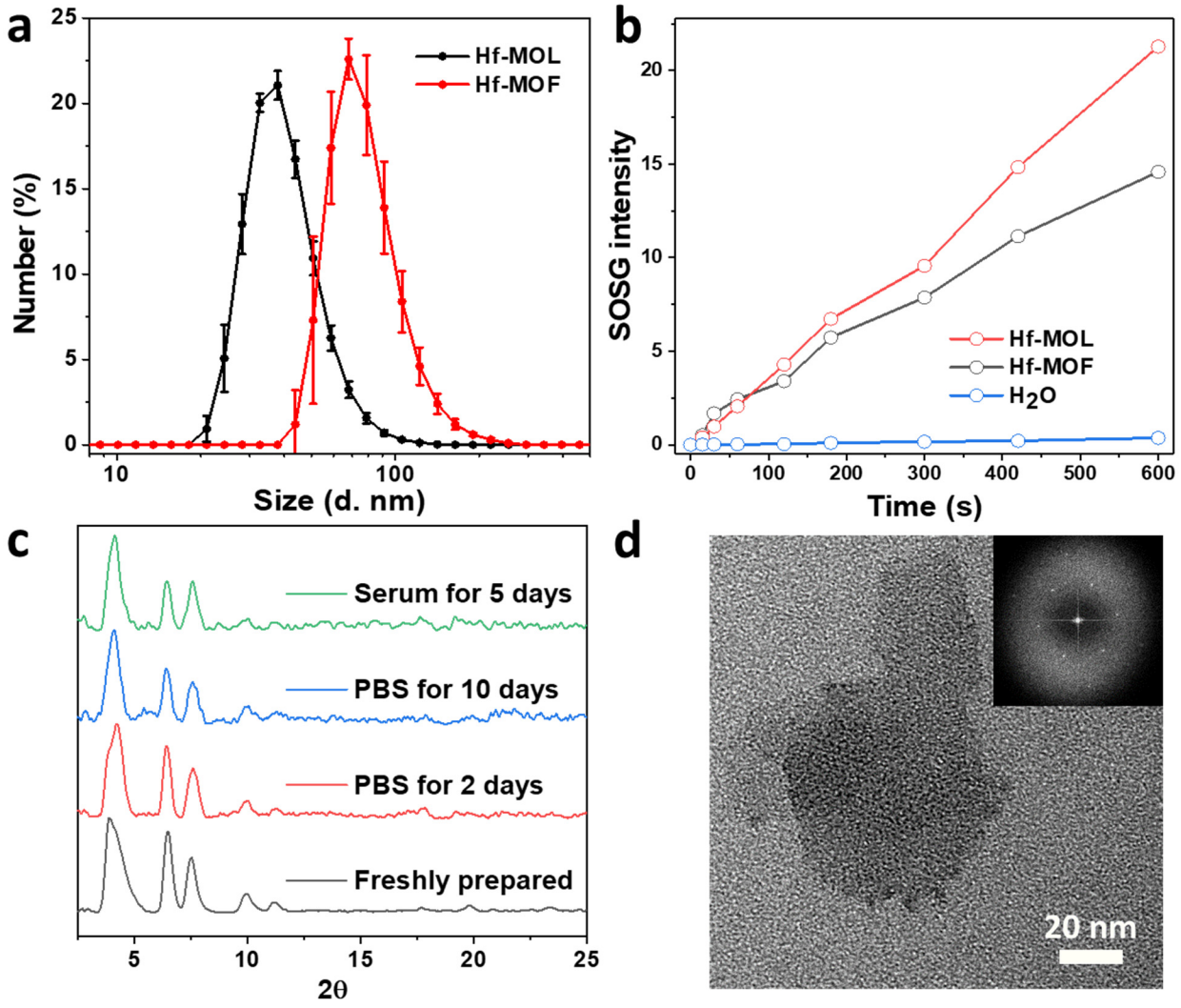

Figure 4-4 (a) Number-average diameter of Hf-MOL (black line) and Hf-MOF (red line) in water, n = 3. (b) $^1O_2$ generation was detected using SOSG with Hf-MOL (black line) Hf-MOF (red line) or water (blue line). (c) PXRD patterns of Hf-MOL samples that were freshly prepared or incubated in 6 mM PBS for 2, or 10 days or in serum for 5 days. (d) Representative TEM image of Hf-MOL incubated with 6 mM PBS solution with its fast Fourier transform (FFT) pattern shown in inset of (d). Scale bar = 20 nm. Reprinted with permission from *Matter*, **2019**, *1*, 1331-1353. Copyright 2019 Elsevier Inc.

To further evaluate the RDT effects of Hf-MOL, Hf_{12}-DBA previously reported in Chapter 2, (denoted as Hf-DBA), was synthesized and used as a control. Hf-DBA is constructed from non-photosensitizing DBA bridging ligand and the same $Hf_{12}(\mu_3\text{-}O)_8(\mu_3\text{-}OH)_8(\mu_2\text{-}OH)_6$ SBU and enhances RT only.

4.2.2 *In vitro* anti-tumor effect of Hf-MOL-enabled RT-RDT

Murine triple-negative breast cancer cell 4T1 was employed for all *in vitro* experiment. Clonogenic assays were performed on cells first treated with Hf-MOL or Hf-DBA at a Hf concentration of 20 μM for 4 h followed by irradiation with either X-ray or ^{60}Co isotope γ-ray source at 0-16 Gy. The irradiated cells were cultured for an additional 10 days to form visible colonies, which were counted to determine the survival fraction. At the same Hf concentration, Hf-MOL outperformed Hf-DBA with an REF_{10} value of 2.29 compared to 1.45 for Hf-DBA upon X-ray radiation (**Figure 4-5a**). Upon irradiation with γ-rays from a ^{60}Co source, Hf-MOL exhibited an REF_{10} value of 1.45 compared to 1.25 for Hf-DBA on 4T1 cells (**Figure 4-5b**). This result suggests that Hf-MOL can be activated with γ-rays from linear accelerators commonly used in the clinic for RT treatment. For convenience, we denote PBS, Hf-MOL, H_2DBP, or Hf-DBA plus X-ray radiation as PBS(+), Hf-MOL(+), H_2DBP(+), or Hf-DBA(+), respectively, and PBS, Hf-MOL, or Hf-DBA without X-ray radiation as PBS(-), Hf-MOL(-), H_2DBP(-), or Hf-DBA(-), respectively.

MTS assays further showed that Hf-MOL(+) exhibited much higher acute cytotoxicity than Hf-DBA(+) and H_2DBP(+). At 2 Gy, the IC_{50} value for Hf-MOL against 4T1 cells was calculated to be 8.18 ± 3.15 μM while IC_{50} values for H_2DBP and Hf-DBA both exceeded 100 μM (**Figure 4-5c**). No cytotoxicity was observed without irradiation for any group (**Figure 4-5d**). The colony and MTS results indicate higher radioenhancing effects of Hf-MOL over Hf-DBA, likely due to the RT-RDT effect and the enhanced ROS diffusion in Hf-MOL. Cell death pathways were investigated with an Annexin V/Cell death kit. Significant amounts of cells underwent apoptosis/necrosis when treated with Hf-MOL(+) with only 38.2% healthy cells, compared to 90.2% and 86.5% healthy cells for H_2DBP(+) and Hf-DBA(+), respectively (**Figure 4-6a**). More than 90% cells remained healthy in dark controls and PBS(+) group, indicating that Hf-DBA, H_2DBP, and

Hf-MOL are not intrinsically cytotoxic and low dose X-ray elicits negligible cytotoxicity with PBS treatment. These results were further confirmed by confocal laser scanning microscopy (CLSM) which showed the majority of cells after Hf-MOL(+) treatment were apoptotic with red and green fluorescence (**Figure 4-6b**).

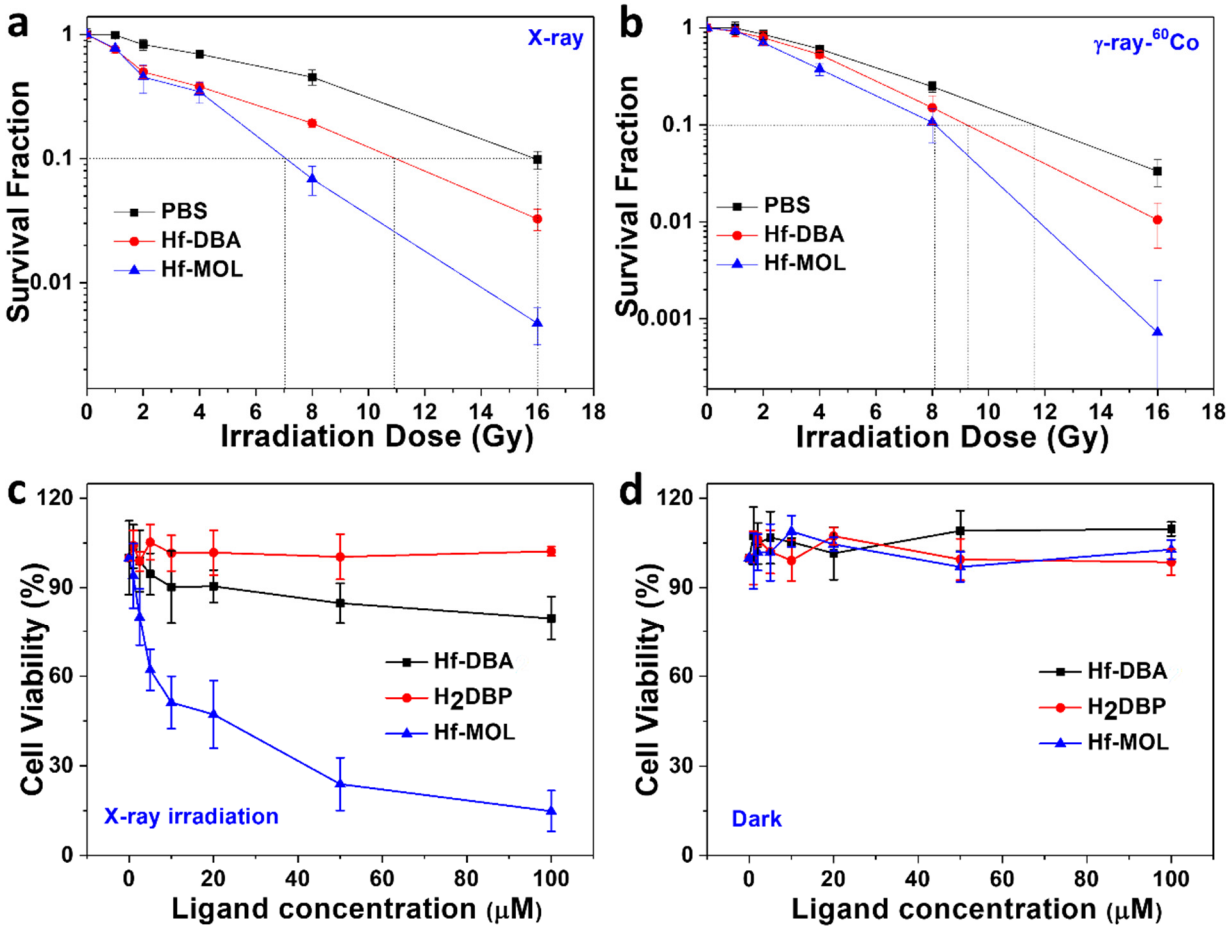

Figure 4-5 Clonogenic assays to evaluate radioenhancement of Hf-DBA and Hf-MOL on 4T1 cells upon (a) orthovoltage X-ray and (b) ^{60}Co γ-ray irradiation, n = 6. Cytotoxicity of Hf-DBA, H_2DBP, or Hf-MOL upon X-ray irradiation at a dose of 2 Gy (c) or 0 Gy (d) on 4T1 cells, n = 6. Reprinted with permission from *Matter*, **2019**, *1*, 1331-1353. Copyright 2019 Elsevier Inc.

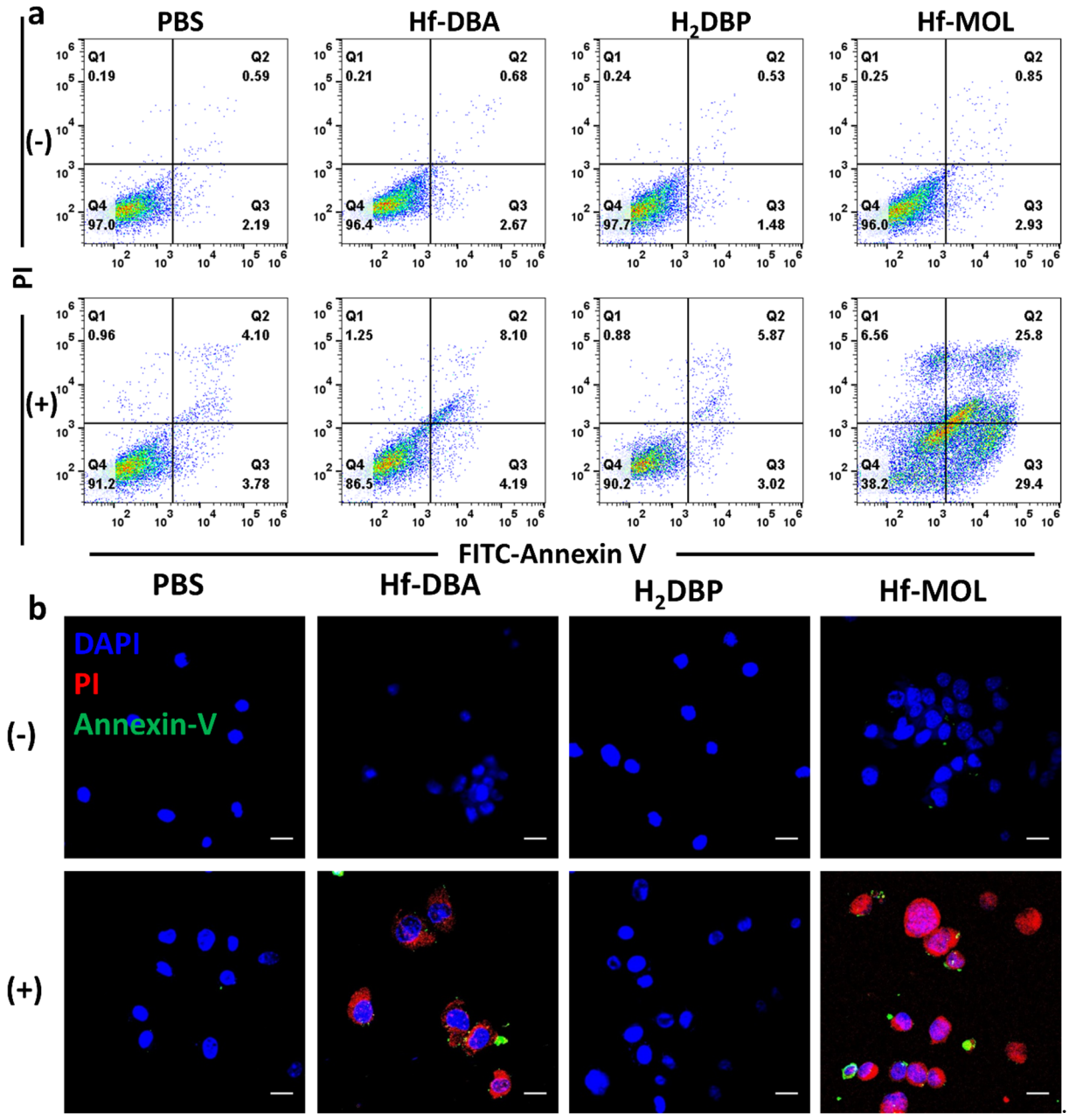

Figure 4-6 Annexin V/PI analysis by flow cytometry (a) and CLSM (b) showing apoptosis and necrosis of 4T1 cells treated with PBS, Hf-DBA, H_2DBP or Hf-MOL and irradiated upon X-ray at a dose of 0 (-) or 2 (+) Gy. (a) The quadrants from lower left to upper left (counter clockwise) represent healthy, early apoptotic, late apoptotic, and necrotic cells, respectively. The percentage of cells in each quadrant was shown on the graphs. (b) Blue, red and green fluorescence represent DAPI, PI and Annexin-V-conjugated Alexa-488, respectively. Scale bar = 20 μm. Reprinted with permission from *Matter*, **2019**, *1*, 1331-1353. Copyright 2019 Elsevier Inc.

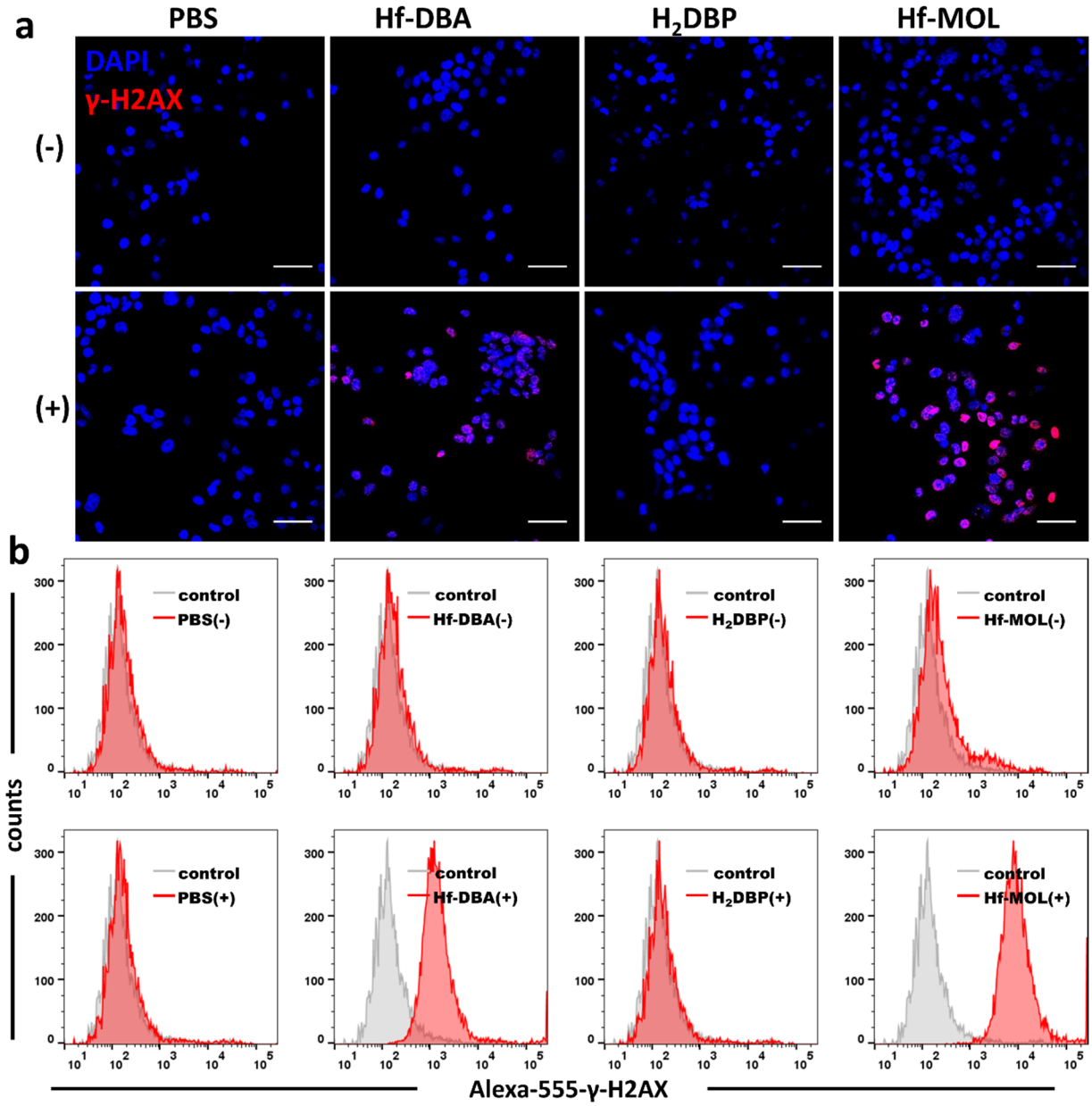

Figure 4-7 DNA double strand break of 4T1 was assessed after incubation with PBS, Hf-DBA, H_2DBP or Hf-MOL and irradiated with X-ray at 0 (-) or 2 (+) Gy by CLSM (a) or flow cytometry (b). (a) Blue and red fluorescence show DAPI-stained nucleus and antibody-labeled γ-H2AX in the cells, respectively. Scale bar = 100 μm. (b) Grey histogram (control) and red histogram show the difference of γ-H2AX level in the cells. Reprinted with permission from *Matter*, **2019**, *1*, 1331-1353. Copyright 2019 Elsevier Inc.

We further performed DNA DSB quantification to determine the RT effects from generated ·OH. Phosphorylated γ-H2AX was immunostained to quantify the DSBs in cells treated with PBS, Hf-DBA, H_2DBP, or Hf-MOL at an X-ray dose of 0 or 2 Gy to evaluate the RT enhancing effect. 6 h after irradiation, significantly higher red γ-H2AX fluorescence was observed in the group treated with Hf-MOL(+) than that treated with Hf-DBA(+), while no fluorescence was observed in groups either without X-ray irradiation or without Hf-based nanoparticle (**Figure 4-7a**). Flow cytometric analyses further showed that cells treated with Hf-MOL(+) exhibited stronger red γ-H2AX fluorescence than Hf-DBA(+) treatment, confirming the stronger RT enhancement of Hf-MOL (**Figure 4-7b**)

$^1O_2$ generation was determined to probe the Hf-MOL enabled RDT process. No green fluorescence was detected in PBS(+), Hf-DBA(+), or H_2DBP(+) treated 4T1 cells or in the Hf-MOL(-) treatment group after co-cultured with SOSG. In contrast, 4T1 cells treated with Hf-MOL(+) presented strong green fluorescence in CLSM images, indicating the generation of $^1O_2$ in Hf-MOL-enabled RDT process (**Figure 4-8a**). Transwell invasion assay was then performed to evaluate the anti-migration effect of RT-RDT treatment. Upon X-ray irradiation, Hf-MOL treatment represses invasion of 4T1 cells compared with other groups (**Figure 4-8b**). Taken together, Hf-MOL(+) elicits strong anti-cancer effects via a distinct RT-RDT mechanism of action through a combination of electron-dense Hf_{12}-based SBUs and porphyrin-based photosensitizing bridging ligands. The ultrathin 2D structure of Hf-MOL facilitates ROS diffusion to further enhance both acute and chronic cell death. Hf-MOL(+) treatment also exhibits anti-migration effect on tumor cells, prompting us to examine its ability to prevent metastasis of 4T1 tumor cells to distant sites.

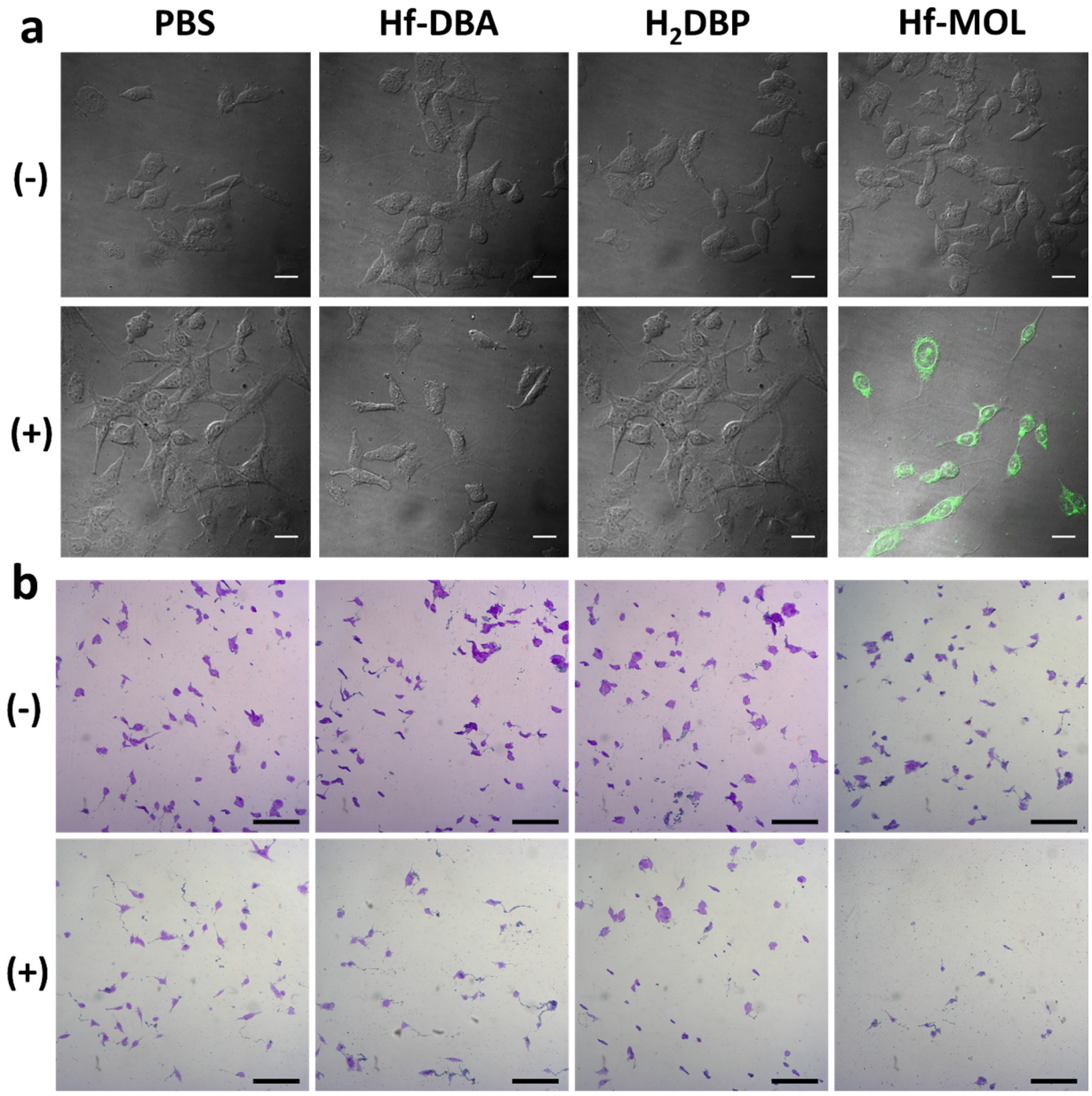

Figure 4-8 Intracellular $^1O_2$ generation detected by SOSG (a) and images of crystal violet-stained invading (b) 4T1 cells incubated with PBS, Hf-DBA, H_2DBP or Hf-MOL and irradiated upon X-ray at 0 (-) or 2 (+) Gy. Scale bar = 20 μm (a) or 50 μm (b). Reprinted with permission from *Matter*, **2019**, *1*, 1331-1353. Copyright 2019 Elsevier Inc.

4.2.3 Immunogenicity

We investigated immunogenic cell death (ICD) induced by Hf-MOL(+) treatment *via* detecting cell-surface exposure of CRT by flow cytometry and CLSM as well as high mobility group box protein 1 (HMGB-1) release and adenosine triphosphate (ATP) excretion by enzyme-linked immunosorbent assay (ELISA). Quantitative flow cytometric analysis demonstrated that both Hf-DBA(+) and Hf-MOL(+) treated groups showed high cell surface CRT expression (**Figure 4-9a**). The Hf-MOL(+) treated group exhibited higher CRT fluorescence than the Hf-DBA(+) treated group, suggesting that Hf-MOL(+) enabled RT-RDT induced more ICD than Hf-DBA(+)-mediated RT. CRT exposure on cell surface was further confirmed by CLSM imaging. Stronger green fluorescence was observed in the group treated with Hf-MOL(+) than in the groups treated with PBS(+), H_2DBP(+), and Hf-DBA(+), which well merged with CellMask, a red fluorophore labeling cell membranes. The CLSM results support higher immunogenicity induced by Hf-MOL(+) treatment (**Figure 4-9b**).

To further validate ICD, HMGB-1 and ATP excretion were examined by ELISA. Compared to groups treated with either Hf-DBA(+) or H_2DBP(+), cells treated with Hf-MOL(+) showed higher excretion of HMGB-1(**Figure 4-10a**) and ATP (**Figure 4-10b**), providing further support to more ICD by Hf-MOL(+) treatment. We then performed an anti-tumor vaccination experiment to confirm the ICD induced by Hf-MOL(+)-treated cells *in vivo*. 4T1 cells incubated with Hf-MOL followed by irradiation with X-rays were inoculated into BALB/c mice as a tumor vaccine. Seven days later, the mice were challenged with live 4T1 cells by subcutaneous transplantation to the contralateral flanks. As shown in **Figure 4-10c**, mice receiving Hf-MOL(+)-treated 4T1 cells were protected against challenge with live 4T1 cells. This result indicates that Hf-MOL(+) treatment

induced strong ICD in 4T1 cells and Hf-MOL(+)-treated cells acted as an effective vaccine against live tumor cells in immunocompetent mice.

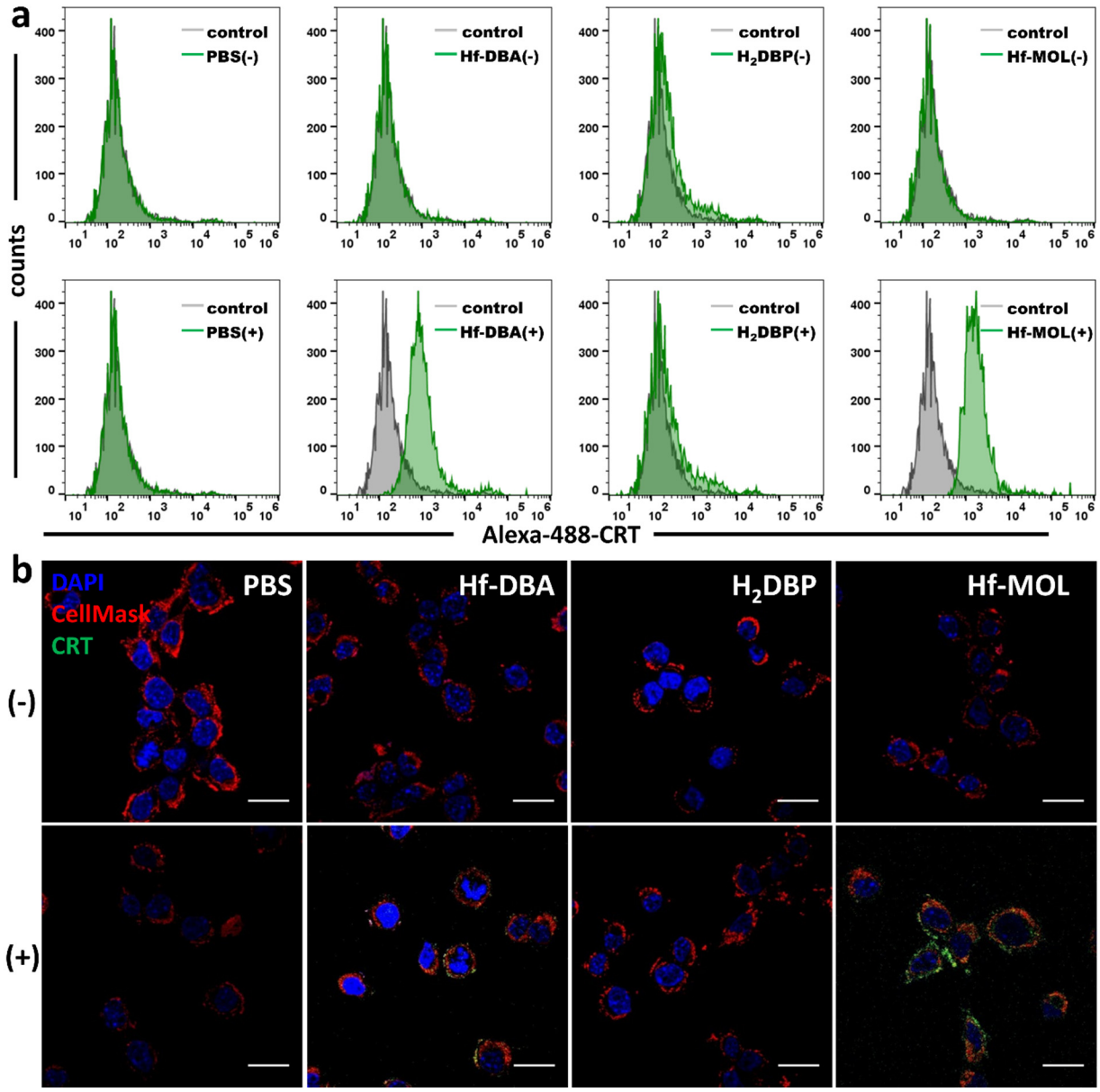

Figure 4-9 *In vitro* CRT exposure on the cell surface of 4T1 was assessed after incubation with PBS, Hf-DBA, H_2DBP, or Hf-MOL upon X-ray irradiation at a dose of 2 Gy by (a) flow cytometry and (b) immunofluorescence microscopy. (+) and (-) refer to with and without irradiation, respectively. Blue, red and green fluorescence show DAPI-stained nucleus, RedMask-stained cell membrane and CRT exposure on the cell surface, respectively. Scale bar = 20 μm. Reprinted with permission from *Matter*, **2019**, *1*, 1331-1353. Copyright 2019 Elsevier Inc.

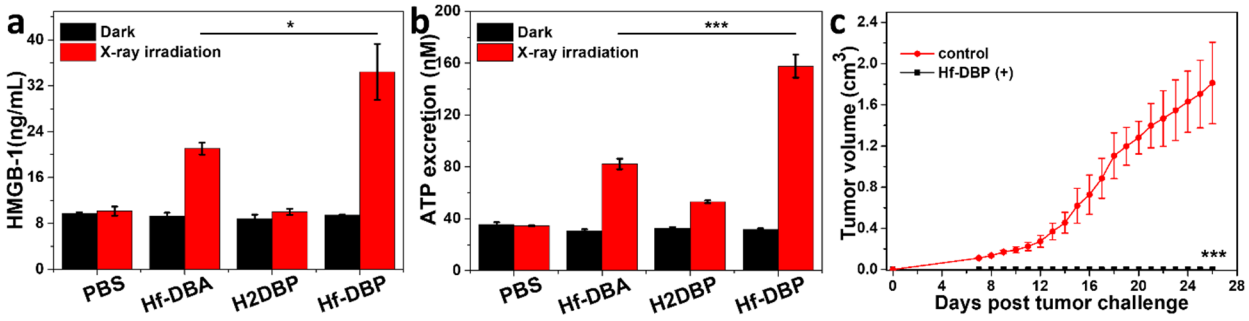

Figure 4-10 HMGB-1 release (a) and ATP extracellular secretion from the cells incubated with PBS, Hf-DBA, H_2DBP, or Hf-MOL with or without X-ray irradiation at a dose of 2 Gy, n = 3. (c) Volumes of challenge tumors, n = 6. 4T1 cells treated with Hf-MOL or PBS upon X-ray irradiation in vitro were inoculated subcutaneously in BALB/c mice. After 7 days, mice were challenged with live 4T1 cells. Reprinted with permission from *Matter*, **2019**, *1*, 1331-1353. Copyright 2019 Elsevier Inc.

4.2.4 Abscopal effects of Hf-MOL-enabled RT-RDT plus immune checkpoint blockade

After demonstrating the anti-tumor effects of Hf-MOL(+) and its ability to induce ICD *in vitro*, we combined Hf-MOL(+) with CBI to extend the local RT-RDT treatment to systemic cancer management. A bilateral model of 4T1 tumor was established to assess the systemic anticancer efficacy of Hf-MOL(+) in combination with anti-PD-L1 CBI. Hf-MOL was intratumorally injected to the primary tumors at a dose of 0.11 mg/mouse on days 10 and 14 post tumor inoculation, with daily X-ray irradiation at a dose of 1 Gy/fraction beginning on day 10 for a total of 8 fractions. 75 μg of anti-PD-L1 antibody (α-PD-L1) was administered every three days by intraperitoneal injection for a total of 3 doses. As shown in **Figure 4-11a-c**, PBS(+) and PBS(-) groups did not show any difference in tumor growth, indicating that low dose X-rays alone had no radiotherapeutic effects. Anti-PD-L1 plus fractionated X-ray irradiation [α-PD-L1(+)] moderately delayed 4T1 tumor progression on both primary and distant tumors. Hf-MOL(+) alone regressed local tumors, but only moderately delayed the growth of distant tumors. The combination of Hf-MOL(-) and anti-PD-L1 [Hf-MOL(-)/α-PD-L1] showed similar modest inhibition of both primary

and distant tumors as anti-PD-L1 alone. In contrast, the combination treatment of Hf-MOL(+) and anti-PD-L1 [Hf-MOL(+)/α-PD-L1] significantly regressed both primary and distant 4T1 tumors, indicating a strong synergy between Hf-MOL(+) and α-PD-L1. Histological analysis showed that Hf-MOL(+) caused apoptosis/necrosis in local tumors, while only Hf-MOL(+)/α-PD-L1 treatment afforded the highest levels of apoptosis/necrosis in the un-irradiated distant tumor (**Figure 4-11e**). In addition, no weight loss (**Figure 4-11d**) or obvious histopathological changes in the main organs were observed in the treated groups, indicating the absence of general systemic toxicity (**Figure 4-11f**). After treatment, four out of six mice had both of their primary and distant tumors completely eradicated, affording a cure rate of 66.7%. Tumors in the other two mice shrank to minute sizes, but eventually regrew.

30 days post tumor eradication, treated mice and naïve control mice were challenged with 2 × 10^6 4T1 cells subcutaneously. None of the treated mice developed tumors on the left flank within 27 days post tumor inoculation when the distant tumors of the control mice reached 2cm^3 (**Figure 4-12a**). This result indicates that tumor specific immune memory was generated in mice after tumor eradication by the combination of Hf-MOL(+) and α-PD-L1. We further confirmed immune involvement in the therapeutic effects of Hf-MOL(+)/α-PD-L1 by depleting $CD4^+$ T cells, $CD8^+$ T cells, or B cells. Mice receiving intraperitoneal injections of anti-CD4, anti-CD8, mouse IgG antibodies or B cell inhibitor ibrutinib were treated simultaneously with Hf-MOL(+)/α-PD-L1. Mouse IgG did not have any effect on tumor growth, but T/B cell depletion groups all showed rapid tumor growth after cessation of Hf-MOL(+)/α-PD-L1 treatment (**Figure 4-12b**). Significantly, all groups inhibiting the immune system showed no abscopal effect on distant tumors (**Figure 4-12c**). These results indicate that T and B cells play essential roles in the anticancer efficacy of both local RT-RDT treatment and distant abscopal effects. The depletion

studies thus support the immunotherapic effect of the combination treatment and the rationale of using Hf-MOL(+) to potentiate CBI.

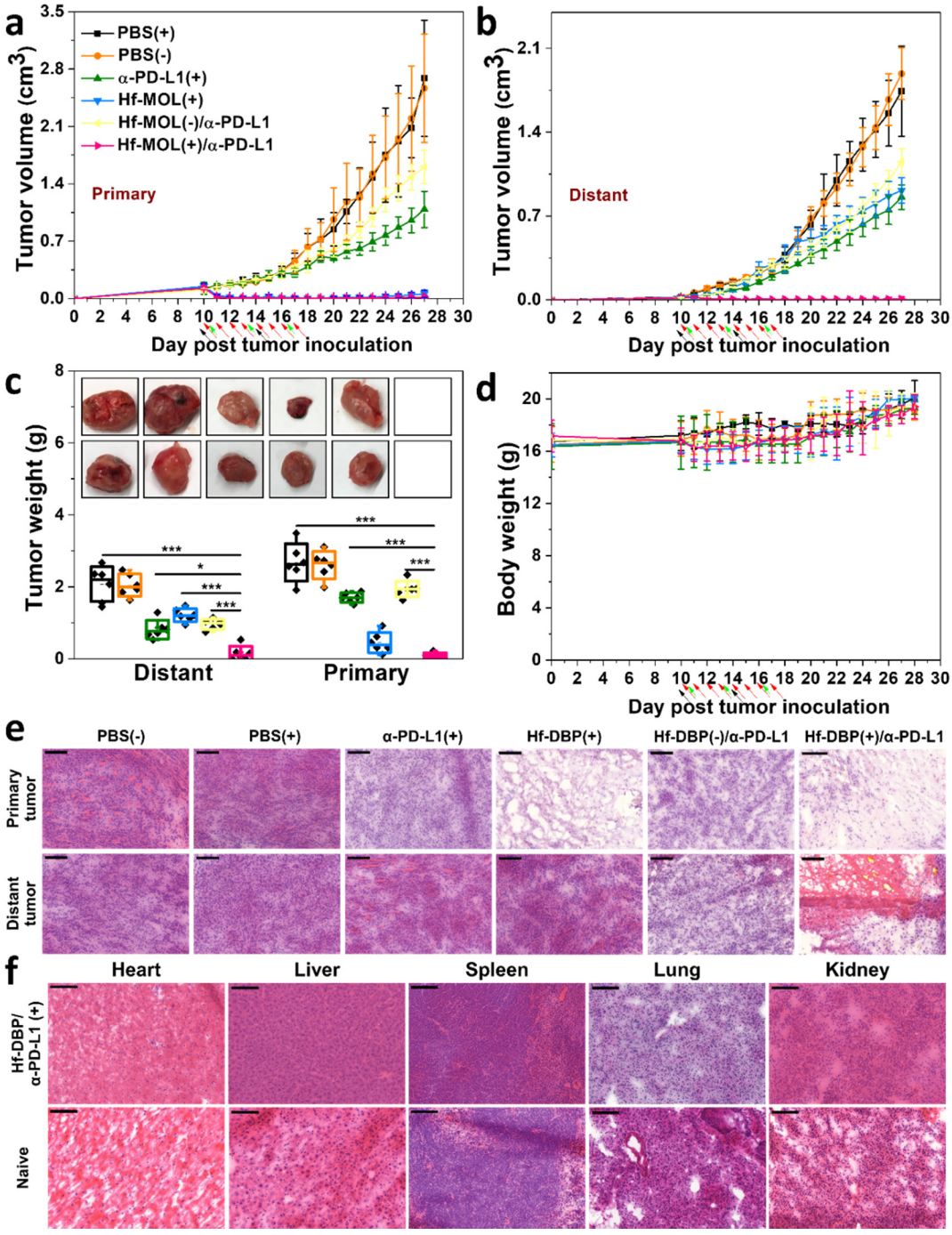

Figure 4-11 Tumor growth curves of primary (a), distant (b) tumors, body weights (d) and tumor histology (e) of 4T1 bilateral tumor-bearing mice treated with PBS(-), PBS(+),α -PD-L1(+), Hf-

Figure 4-11, continued MOL(-)/α -PD-L1 and Hf-MOL(+)/α-PD-L1, n = 6. (c) Tumor weights with representative optical images of tumors sectioned from groups in (a) & (b) shown in inset. Top row: primary tumors; bottom row: distant tumors. From left to right: PBS(-), PBS(+),α -PD-L1(+), Hf-MOL(-)/α-PD-L1 and Hf-MOL(+)/α-PD-L1. (f) Representative histology of frozen sections of major organs of bilateral 4T1 tumors-bearing mice treated with Hf-MOL(+)/α-PD-L1 compared with organs of healthy mouse. Scale bar = 100 μm. Reprinted with permission from *Matter*, **2019**, *1*, 1331-1353. Copyright 2019 Elsevier Inc.

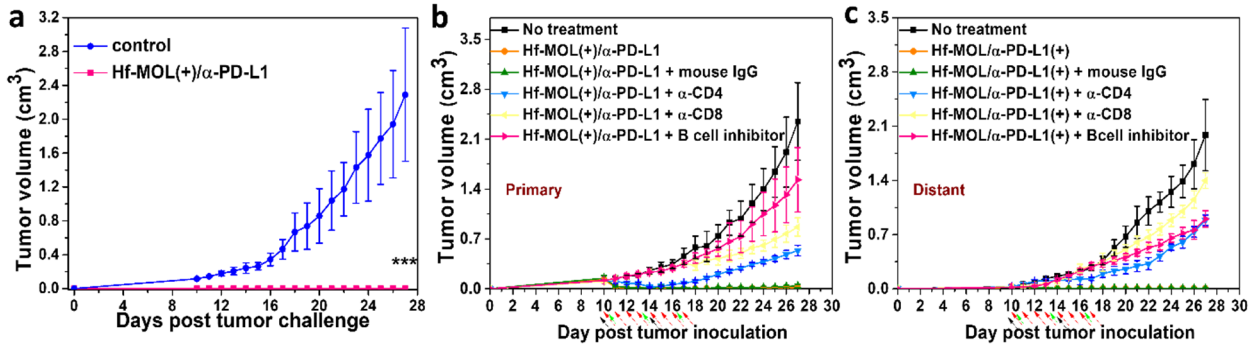

Figure 4-12 (a) Growth curves of challenged tumor on tumor-free mice treated with Hf-MOL(+)/α-PD-L1, n = 4. Tumor growth curves of primary (b) and distant (c) tumors of 4T1 bilateral tumor-bearing mice with T cell or B cell depletion and treatment with Hf-MOL(+)/α-PD-L1, n = 6. Reprinted with permission from *Matter*, **2019**, *1*, 1331-1353. Copyright 2019 Elsevier Inc.

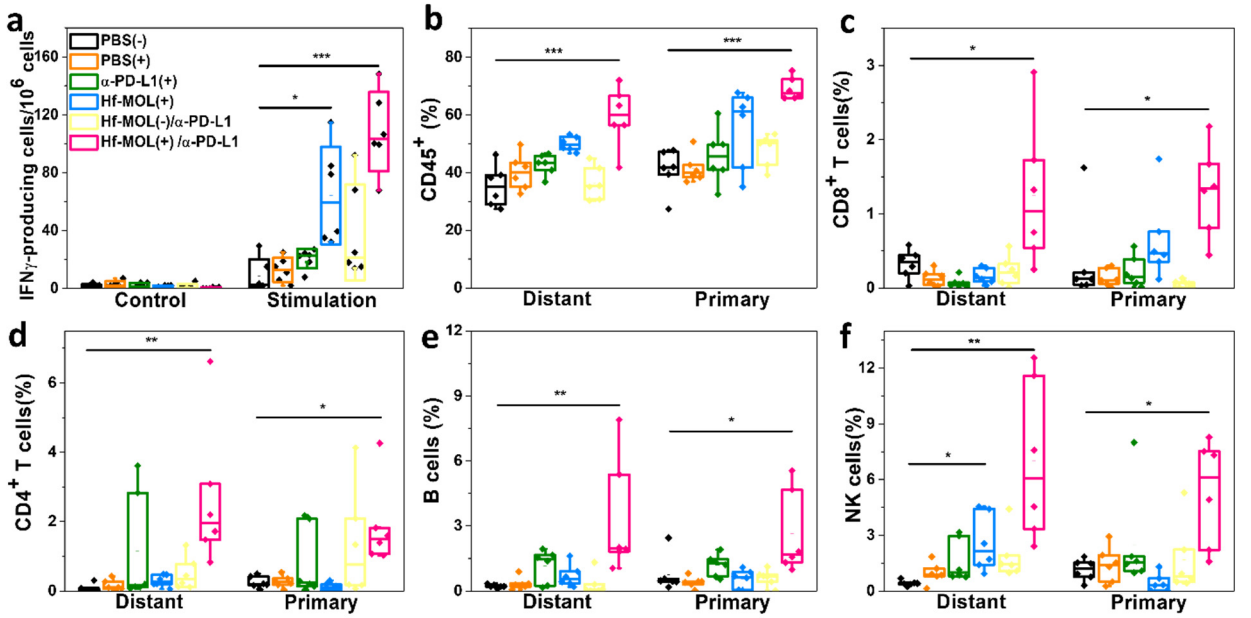

Figure 4-13 (a) ELISpot assay was performed to detect tumor-specific IFN-γ producing T cells. The primary and distant tumors were collected from tumor-bearing mice with as-mentioned

Figure 4-13, continued treatments for flow cytometry analysis and the percentages of tumor-infiltrating $CD45^+$ cells (b), $CD8^+$ T cells (c), $CD4^+$ T cells (d), B cells (e) and NK cells (f) with respect to the total tumor cells. (+) and (-) refer to with and without irradiation, respectively. Data are expressed as means ± s.d., n = 5. *P < 0.05, **P < 0.01 and ***P < 0.001 by t-test. Central lines, bounds of box and whiskers represent mean values, 25% to 75% of the range of data and 1.5 fold of interquartile range away from outliers, respectively. Reprinted with permission from *Matter*, **2019**, *1*, 1331-1353. Copyright 2019 Elsevier Inc.

4.2.5 Anti-tumor immunity

The inhibition of distant tumors and the rejection of challenged tumors suggest the effective induction of a systemic antitumor immune response. We first determined the presence of tumor-antigen specific cytotoxic T cells with an IFN-γ Enzyme-Linked ImmunoSpot (ELISpot) assay. On day 10 after the first treatment, splenocytes were harvested from 4T1-bearing mice and stimulated with X-ray irradiated 4T1 cells for 42 hours and the IFN-γ spot forming cells were counted with an Immunospot Reader. The number of antigen-specific IFN-γ producing T cells per 10^6 splenocytes significantly increased in tumor-bearing mice treated with Hf-MOL(+) and Hf-MOL(+)/α-PD-L1 [64.2 ± 33.7 and 108.3 ± 27.5 compared to 8.6 ±11.6 for PBS(-), **Figure 4-13a**], suggesting that Hf-MOL(+) effectively generates a tumor-specific T cell response. We further profiled infiltrating leukocytes in both primary and distant tumors. There was no significant difference between PBS(+) and PBS(-) treatment groups, demonstrating that low-dose X-ray irradiation did not influence the immunological environment of 4T1 tumors. Hf-MOL(+)/α-PD-L1 treatment group showed significant increase of tumor-infiltrating leukocytes, $CD4^+$ T cells and $CD8^+$ T cells in both primary and distant tumors (**Figure 4-13b-d**). Specifically, after treatment with Hf-MOL(+)/α-PD-L1, the percentages of $CD8^+$ T cells in the total primary and distant tumor cells significantly increased to 1.3 ± 0.6 % and 1.3 ± 1.0 % from 0.3 ± 0.2 % and 0.4 ± 0.6 % in PBS(-) group, respectively (**Figure 4-13c**). Hf-MOL(+)/α-PD-L1 group also showed significant

increase of tumor-infiltrating B cells and NK cells (**Figure 4-13e,f**) in both tumors. These results suggest that the combination of Hf-MOL(+) and α-PD-L1 not only induces innate immune response but also augments tumor-specific adaptive response in both local, irradiated and distant, un-irradiated tumors.

4.2.6 Efficacy of Hf-MOL-enabled RT-RDT in other synergistic tumor models

The triple negative breast cancer 4T1 model has moderate PD-L1 expression and resistance to RT. To demonstrate the efficacy of Hf-MOL(+) andα-PD-L1 on a broad spectrum of cancers, we further evaluated the anti-tumor activity on a bilateral CT26 colorectal tumor model in BALB/c c mice with high PD-L1 expression and low resistance to RT and a bilateral SCC VII squamous cell carcinoma tumor model in C3H mice with low PD-L1 expression and high resistance to RT. Similar tumor regression was observed in both CT26 and SCC VII tumor models after combination treatment with Hf-MOL(+) and α-PD-L1 (**Figure 4-14**). Tumor growth inhibition indices, defined as [1-(mean volume of treated tumors/mean volume of control tumors)]×100%, of primary and distant tumors are 99.5% and 98.0% for CT26 and 94.7% and 92.2% for SCC VII tumor models, respectively, which are significantly higher than control groups (**Table 4-1**). In addition, several other checkpoint inhibitors were tested in combination with Hf-MOL(+) to explore broader applications of RT-RDT in potentiating different CBIs. Hf-MOL(+) significantly enhanced the therapeutic efficacy of anti-PD-1 antibody (α-PD-1) and anti-CTLA-4 antibody (α-CTLA-4) on CT26 and SCC VII tumor models, leading to effective regression of both primary and distant tumors. These results demonstrate that Hf-MOL(+) synergizes with multiple checkpoint inhibitors to afford robust abscopal effects on several different mouse tumor models with varied immunogenicity, suggesting the potential of using Hf-MOL(+) to significantly boost the therapeutic efficacy of checkpoint blockade immunotherapies on a broad spectrum of cancers.

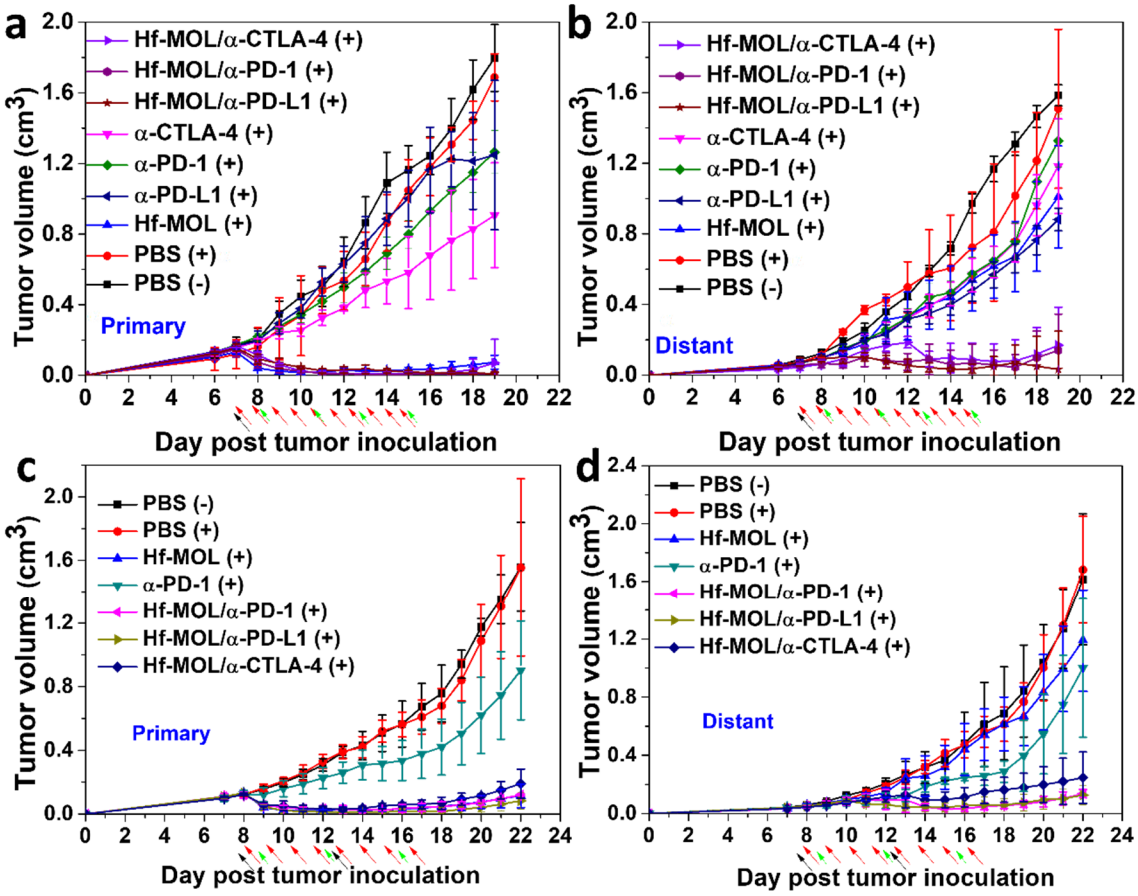

Figure 4-14 Abscopal effect of RT-RDT synergized CBI on CT26 (a,b) and SCC VII (c,d) bilateral tumor model. Tumor growth curves of primary (a) and (b) distant tumors of CT26 bilateral tumor-bearing BALB/c mice or primary (c) and (d) distant tumors of SCC VII bilateral tumor-bearing C3H mice treated with PBS (with or without X-ray irradiation), Hf-MOL with X-ray irradiation, anti-PD-1, anti-PD-L1 or anti-CTLA-4 antibody with X-ray irradiation, Hf-MOL with X-ray irradiation combined with anti-PD-1, anti-PD-L1 or anti-CTLA-4 antibody. N = 5 (CT26) or 4 (SCC VII). Black, red, and green arrows refer to the times of PBS or particle injections, X-ray irradiation, and antibody administration, respectively. Central lines, bounds of box and whiskers represent mean values, 25% to 75% of the range of data and 1.5 fold of interquartile range away from outliers, respectively. Reprinted with permission from *Matter*, **2019**, *1*, 1331-1353. Copyright 2019 Elsevier Inc.

Table 1. TGIs of CT26 and SCC VII tumor models with different treatments.

TGI (%)	CT26		SCC VII	
	Primary	Distant	Primary	Distant
PBS(+)	6.1	4.8	0.3	0.0
α-CTLA-4(+)	49.6	25.3	-	-
α-PD-1(+)	28.0	16.6	42.0	38.0
α-PD-L1(+)	30.6	44.4	-	-
Hf-MOL (+)	95.9	36.3	92.7	26.3
Hf-MOL/α-CTLA-4 (+)	96.1	95.6	92.3	91.6
Hf-MOL/α-PD-1(+)	99.4	91.2	88.2	84.8
Hf-MOL/α-PD-L1(+)	99.5	98.0	94.7	92.2

4.2.7 Anti-metastatic effect

We then investigated the anti-tumor activity and anti-metastatic effect of Hf-MOL(+) in combination with α-PD-L1 on an orthotopic 4T1 tumor model. 4T1 cells were implanted into the mammary fat pads of immunocompetent BALB/c mice and allowed to form primary breast tumors of sizes of 100-150 mm^3 in volume. Hf-MOL at a dose of 0.11 mg/mouse was intratumorally injected followed by daily X-ray irradiation at a dose of 1 Gy/fraction for a total of 8 fractions. Anti-PD-L1 antibody was administered every three days at a dose of 75 μg/mouse for a total of 3 doses. As shown in **Figure 4-15a-c**, α-PD-L1 (+) moderately delayed 4T1 tumor progression whereas Hf-MOL(-) showed no effect on tumor growth. In comparison, Hf-MOL(+) significantly inhibited tumor growth initially, but tumors regrew 5 days after cessation of treatment. Notably, Hf-MOL(+)/α-PD-L1 treatment nearly eradicated primary 4T1 tumors with a TGI of 98.9% on

day 17 post treatment. Combination treatment thus markedly improved the therapeutic efficacy over Hf-MOL(+) or α-PD-L1 alone. Terminal-deoxynucleoitidyl transferase mediated nick end labeling (TUNEL) assay showed that the Hf-MOL(+)/α-PD-L1 group induced the most DNA fragmentation and apoptosis (**Figure 4-15e**), supporting its superior anticancer efficacy over monotherapy controls. Body weights were monitored daily and no systemic toxicity was observed (**Figure 4-15d**).

The anti-metastatic effect was evaluated by examining lung tissues for tumor nodules at the end of the study. 4T1 cells can rapidly metastasize to the lungs from the mammary fat pad.[4] Compared to the PBS control group, Hf-MOL(+) or α-PD-L1 alone showed little effect preventing lung metastasis (**Figure 4-16a**). In contrast, Hf-MOL(+)/α-PD-L1 significantly reduced tumor nodules in the lungs, resulting in a 93.3% decrease in the number of macroscopically visible pulmonary metastases. Examination of the lungs revealed that mice treated with PBS had an average of 39.7 ± 8.34 visible lesions while mice treated with Hf-MOL(+)/α-PD-L1 exhibited an average of 2.7 ± 0.6 macroscopic lung metastases (**Figure 4-16d**). The proportion of the metastasis area relative to the whole lung was further quantified by H&E staining (**Figure 4-16b**). Hf-MOL(+) or α-PD-L1(+) alone only slightly suppressed spontaneous metastasis with metastatic nodules covering 34.5 ± 5.3 % and 21.8 ± 4.8 % of the lung, respectively, compared to nodules covering 42.7 ± 5.8% of the lung in the PBS group (**Figure 4-16e**). Hf-MOL(+)/α-PD-L1 treatment on the other hand significantly decreased the presence of lung metastasis to 2.2 ± 1.6%. Combination treatment with Hf-MOL(+)/α-PD-L1 is thus much more effective in preventing lung metastasis than Hf-MOL(+) or α-PD-L1(+) alone.

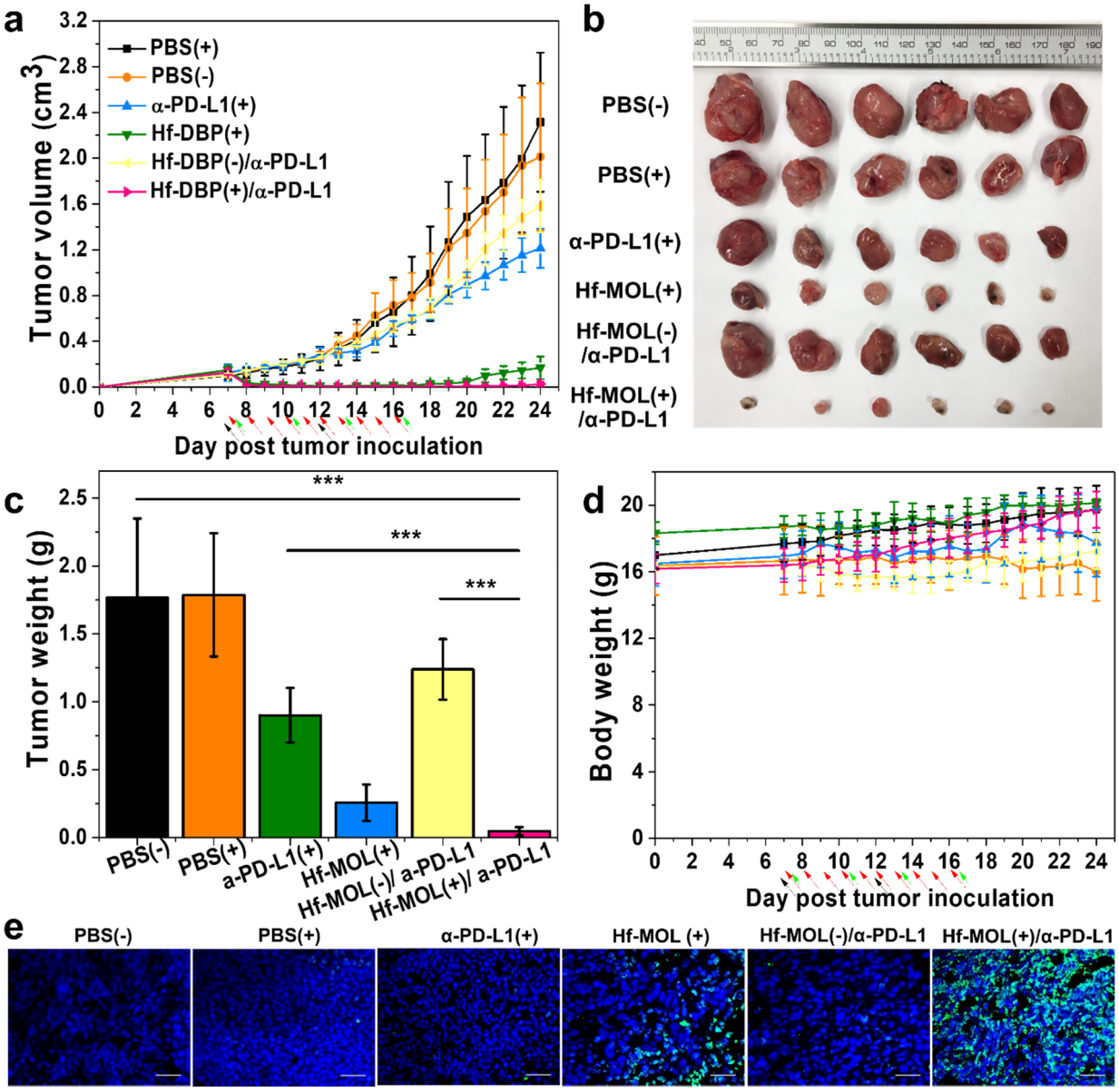

Figure 4-15 Tumor growth curves (a) and body weights (d) of 4T1 orthotopic tumor-bearing mice treated with PBS(-), PBS(+),α-PD-L1(+), Hf-MOL(-)/α-PD-L1 and Hf-MOL(+)/α-PD-L1. Black, red, and green arrows refer to the times of PBS or nanoparticles injections, X-ray irradiation, and antibody administration, respectively. Optical images (b), tumor weights (c) and TUNEL immunofluorescence staining (e) of excised tumors sectioned from groups in (a) at the endpoint. Data are expressed as means ± s.d., n = 6. Scale bar = 100 μm. *P < 0.05, ** P < 0.01, *** P < 0.001. Reprinted with permission from *Matter*, **2019**, *1*, 1331-1353. Copyright 2019 Elsevier Inc.

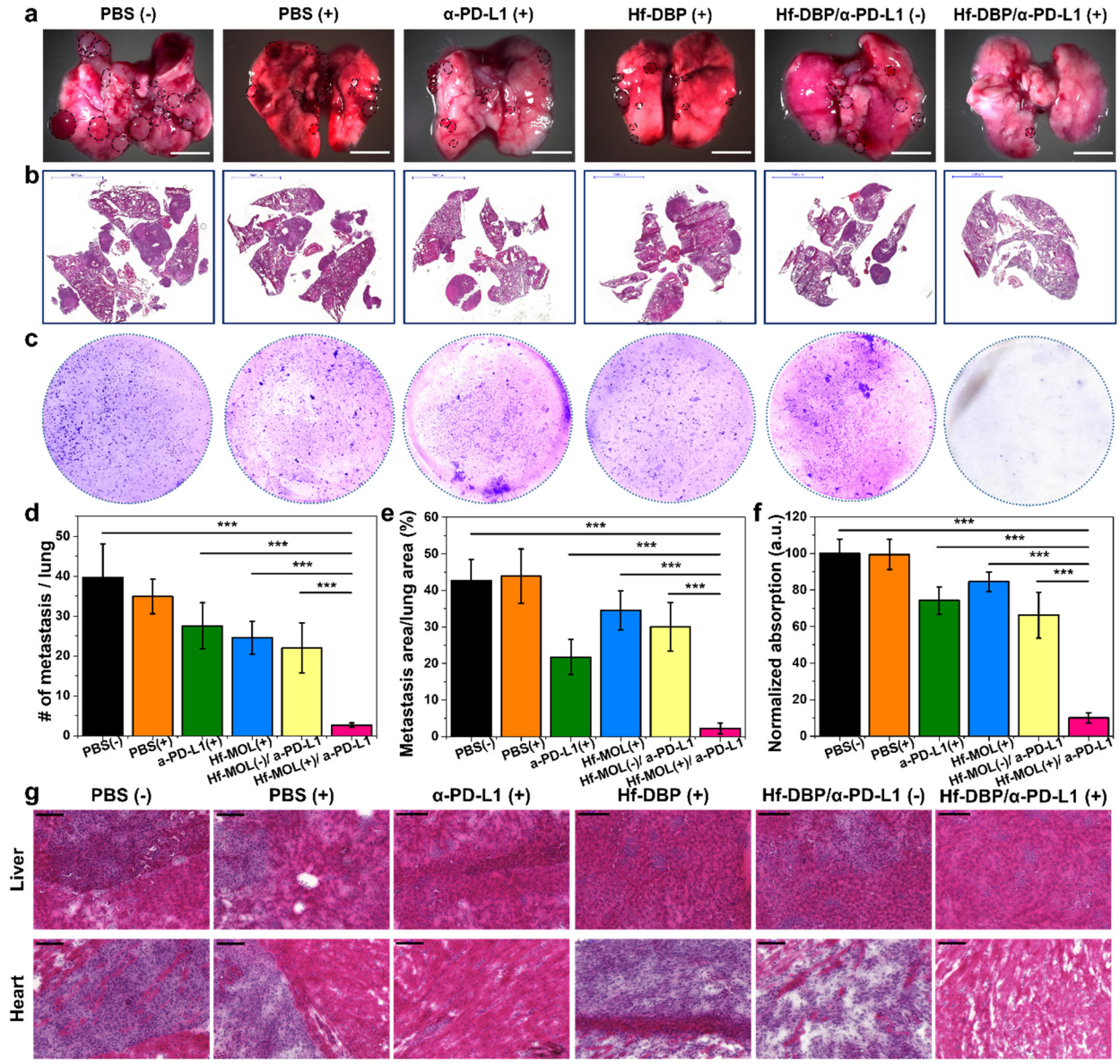

Figure 4-16 (a) Representative pictures showing the gross appearance of tumor nodules in the lungs. (b) Representative lung sections stained with H&E. (c) Representative pictures showing the colonies formed after culturing in the presence of 6-thiogunine for 10 days. (d) The numbers of tumor nodules present in the lungs. (e) Percentage of metastasis area in lung. (f) Normalized absorbance of crystal violet in different treatment groups. Representative histology with H&E staining of liver or heart slices to detect metastasis on orthotopic 4T1 tumor-bearing mice receiving intratumoral injection of Hf-MOL or PBS and X-ray irradiation treatment with or without antibody treatment. Scale bar = 5000 μm (a) or 100 μm (g). Data are expressed as means ± s.d., n = 6. Scale bar = 100 μm. *P < 0.05, ** P < 0.01, *** P < 0.001. Reprinted with permission from *Matter*, **2019**, *1*, 1331-1353. Copyright 2019 Elsevier Inc.

We then performed colony assays to quantitatively assess lung metastases after various treatments. At the end of the treatment, lungs were digested and the cells were harvested and cultured in the presence of 60 M 6-thioguanine for 10 days. After being fixed with methanol, colonies formed by clonogenic metastatic cancer cells were stained with 0.1% crystal violet. Because 4T1 tumor cells are resistant to 6-thioguanine, only metastasized tumor cells can proliferate to form colonies. As shown in **Figure 4-16c**, only the Hf-MOL(+)/α-PD-L1 treatment significantly reduced the number of colonies, decreasing the absorbance of crystal violet to only 10.0% of the PBS control group (**Figure 4-16f**). Hf-MOL(+) or α-PD-L1 treatment alone reduced the absorbance of crystal violet to 84.5% or 74.3% of the PBS control group, respectively. Clonogenic assay results indicate that mice treated with Hf-MOL(+)/α-PD-L1 have far fewer clonogenic metastatic 4T1 cells in the lungs than other treatment groups. We also examined metastases in other major organs as shown in (**Figure 4-16g**). The Hf-MOL(+)/α-PD-L1 group significantly reduced the number of macroscopically visible cardiac and hepatic metastases compared to the control groups.

4.2.8 Anti-metastatic mechanism

In order to understand the anti-metastatic mechanism, we examined the anti-tumor immunity of orthotopic 4T1 tumor-bearing mice treated with Hf-MOL(+)/α-PD-L1 by ELISpot and immunostaining flow cytometry. We first determined the presence of tumor-antigen specific cytotoxic T cells with an IFN-γ ELISpot assay. On day 12 after the first treatment, splenocytes were harvested from treated mice and stimulated with 4T1 cells, which exposed to ^{60}Co γ-ray irradiation at a dose of 50 Gy to release tumor antigens, for 42 hours and the IFN-γ spot forming cells were counted. The number of antigen-specific IFN-γ producing T cells significantly increased in tumor-bearing mice treated with Hf-MOL(+)/α-PD-L1 (**Figure 4-17a**), suggesting that Hf-

MOL(+)/α-PD-L1 treatment effectively generates systemic tumor-specific T cell response on the orthotopic 4T1 model. We further profiled infiltrating leukocytes in both breast tumors and lungs. The Hf-MOL(+)/α-PD-L1 group showed a significant increase of leukocytes, in particular $CD4^+$ T cells and $CD8^+$ T cells, in both primary tumors and distant lungs (**Figure 4-17b-d**). The increase of $CD8^+$ T cells in the lungs of the Hf-MOL(+)/α-PD-L1 group was confirmed with immunostaining under CLSM (**Figure 4-17g**). Interestingly, the Hf-MOL(+)/α-PD-L1 group showed significant increases of NK cells and B cells (**Figure 4-16e-f**) in the breast tumors but not in the lungs.

We also profiled both monocytic MDSCs (mMDSCs, $CD11b^+Ly6C^{hi}Ly6G^-$ phenotype) and granulocytic MDSCs (gMDSCs, $CD11b^+Ly6C^{low}Ly6G^+$ phenotype) in primary breast tumors and distant lungs. Significant reduction of mMDSCs was observed in the primary tumors and lungs after Hf-MOL(+)/α-PD-L1 treatment (**Figure 4-18a**). Significant reduction of gMDSCs was also observed in the lungs (**Figure 4-18b**). It is well-established that both mMDSCs and gMDSCs suppress T cell-mediated anti-tumor immunity and directly inhibit T cell proliferation. Hf-MOL(+)/α-PD-L1 treatment thus relieves inhibitory effects of MDSCs and enhances T cell activation and proliferation in both primary tumors and distant sites to suppress metastasis. Furthermore, it was reported that gMDSCs play an important role in mesenchymal-epithelial transition (MET) of circulating tumor cells and gMDSCs in the hematopoietic system support metastasis formation.[5] Immune cell profiling studies indicated a reduction of gMDSCs in bone marrow and spleen for the Hf-MOL(+)/α-PD-L1 group, suggesting that Hf-MOL(+)/α-PD-L1 inhibits metastasis through suppressing the pro-tumor effect of gMDSCs and weakening MET. The significant decrease of gMDSCs in both distant lungs and bone marrow further suggests the suppression of distant metastasis via worsening the environments for metastatic seeds.

Interestingly, we observed a correlation between the level of metastasis and spleen enlargement in this study. As a highly lung-metastatic breast tumor model, 4T1-bearing mice show severe spleen enlargement compared with other non-lung-metastatic breast tumor models such as TUBO and MCF-7. The spleens of the mice receiving different treatments were harvested, imaged and grounded. The splenocytes were harvested and counted. The spleens from Hf-MOL(+)/α-PD-L1-treated mice displayed a normal morphology as those from naïve mice, while the spleens from other treatment groups were enlarged (**Figure 4-18c**). The spleens from the mice treated with Hf-MOL(+)/α-PD-L1 had similar average weight as those from naïve mice but were only ~1/4 of those from other treatment groups (**Figure 4-18d**). The number of splenocytes from the mice treated with Hf-MOL(+)/α-PD-L1 were similar to those of naïve mice but only ~ 1/3 of those from other treatment groups (**Figure 4-18e**). We profiled the splenocytes and detected significate upregulation of gMDSCs in the groups with enlarged spleens. Only the Hf-MOL(+)/α-PD-L1 treatment afforded a significant decrease of gMDSC, indicating that MOL(+)/α-PD-L1 systemically depletes gMDSCs and prevents abnormal spleen enlargement which is a typical syndrome in mice with highly metastatic tumors (**Figure 4-18f**).

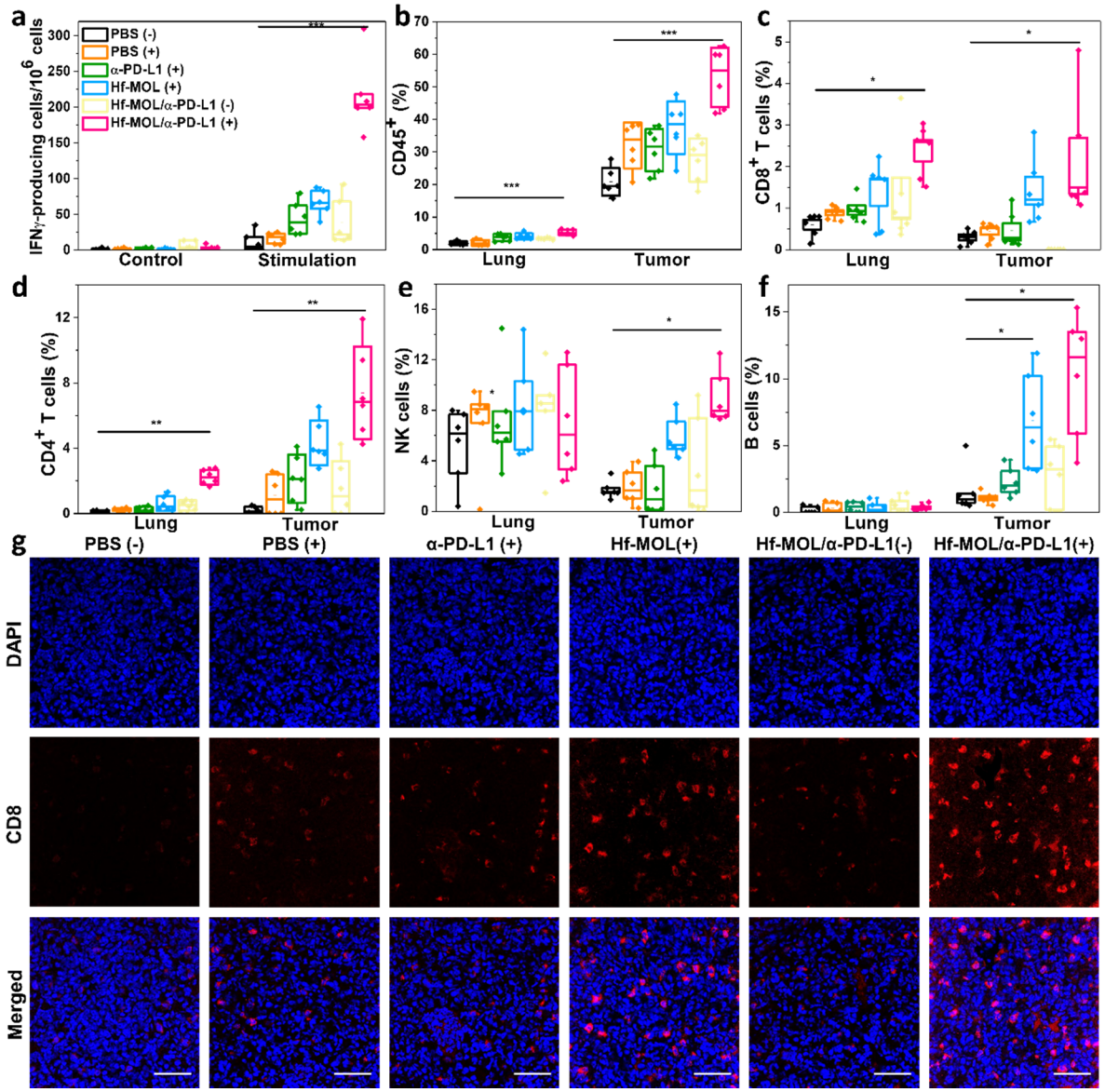

Figure 4-17 (a) ELISpot assay was performed to detect tumor-specific IFN-γ producing T cells. The tumors and lungs were collected from 4T1 tumor-bearing mice for flow cytometry analysis and the percentages of tumor-infiltrating $CD45^+$ cells (b), $CD8^+$ T cells (c), $CD4^+$ T cells (d), NK cells (e) and B cells (f) with respect to the total tumor cells. (+) and (-) refer to with and without irradiation, respectively. Data are expressed as means ± s.d., n = 6. *P < 0.05, **P < 0.01 and ***P < 0.001 by t-test. Central lines, bounds of box and whiskers represent mean values, 25% to 75% of the range of data and 1.5 fold of interquartile range away from outliers, respectively. (g) Immunofluorescence staining showing $CD8^+$ T cell (red) infiltration on 4T1 orthotopic tumors. Scale bar = 100 μm. Reprinted with permission from *Matter*, **2019**, *1*, 1331-1353. Copyright 2019 Elsevier Inc.

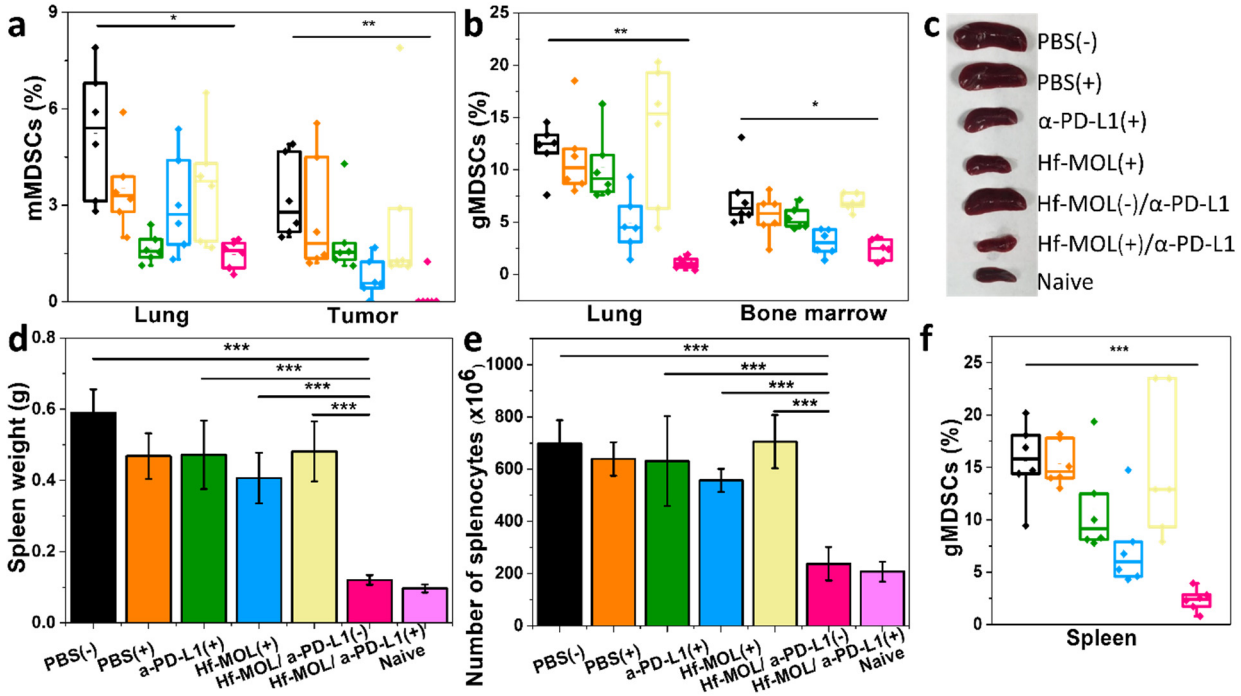

Figure 4-18 Tumors, lungs and bone marrows were collected from 4T1 tumor-bearing mice for flow cytometry analysis and the percentages of tumor-infiltrating mMDSCs (a) and gMDSCs (b) with respect to the total tumor cells. Spleen on 4T1 orthotopic tumor-bearing mice treated with PBS or Hf-MOL with or without anti-PD-L1 was collected, weighted and ground through the cell strainers to get single cell suspensions. Splenocytes were then counted by hemocytometer. The images (c) and weights (d) of spleens from as-treated groups. (e) The numbers of splenocytes. (f) gMDSCs with respect to the total splenocytes. Data are expressed as means ± s.d., n = 6. *P < 0.05, **P < 0.01 and ***P < 0.001 by t-test. Central lines, bounds of box and whiskers represent mean values, 25% to 75% of the range of data and 1.5 fold of interquartile range away from outliers, respectively. Reprinted with permission from *Matter*, **2019**, *1*, 1331-1353. Copyright 2019 Elsevier Inc.

4.3 Discussion

Tumor metastasis is one of the major reasons for the failure of cancer management in the clinic.[6-8] Significant current efforts are focused on developing combination therapies that synergize local cancer treatment with systemic anti-metastasis efficacy.[9-13] We used the highly metastatic murine triple-negative breast cancer model 4T1 to evaluate anti-metastasis efficacy of Hf-MOL-enabled RT-RDT. MDSCs are known to play a significant role on tumor progression and metastasis. It is thus logical to develop anti-metastasis therapeutics by targeting MDSCs.[14-15] We observed ubiquitous spleen enlargement in the groups with poor therapeutic efficacy but no spleen enlargement in the Hf-MOL(+)/α-PD-L1 group. Similar spleen enlargement was reported for late stages of 4T1 model in several studies,[16-17] and a recent study established the correlation between spleen enlargement and tumor metastasis.[18] Significant increase of gMDSCs in both bone marrow and spleen leads to pulmonary infiltration of gMDSCs to then enhance MET process and facilitate the formation of metastatic niches. In the meanwhile, the increase of infiltrated mMDSCs in primary tumor site induces epithelial–mesenchymal transition (EMT) process to facilitate tumor cell dissemination. We found the link between the lack of spleen enlargement and the decrease of gMDSC populations in the spleen, bone marrow, and lung, which is correlated with significantly reduced lung metastasis and better prognosis.

4.4 Conclusion

In this work, we have designed a novel ultrathin based on electron-dense SBUs and photosensitizing ligands for effective RT-RDT with low dose X-rays by taking advantage of enhanced ROS diffusion. The synergistic combination of Hf-MOL-enabled RT-RDT and immune checkpoint inhibitors led to superb anti-tumor efficacy on bilateral models of colon, head and neck, and breast cancers and significant anti-metastatic effects on an orthotopic model of lung-metastatic triple-negative breast cancer. This combination extends the local therapeutic effects of RT-RDT to distant tumors *via* systemic antitumor immunity and inhibits metastasis by re-activating T cells and inhibiting immunosuppressive MDSCs in both orthotopic tumors and metastatic lung lesions. Rational tuning of MOL compositions and structures promises to lead to even more potent RT-RDT to potentiate CBI for the treatment of metastatic tumors.

4.5 Methods

Materials, cell lines, and animals: All of the starting chemicals were purchased from Sigma-Aldrich and Fisher (USA), unless otherwise noted, and used without further purification.

Murine triple-negative breast cancer cell line 4T1 was kindly provided by Dr. Stephen J. Kron at University of Chicago Murine colon adenocarcinoma cell CT26 and murine squamous cell carcinoma SCC VII were purchased from the American Type Culture Collection (Rockville, MD, USA). CT26 cells was cultured in Roswell Park Memorial Institute (RPMI) 1640 medium (GE Healthcare, USA). 4T1 and SCC VII cells were cultured in Dulbecco's Modified Eagle's Medium (DMEM) medium (GE Healthcare, USA). All media were supplemented with 10% FBS, 100 U/mL penicillin G sodium and 100 μg/mL streptomycin sulfate. Cells were cultured in a humidified atmosphere containing 5% CO_2 at 37ºC. Mycoplasma was tested before use by MycoAlert detection kit (Lonza Nottingham, Ltd.) BALB/c mice (6-8 weeks) and C3H mice (6-8 weeks) were obtained from Harlan-Envigo Laboratories, Inc (USA). The study protocol was reviewed and approved by the Institutional Animal Care and Use Committee (IACUC) at the University of Chicago.

Synthesis of Hf-MOL: To a 1-dram glass vial was added 0.5 mL of $HfCl_4$ solution [2 mg/mL in N,N-dimethylformamide (DMF)], 0.5 mL of the H_2DBP solution (3.5 mg/mL in DMF), 55 μL acetic acid and 5 μL of H_2O. The reaction mixture was kept in a 80 °C oven for 2 days. The purple precipitate was collected by centrifugation and washed with DMF, 1% triethylamine in ethanol (v/v), and ethanol.

Clonogenic assay: The clonogenic assay was performed according to a modified protocol. 4T1 cells were cultured in a 6-well plate overnight and incubated with particles at a Hf concentration

of 20 μM for 4 h followed by irradiation with 0, 1, 2, 4, 8 and 16 Gy X-ray or γ- ray . Cells were trypsinized and counted immediately. 200-2000 cells were seeded in a 6-well plate and cultured with 2 mL medium for 15 days. Once colony formation was observed, the culture medium was discarded. The plates were rinsed twice with PBS, then stained with 500 μL of 0.5% w/v crystal violet in 50% methanol/H_2O. The wells were rinsed with water for three times and the colonies were counted manually.

Apoptosis/necrosis: 4T1 cells were cultured in a 6-well plate overnight and incubated with PBS, Hf-DBA, H_2DBP, or Hf-MOL at an equivalent concentration of 20 μM for 4 h followed by irradiation at 0 and 2 Gy X-ray. 24 h later, the cells were stained according to the AlexaFluor 488 Annexin V/dead cell apoptosis kit (Life technology, USA) and quantified by flow cytometry.

DNA damage: 4T1 cells were cultured in a 6-well plate overnight and incubated with PBS, Hf-DBA, H_2DBP, or Hf-MOL at an equivalent concentration of 20 μM for 4 h followed by irradiation at 0 and 2 Gy X-ray. Cells were stained 6 h after irradiation with the HCS DNA damage kit (Life Technology, USA) for confocal laser scanning microscopy (CLSM, FV1000, Olympus, Japan) and flow cytometry.

Transwell invasion: 4T1 cells were cultured in a 6-well plate overnight and incubated with PBS, Hf-DBA, H_2DBP, or Hf-MOL at an equivalent concentration of 20 μM for 4 h followed by irradiation with 0 or 2 Gy X-ray. The cells were collected, washed three times with PBS, and then adjusted to a concentration of 2×10^5 cells/mL in serum-free medium. 200mL of the cell suspension was seeded onto the upper chamber of a Millicell Cell Culture Insert with 8.0 mm pores (Millipore, USA). The lower chamber contained 1 mL medium with 10% FBS. After 24 h, the non-invading cells on the upper surface were removed with a cotton swab and the invading cells

on the lower surface were fixed with 4% paraformaldehyde and stained with 0.1% crystal violet. The invading cells were observed and photographed under an Axioskop inverted microscope (Zeiss, Germany) at 10× magnification.

Immunogenic cell death: 4T1 cells were cultured in a 6-well plate overnight and incubated with PBS, Hf-DBA, H_2DBP, or Hf-MOL at an equivalent concentration of 20 μM for 4 h followed by irradiation with 0 or 2 Gy X-ray. After incubation for 4 h, supernatant was harvested for extracellular HMGB-1 and ATP secretion assayed by HMGB-1 ELISA kit (Invitrogen, USA) and Chemiluminescence ATP Determination kit (Thermo Fisher, USA), respectively. The cells were washed three times with PBS, fixed with 4% paraformaldehyde, incubated with AlexaFluor 488-CRT (Enzo Life Sciences, USA) with 1: 100 dilution for 2 h, stained with DAPI, and observed by CLSM, or collected, incubated with AlexaFluor 488-CRT antibody for 2 h, and then stained with PI for analysis by flow cytometry (LSRFortessa, BD, USA).

Vaccination: 4T1 cells were cultured in a 3.5-cm dish overnight and incubated with Hf-MOL at an Hf concentration of 20 μM for 4 h followed by irradiation 4 Gy X-ray. After incubation for 48 h, cells were harvested and injected subcutaneously as vaccine. Mice injected with same amount of PBS serves as control. 7 days after vaccination, mice were challenged with live 4T1 cells.

Abscopal Effect: Three synergistic bilateral tumor models, 4T1, CT26 and SCC VII were established to evaluate the in vivo anti-cancer efficacy of combination of Hf-MOL-enabled RT-RDT and CBI. For 4T1, 1×10^6 and 5×10^5 4T1 cells were subcutaneously inoculated onto the right and left flanks of BALB/c mice for respective primary and secondary tumors. For CT26, 2×10^6 and 1×10^6 CT26 cells were subcutaneously inoculated onto the right and left flanks of BALB/c mice for respective primary and secondary tumors. For SCCVII, 1×10^6 and 2×10^5 SCC VII cells

were by subcutaneously inoculated onto the right and left flanks of C3H mice for respective primary and secondary tumors. When the primary tumors reached 100-150 mm^3 in volume, mice were injected intratumorally with Hf-MOL at a dose of 0.2 μmol Hf or PBS. 12 h after injection, mice were anaesthetized with 2% (v/v) isoflurane and the primary tumors were irradiated with 0.5 or 1 Gy X-ray/fraction for a total of 8 or 10 daily fractions. Antibodies (α-PD-L1, Clone: 10F.9G2; α-PD-1, Clone: RMP1-14; α-CTLA-4, Clone: 9D9, all from BioXCell) were given every three days by intraperitoneal injection at a dose of 75 μg/mouse. The tumor sizes were measured daily with a caliper where tumor volume equals (width2 × length)/2. Mice with 4T1, CT26 or SCCVII were sacrificed on Day 27, 19 or 22, respectively.

T/B cell depletion: The bilateral subcutaneous model was established as for the in vivo anti-cancer efficacy. When the primary tumors reached 100-150 mm^3 in volume, mice were injected intratumorally with nMOFs at a dose of 0.11 mg/mouse or PBS. Anti-CD4 (GK1.5, BioXCell, USA), anti-CD8 (OKT-8, BioXCell, USA), mouse IgG (C1.18.4, BioXCell, USA) antibodies Or B cell inhibitor ibrutinib (PCI-32765, Selleckchem) were intraperitoneally injected into the mice (200 μg/mouse) on Day 0 and 5 after the first treatment. Twelve hours post-injection, mice were anesthetized with 2% (v/v) isoflurane, and tumors were irradiated with X-ray at 225 kVp and 13 mA with a 0.3-mm Cu filter.

Tumor challenge studies: On day 50 post tumor inoculation, mice were challenged with 2×10^6 cells on the contralateral flank. Healthy mice were simultaneously inoculated as control. The mice were sacrificed when the tumors of the control mice reached 2 cm^3.

ELISpot assay: Tumor-specific immune responses to IFN-γ was measured *ex vitro* by ELISpot assay (Mouse IFN gamma ELISPOT Ready-SET-Go!®; Cat. No. 88-7384-88; eBioscience). A

4T1 cells were irradiated with X-ray irradiator at a dose of 50 Gy to expose tumor-specific antigen. Millipore Multiscreen HTS-IP plates was coated overnight at 4°C with anti-Mouse IFN-γ capture antibody. Single-cell suspensions of splenocytes were obtained from 4T1 tumor-carrying mice and seeded onto the antibody-coated plate at a concentration of 2×10^5 cells/well. Cells were incubated with or without antigen-exposed 4T1 cell stimulation (1×10^4 cells per well) for 42 h at 37 °C and then discarded. The plate was then incubated with biotin-conjugated anti-IFN-γ detection antibody at room temperature (r.t.) for 2 h, followed by incubation with Avidin-HRP for 2 h at r.t. 3-amino-9-ethylcarbazole substrate solution (Sigma, Cat. AEC101) was added for cytokine spot detection. Spots were imaged and quantified with a CTL ImmunoSpot Analyzer (Cellular Technology Ltd, USA).

Flow Cytometry: Tumors were harvested, treated with 1 mg/mL collagenase I (Gibco™, USA) for 1 h, and ground by the rubber end of a syringe. Cells were filtered through nylon mesh filters with size of 40 μm and washed with PBS. tumor-draining lymph nodes were collected and directly ground through the cell strainers. The single-cell suspension was incubated with anti-CD16/32 (clone 93) to reduce nonspecific binding to FcRs. Cells were further stained with the following fluorochrome-conjugated antibodies: CD45 (30-F11), TCRβ (H57-597), CD4 (GK1.5), CD8 (53-6.7), Foxp3 (FJK-16s), CD25 (PC61.5), Nkp46 (29A1.4), F4/80 (BM8), B220 (RA3-6B2), CD11b (M1/70), Ly6C (HK1.4), Ly6G (RB6-8C5) and yellow-fluorescent reactive dye (all from eBioscience). Antibodies were used with the dilution of 1: 200. Representative gating strategies for different immune cells are shown in **Figure 4-19**. LSR Fortessa (BD Biosciences) was used for cell acquisition and data analysis was carried out with FlowJo software (Tree Star, Ashland, OR).

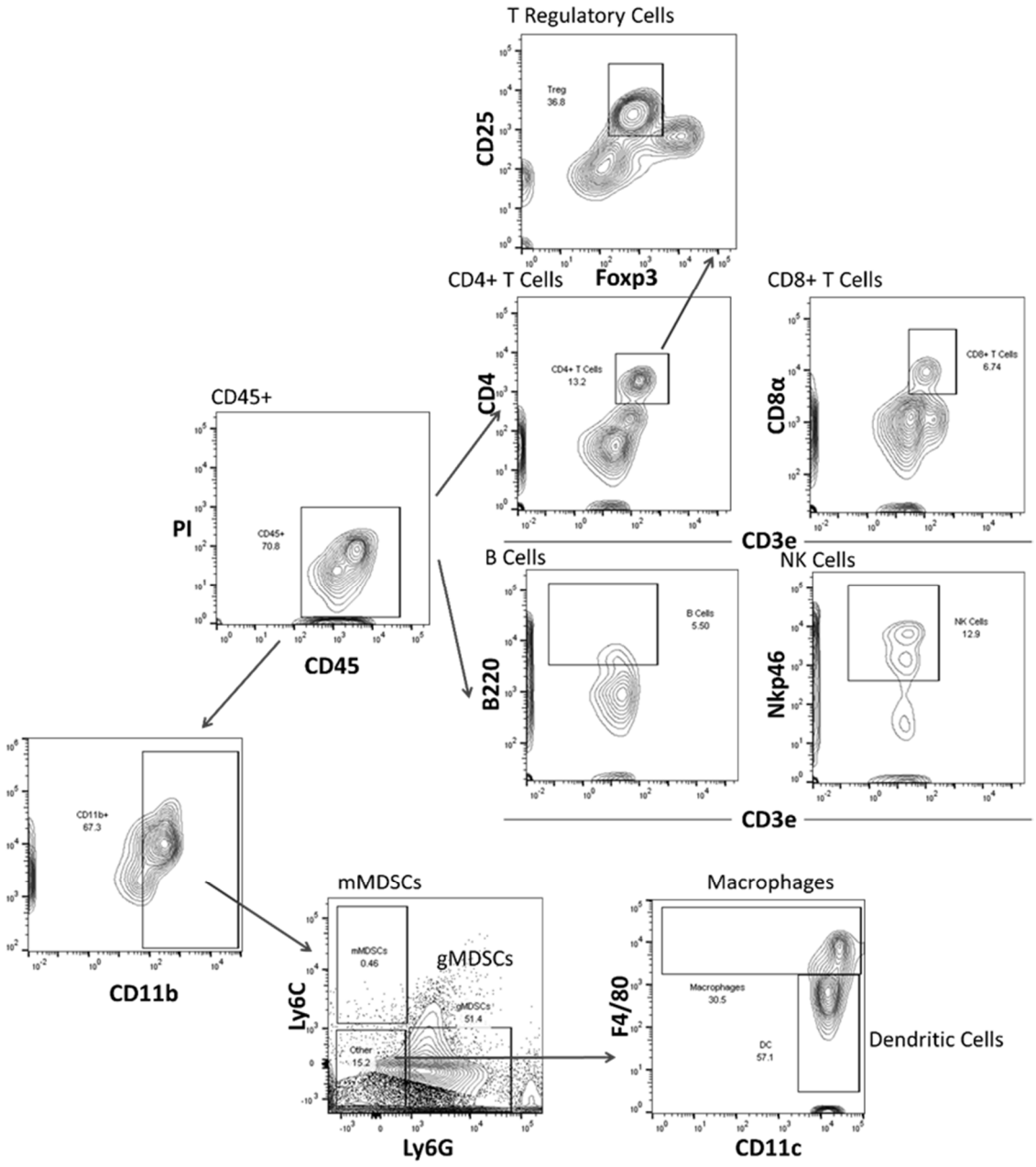

Figure 4-19 Representative gating strategies for $CD45^+$ cells, $CD4^+$ T cells, $CD8^+$ T cells, T regulatory cells, B cells, NK cells, mMDSCs, gMDSCs, dendritic cells and macrophages. Reprinted with permission from *Matter*, **2019**, *1*, 1331-1353. Copyright 2019 Elsevier Inc.

***In vivo* anti-metastasis effect:** Orthotopic 4T1 model was established by inoculating 4T1 cells into the mammary fat pads of BALB/c mice. When the primary tumors reached 100-150 mm^3 in

volume, mice were injected intratumorally with Hf-MOL at a dose of 0.2 μmol Hf or PBS. 12 h after injection, mice were anaesthetized with 2% (v/v) isoflurane and the orthotopic tumors were irradiated with 0.5 Gy X-ray/fraction for a total of 10 daily fractions. Antibodies were given every three days by intraperitoneal injection at a dose of 75 μg/mouse. Body weights and tumor volumes were monitored and recorded over a period of 24 days. At the end of experiment, mice were sacrificed, and tumors were excised, weighed and photographed. Lungs were also harvested, observed for the gross examination of tumor nodules, or sectioned and stained with H&E for quantification of metastasis area, or digested with collagenase type IV/elastase cocktail and cultured with 60 μM 6-thiogunine for 10 days. The colonies formed by clonogenic metastatic cancer cells were then fixed with methanol and stained with 0.1% crystal violet. For quantification, the crystal violet stained colonies were dissolved with 10% acetic acid and their absorbance at 590 nm was measured and normalized to the PBS control group.

4.6 References

1. Lan, G.; Ni, K.; Xu, R.; Lu, K.; Lin, Z.; Chan, C.; Lin, W., Nanoscale metal–organic layers for deeply penetrating X-ray-induced photodynamic therapy. *Angewandte Chemie International Edition* **2017,** *129* (40), 12270-12274.

2. Lan, G.; Ni, K.; Veroneau, S. S.; Song, Y.; Lin, W., Nanoscale metal–organic layers for radiotherapy–radiodynamic therapy. *Journal of the American Chemical Society*. **2018,** *140* (49), 16971-16975.

3. Lu, K.; He, C.; Guo, N.; Chan, C.; Ni, K.; Lan, G.; Tang, H.; Pelizzari, C.; Fu, Y.-X.; Spiotto, M. T., Low-dose X-ray radiotherapy–radiodynamic therapy *via* nanoscale metal–organic frameworks enhances checkpoint blockade immunotherapy. *Nature Biomedical Engineering* **2018,** *2* (8), 600.

4. Ye, Y.; Wang, C.; Zhang, X.; Hu, Q.; Zhang, Y.; Liu, Q.; Wen, D.; Milligan, J.; Bellotti, A.; Huang, L., A melanin-mediated cancer immunotherapy patch. *Science Immunology* **2017,** *2*, 5692.

5. Ouzounova, M.; Lee, E.; Piranlioglu, R.; El Andaloussi, A.; Kolhe, R.; Demirci, M. F.; Marasco, D.; Asm, I.; Chadli, A.; Hassan, K. A., Monocytic and granulocytic myeloid derived suppressor cells differentially regulate spatiotemporal tumour plasticity during metastatic cascade. *Nature Communications* **2017,** *8*, 14979.

6. Lee, A.; Djamgoz, M. B., Triple negative breast cancer: emerging therapeutic modalities and novel combination therapies. *Cancer Treatment Reviews* **2018,** *62*, 110-122.

7. Pereira, E. R.; Kedrin, D.; Seano, G.; Gautier, O.; Meijer, E. F.; Jones, D.; Chin, S.-M.; Kitahara, S.; Bouta, E. M.; Chang, J., Lymph node metastases can invade local blood vessels, exit the node, and colonize distant organs in mice. *Science* **2018,** *359* (6382), 1403-1407.

8. Duan, X.; Chan, C.; Guo, N.; Han, W.; Weichselbaum, R. R.; Lin, W., Photodynamic therapy mediated by nontoxic core–shell nanoparticles synergizes with immune checkpoint blockade to elicit antitumor immunity and antimetastatic effect on breast cancer. *Journal of the American Chemical Society* **2016,** *138* (51), 16686-16695.

9. Zhai, Y.; Ran, W.; Su, J.; Lang, T.; Meng, J.; Wang, G.; Zhang, P.; Li, Y., Traceable bioinspired nanoparticle for the treatment of metastatic breast cancer *via* NIR-trigged intracellular delivery of methylene blue and cisplatin. *Advanced Materials* **2018,** *30* (34), 1802378.

10. Wang, C.; Wang, J.; Zhang, X.; Yu, S.; Wen, D.; Hu, Q.; Ye, Y.; Bomba, H.; Hu, X.; Liu, Z., In situ formed reactive oxygen species–responsive scaffold with gemcitabine and checkpoint inhibitor for combination therapy. *Science Translational Medicine* **2018,** *10* (429), 3682.

11. Bourgeois-Daigneault, M.-C.; Roy, D. G.; Aitken, A. S.; El Sayes, N.; Martin, N. T.; Varette, O.; Falls, T.; St-Germain, L. E.; Pelin, A.; Lichty, B. D., Neoadjuvant oncolytic virotherapy before surgery sensitizes triple-negative breast cancer to immune checkpoint therapy. *Science Translational Medicine* **2018,** *10* (422), 1641.

12. Chiang, C.-S.; Lin, Y.-J.; Lee, R.; Lai, Y.-H.; Cheng, H.-W.; Hsieh, C.-H.; Shyu, W.-C.; Chen, S.-Y., Combination of fucoidan-based magnetic nanoparticles and immunomodulators enhances tumour-localized immunotherapy. *Nature Nanotechnology* **2018,** *13* (8), 746-754.

13. Su, L.; Li, R.; Khan, S.; Clanton, R.; Zhang, F.; Lin, Y.-N.; Song, Y.; Wang, H.; Fan, J.; Hernandez, S., Chemical design of both a glutathione-sensitive dimeric drug guest and a glucose-derived nanocarrier host to achieve enhanced osteosarcoma lung metastatic anticancer selectivity. *Journal of the American Chemical Society* **2018,** *140* (4), 1438-1446.

14. Condamine, T.; Ramachandran, I.; Youn, J.-I.; Gabrilovich, D. I., Regulation of tumor metastasis by myeloid-derived suppressor cells. *Annual Review of Medicine* **2015,** *66*, 97-110.

15. Toor, S. M.; Elkord, E., Therapeutic prospects of targeting myeloid-derived suppressor cells and immune checkpoints in cancer. *Immunology and Cell Biology* **2018,** *96* (9), 888-897.

16. Hu, Q.; Sun, W.; Wang, J.; Ruan, H.; Zhang, X.; Ye, Y.; Shen, S.; Wang, C.; Lu, W.; Cheng, K., Conjugation of haematopoietic stem cells and platelets decorated with anti-PD-1 antibodies augments anti-leukaemia efficacy. *Nature Biomedical Engineering* **2018,** *2* (11), 831-840.

17. Tao, K.; Fang, M.; Alroy, J.; Sahagian, G. G., Imagable 4T1 model for the study of late stage breast cancer. *BMC Cancer* **2008,** *8* (1), 228.

18. Ouzounova, M.; Lee, E.; Piranlioglu, R.; El Andaloussi, A.; Kolhe, R.; Demirci, M. F.; Marasco, D.; Asm, I.; Chadli, A.; Hassan, K. A., Monocytic and granulocytic myeloid derived suppressor cells differentially regulate spatiotemporal tumour plasticity during metastatic cascade. *Nature Communications* **2017,** *8* (1), 1-13.

CHAPTER 5. Nanoscale Metal-Organic Frameworks Mediate Radiotherapy-Radiodynamic Therapy and Deliver CpG Oligodeoxynucleotides to Enhance Antigen Presentation and Cancer Immunotherapy

5.1 Rationale for the project design

In previous Chapters, we report the strategies to enhance nMOF-mediated radiotherapy (RT) by optimizing Hf-oxo based SBUs and nMOF-mediated radiotherapy-radiodynamic therapy (RT-RDT) by assembling Hf-SBUs with photosensitizing ligands to promote local inflammation *via* generating reactive oxygen species (ROS). nMOF-mediated immunogenic local treatment as X-ray-induced *in situ* cancer vaccination can generate danger-associated molecular patterns (DAMPs) and tumor antigens to further synergize with CBI, attenuating T cell exhaustion, to awaken systemic anti-tumor immunity.

Besides immunogenic local treatment, stimulation of dendritic cells (DCs) with immunoadjuvants such as stimulator of interferon genes (STING) agonist[1-3] or CpG oligodeoxynucleotides further promotes antigen presentation and immune responses[4]. Naturally existing as microbial DNAs known as pathogen-associated molecular patterns (PAMPs), CpGs are short DNA strands explored widely as vaccine adjuvants for toll-like receptor 9 (TLR9) stimulation, DC maturation, antigen presentation, and the priming of tumor-specific cytotoxic T lymphocytes (CTL)[5]. In addition, antigen presentation by immature DCs in the absence of immunoadjuvants induces tolerance rather than stimulates an immune reaction[6]. In particular, class C CpGs enhance Type I interferon (IFN) production to activate DCs and stimulate B cells, which in turn upregulates co-stimulatory molecules and secretes pro-inflammatory cytokines to afford

superb anticancer effects[7-8]. However, even locally administrated CpGs are prone to enzymatic degradation and cannot be efficiently internalized by APCs due to their anionic nature[9].

In this Chapter, we designed two cationic nMOFs, Hf-DBB-Ir and Hf-DBB^{F}-Ir to release DAMPs and tumor antigens *via* X-ray activated RT-RDT and to deliver class C CpGs *via* electrostatic interactions. Activated by X-rays, the *in situ* vaccination afforded by nMOFs effectively expand cytotoxic T cells in tumor-draining lymph nodes to reinvigorate the adaptive immune system for tumor regression (**Figure 5-1**). The local therapeutic effects of the nMOF-based *in situ* vaccines were extended to distant tumors by combination treatment with an anti-PD-L1 antibody to afford an 83.3% cure rate on an MC38 colorectal cancer model.

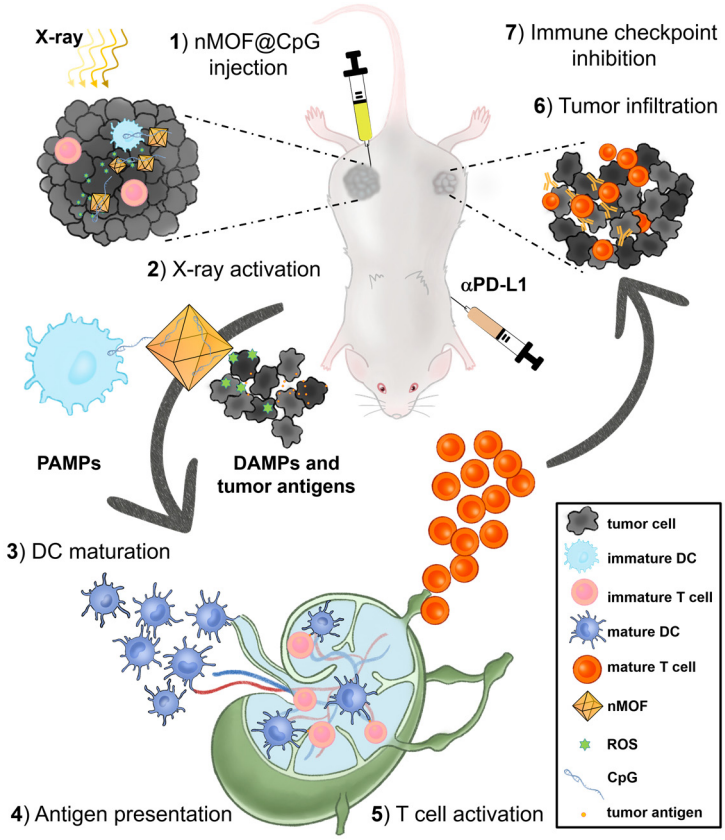

Figure 5-1 Illustration of anti-tumor effect of *in situ* cancer vaccination *via* nMOFs plus CBI. (1) Hf-DBB^{F}-Ir@CpG was intratumourally administrated in the primary tumor. (2) Upon X-

Figure 5-1, continued ray activation, Hf-DBB^F-Ir generate ROSs to induce immunogenic cell death to expose tumor antigens and DAMPs, while CpG as PAMPs deliver to antigen presenting cells assisted by cationic Hf-DBB^F-Ir. (3) DAMPs and PAMPs promote DC maturation. (4) Tumor antigens are presented by mature DCs onto T cell in tumor-draining lymph nodes. (5) T cells are expanded and primed to the distant tumor as well as the primary tumor. (6) Systemically administrated immune checkpoint blockade inhibitor αPD-L1 attenuates T cell exhaustion.

5.2 Results

5.2.1 Synthesis and characterization of nMOFs

Scheme 5-1 Synthesis routes of DBB^F-Ir and DBB-Ir.

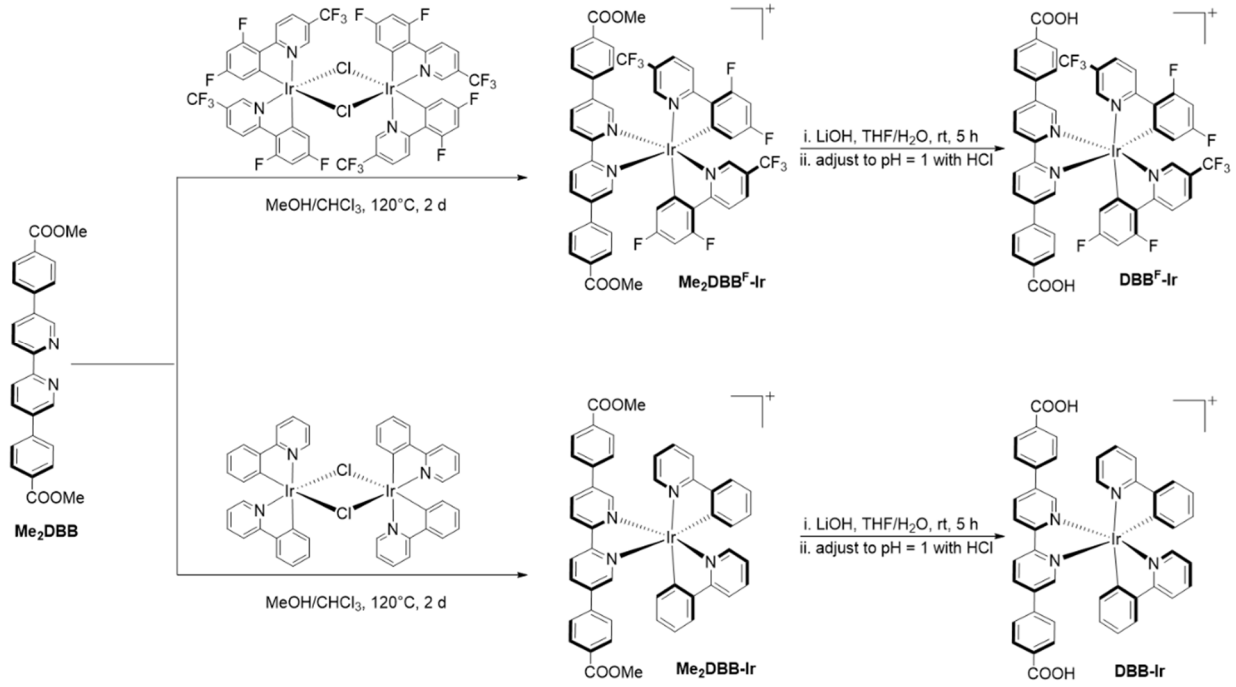

To generate DAMPs and tumor antigens through RT-RDT and deliver PAMPs with high CpG loading, we designed two cationic photosensitizing DBB^F-Ir and DBB-Ir ligands (**Scheme 5-1**) to assemble with high-Z metal Hf_6 SBUs to generate two positively charged nMOFs, Hf-DBB^F-Ir and Hf-DBB-Ir, respectively. Hf-DBB^F-Ir and Hf-DBB-Ir nMOFs possessed UiO-like structures

(**Figure 5-2f**) with a formula of $Hf_6(\mu_3\text{-}O)_4(\mu_3\text{-}OH)_4L_6$, where L = DBB^F-Ir or DBB-Ir. Hf-DBB^F-Ir and Hf-DBB-Ir exhibited spherical to octahedral morphologies with diameters of ~100 nm, as revealed by transmission electron microscopy (TEM) imaging (**Figure 5-2a-d**) and dynamic light scattering (DLS) measurements (**Figure 5-2e**). The photosensitizing characteristics of Hf-DBB^F-Ir and Hf-DBB-Ir were confirmed by UV-Vis absorption and luminescence spectroscopy (**Figure 5-3**), where Hf-DBB^F-Ir and Hf-DBB-Ir showed similar absorbance and luminescence to those of DBB^F-Ir and DBB-Ir, respectively.

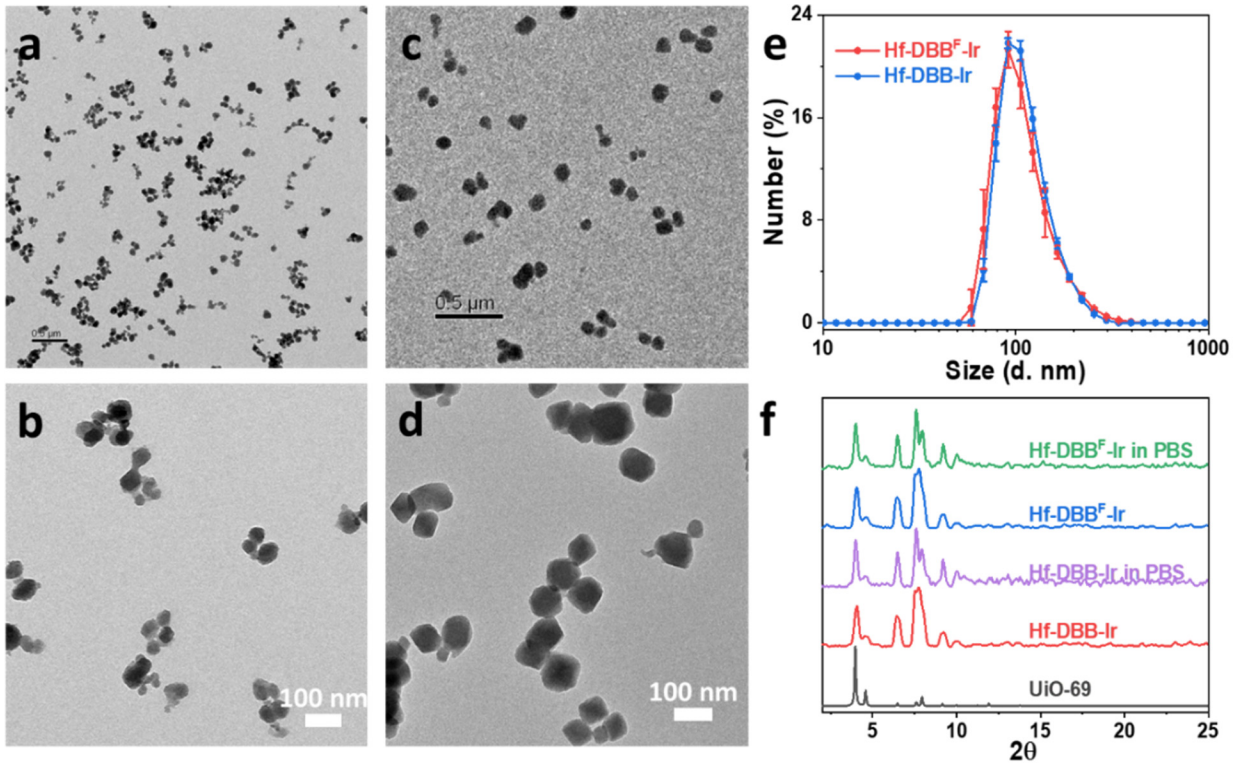

Figure 5-2 Large-area TEM images and small-area TEM images of Hf-DBB-Ir (a,b) and Hf-DBB^F-Ir (c,d), respectively. Hf-DBB^F-Ir@CpG (C & D). (e) Number-averaged diameters of Hf-DBB^F-Ir (112.2 ± 2.8 nm) and Hf-DBB-Ir (113.9 ± 1.6 nm) in EtOH. (f) PXRD patterns of Hf-DBB^F-Ir and Hf-DBB-Ir, freshly prepared or after 24 h incubation in 0.6 mM PBS, in comparison to that of UiO-69.[10] Scale bar = 500 nm (a,c) or 100 nm (b,c).

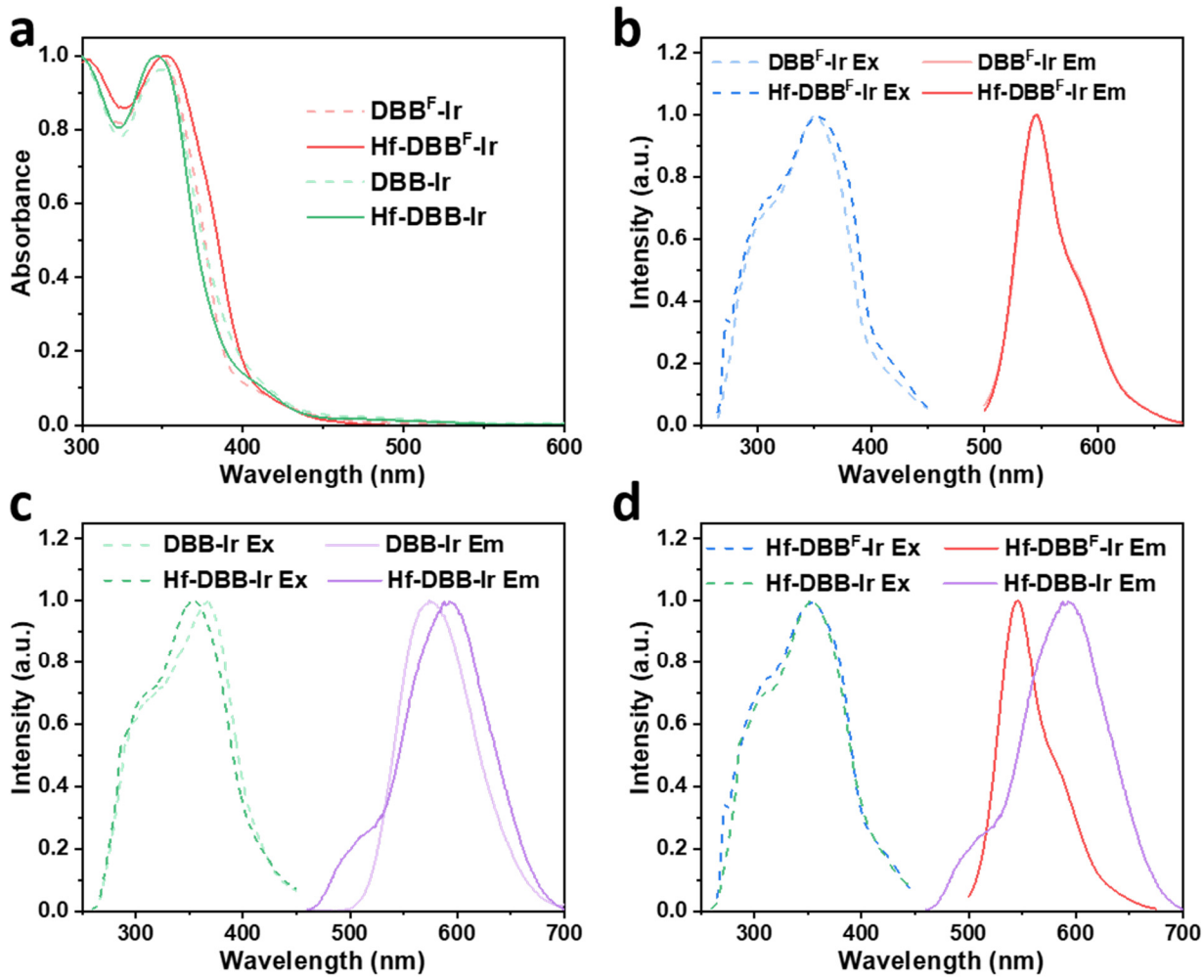

Figure 5-3 (a) UV-Vis spectra of Hf-DBB^F-Ir and Hf-DBB-Ir, in comparison to those of H_2DBB^F-Ir and H_2DBB-Ir, respectively. Excitation and emission spectra of Hf-DBB^F-Ir (b) and Hf-DBB-Ir (c), in comparison to those of H_2DBB^F-Ir and H_2DBB-Ir, respectively. (d) Excitation and emission spectra of Hf-DBB^F-Ir and Hf-DBB-Ir.

5.2.2 ROS generation

We proposed that photosensitizing Hf-DBB^F-Ir and Hf-DBB-Ir could generate multiple reactive oxygen species (ROS) upon X-ray irradiation, including $^{\bullet}$OH through water radiolysis of Hf_6 SBUs, and $^1O_2$ and O_2^- through excitation of photosensitizing ligands (**Scheme 5-2**).

Scheme 5-2 Schematic showing synthesis of Hf-DBB-Ir and Hf-DBB^{F}-Ir nMOFs based on Hf-oxo clusters and DBB^{F}-Ir or DBB-Ir ligands, respectively. Upon X-ray irradiation, Hf-oxo clusters absorb X-ray to generate $^{\bullet}$OH through radiolysis and transfer energy to adjacent photosensitizing ligands to generate $^{1}O_2$ and/or O_2^{-}.

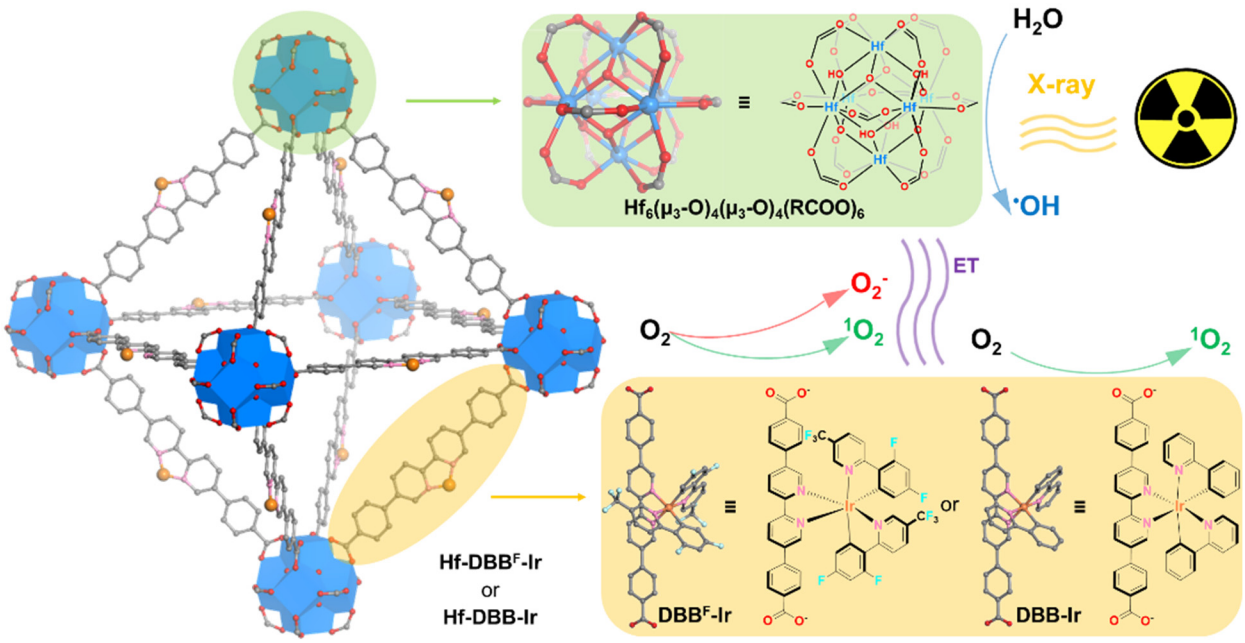

As quantified by APF and SOSG assays, both Hf-DBB^{F}-Ir plus X-ray irradiation [denoted Hf-DBB^{F}-Ir(+)] and Hf-DBB-Ir(+) exhibited significantly enhanced $^{\bullet}$OH and $^{1}O_2$ generation in comparison to their ligand controls (**Figure 5-4a-d**). However, only Hf-DBB^{F}-Ir(+) displayed efficient O_2^{-} generation as determined by BMPO assay, which is ascribed to the higher reduction potential of DBB^{F}-Ir than DBB-Ir (**Figure 5-4e**).[11]

Prior to detect ROS generation *in vitro*, we first evaluated the uptake of Hf-DBB-Ir and Hf-DBB^{F}-Ir by MC38 cells. Inductively coupled plasma-mass spectrometry (ICP-MS) studies showed the two nMOFs reached similar intracellular Hf levels after 4 h incubation (**Figure 5-5**). We then probed *in vitro* $^{1}O_2$ and O_2^{-} generation by SOSG and superoxide assay kits, respectively. Both Hf-DBB-Ir(+) and Hf-DBB^{F}-Ir(+) induced strong green fluorescence, indicating significant $^{1}O_2$ generation. However, only Hf-DBB^{F}-Ir (+) exhibited strong red fluorescence, indicating the

generation of O_2^- through Hf-DBB^F-Ir-mediated RT-RDT process (**Figure 5-6**). To confirm the RT effect, $^{\bullet}$OH induced DNA double-strand breaks (DSBs) were quantified by flow cytometric analysis of phosphorylated γ-H2AX in cells treated with PBS, ligands or nMOFs with or without X-ray. Interestingly, 2 h after irradiation, significantly higher red γ-H2AX fluorescence was observed in the group treated with Hf-DBB^F-Ir(+) than Hf-DBB-Ir(+), likely due to the biotransformation O_2^- to $^{\bullet}$OH by superoxidase dismutase. No fluorescence was observed in the groups without X-ray irradiation or without nMOF incubation (**Figure 5-7**).

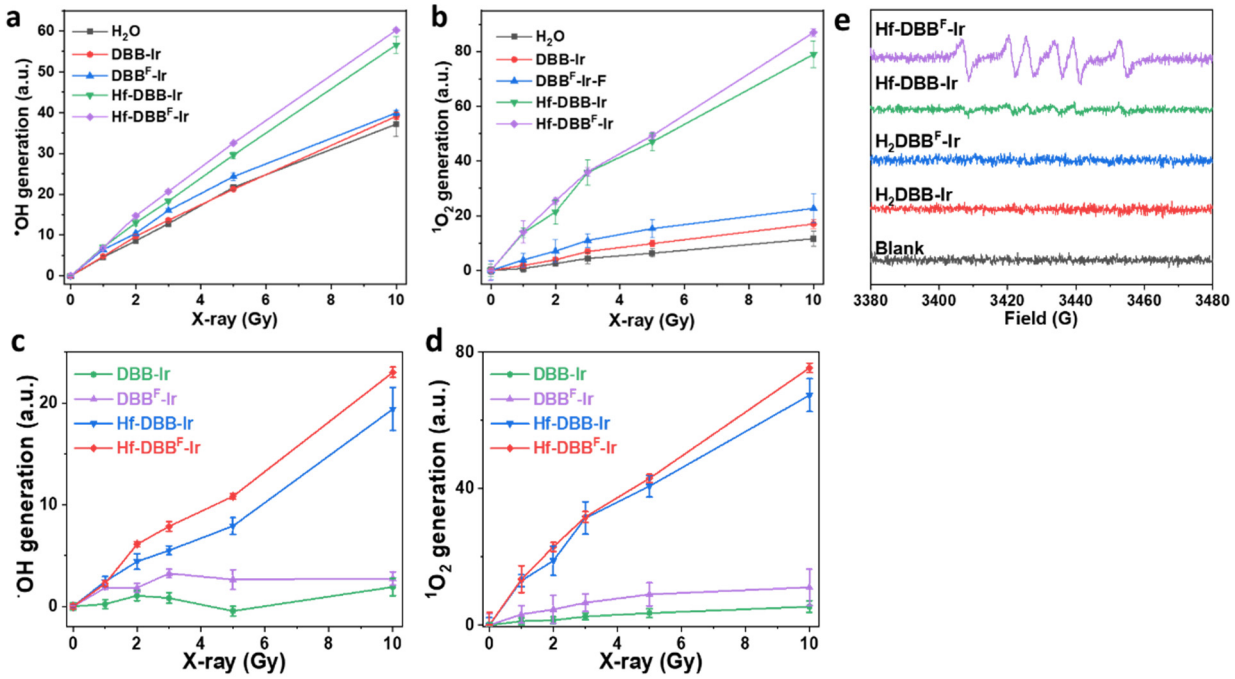

Figure 5-4 $^{\bullet}$OH generation determined by APF assay (a,c), $^1O_2$ generation determined by SOSG assay (b,d), and O_2^- generation probed by BMPO in EPR (e) of H_2O, DBB-Ir, DBB^F-Ir, Hf-DBB-Ir, and Hf-DBB^F-Ir.

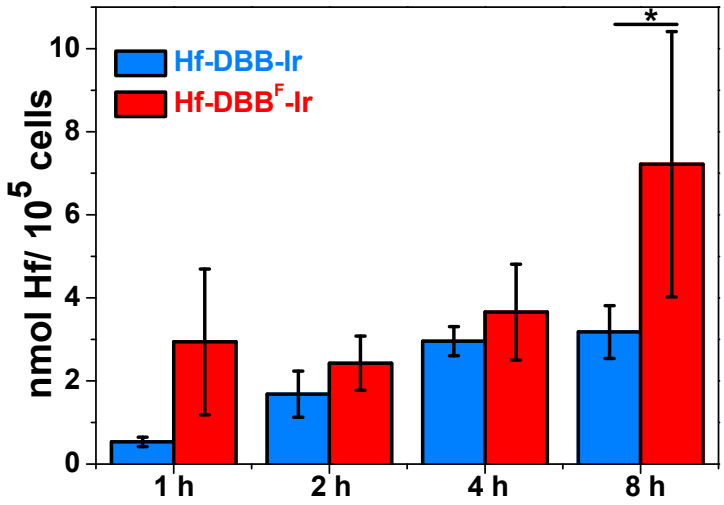

Figure 5-5 Cellular uptake of Hf-DBB-Ir and Hf-DBB^F-Ir on MC38 cells after incubation with 20 μM Hf, n = 3. The Hf concentrations were determined by ICP-MS.

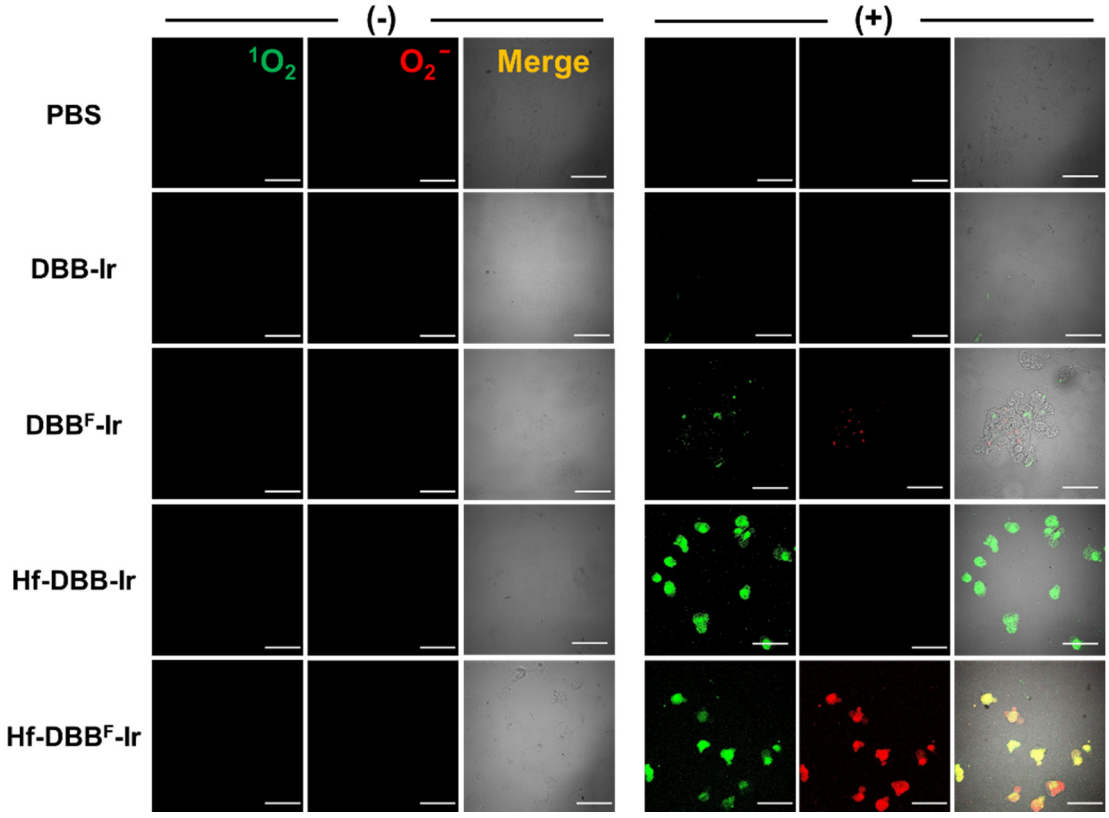

Figure 5-6 Generation of $^1O_2$ and O_2^- in MC38 cells treated with PBS, DBB-Ir, DBB^F-Ir, Hf-DBB-Ir, or Hf-DBB^F-Ir with (+) or without (-) X-ray irradiation as detected by SOSG and superoxide kits. Green ($^1O_2$) and red (O_2^-) florescence merged to appear as yellow florescence. Scale bar = 50 μm.

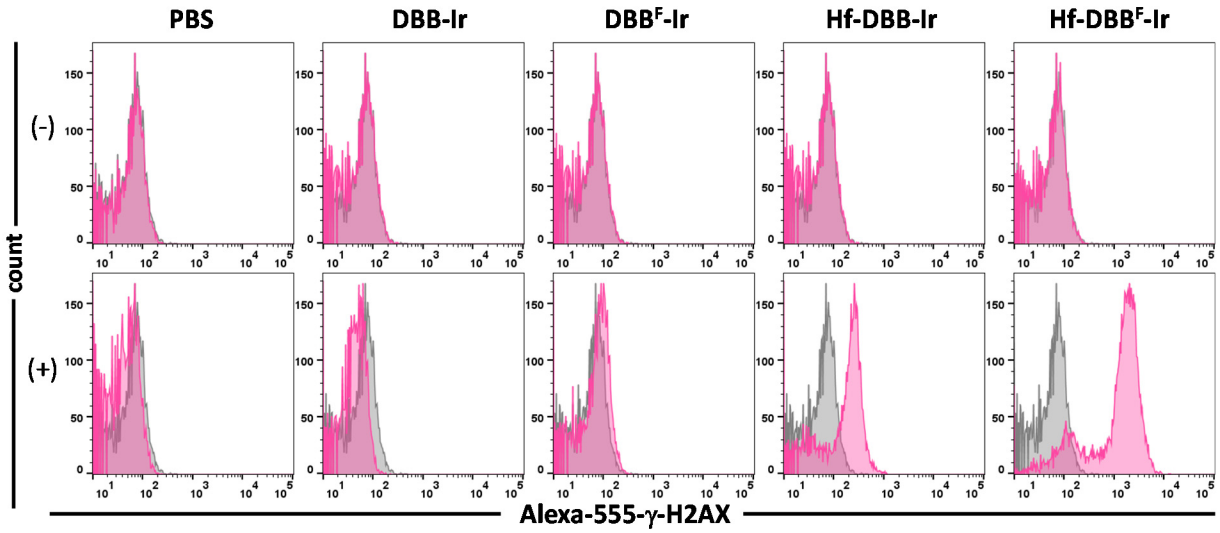

Figure 5-7 Flow cytometric analysis of DNA double strain breaks (DSBs) probed by γ-H2AX in MC38 cells treated with PBS, H_2DBB-Ir, H_2DBB^F-Ir, Hf-DBB-Ir, or Hf-DBB^F-Ir for 4 h and then irradiated upon X-ray at a dose of 0 (-) or 2 (+) Gy. Grey histogram (control), and carmine histogram show the difference of γ-H2AX level in the cells, respectively.

5.2.3 Release of DAMPs and *in vitro* immunogenicity

To test the hypothesis that the myriad of ROSs generated by Hf-DBB^F-Ir damages cancer cells more effectively than other treatments, we evaluated Hf-DBB^F-Ir mediated cell damage and DAMP generation. Clonogenic assays showed that Hf-DBB^F-Ir(+) slightly outperformed Hf-DBB-Ir(+) with an REF_{10} value of 1.75 vs 1.68 (**Figure 5-8a**). MTS assays further showed that Hf-DBB^F-Ir(+) exhibited higher cytotoxicity than Hf-DBB-Ir(+) with IC_{50} values of 4.28 ± 1.15 μM and 7.85 ±2.41 μM, respectively, at 2 Gy (**Figure 5-8b**). A greater level of cell death was also observed for Hf-DBB^F-Ir(+) by live/dead cell imaging (**Figure 5-8c**) and apoptotic cell quantification by CLSM and flow cytometry (**Figure 5-9**). These results indicate a stronger cell killing effect by Hf-DBB^F-Ir(+) via the RT-RDT process.

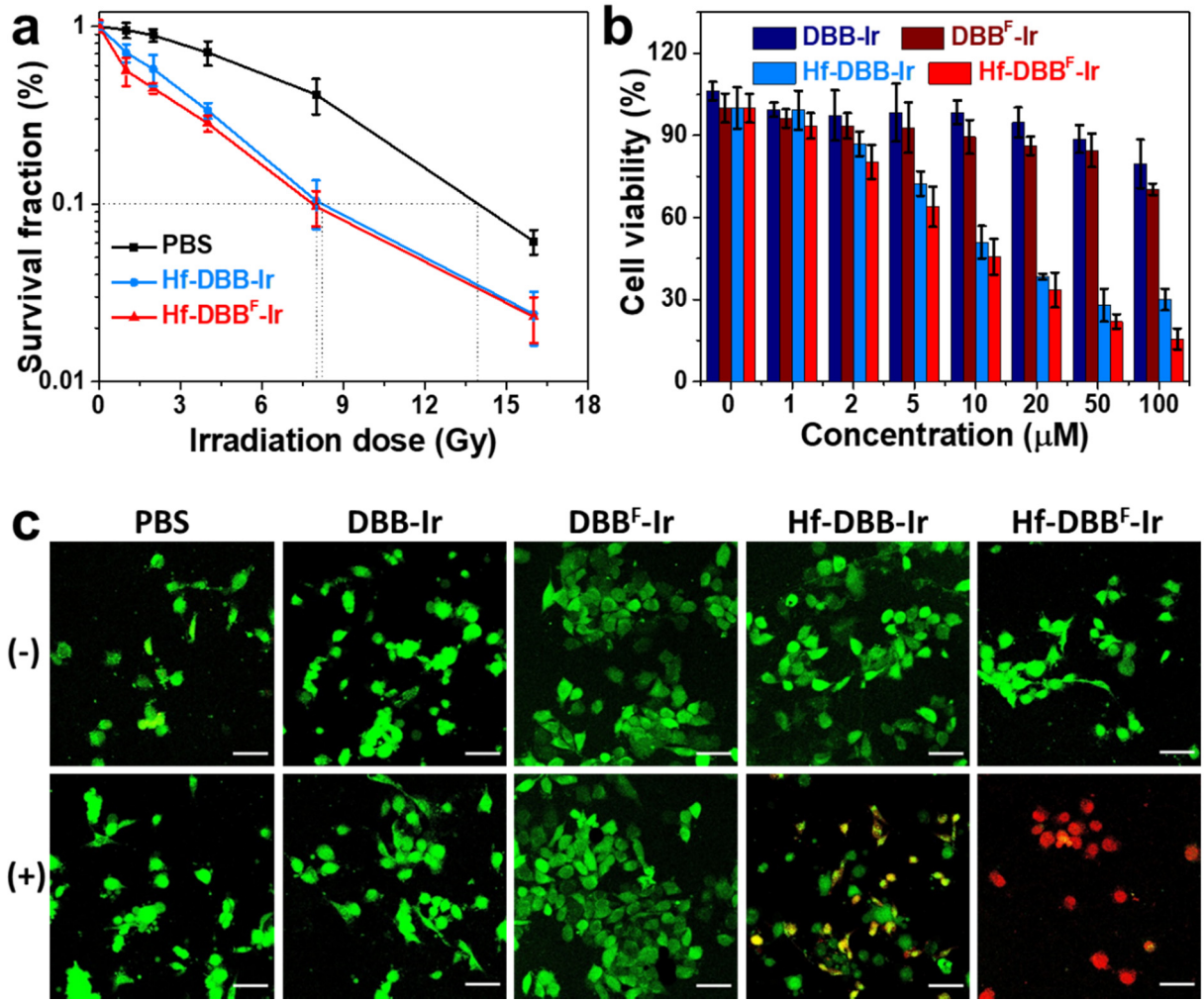

Figure 5-8 (a) Clonogenic assays to evaluate radioenhancement of Hf-DBB-Ir or Hf-DBB^F-Ir on MC38 cells upon X-ray irradiation, n = 6. (b) Cytotoxicity of Hf-DBB-Ir or Hf-DBB^F-Ir upon X-ray irradiation at a dose of 2 Gy on MC38 cells, n = 6. (c) Representative CLSM imaging of Live/dead cell analysis on MC38 cells treated with PBS, DBB-Ir, DBB^F-Ir, Hf-DBB-Ir, or Hf-DBB^F-Ir for 4 h and irradiated upon X-ray at a dose of 0 (-) or 2 (+) Gy. Green and red fluorescence represent Calcein AM and PI signal, indicating live or dead cells, respectively. Scale bar = 50 μm.

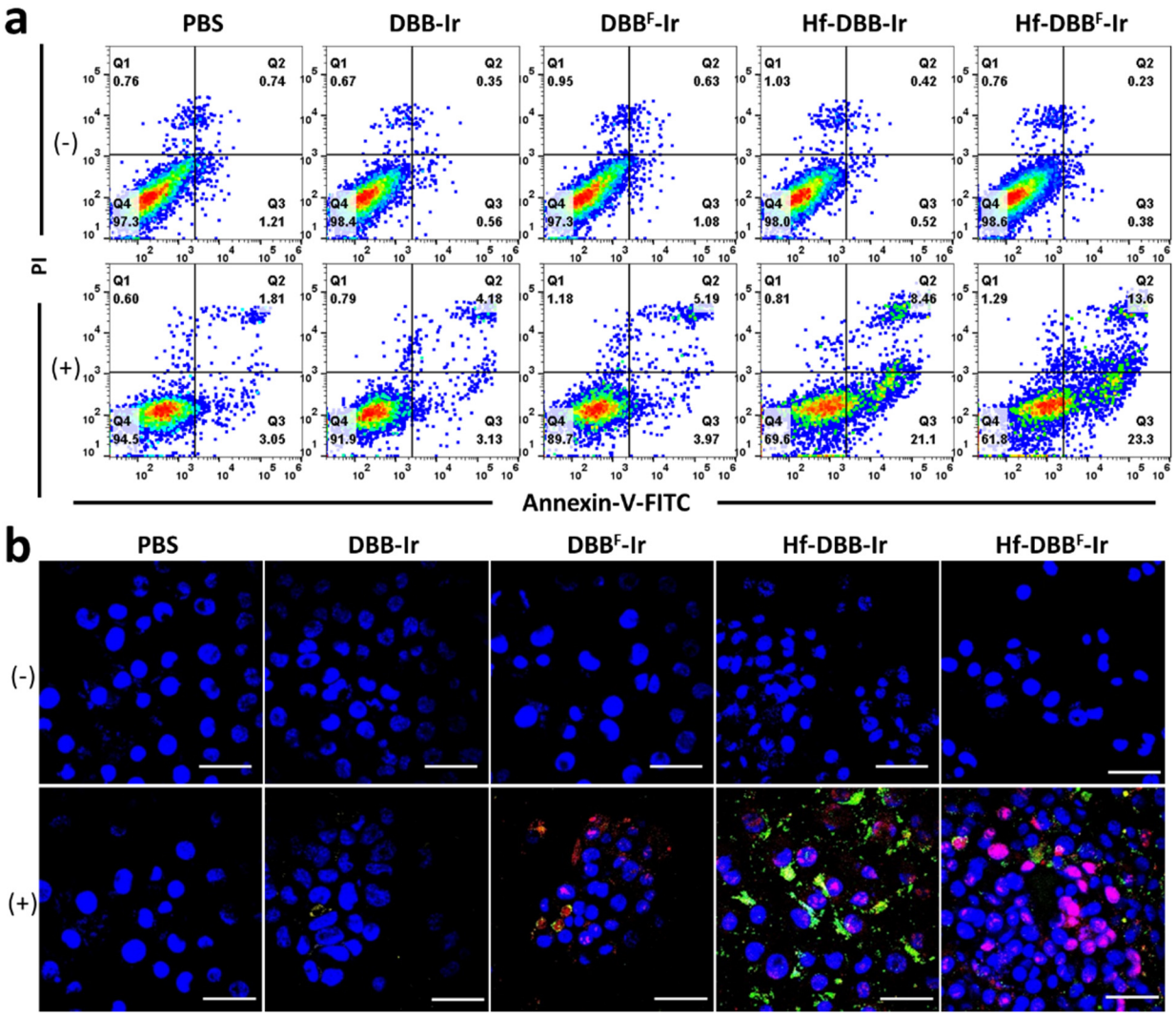

Figure 5-9 Flow cytometric Annexin V/PI analysis (a) and representative CLSM images of MC38 cells treated with PBS, DBB-Ir, DBB^F-Ir, Hf-DBB-Ir, or Hf-DBB^F-Ir for 4 h and then irradiated upon X-ray at a dose of 0 (-) or 2 (+) Gy. (a) The quadrants from lower left to upper left (counter clockwise) represent healthy, early apoptotic, late apoptotic, and necrotic cells, respectively. The percentage of cells in each quadrant was shown on the graphs. (b) Blue, red and green fluorescence represent DAPI, PI and Annexin-V-conjugated Alexa-488, respectively. Scale bar = 50 μm.

We next investigated the generation of DAMPs from nMOF-mediated RT-RDT by examining immunogenic cell death (ICD) of tumor cells and phagocytosis of dying tumor cells and their apoptotic debris by APCs. In the ICD process, calreticulin (CRT) is translocated to cell membrane as an “eat-me” signal which is recognized by macrophages and DCs to engulf dying tumor cells

and their apoptotic debris. Flow cytometric quantification revealed that Hf-DBB^{F}-Ir(+) treated cells exhibited higher CRT fluorescence, suggesting that Hf-DBB^{F}-Ir(+) induced stronger ICD with higher cytotoxicity (**Figure 5-10**).

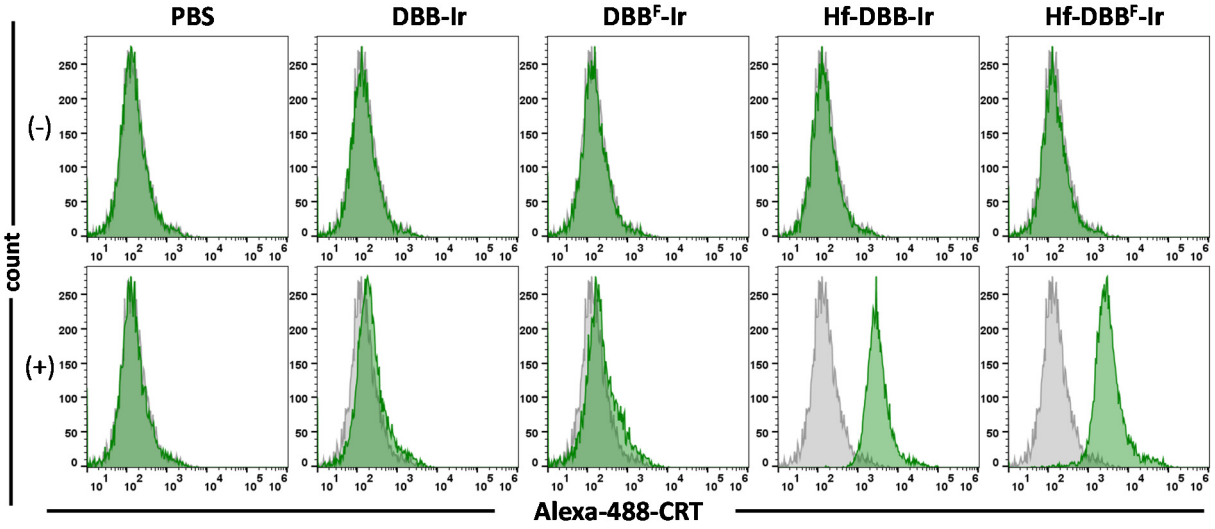

Figure 5-10 Flow cytometric analysis of calreticulin exposure (CRT) in MC38 cells treated with PBS, DBB-Ir, DBB^{F}-Ir, Hf-DBB-Ir, or Hf-DBB^{F}-Ir for 4 h and then irradiated upon X-ray at a dose of 0 (-) or 2 (+) Gy. Grey histogram (control) and green histogram show the difference of CRT level in the cells, respectively.

To assess the impact of nMOF-mediated RT-RDT on antigen processing by and immune activation of APCs, DCs differentiated from bone marrow cells were co-cultured with CFSE-labeled MC38 cells treated with PBS, DBB-Ir, DBB^{F}-Ir, Hf-DBB-Ir, or Hf-DBB^{F}-Ir with or without X-ray irradiation. Flow cytometry showed that the population of CFSE+ MC38 cells gated from CD11c^{+} cells significantly increased in cells with Hf-DBB^{F}-Ir(+) treatment (**Figure 5-11a,b**). CLSM imaging confirmed that Hf-DBB^{F}-Ir(+) treated cells recruited more DCs (labeled with PE-Cy5.5 conjugated CD11c) for phagocytosis (**Figure 5-11c**) than all other treatment groups, indicating enhanced immune stimulation mediated by cationic nMOFs.

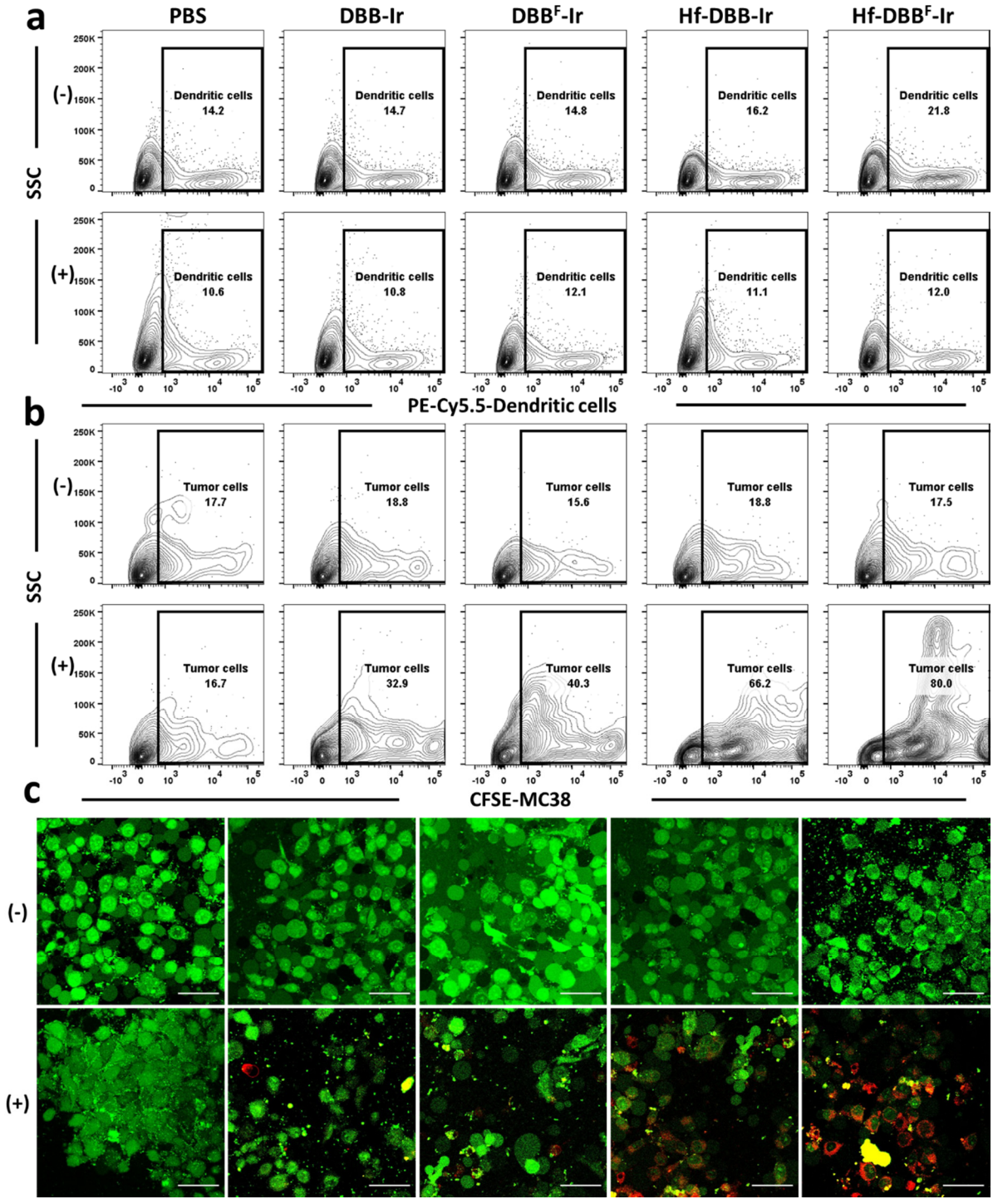

Figure 5-11 Phagocytosis of CFSE-labelled MC38 cells by DCs treated with PBS, DBB-Ir, DBB^F-Ir, Hf-DBB-Ir, or Hf-DBB^F-Ir for 4 h and then irradiated upon X-ray at a dose of 0 (-) or 2 (+) Gy by flow cytometry. DCs co-cultured with treated MC38 cells were stained with PE-Cy5.5-conjugated CD11c antibody as shown in (a). MC38 cells were gated on PE-Cy5.5-positive cells as shown in (b). (c) Red and green fluorescence represents DCs and MC38 cancer cells, respectively. Scale bar = 50 μm.

5.2.4 *In vitro* delivery of PAMPs

We rationalized that fluorination of the DBB^F ligand in Hf-DBB^F-Ir could introduce electron-withdrawing effects to increase the surface charge for more efficient delivery of CpG. Hf-DBB^F-Ir and Hf-DBB-Ir exhibited ζ-potential values of 31.6 ± 1.2 mV and 23.8 ± 0.8 mV, respectively, confirming a more cationic skeleton of Hf-DBB^F-Ir for electrostatic adsorption of anionic CpG (**Figure 5-12a**). 1 mg of CpG was incubated in 20 mL PBS solution of Hf-DBB^F-Ir or Hf-DBB-Ir with an equivalent Hf concentration of 10 mM for 10 mins. After centrifugation, DNA gel electrophoresis showed the adsorption of 82.7% CpG onto Hf-DBB^F-Ir and 46.5% CpG onto Hf-DBB-Ir, with 8.6% and 43.8% of CpG remaining in the corresponding supernatants as quantified by NanoDrop spectrophotometry (**Figure 5-12b**). We next examined CpG internalization by DCs. Flow cytometry and CLSM imaging showed that Hf-DBB^F-Ir delivered the highest amount of CpG to DCs after they were cultured with FITC-labeled free CpG, Hf-DBB-Ir@CpG or Hf-DBB^F-Ir@CpG (**Figure 5-13**). These results confirm the superior ability of Hf-DBB^F-Ir in delivering CpG as PAMPs to APCs.

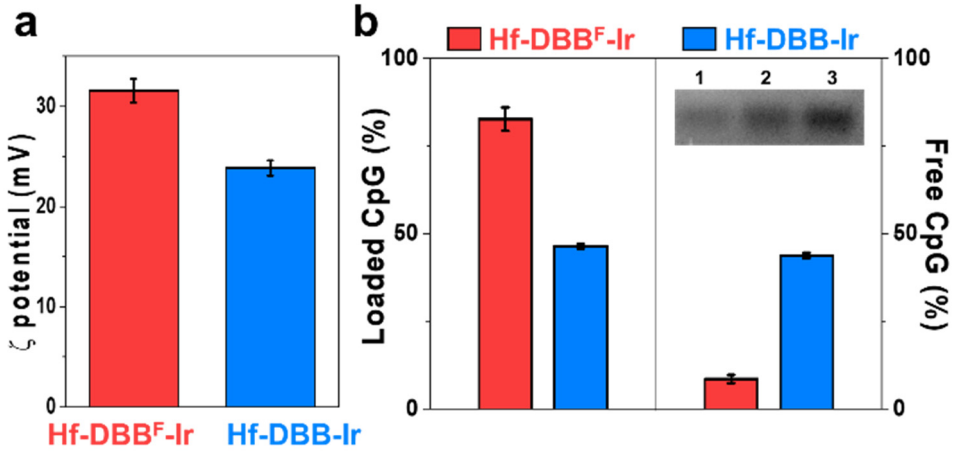

Figure 5-12 (a) Zeta potential of Hf-DBB-Ir and Hf-DBB^F-Ir. (b) Left lanes, quantification of adsorbed CpG with DNA gel. Right lanes: non-absorbed CpG by NanoDrop with free CpG served as control.

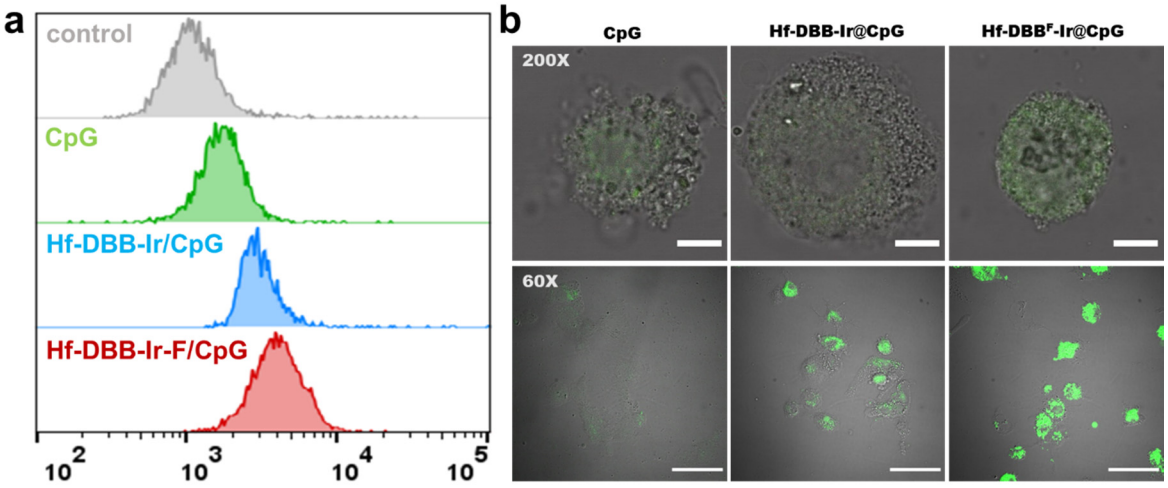

Figure 5-13 (a) FITC-labeled CpG uptake by DCs incubated with free CpG, Hf-DBB-Ir@CpG or Hf-DBB^{F}-Ir@CpG quantified with flow cytometry and observed under CLSM. Scale bar = 4 μm.

5.2.5 *In vitro* DC maturation

To evaluate the effects of CpG delivery on DC maturation, we incubated bone marrow derived DCs with CpG, Hf-DBB-Ir@CpG or Hf-DBB^{F}-Ir@CpG at CpG concentrations of 0, 62.5, 125, 250, 500 and 1000 ng/mL for 60 h. The cells were harvested and stained for the detection of DCs maturation markers, including MHC-II and co-stimulatory molecules CD80 and CD86. The supernatants were also collected and assayed for the presence of cytokines interferon-alpha (IFN-α and interleukin-6 (IL-6). Both Hf-DBB-Ir@CpG and Hf-DBB^{F}-Ir@CpG effectively promoted DC maturation with increased MFI signals of CD80 (**Figure 5-14a**), CD86 (**Figure 5-14b**) and MHC-II compared to free anionic CpG (**Figure 5-14c**). Hf-DBB^{F}-Ir@CpG outperformed Hf-DBB-Ir@CpG in the upregulation of CD80, CD86, and MHC-II signals as a result of its more effective CpG delivery. Only cationic nMOF-delivered CpG showed elevated IFN-α levels while free CpG completely had no effect (**Figure 5-15a**). Moreover, DCs treated with free CpG excreted

IL-6 only in high CpG concentrations, while treated with nMOFs/CpG excreted IL-6 at low CpG concentrations (**Figure 5-15c**). qPCR of IL-6 and IFN- α expression confirmed that Hf-DBB^{F}-Ir more efficiently delivered CpG as PAMPs to activate DCs (**Figure 5-15b,d**).

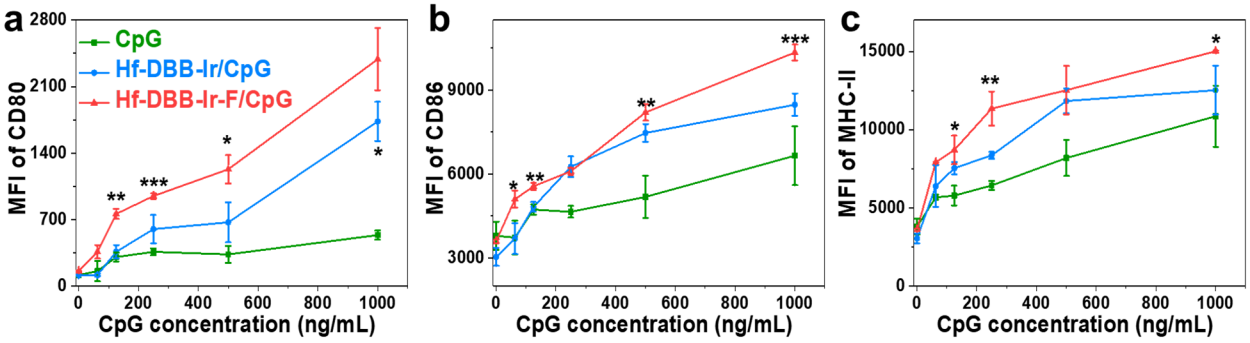

Figure 5-14 Functional surface markers CD80 (a), CD86 (b) and MHC-II (c) on DCs stimulated with free CpG, Hf-DBB-Ir@CpG or Hf-DBB^{F}-Ir@CpG with increasing CpG concentrations quantified by flow cytometry, n=6.

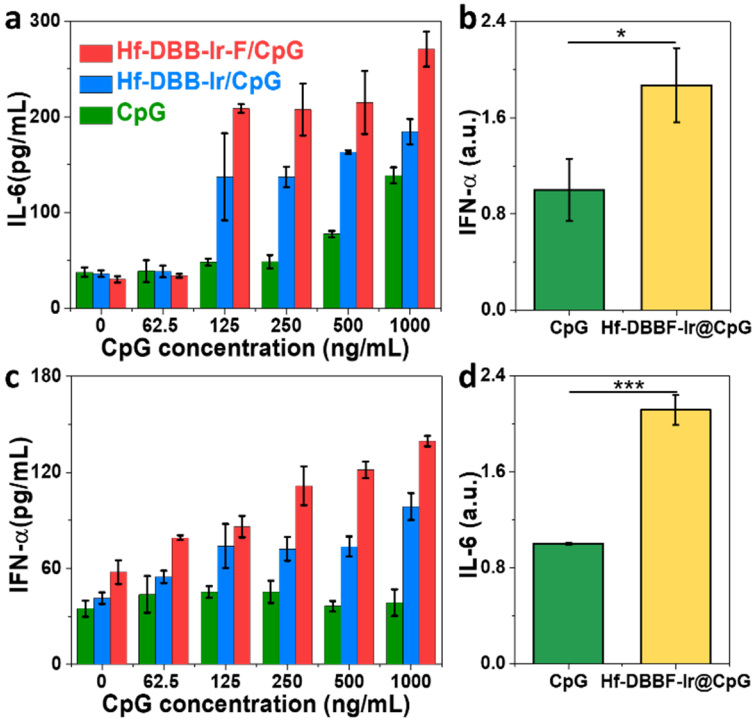

Figure 5-15 Biomarkers IL-6 (a,b) and IFN-α (c,d) by ELISA (a,c) or qPCR (b,d) of DCs stimulated with free CpG, Hf-DBB-Ir@CpG or Hf-DBB^{F}-Ir@CpG with increasing CpG concentrations, n=6.

To directly demonstrate the enhanced antigen presentation property of DCs after Hf-DBB^{F}-Ir@CpG stimulation, MC38 cells transfected with ovalbumin antigen (OVA, cell line denoted as MC38-ova) were cultured with CpG, Hf-DBB-Ir@CpG or Hf-DBB^{F}-Ir@CpG stimulated DCs in a 3:1 ratio. Tumor antigen uptake and presentation was examined by detecting the expression of H-2Kb-SIINFEKL complex (Kb-ova) on DCs surface. Hf-DBB^{F}-Ir@CpG outperformed Hf-DBB-Ir@CpG and free CpG on promoting antigen uptake and presentation by DCs (**Figure 5-16**), likely as a result of more efficient delivery of PAMPs and antigen presentation.

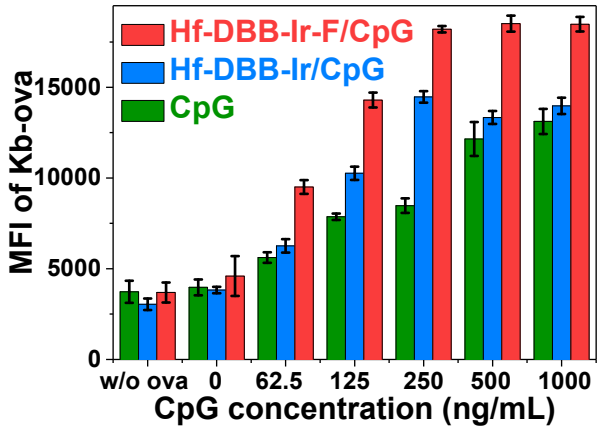

Figure 5-16 Expression level of SIINFEKL-Kb on DCs co-cultured with MC38-ova cells at a 1:3 ratio, n=6. DCs stimulated with free CpG, Hf-DBB-Ir@CpG or Hf-DBB^{F}-Ir@CpG with increasing CpG concentrations, n=6.

5.2.6 X-ray triggered *In situ* cancer vaccines

We next investigated the local anti-tumor effect of Hf-DBB^{F}-Ir@CpG(+) as an *in situ* cancer vaccine. We first showed that intravenous injection of 2 μmol DBB^{F}-Ir or Hf-DBB^{F}-Ir biweekly for a total of 4 doses did not cause toxicity on C57BL/6 mice as judged from the steady bodyweight gains (**Figure 5-17**).

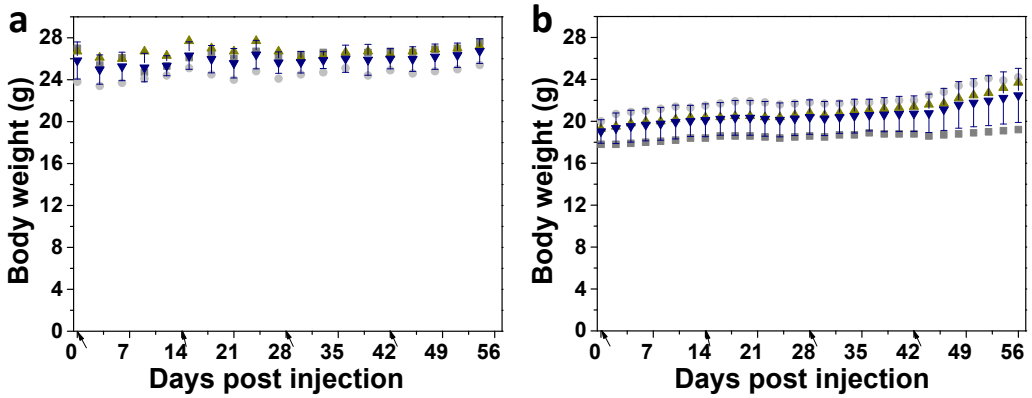

Figure 5-17 Toxicity test of DBB^F-Ir or Hf-DBB^F-Ir on C57Bl/6 mice, n = 3. Body weights of C57BL/6 mice were monitored after receiving H_2DBB^F-Ir at a dose of 2 μmol biweekly with a total of four injections (a) or Hf-DBB^F-Ir at a dose of 2 μmol based on Hf biweekly with a total of four injections (b). Black arrows refer to the times of injections.

We then established a murine colorectal model MC38 on C57BL/6c mice by subcutaneous injection on right flanks. When the tumors reached 100-150 mm^3, PBS, Hf-DBB-Ir, Hf-DBB^F-Ir, or Hf-DBB^F-Ir@CpG was injected intratumorally at a Hf dose of 0.2 μmol and/or CpG dose of 1 μg. 12 h later, the tumors were irradiated with 1Gy of X-ray (225 kVp, 13 mA, 1 Gy) and followed by four more daily irradiation of X-ray (1 Gy). Hf-DBB^F-Ir(+) outperformed Hf-DBB-Ir(+) with a tumor growth inhibition index (TGI) of 81.9% vs 64.7%, suggesting more efficient release of DAMPs by Hf-DBB^F-Ir-mediated RT-RDT *in vivo*. Hf-DBB^F-Ir-@CpG(+) showed enhanced tumor regression over CpG(+) (TGI of 99.6% vs 34.8%) or Hf-DBB^F-Ir(+) on Day 31, indicating the synergy of DAMPs released by nMOF-mediated RT-RDT and PAMPs delivered by cationic nMOFs (**Figure 5-18a**). The anti-tumor efficacy was confirmed by optical images (**Figure 5-18c**) and averaged weights (**Figure 5-18d**) of excised tumors on Day 31. Immunofluorescence of terminal deoxynucleotidyl transferase dUTP nick end labeling (TUNEL) and H&E staining indicated significant apoptosis of tumor cells with Hf-DBB^F-Ir@CpG(+) treatment (**Figure 5-18e,f**). No systemic toxicity was observed for all treatment groups (**Figure 5-18b,g**).

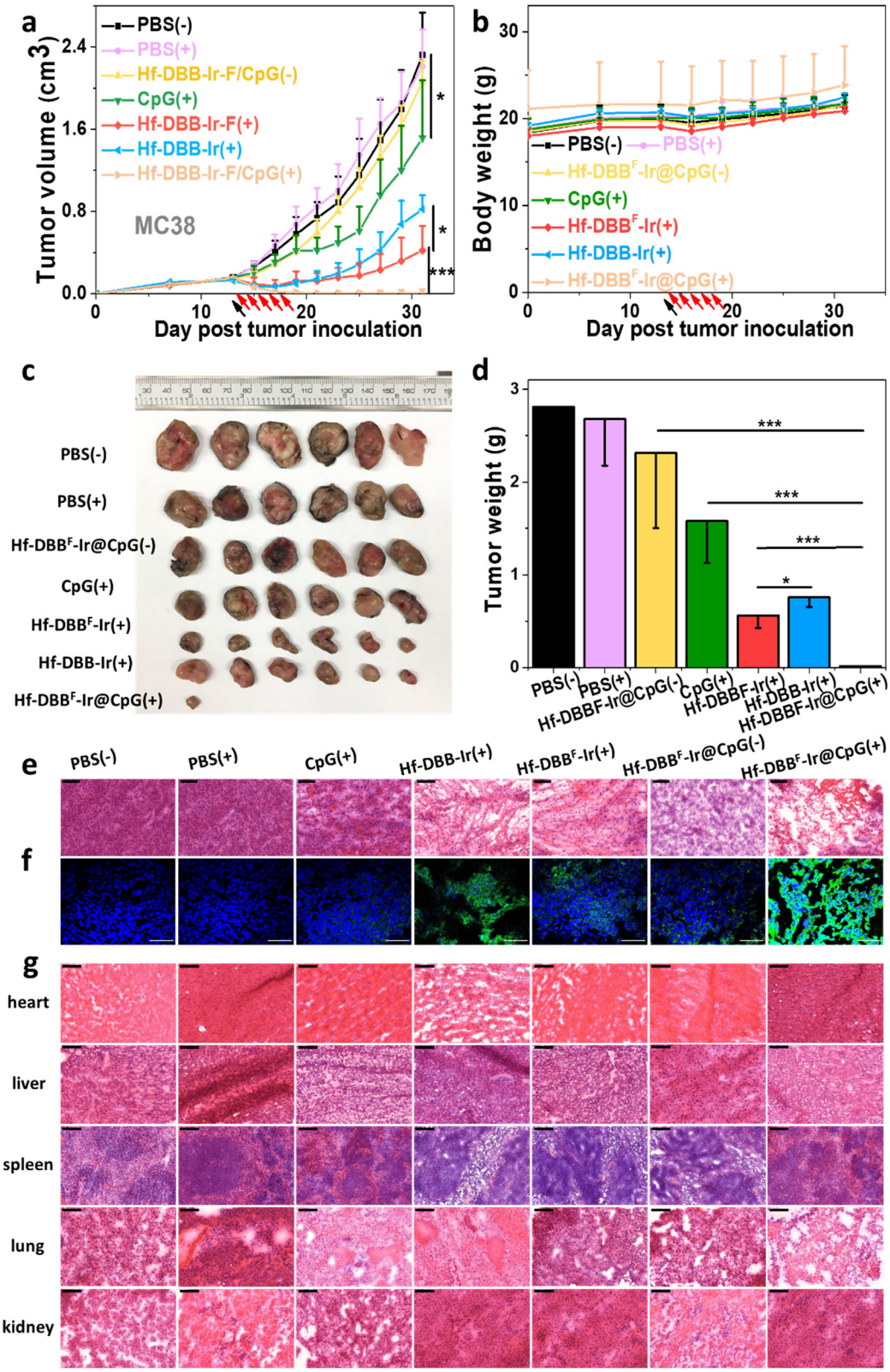

Figure 5-18 Tumor growth curves (a) and body weights (b) of MC38 tumor-bearing mice treated

Figure 5-18, continued with PBS(-), PBS(+), CpG(+), Hf-DBB^F-Ir(+), Hf-DBB^F-Ir@CpG(-), or Hf-DBB^F-Ir@CpG(+). Hf-DBB-Ir(+) served as control group on the MC38 model, n = 6. (c) Photo of excised tumors of MC38-bearing C57BL/6 mice, n = 6. From top to bottom: PBS(-), PBS(+), Hf-DBB^F-Ir/CpG(-), CpG(+), Hf-DBB^F-Ir(+), Hf-DBB-Ir(+), and Hf-DBB^F-Ir/CpG(+). (d) Weights of excised tumors of the MC38-bearing mice. Data are expressed as means ± s.d., n = 6. *P < 0.05 and ***P < 0.001 by t-test. H&E staining (e) and TUNEL assay (f) of excised tumors of MC38-bearing C57BL/6 mice. (g) Representative histology of frozen sections of major organs of MC38-bearing C57BL/6 mice receiving intratumoral injection of PBS or Hf-DBB^F-Ir/CpG with (+) or without (-) X-ray irradiation, and CpG, Hf-DBB-Ir, or Hf-DBB^F-Ir with X-ray irradiation. Scale bar = 100 μm.

We further evaluated the antitumor activity on a murine pancreatic cancer model, Panc02, on C57BL/6c mice with high radioresistance and poor immunogenicity. Hf-DBB^F-Ir@CpG(+) afforded superior tumor growth inhibition over other groups (**Figure 5-19** and **Table 5-1**), suggesting the potential of using Hf-DBB^F-Ir@CpG(+) as *in situ* cancer vaccine on a broad spectrum of cancers with varied immunogenicity.

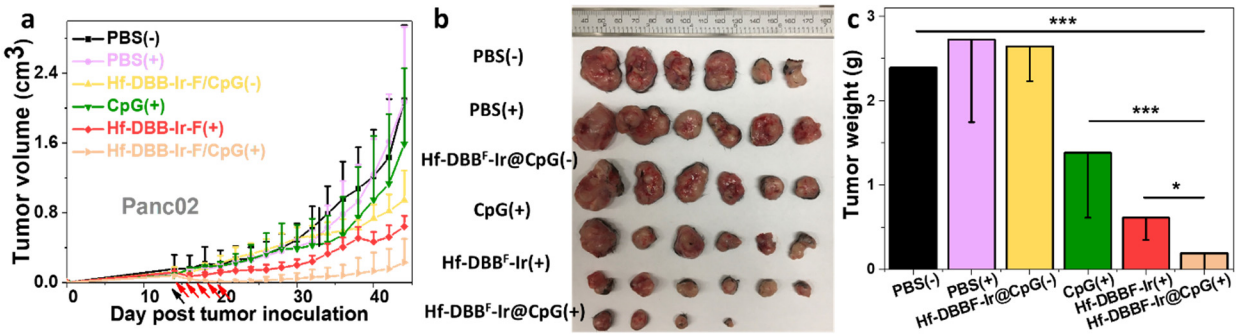

Figure 5-19 (a) Tumor growth curves of Panc02 tumor-bearing mice treated with PBS(-), PBS(+), CpG(+), Hf-DBB^F-Ir(+), Hf-DBB^F-Ir@CpG(-), or Hf-DBB^F-Ir@CpG(+). (b) Photo of excised tumors of MC38-bearing C57BL/6 mice, n = 6. From top to bottom: PBS(-), PBS(+), Hf-DBB^F-Ir/CpG(-), CpG(+), Hf-DBB^F-Ir(+),and Hf-DBB^F-Ir/CpG(+). (c) Weights of excised tumors of the MC38-bearing mice. Data are expressed as means ± s.d. *P < 0.05 and ***P < 0.001 by t-test.

Table 5-1. TGIs of MC38 and Panc02 tumor models with different treatments.

TGI (%)	MC38	Panc02
PBS(+)	4.8	0.9
CpG(+)	34.8	54.8
Hf-DBB-Ir(+)	64.7	-
Hf-DBB^{F}-Ir(+)	81.9	69.4
Hf-DBB^{F}-Ir/CpG(-)	11.3	24.1
Hf-DBB^{F}-Ir/CpG(+)	99.6	89.1

5.2.7 Innate immunity after *in situ* cancer vaccination

Flow cytometry showed significant increases of tumor- and tumor-draining lymph node (DLN)-infiltrating APCs, including macrophages (**Figure 5-20a**) and DCs (**Figure 5-20b**), in the Hf-DBB^{F}-Ir@CpG(+) treatment group, which indicates the synergistic effect of DAMPs and tumor antigens released by nMOF-mediated RT-RDT and PAMPs delivered by cationic nMOFs. The increase of APC populations was further confirmed by CLSM (**Figure 5-20d**). DC maturation promoted by Hf-DBB^{F}-Ir@CpG(+) was further demonstrated with elevated expression of MHC-II and costimulatory CD80 molecules (**Figure 5-20c**). Furthermore we assayed plasma IL-6 and IFN-α concentrations by ELISA and determined gene expression in tumors and DLNs by qPCR 24 h post treatment to evaluate the innate immune response. Hf-DBB^{F}-Ir@CpG(+) treatment showed significantly elevated levels of plasma and intratumoral IL-6 and IFN-α over CpG(+) or Hf-DBB^{F}-Ir(+) treatment (**Figure 5-21**). Elevations of total IgG (**Figure 5-22a**) and IgM (**Figure 5-22b**) in plasma 2 and 12 days after Hf-DBB^{F}-Ir@CpG(+) treatment suggest effective promotion of humoral immunity mediated by B cells. As IgM can bind and activate the complement system to promote the opsonization and degradation of antigens and antigen presentation by phagocytes,

the increased levels of plasma IgG and IgM results imply an important role of B cells in promoting antigen presentation after *in situ* vaccination.

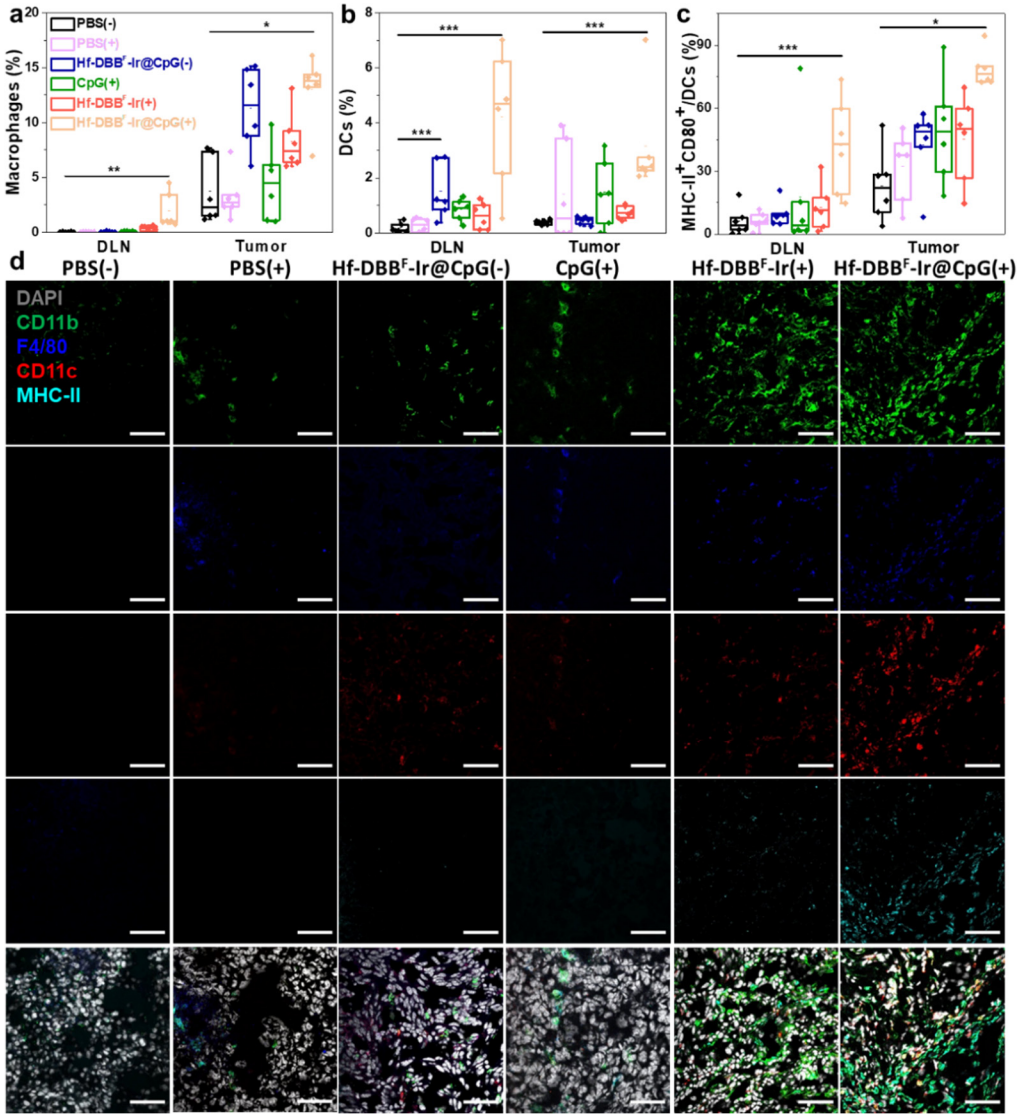

Figure 5-20 The percentages of macrophages (a) and DCs (b) with respect to the total cells in tumors and tumor-draining lymph nodes excised from MC38-bearing mice 2 days post treatment. The percentages of tumor-infiltrating $CD80^+$ $MHCII^+$ cells (c) with respect to DCs in tumors and tumor-draining lymph nodes excised from MC38-bearing mice day 2 post treatment. (d) Representative immunofluorescence imaging for infiltration of antigen presenting cells into MC38 tumors-bearing mice receiving treatment of PBS(-), PBS(+), Hf-DBB^F-Ir@CpG(-), CpG(+), Hf-DBB^F-Ir(+), and Hf-DBB^F-Ir@CpG(+). Grey, green, blue, red and cyan fluorescence indicate nucleus, CD11b, F4/80, CD11c and MHC-II, respectively. Scale bar = 100 μm. Data are expressed as means ± s.d. *P < 0.05, **P < 0.005 and ***P < 0.001 by t-test.

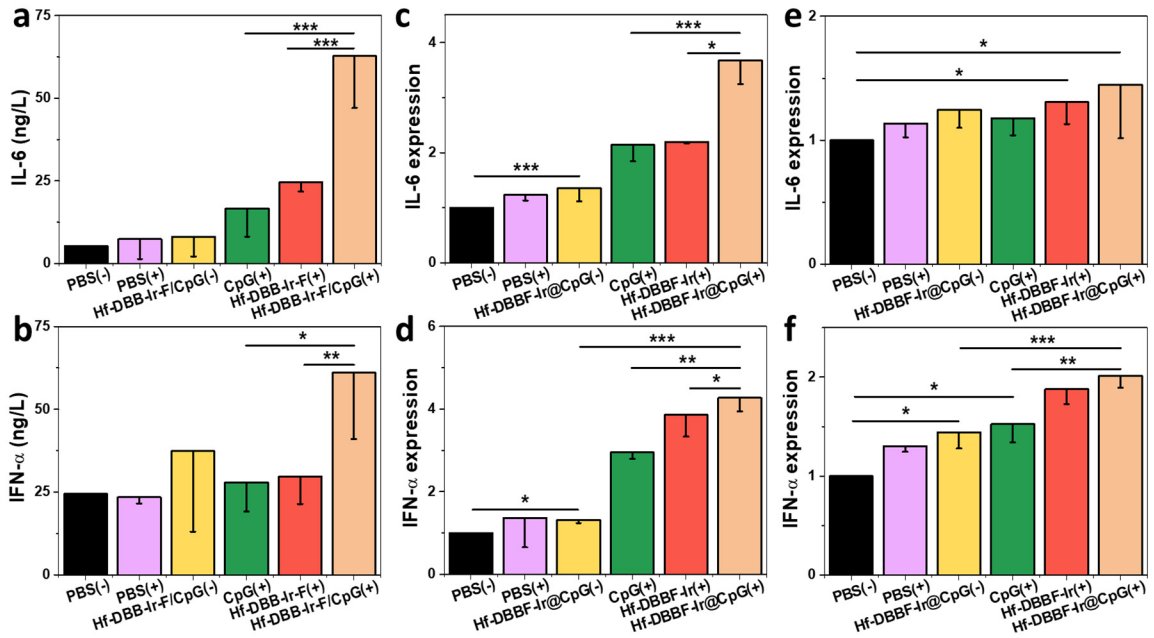

Figure 5-21 Plasma concentration of IL-6 (a) and IFN-α (b) 48 h after first irradiation quantified by ELISA, n=6. IL-6 (c, e) or IFN-α (d, f) expression level extracted from tumors (c, d) or tumor-draining lymph nodes (e, f) of MC38-bearing C57BL/6 mice treated by PBS(-), PBS(+), Hf-DBB^{F}-Ir@CpG(-), CpG(+), Hf-DBB^{F}-Ir(+), or Hf-DBB^{F}-Ir@CpG(+) quantified by qPCR, n = 4. GAPDH was used as a housekeeping gene for comparison of gene expression. Data are expressed as means ± s.d. *P < 0.05 and ***P < 0.001 by t-test.

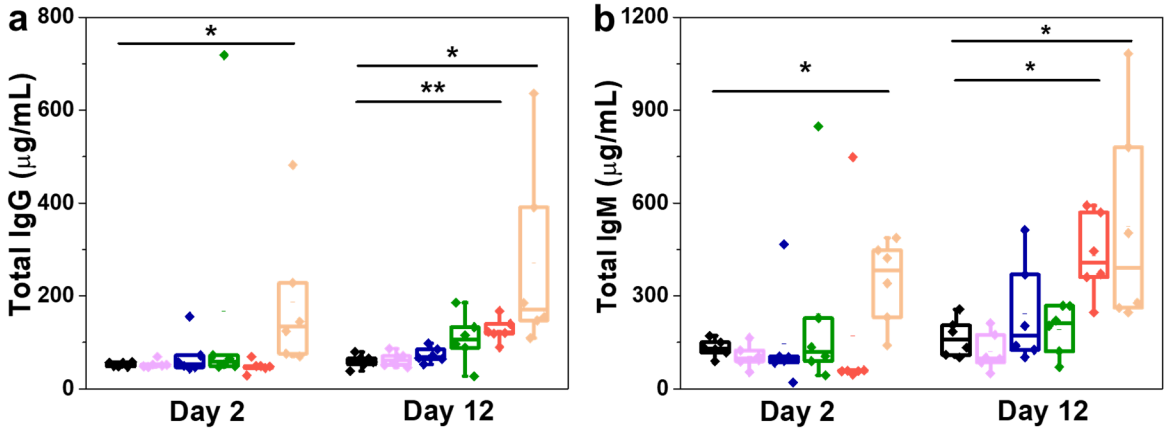

Figure 5-22 Total IgG (a) and total IgM (b) in plasma 2 days and 12 days post irradiation on MC38 tumors-bearing mice receiving treatment of PBS(-), PBS(+), Hf-DBB^{F}-Ir@CpG(-), CpG(+), Hf-DBB^{F}-Ir(+), and Hf-DBB^{F}-Ir@CpG(+), n = 6. Data are expressed as means ± s.d. *P < 0.05, and **P < 0.005 by t-test.

We then generate MC38-ova model to probe the antigen presentation process. The expression of Kb-ova complex (SIINFEKL-H2Kb gated from CD45^{+} cells) was significantly upregulated post

Hf-DBB^F-Ir@CpG(+) treatment on the MC38-ova model, confirming the facilitated antigen presentation process (**Figure 5-23**). Hf-DBB^F-Ir@CpG(+) group also exhibited enlarged DLNs (**Figure 5-24a,b**), suggesting T cell expansion in DLNs. The increased expression of Ki67 in DLNs by CLSM supported T cell expansion in DLNs following Hf-DBB^F-Ir@CpG(+) treatment (**Figure 5-24c**).

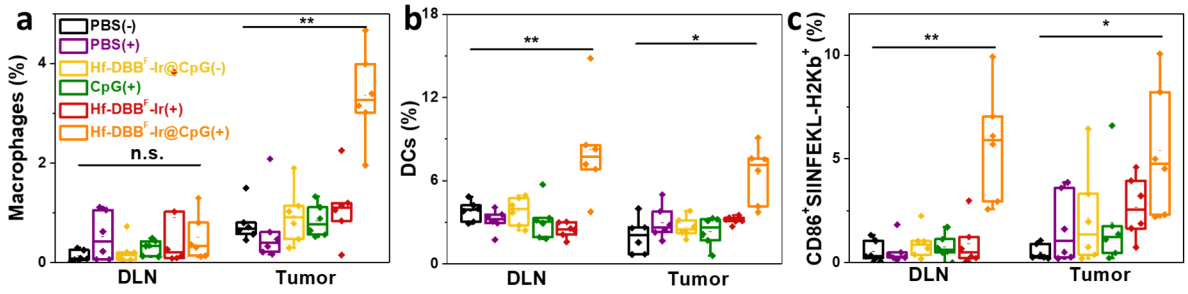

Figure 5-23 Percentages of macrophages (a), DCs (b) and SIINFEKL-H_2Kb^+ cells (c) with respect to the total cells. Tumor-draining lymph nodes or tumors were excised from MC38-ova tumor-bearing mice 6 days after treated with PBS(-), PBS(+), Hf-DBB^F-Ir@CpG(-), CpG(+), Hf-DBB^F-Ir(+), and Hf-DBB^F-Ir@CpG(+). Data are expressed as means ± s.d., n=6. *P < 0.05, **P < 0.005, and ***P < 0.001 by t-test. Central lines, bounds of box and whiskers represent mean values, 25% to 75% of the range of data and 1.5 fold of interquartile range away from outliers, respectively.

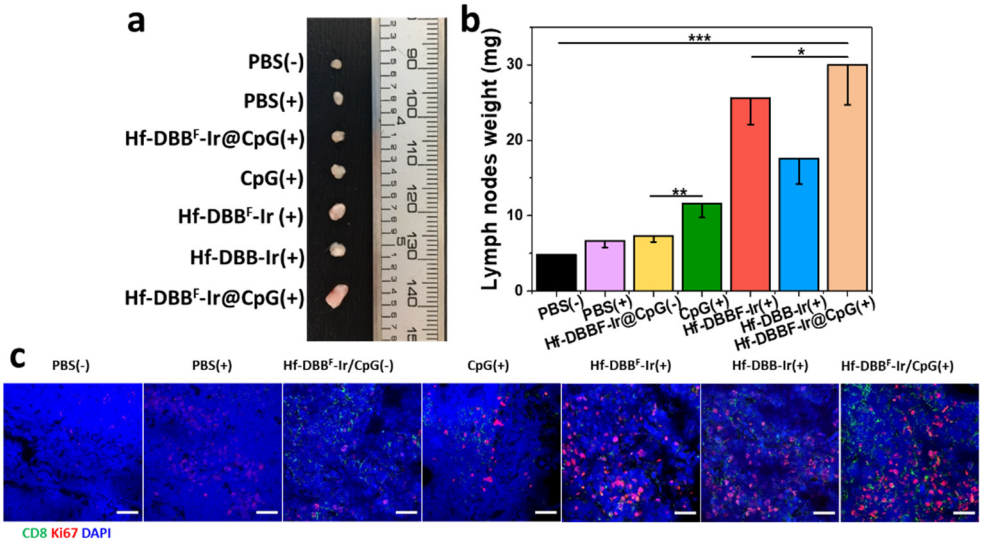

Figure 5-24 (a) Photo of excised tumor-draining lymph nodes of MC38-bearing C57BL/6 mice. From top to bottom: PBS(-), PBS(+), Hf-DBB^F-Ir@CpG(-), CpG(+), Hf-DBB^F-Ir(+), Hf-DBB-

Figure 5-24, continued Ir(+), and Hf-DBB^{F}-Ir@CpG(+). (b) Weights of excised tumor-draining lymph nodes of the MC38-bearing mice. Data are expressed as means ± s.d., n = 6. *P < 0.05, **P < 0.005, and ***P < 0.001 by t-test. (c) Representative immunofluorescence imaging of excised tumor-draining lymph nodes of MC38-bearing C57BL/6 mice for detecting T cell expansion. Blue, green, and red fluorescence indicate nucleus, CD8α and Ki67, respectively. Scale bar = 100 μm.

Finally, MC38-ova tumors were established on immuno-deficient Rag2$^{-/-}$ mice and then treated with Hf-DBB^{F}-Ir(+) or Hf-DBB^{F}-Ir@CpG(+) plus adoptive transfer of OT-I T cells. Mice treated with Hf-DBB^{F}-Ir@CpG(+) plus OT-I T cell transfer showed more effective tumor suppression than either Hf-DBBF-Ir(+) plus OT-I T cell transfer or Hf-DBB^{F}-Ir@CpG(+) alone (**Figure 5-25**), supporting an effective antigen presentation process after Hf-DBB^{F}-Ir@CpG(+) treatment as an in situ cancer vaccine.

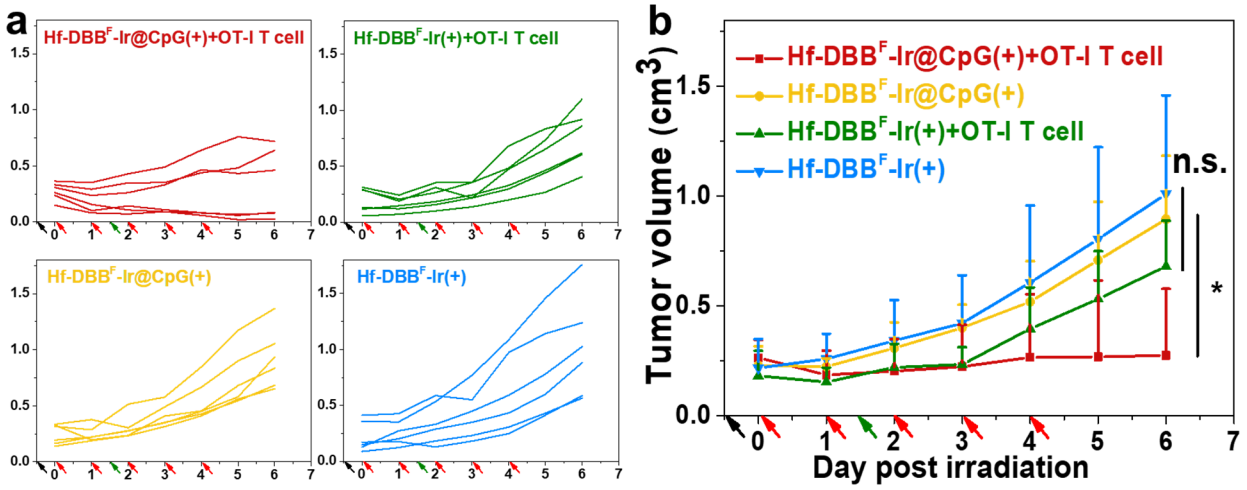

Figure 5-25 Individual (a) and average (b) growth curves of MC38-ova tumor-bearing Rag2$^{-/-}$ mice treated with Hf-DBB^{F}-Ir(+) or Hf-DBB^{F}-Ir@CpG(+) with or without OT-I T cell transfer study. Black, red, and green arrows refer to i.t. injections, X-ray irradiation, and adoptive T cell transfer, respectively. Data are expressed as means ± s.d., n = 6. n.s. P > 0.05 and *P < 0.05 by t-test.

Interestingly, we observed macrophage repolarization with an increased ratio of pro-inflammatory M1 subtype to anti-inflammatory (tumor-promoting) M2 subtype following Hf-DBB^{F}-Ir@CpG(+) treatment (**Figure 5-26**).

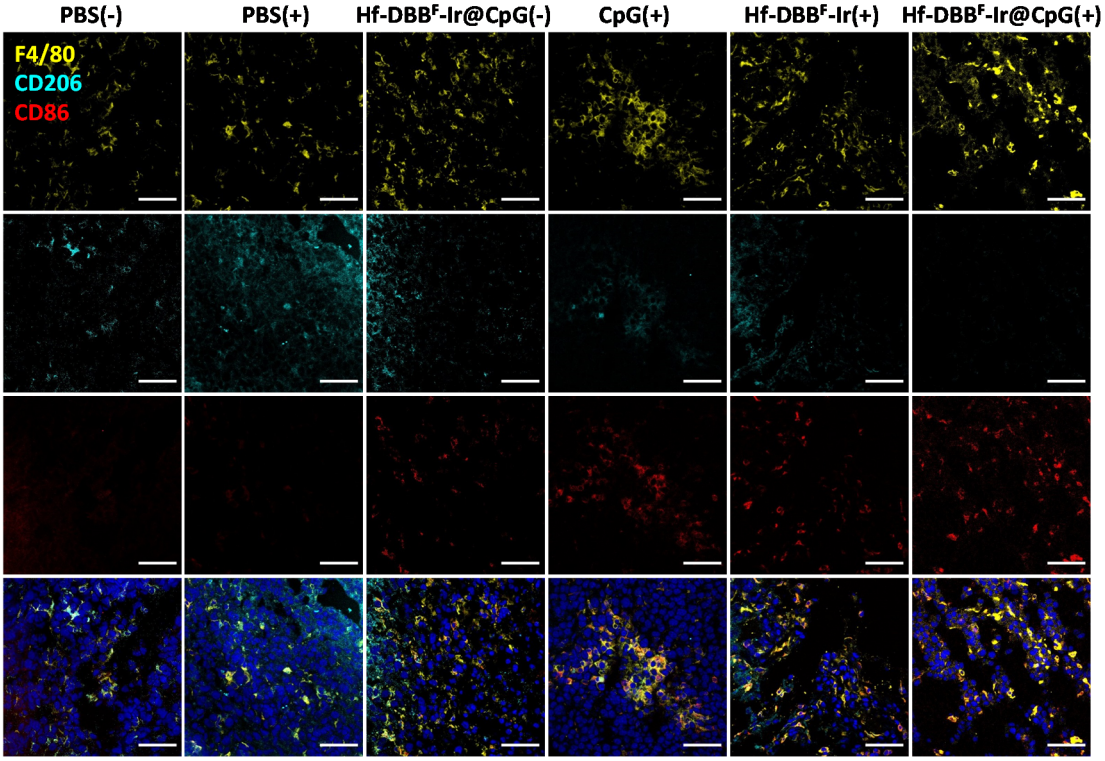

Figure 5-26 Representative immunofluorescence imaging for infiltration of antigen presenting cells into MC38 tumors-bearing mice receiving treatment of PBS(-), PBS(+), Hf-DBB^{F}-Ir@CpG(-), CpG(+), Hf-DBB^{F}-Ir(+), and Hf-DBB^{F}-Ir@CpG(+). Grey, green, blue, red and cyan fluorescence indicate nucleus, CD11b, F4/80, CD11c and MHC-II, respectively. Scale bar = 100 μm.

5.2.8 Abscopal effect

A bilateral model of MC38 was then established to assess the systemic anticancer efficacy of Hf-DBB^{F}-Ir@CpG(+) in combination with anti-PD-L1 (αPD-L1) CBI. Hf-DBB^{F}-Ir@CpG was intratumorally injected into primary tumors at a dose of 0.2 μmol Hf and 1 μg CpG 14 days post tumor inoculation, with daily X-ray irradiation at a dose of 1 Gy/fraction beginning on day 15 for

a total of 5 fractions. 75μg of αPD-L1 was administered every three days by intraperitoneal injection for a total of 3 doses. Without αPD-L1, Hf-DBB^{F}-Ir@CpG(+) almost eradicated primary tumors but only moderately delayed progression of distant tumors. In stark contrast, the combination of Hf-DBB^{F}-Ir@CpG(+) and αPD-L1 significantly regressed both primary and distant tumors with a cure rate of 83.3% (**Figure 5-27**). This result indicates a strong synergy between Hf-DBB^{F}-Ir@CpG(+) based *in situ* cancer vaccination and CBI.

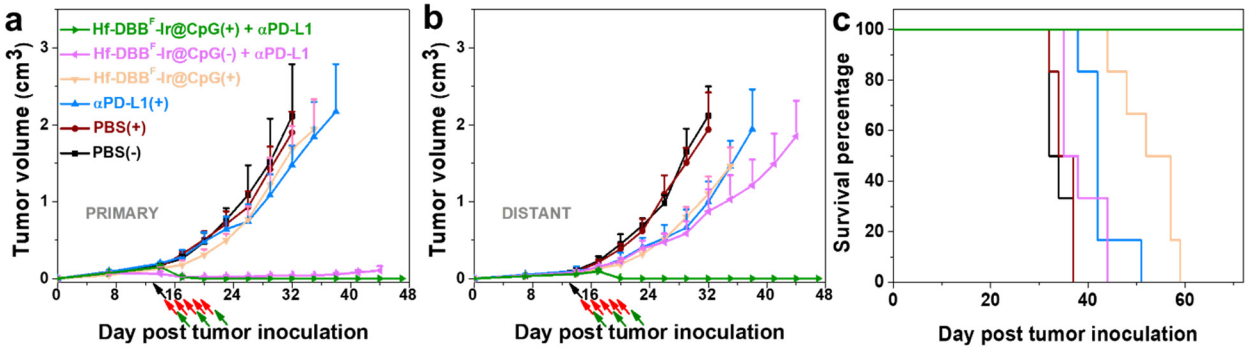

Figure 5-27 Primary treated (a), distant untreated (b) tumor growth curves and survival curves (c) of MC38 tumor-bearing mice treated with PBS(-), PBS(+), αPD-L1(+), Hf-DBB^{F}-Ir@CpG(+), Hf-DBB^{F}-Ir@CpG(-)+αPD-L1, or Hf-DBB^{F}-Ir@CpG(+)+αPD-L1. Black, red, and green arrows refer to the times of i.t. injections, X-ray irradiation, and i.p. injection, respectively, n = 6.

5.2.9 Adaptive immunity

We profiled infiltrating leukocytes in both primary and distant tumors 10 days post irradiation. Hf-DBB^{F}-Ir@CpG(+)+αPD-L1 treatment group showed significant increase of tumor-infiltrating CD45^{+} leukocytes, DCs, and CD80^{+}MHC-II^{+} cells (**Figure 5-28a-c**) in both primary and distant tumors, implying a strengthened innate immune response after *in situ* vaccination. Specifically, after treatment with Hf-DBB^{F}-Ir@CpG(+)+αPD-L1, the percentages of natural kill cells, CD4^{+} T cells and CD8^{+} T cells of the total primary and distant tumor cells significantly increased to

0.52±0.42 % and 1.21±0.89 %, 0.25±0.23 % and 1.15±1.14 %, and 1.46±0.59 % and 1.43±0.55 % from 0.06 ±0.05 % and 0.13 ±0.19 %, 0.05 ±0.04 % and 0.03±0.02 %, and 0.41±0.30 % and 0.36 ±0.27 % in PBS(-) group, respectively (**Figure 5-28d-f**). The effector T cell infiltration was shown by both representative flow cytometry (**Figure 5-28g**) and CLSM (**Figure 5-28h**).

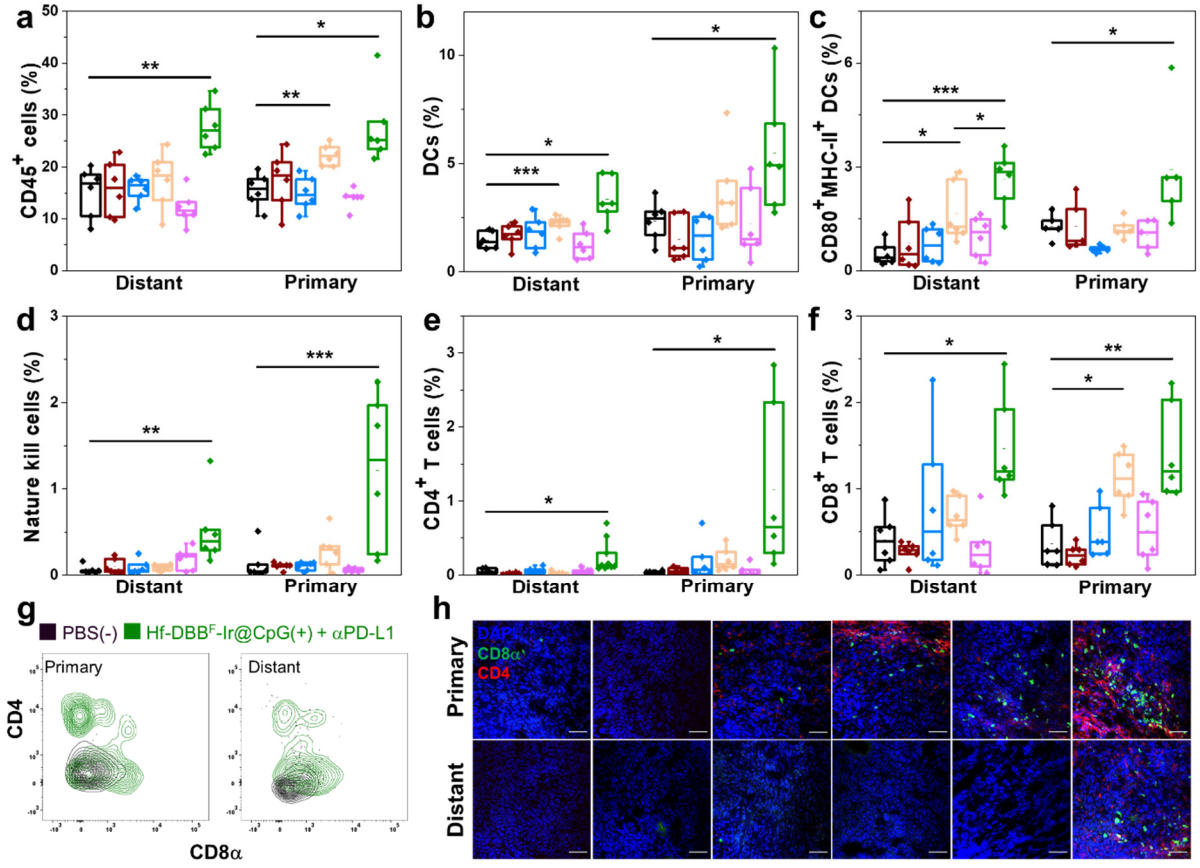

Figure 5-28 The percentages of tumor-infiltrating $CD45^+$ cells (a), DCs (b) $CD80^+$ $MHC\text{-}II^+$ DCs (c), NK cells (d), $CD4^+$ T cells (e), and $CD8^+$ T cells (f) with respect to the total cells. Data are expressed as means ± s.d., n = 6. *P < 0.05, **P < 0.01 and ***P < 0.001 by t-test. Central lines, bounds of box and whiskers represent mean values, 25% to 75% of the range of data and 1.5 fold of interquartile range away from outliers, respectively. (g) Representative flow cytometric plots showing infiltration of $CD4^+$ and $CD8^+$ T cells on both primary and distant tumors treated by PBS(-) or Hf-DBB^F-Ir@CpG(+)+αPD-L1 shown in black or green contours, respectively. (h) Representative pictures showing the infiltration of T cells on excised tumor section slides. Blue, green and red fluorescence represent DAPI, CD8α and CD4, respectively. Scale bar = 50 μm.

DLNs on both sides were harvested, weighed and immunostained to detect T cell expansion, which indicating that Hf-DBB^F-Ir@CpG(+)+αPD-L1 treatment promoted T cell expansion on bilateral DLNs (**Figure 5-29**). These results suggest that the combination of Hf-DBB^F-Ir@CpG(+)+αPD-L1 not only induces innate immune response but also augments adaptive immunity in both treated local and untreated distant tumors.

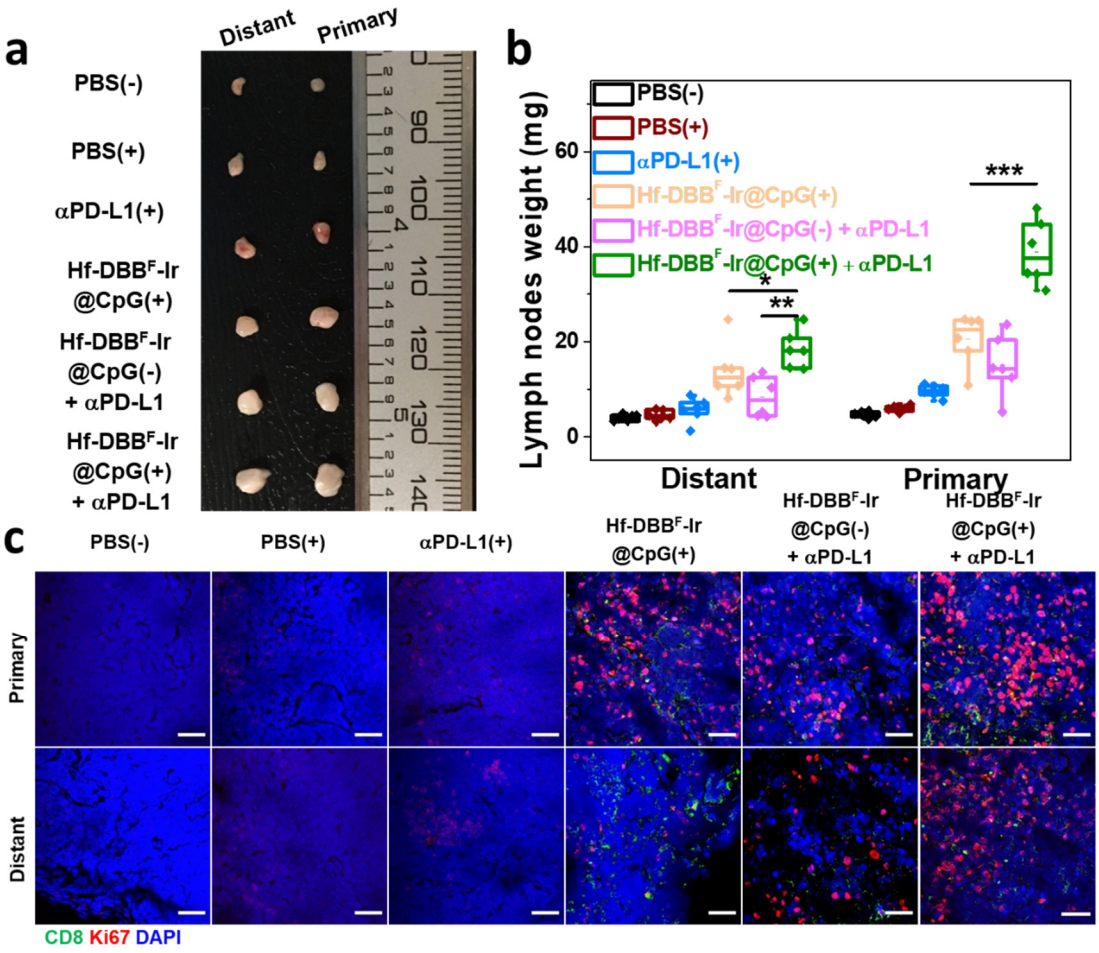

Figure 5-29 (a) Photo of excised tumor-draining lymph nodes of MC38-bearing C57BL/6 mice. From top to bottom: PBS(-), PBS(+), α-PD-L1(+), Hf-DBB^F-Ir@CpG(+), Hf-DBB^F-Ir(-)@CpG+α-PD-L1, and Hf-DBB^F-Ir@CpG(+)+α-PD-L1. (b) Weights of excised tumor-draining lymph nodes of the MC38-bearing mice. Data are expressed as means ± s.d., n = 6. *P < 0.05, **P < 0.005, and ***P < 0.001 by t-test. (c) Representative immunofluorescence imaging of excised tumor-draining lymph nodes of MC38-bearing C57BL/6 mice for detecting T cell expansion. Blue, green, and red fluorescence indicate nucleus, CD8α and Ki67, respectively. Scale bar = 100 μm.

We then determined the presence of tumor-antigen specific cytotoxic T cells with an IFN-γ Enzyme-Linked ImmunoSpot (ELISpot) assay. Splenocytes were harvested from MC38-bearing mice 10 days post first irradiation and stimulated with the peptide sequence KSPWFTTL for 42 hours. IFN-γ spot forming cells were counted with an Immunospot Reader. The number of antigen-specific IFN-γ producing T cells per 10^6 splenocytes significantly increased in tumor-bearing mice treated with Hf-DBB^F-Ir@CpG(+) and Hf-DBB^F-Ir@CpG(+)+αPD-L1 (60.2 ± 39.6 with $P < 0.04$ and 139.0 ± 52.4 compared to 16.4 ± 5.9 for PBS(-), **Figure 5-30**), suggesting that both Hf-DBB^F-Ir@CpG(+) and Hf-DBB^F-Ir@CpG(+)+αPD-L1 effectively generate tumor-specific T cell responses.

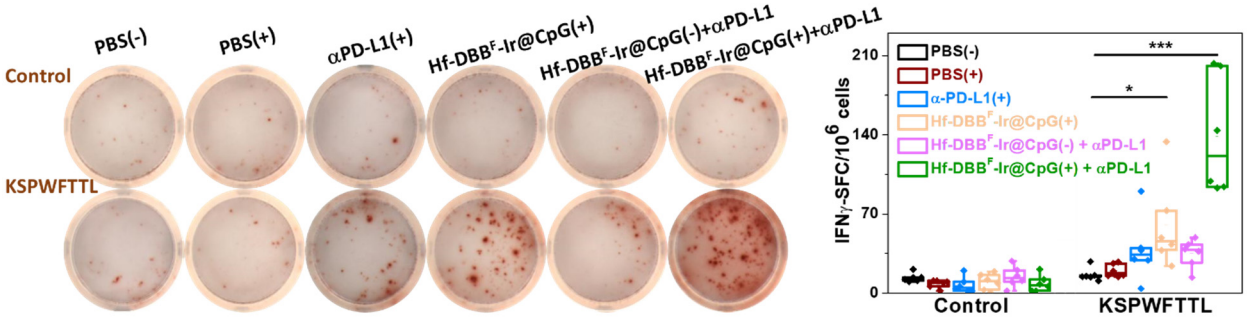

Figure 5-30 Representative images of colonies (left) and statistical analysis (right) of ELISpot assay performed to detect tumor-specific IFN-γ producing T cells, n = 6.

To further investigate the specific antitumor immunity, we treated MC38 primary tumors with Hf-DBB^F-Ir@CpG(+) or Hf-DBB^F-Ir@CpG(+)+αPD-L1 to observe if the treatment could regress unmatched syngeneic tumors on distant flanks. As illustrated in **Figure 5-31a**, MC38 were used as the primary treated tumors and syngeneic tumor cell lines B16F10 and LL2 were implanted concurrently as the distant untreated tumors. Both Hf-DBB^F-Ir@CpG(+) and Hf-DBB^F-Ir@CpG(+)+αPD-L1 treatments effectively regressed the primary MC38 tumors but had no effect

on the distant B16F10 or LL2 tumors (**Figure 5-31b-e**). These experiments indicate tumor-specificity and personalized nature of the newly expanded T cells following in situ vaccination with the Hf-DBB^{F}-Ir@CpG(+)+αPD-L1 treatment.

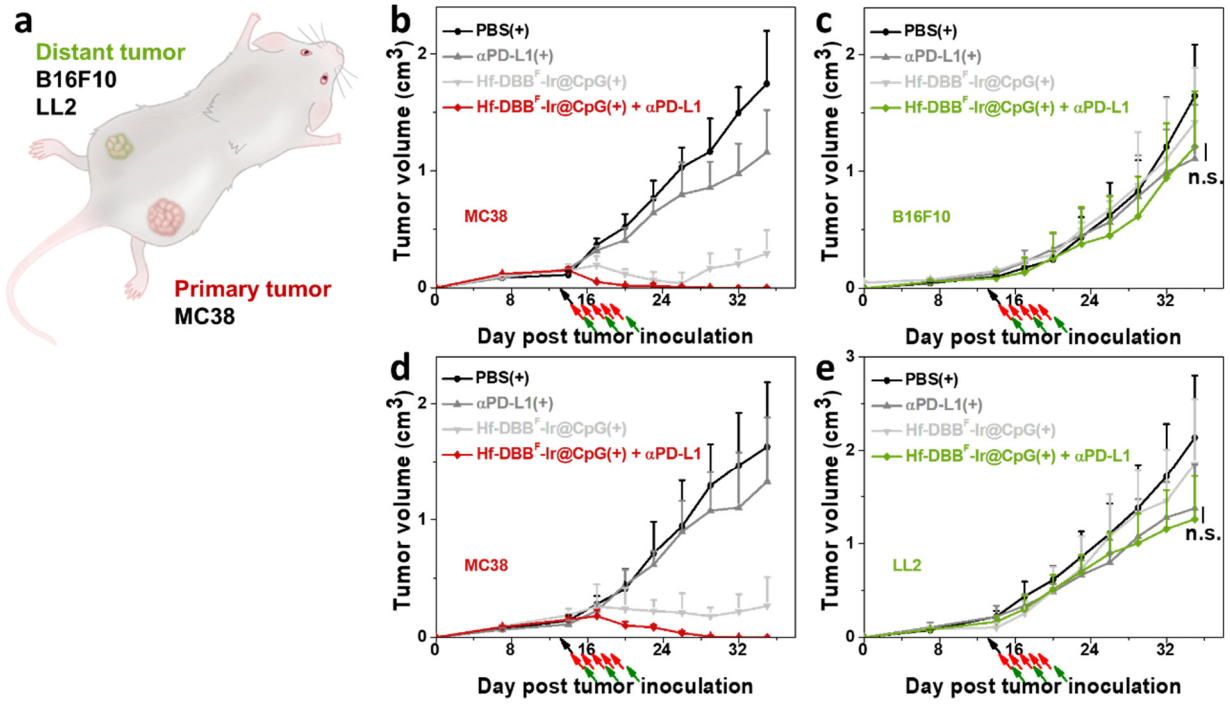

Figure 5-31 (a) Schematic illustration of bilateral models established by s.c. injection of MC38 and B16F10 or LL2 cells onto flanks as primary and distant tumors, respectively. Primary treated MC38 (b, d) and distant untreated (B16F10 for c and LL2 for e) tumor growth curves on unmatched bilateral tumor models treated with PBS(+),αPD-L1(+), Hf-DBB^{F}-Ir@CpG(+), or Hf-DBB^{F}-Ir@CpG(+)+αPD-L1, n = 4.

The involvement of cytotoxic T cells in efficient abscopal effect was further supported by the lack of efficacy of Hf-DBB^{F}-Ir@CpG(+)+αPD-L1 treatment on a bilateral subcutaneous model of MC38 on Rag2$^{-/-}$ C57BL/6 mice deficient of mature T and B cells. The primary tumors treated with Hf-DBB^{F}-Ir@CpG(+)+αPD-L1 were initially suppressed, but grew rapidly after the end of X-ray irradiation. No abscopal effect was observed on the distant tumors (**Figure 5-32**). This result

confirms that both the abscopal effect and local tumor regression/eradication require the presence of tumor-specific adaptive immunity.

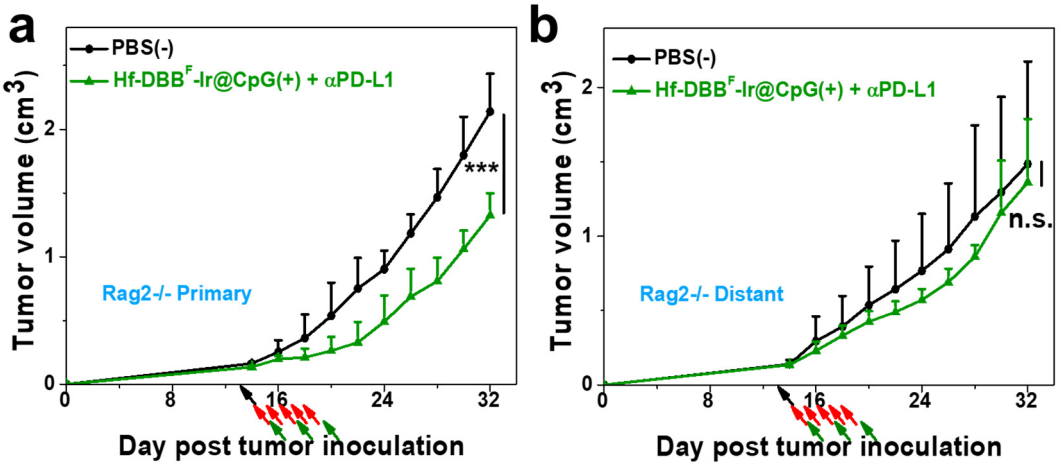

Figure 5-32 Primary (a) and distant (b) tumor growth curves on MC38-bearing Rag2$^{-/-}$ models treated with PBS(-) or Hf-DBB^F-Ir@CpG(+)+αPD-L1, n = 6.

Finally, we carried out a tumor rechallenge study to confirm the long-term immune memory effect. For the mice completely cured after treatment with Hf-DBB^F-Ir@CpG(+)+α PD-L1, 5×10^5 MC38 cells were inoculated on the contralateral, left flank 30 days post tumor eradication and those cured mice remained tumor-free after first challenge, indicating strong antitumor immune memory effect. 2 months after the first challenge, 2×10^6 B16F10 cells were inoculated on the right flank and the cured mice established tumors similarly to naïve mice, suggesting the tumor-specificity of the immune memory effect (**Figure 5-33a**). We also profiled memory effector cells ($CD3\varepsilon^+CD8\alpha^+CD44^{high}CD62L^{low}$ phenotype) in splenocytes after the combination treatment. As shown in **Figure 5-33b**, significant increase of memory effector cells was observed in spleens after Hf-DBB^F-Ir@CpG(+)+αPD-L1 treatment.

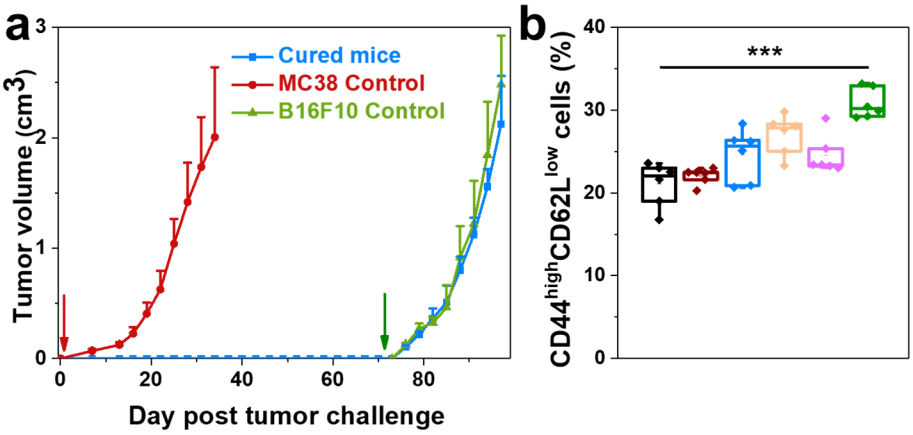

Figure 5-33 (a) Tumor growth curves after challenge with MC38 tumor cells and rechallenge with B16F10 cells on cured mice as treated from **Figure 5-27**. (b) The percentages of $CD44^{high}CD62L^{low}$ cells with respect to the total splenocytes, n = 6.

5.3 Discussion

Checkpoint blockade immunotherapy has become a standard of care for some cancers by targeting T cell inhibitory checkpoint signaling pathways to afford durable anticancer efficacy with low side effects. Immune checkpoint inhibition, however, only elicits durable responses in a minority of cancer patients due to the reliance on immunogenic tumor microenvironments, so-called "hot" tumors. For patients with relatively "cold" tumors, e.g., low tumor mutation burden, low PD-L1 expression level and/or low abundance of pre-existing T cells, immunoadjuvant treatments to turn "cold" tumors "hot" are actively examined in combination with checkpoint inhibitors to overcome immune tolerance and potentiate antitumor immunity in the host system. Here, to increase the difficulty for CBI, few cells were subcutaneously injected to establish a 14-day MC38 mice model with strong immunosuppression (data not shown).

Personalized vaccines overcoming tumor heterogeneity are lengthy, complicated, and expensive[12]. *In situ* cancer vaccination induced by immunostimulatory treatments can afford systemic antitumor immune responses in a personalized fashion and modulate local tumor microenvironments to relieve immunosuppression[13]. Having previously described the abscopal effect in the setting of RT (Chapter 2) and RT-RDT (Chapter 4) as immunoadjuvant therapies, we propose that local treatment generating innate immunity with tumor antigen exposure may effectively reinvigorate "cold" tumors to immunogenic hotbeds. Furthermore, two pattern recognition receptor (PRR) pathways[14], cGAS-STING induced by DAMPs after RT damage[3, 15] and TLR pathway induced by PAMPs like CpG[16] operate independently[17], indicating that they may be activated simultaneously to achieve an additive or synergistic effect on immune stimulation. Cationic Hf-based nMOF, Hf-DBB^{F}-Ir, stimulates non-viral *in situ* vaccination by mediating efficient RT-RDT to generate immunogenic tumor antigens and DAMPs and to deliver anionic

CpG as PAMPs. To our knowledge, Hf-DBB^{F}-Ir@CpG(+) provides the first treatment with synergistic DAMPs and PAMPs packaged in the *in situ* cancer vaccine in local tumors while engaging lymphoid organs for antigen presentation to synergize with CBI to induce CTL infiltration in distant tumors. Furthermore, the 83.3% cure rate achieved by Hf-DBB^{F}-Ir@CpG(+)+αPD-L1 on a relatively immunosuppressive 14-day MC38 colorectal cancer model suggests the potential use of nMOF-based *in situ* vaccines on immunologically "cold" tumors.

The *in situ* cancer vaccination afforded by nMOFs has several potential advantages over traditional cancer vaccines. First, the *in situ* vaccine afforded by nMOFs is personalized from autologous antigens released from tumors by a myriad of ROSs, and can overcome the tumor heterogeneity issue facing traditionally manufactured peptide vaccines. Second, cationic nMOFs can capture DAMPs and tumor antigens from dying cancer cells via electrostatic interactions, and with virus-like size distribution, can be recognized and taken up by APCs for efficient antigen presentation to stimulate a strong cytotoxic T-cell response. Third, cationic nMOFs deliver and protect anionic CpGs from enzymatic degradation for TLR stimulation and downstream immunologic processes. Fourth, tumor antigens and DAMPs released by the nMOF-mediated RT-RDT process and CpG-based PAMPs delivered by cationic nMOFs work synergistically to stimulate DC maturation to promote antigen presentation and adaptive immunity. Fifth, the nMOF-based vaccine is activated by X-rays to release DAMPs and tumor antigens with relatively nontoxic components, and is thus expected to have few side effects. Furthermore, systemic administration of αPD-L1 blocks the immunosuppressive co-inhibitory marker PD-L1 to augment antigen presentation and attenuate T cell exhaustion. The combination of nMOF-mediated *in situ* cancer vaccine with CBI affords tumor-specific and long-term antitumor immunity.

5.4 Conclusion

In this chapter, we have designed a novel nMOF, Hf-DBB^{F}-Ir, by rationally fluorinating photosensitizing ligands for effective ROS generation through RT-RDT and tuning nMOF surface charge for efficient CpG loading. Following intratumoral administration of Hf-DBB^{F}-Ir and X-ray irradiation, the *in situ* released DAMPs and tumor antigens and PAMPs delivered by Hf-DBB^{F}-Ir synergistically function as a potent personalized cancer vaccine to activate APCs and expand cytotoxic T cells in tumor-draining lymph nodes to reinvigorate the adaptive immune system for local tumor regression. CpG effectively promoted the innate immunity stimulated by local RT-RDT on an immunosuppressive murine colorectal cancer model, solidified with promoted innate immunity, expanding T cell population in tumor-draining lymph node, and adoptive T cell transfer on immunodeficient mice. When combined with an immune checkpoint inhibitor, innate and adaptive immunity from the nMOF-based cancer vaccine were further enhanced to generate superb antitumor efficacy with tumor specificity and long-term immune memory effect. This combination treatment extends the local therapeutic effects of the *in situ* cancer vaccine to distant tumors *via* systemic antitumor immunity by re-activating CTLs to afford a durable tumor-specific immunity.

5.5 Methods

Cell lines and animals: All of the starting chemicals were purchased from Sigma-Aldrich and Fisher (USA), unless otherwise noted, and used without further purification.

Murine colorectal adenocarcinoma cell line MC38, Lewis lung carcinoma cell line LL2, and melanoma cell line B16F10 were purchased from the American Type Culture Collection (Rockville, MD, USA). Murine pancreatic cancer cell line Panc02 was kindly provided by Dr. Hans Schreiber from Department of Pathology, University of Chicago. MC38-ova cell line (OVA(257-264)-ZSGREEN) was generated by transfection of MC38 cells with LZRS-based retrovirus. All of the cells were cultured in Dulbecco's Modified Eagle's Medium (DMEM) medium (GE Healthcare, USA) supplemented with 10% FBS, 100 U/mL penicillin G sodium and 100 μg/mL streptomycin sulfate. C57BL/6 mice (6 - 8 weeks) were obtained from Harlan-Envigo Laboratories, Inc (USA). The study protocol was reviewed and approved by the Institutional Animal Care and Use Committee at the University of Chicago.

$^{\bullet}$OH generation: Aminophenyl fluorescein (APF, ThermoFisher, USA) reacts with $^{\bullet}$OH to give bright green fluorescence (excitation/emission maxima 490/515 nm). H_2DBB-Ir, H_2DBB^F-Ir, Hf-DBB-Ir, or Hf-DBB^F-Ir were suspended in water at an equivalent concentration of 20 μM in the presence of 5 μM APF. A water solution of 5 μM APF was used as blank control. 100 μL of each suspension was added to a 96-well plate and then irradiated with X-rays at 0, 1, 2, 3, 5, or 10 Gy. The fluorescence signal was immediately collected with an IVIS 200 imaging system (Xenogen, USA).

$^1O_2$ generation: Singlet oxygen sensor green (SOSG, ThermoFisher, USA) reacts with $^1O_2$ to give bright green fluorescence (excitation/emission maxima 504/525 nm). H_2DBB-Ir, H_2DBB^F-Ir,

Hf-DBB-Ir, or Hf-DBB^{F}-Ir were suspended in water at an equivalent concentration of 20 μM in the presence of 12.5 μM SOSG. A water solution of 12.5 μM SOSG was used as blank control. 100 μL of each suspension was added to a 96-well plate and then irradiated with X-rays at 0, 1, 2, 3, 5, or 10 Gy. The fluorescence signal was immediately collected with a Xenogen IVIS 200 imaging system.

O_2^- generation: 5-tert-butoxycarbonyl 5-methyl-1-pyrroline N-oxide (BMPO) is a nitrone spin trap, which can form distinguishable adducts with O_2^- (BNPO-O_2^-) with a long half-life ($t_{1/2}$ = 23 minutes). PBS, H_2DBB-Ir, H_2DBB^{F}-Ir, Hf-DBB-Ir, or Hf-DBB^{F}-Ir were suspended in benzene at an equivalent concentration of 200 μM in the presence of 25 mM BMPO. A benzene solution of 25 mM BMPO was used as a blank control. 1 mL of each suspension was added to a 4 mL vial and then irradiated with X-ray at 5 Gy. The electron paramagnetic resonance (EPR) signal was immediately collected by an X-Band ELEXSYS-II 500 EPR (Bruker, USA).

Clonogenic assay: The clonogenic assay was performed according to a modified protocol. MC38 cells were cultured in a 6-well plate overnight and incubated with particles at a Hf concentration of 20 μM for 4 h followed by irradiation with 0, 1, 2, 4, 8 and 16 Gy X-ray or γ- ray. Cells were trypsinized and counted immediately. 200-2000 cells were seeded in a 6-well plate and cultured with 2 mL medium for 15 days. Once colony formation was observed, the culture medium was discarded. The plates were rinsed twice with PBS, then stained with 500 μL of 0.5% w/v crystal violet in 50% methanol/H_2O. The wells were rinsed with water for three times and the colonies were counted manually.

Cytotoxicity: 3-(4,5-dimethylthiazol-2-yl)-5-(3-carboxymethoxyphenyl)-2-(4-sulfo-phenyl)-2H-tetrazolium (MTS) assay (Promega, USA) was used to evaluate cytotoxicity with X-ray irradiation.

MC38 cells were seeded on 96-well plates at 1×10^4/well and further cultured for 12 h. PBS, H_2DBB-Ir, H_2DBB^F-Ir, Hf-DBB-Ir, or Hf-DBB^F-Ir was added to the cells at an equivalent ligand dose of 0, 1, 2, 5, 10, 20, 50 and 100 μM and incubated for 4 h. The cells were then irradiated with X-rays at a dose of 2 Gy. The cells were further incubated for 72 h before determining the cell viability by MTS assay.

Live/dead cell analysis: The live/dead cell analysis was evaluated with cell permeable dye calcein AM and propidium iodide (PI) kit. MC38 cells were cultured in a 6-well plate at 5×10^5/well overnight and incubated with PBS, H_2DBB-Ir, H_2DBB^F-Ir, Hf-DBB-Ir, or Hf-DBB^F-Ir at an equivalent concentration of 20 μM for 4 h by irradiation with 0 or 2 Gy. The cells were then washed with PBS gently and stained with calcein AM (green) for visualization of live cells and with PI (red) for visualization of dead cells under FLUOVIEW FV1000 confocal laser scanning microscope (Olympus, Japan).

Immunogenic cell death: The immunogenic cell death was examined by calreticulin (CRT) exposure. MC38 cells were cultured in a 6-well plate at 5×10^5/well overnight and incubated with PBS, H_2DBB-Ir, H_2DBB^F-Ir, Hf-DBB-Ir, or Hf-DBB^F-Ir at an equivalent concentration of 20 μM followed by irradiation at 0 and 2 Gy (Philips RT250 X-ray generator, 250 kVp, 15 mA, 1 mm Cu filter). The cells were then washed with PBS gently and stained with AlexaFluor 488-CRT antibody (Enzo Life Sciences, USA) with 1: 100 dilution for flow cytometric analysis.

Phagocytosis: C57BL/C bone-marrow-derived monocytic cells were harvested, cultured and activated. Murine granulocyte–macrophage colony-stimulating factor (GM-CSF) and IL-4 were supplied to a final concentration of 1% for 168 h and the non-adherent cells as immature DCs were harvested for following studies. Medium was replaced every 2–3 days and cells were used after 6

to 8 days of culture. 5×10^5 CFSE-labeled (Life Technologies, USA) MC38 cells were cultured in a 6-well plate overnight and incubated with PBS, H_2DBB-Ir, H_2DBB^F-Ir, Hf-DBB-Ir, or Hf-DBB^F-Ir at an equivalent dose of 20 μM for 4 h followed by X-ray irradiation at a dose of 0 or 2 Gy. 1×10^6 PE-Cy5.5-labeled DCs were added and co-cultured with the treated MC38 cells at 37 °C for 4 h. Cells were then collected, washed twice with cold PBS, imaged by CLSM or analyzed by flow cytometry.

***In situ* vaccination on syngeneic models:** Synergistic tumor models, MC38, MC38-ova and Panc02 were established to evaluate the in vivo anti-cancer efficacy of nMOF-mediated in situ vaccination. For single tumor models, 5×10^5 MC38 cells, 1×10^6 MC38-ova cells or 1×10^6 Panc02 cells were subcutaneously inoculated onto the right flanks of C57BL/6 mice. When the tumors reached 100-150 mm^3 in volume, mice were injected intratumourally with nMOFs at a dose of 0.2 μmol Hf, CpG at a dose of 1 μg or PBS. 12 h after injection, mice were anaesthetized with 2% (v/v) isoflurane and the tumors were irradiated with 1 Gy X-ray/fraction for a total of 5 daily fractions. For bilateral tumor models, 5×10^5 MC38 cells were subcutaneously inoculated onto the right flanks as primary tumors while 2×10^5 MC38 cells, 2×10^5 B16F10 cells or 5×10^5 LL2 cells were subcutaneously inoculated onto the left flanks as distant tumors of C57BL/6 mice. αPD-L1 (Clone: 10F.9G2, Catalog No. BE0101, BioXCell) were given every three days by intraperitoneal injection at a dose of 75 μg/mouse. The tumor sizes were measured daily with a caliper where tumor volume equals $(width^2 \times length)/2$.

ELISpot assay: Tumor-specific immune responses to IFN-γ was measured *ex vitro* by ELISpot assay (Mouse IFN gamma ELISPOT Ready-SET-Go!®; Cat. No. 88-7384-88; eBioscience). Millipore Multiscreen HTS-IP plates was coated overnight at 4°C with anti-Mouse IFN-γ capture antibody. Single-cell suspensions of splenocytes were obtained from MC38 tumor-carrying mice

and seeded onto the antibody-coated plate at a concentration of 2×10^5 cells/well. Cells were incubated with or without peptide sequence (KSPWFTTL) for 42 h at 37 °C and then discarded. The plate was then incubated with biotin-conjugated anti-IFN-γ detection antibody at room temperature (r.t.) for 2 h, followed by incubation with Avidin-HRP for 2 h at r.t. 3-amino-9-ethylcarbazole substrate solution (Sigma, Cat. AEC101) was added for cytokine spot detection. Spots were imaged and quantified with a CTL ImmunoSpot Analyzer (Cellular Technology Ltd, USA).

Flow Cytometry: Tumors were harvested, treated with 1 mg/mL collagenase I (Gibco™, USA) for 1 h, and ground by the rubber end of a syringe. Cells were filtered through nylon mesh filters with size of 40 μm and washed with PBS. tumor-draining lymph nodes were collected and directly ground through the cell strainers. The single-cell suspension was incubated with anti-CD16/32 (clone 93) to reduce nonspecific binding to FcRs. Cells were further stained with the following fluorochrome-conjugated antibodies: CD45 (30-F11), CD3ε (145-2C11), CD4 (GK1.5), CD8 (53-6.7),Nkp46 (29A1.4), F4/80 (BM8), CD11b (M1/70), Gr-1 (RB6-8C5), MHC-II (AF6-120), CD80 (16-10A1), CD86 (GL1), CD206 (C068C2), CD44 (IM7), CD62L (MEL-14), H-2Kb SIINFEKL (25-D1.16), PI, and yellow-fluorescent reactive dye (all from eBioscience). Antibodies were used with the dilution of 1: 200. LSR Fortessa (BD Biosciences) was used for cell acquisition and data analysis was carried out with FlowJo software (Tree Star, Ashland, OR). Gating strategies are shown as **Figure 5-34** and **5-35**.

Adoptive OT-I T cells transfer: 2×10^6 MC38-ova cells were injected subcutaneously onto the right flanks of C57BL/6 $Rag2^{-/-}$ mouse. 14 days later, mice were intratumorally injected with Hf-DBB^F-Ir at a dose of 0.2 μmol Hf with or without CpG at a dose of 1 μg followed by 1 Gy X-ray/fraction for a total of 5 daily fractions. 2 days post the first irradiation, spleen and lymph nodes

were isolated from OT-I mice and $CD8^+$ T cells were negatively sorted using mouse $CD8^+$ T Cell Isolation Kit (Miltenyi Biotec, Germany), 1×10^6 $CD8^+$ T cells were intravenously injected into MC38-ova-bearing $Rag2^{-/-}$ mice. The tumor sizes were measured daily with a caliper where tumor volume equals $(width^2 \times length)/2$.

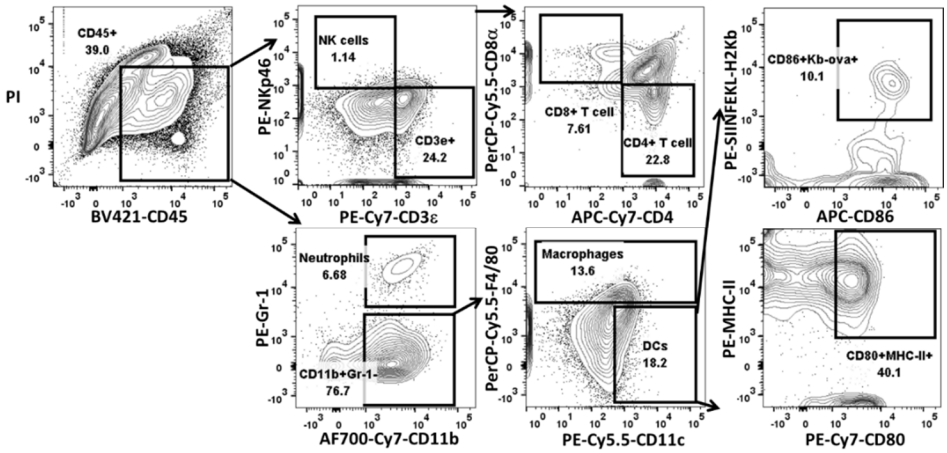

Figure 5-34 Representative gating strategies for $CD45^+$ cells, NK cells, $CD4^+$ T cells, $CD8^+$ T cells, neutrophils, macrophages, dendritic cells, SIINFEKL-H_2Kb^+ cells and $CD80^+$ $MHC\text{-}II^+$ cells profiled from tumor and lymph nodes.

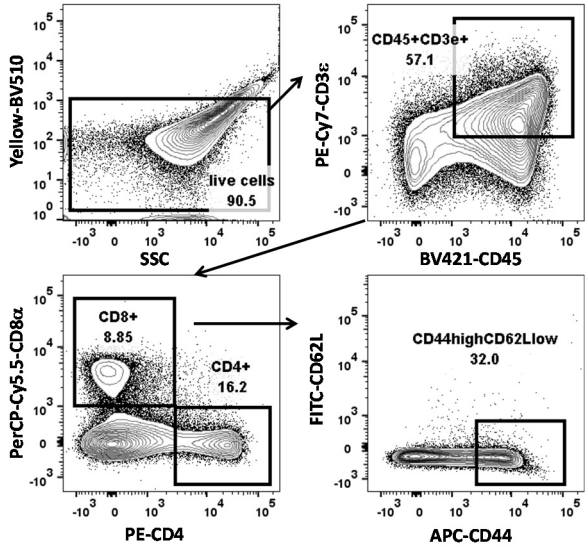

Figure 5-35 Representative gating strategies for $CD44^{high}CD62^{low}$ cells profiled from spleen.

5.6 References

1. Shae, D.; Becker, K. W.; Christov, P.; Yun, D. S.; Lytton-Jean, A. K.; Sevimli, S.; Ascano, M.; Kelley, M.; Johnson, D. B.; Balko, J. M., Endosomolytic polymersomes increase the activity of cyclic dinucleotide STING agonists to enhance cancer immunotherapy. *Nature Nanotechnology* **2019,** *14* (3), 269.

2. Luo, M.; Wang, H.; Wang, Z.; Cai, H.; Lu, Z.; Li, Y.; Du, M.; Huang, G.; Wang, C.; Chen, X., A STING-activating nanovaccine for cancer immunotherapy. *Nature Nanotechnology* **2017,** *12* (7), 648.

3. Deng, L.; Liang, H.; Xu, M.; Yang, X.; Burnette, B.; Arina, A.; Li, X.-D.; Mauceri, H.; Beckett, M.; Darga, T., STING-dependent cytosolic DNA sensing promotes radiation-induced type I interferon-dependent antitumor immunity in immunogenic tumors. *Immunity* **2014,** *41* (5), 843-852.

4. Klinman, D. M., Immunotherapeutic uses of CpG oligodeoxynucleotides. *Nature Reviews Immunology* **2004,** *4* (4), 249.

5. Figdor, C. G.; de Vries, I. J. M.; Lesterhuis, W. J.; Melief, C. J., Dendritic cell immunotherapy: mapping the way. *Nature Medicine* **2004,** *10* (5), 475.

6. Lutz, M. B.; Schuler, G., Immature, semi-mature and fully mature dendritic cells: which signals induce tolerance or immunity? *Trends in Immunology* **2002,** *23* (9), 445-449.

7. Tao, Y.; Ju, E.; Ren, J.; Qu, X., Immunostimulatory oligonucleotides-loaded cationic graphene oxide with photothermally enhanced immunogenicity for photothermal/immune cancer therapy. *Biomaterials* **2014,** *35* (37), 9963-9971.

8. Brody, J. D.; Ai, W. Z.; Czerwinski, D. K.; Torchia, J. A.; Levy, M.; Advani, R. H.; Kim, Y. H.; Hoppe, R. T.; Knox, S. J.; Shin, L. K., *In situ* vaccination with a TLR9 agonist induces systemic lymphoma regression: a phase I/II study. *Journal of Clinical Oncology* **2010,** *28* (28), 4324.

9. Rosi, N. L.; Giljohann, D. A.; Thaxton, C. S.; Lytton-Jean, A. K.; Han, M. S.; Mirkin, C. A., Oligonucleotide-modified gold nanoparticles for intracellular gene regulation. *Science* **2006,** *312* (5776), 1027-1030.

10. Cavka, J. H.; Jakobsen, S.; Olsbye, U.; Guillou, N.; Lamberti, C.; Bordiga, S.; Lillerud, K. P., A new zirconium inorganic building brick forming metal organic frameworks with exceptional stability. *Journal of the American Chemical Society* **2008,** *130* (42), 13850-13851.

11. Lowry, M. S.; Goldsmith, J. I.; Slinker, J. D.; Rohl, R.; Pascal, R. A.; Malliaras, G. G.; Bernhard, S., Single-layer electroluminescent devices and photoinduced hydrogen production from an ionic iridium (III) complex. *Chemistry of Materials* **2005,** *17* (23), 5712-5719.

12. Scheetz, L.; Park, K. S.; Li, Q.; Lowenstein, P. R.; Castro, M. G.; Schwendeman, A.; Moon, J. J., Engineering patient-specific cancer immunotherapies. *Nature Biomedical Engineering* **2019,** *3* (10), 768-782.

13. Wang, H.; Mooney, D. J., Biomaterial-assisted targeted modulation of immune cells in cancer treatment. *Nature Materials* **2018,** *17* (9), 761-772.

14. Kawai, T.; Akira, S., The role of pattern-recognition receptors in innate immunity: update on Toll-like receptors. *Nature Immunology* **2010,** *11* (5), 373.

15. Gong, T.; Liu, L.; Jiang, W.; Zhou, R., DAMP-sensing receptors in sterile inflammation and inflammatory diseases. *Nature Reviews Immunology* **2019**, 1-18.

16. Weiner, G. J.; Liu, H.-M.; Wooldridge, J. E.; Dahle, C. E.; Krieg, A. M., Immunostimulatory oligodeoxynucleotides containing the CpG motif are effective as immune adjuvants in tumor antigen immunization. *Proceedings of the National Academy of Sciences* **1997,** *94* (20), 10833-10837.

17. Emming, S.; Schroder, K., Tiered DNA sensors for escalating responses. *Science* **2019,** *365* (6460), 1375-1376.

CHAPTER 6. Nanoscale Metal-organic Frameworks Mediates Hormone- and Light-Triggered Radical Therapy to Enhance Cancer Immunotherapy

6.1 Rationale for the project design

In previous chapters, we discussed several cases of nMOF-mediated ROS generation upon low-dose X-ray irradiation to potentiate cancer immunotherapy. Besides high energy X-ray/γ-ray, photons provide an alternative energy source for local immunoadjuvant therapy. In photodynamic therapy (PDT), tumors with preferentially accumulated photosensitizers (PSs) are activated by photons to convert tissue oxygen to cytotoxic singlet oxygen ($^1O_2$), which has been demonstrated to be highly immunogenic. RT, RT-RDT, or PDT needs to be activated by external stimuli to generate anti-tumor efficacy *via* ROS.

As an external stimuli-independent radical therapy, chemodynamic therapy (CDT) has attracted more and more attention for immunoadjuvancy. Redox-active metal centers in tumor microenvironment decompose endogenous substrates such as hydrogen peroxide (H_2O_2) to generate cytotoxic hydroxyl radical ($^{\cdot}OH$) and other ROS.[1-2] However, the efficacy of CDT is diminished by many factors in the TME, such as high intracellular concentrations of reducing thiol species[3], hypoxia[4], and insufficient endogenous H_2O_2[5]. It is thus of both fundamental and clinical interest to develop new strategies to counteract these adverse factors to enhance the efficacy of radical therapies.

Hormonal imbalance is a hallmark of many cancers.[6] In particular, high serum levels of estradiol, the major and most potent species of estrogens, have long been linked to increased cancer

risks[7-8]. Estradiol primarily binds to estrogen receptors, ERα and ERβ, whose expression levels directly impact cell proliferation, cell cycle arrest and ultimately, tumorigenesis[9-10]. Indeed, hormone therapy targeting the estrogen pathway to reduce cell proliferation-induced tumorigenesis has been widely used clinically[11-12]. Interestingly, estrogens have also been shown to form stable adducts with DNA via generating ROS in the downstream metabolic process that are catalyzed by bioavailable Cu^{2+} ions[13-15]. This is notable because a localized supply of free Cu^{2+} ions at the tumor sites can potentially be used to hijack the estrogen metabolic pathway and promote cytotoxic ROS generation for effective radical therapy.

In this chapter, we synthesized Cu-TBP for a novel nMOF-mediated radical therapy that utilizes Cu^{2+} to catalyze estradiol-induced CDT and porphyrin-based ligands to perform light-driven PDT to achieve local tumor control in mouse models with high estradiol expression and the combination of the radical therapy with CBI for synergistic systemic tumor rejection in subcutaneous melanoma mouse models. The degradable Cu-TBP efficiently releases Cu^{2+} and H_4TBP intratumorally. Cu^{2+} ions catalyze estradiol metabolism to generate H_2O_2, $^{\cdot}OH$ and O_2^- whereas H_4TBP mediates light-triggered PDT. The nMOF-mediated radical therapy depletes intratumoral estradiol and suppresses tumor growth. nMOF-mediated radical therapy given in conjunction with an anti-PD-L1 antibody not only eradicates local tumors but also regresses distant tumors through systemic antitumor immunity in a syngeneic B16F10 melanoma cancer model (**Figure 6-1**). We also profiled the immune responses to gain further insight into the abscopal effects elicited from the dual-triggered radical therapy with synergistic checkpoint blockade immunotherapy (CBI).

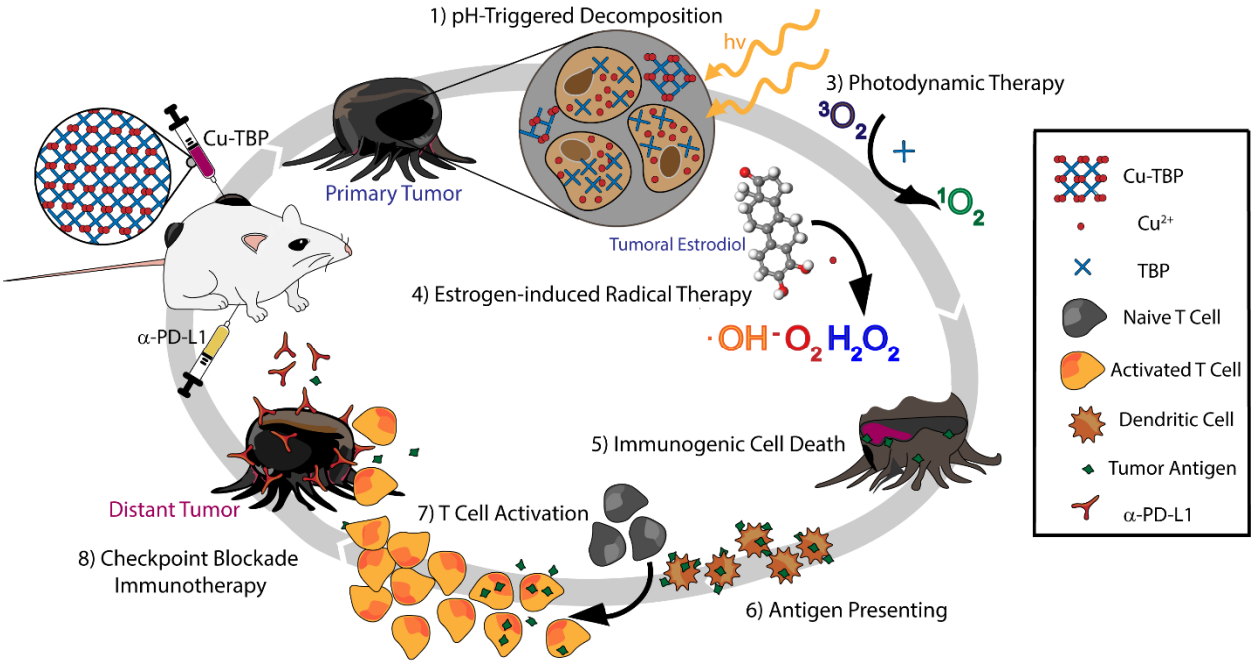

Figure 6-1 nMOF assembled from Cu-cluster and porphyrin-based tetracarboxylic acid was intratumorally injected into the primary tumors of mice bearing bilateral subcutaneous tumors and then decomposed in tumors with low pH to generate free Cu^{2+} and porphyrin. Copper can disturb the metabolism of estradiol, an important estrogen, to generate superoxide, hydroxyl radicals as well as hydrogen peroxide from which disassociated porphyrin can generate singlet oxygen through PDT process. Upon light irradiation on the primary tumors, nMOF-mediated ROS generation via PDT and estrogen-copper mechanism destroys the irradiated tumors, causing immunogenic cell death and releasing tumor antigens. Injected anti-PD-L1 antibody overcomes the suppressive tumor microenvironment by targeting PD-1/PD-L1 axis. The combination of nMOF-mediated ROS generation and anti-PD-L1 checkpoint blockade leads to the effective T cell expansion and tumor-infiltration, which effectively suppresses/eradicates the distant tumors. Adapted with permission from *Chem,* **2019**, 136, 12253–12256. Copyright 2019 Elsevier Inc.

6.2 Results

6.2.1 Synthesis and characterization of Cu-TBP

Cu-TBP nanoplates were synthesized by sonicating a mixture of $CuCl_2$ and H_4TBP in ethanol at room temperature for 2 h and exhibited the same structure as bulk phase Cu-TBP MOF[16]. Cu-TBP nanoplates have a formula of $Cu_2(H_2O)_4(TBP)$ and are assembled from $Cu_2(H_2O)_4$ paddle-wheel secondary building units (SBUs) (**Figure 6-2a**) and four-fold symmetric TBP bridging ligands (**Figure 6-2b,c**).

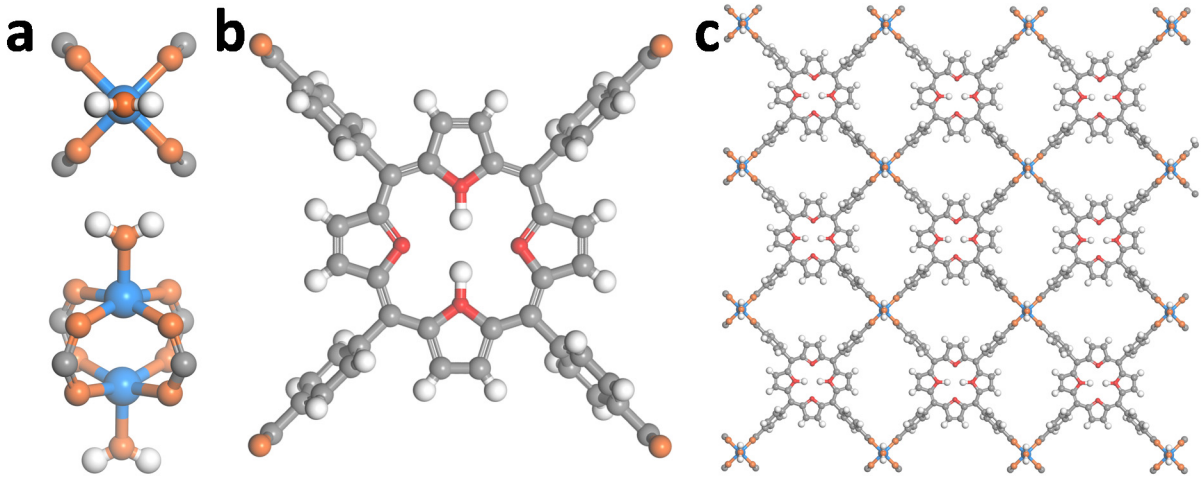

Figure 6-2 Structure of Cu-TBP. (a) Top view (top) and side view (bottom) of $Cu_2(COO)_4$ paddle-wheel SBU. (b) Chemical structure of TBP bridging ligand. (c) Structure of Cu-TBP showing a 2D network of sql topology. Blue: copper; orange: oxygen; red: nitrogen; grey: carbon; white: hydrogen. Adapted with permission from *Chem,* **2019**, 136, 12253–12256. Copyright 2019 Elsevier Inc.

Dynamic light scattering (DLS) measurements gave a number-averaged diameter and polydispersity index of 164.1 ± 48.5 nm and 0.07 ± 0.01, respectively (**Figure 6-3a**); while TEM imaging showed that Cu-TBP exhibited a nanoplate morphology with a diameter of 100~250 nm (**Figure 6-3b**). HRTEM and FFT pattern revealed four-fold symmetry that is consistent with the projection of the sql topology down the c axis (**Figure 6-3c**). PXRD pattern of Cu-TBP was

identical to the simulated pattern based on the single crystal structure of bulk phase Cu-TBP (**Figure 6-3d**). Cu-TBP showed similar absorption peaks as H_4TBP ligands, confirming the presence of non-metalated TBP in the nMOF (**Figure 6-3e**).

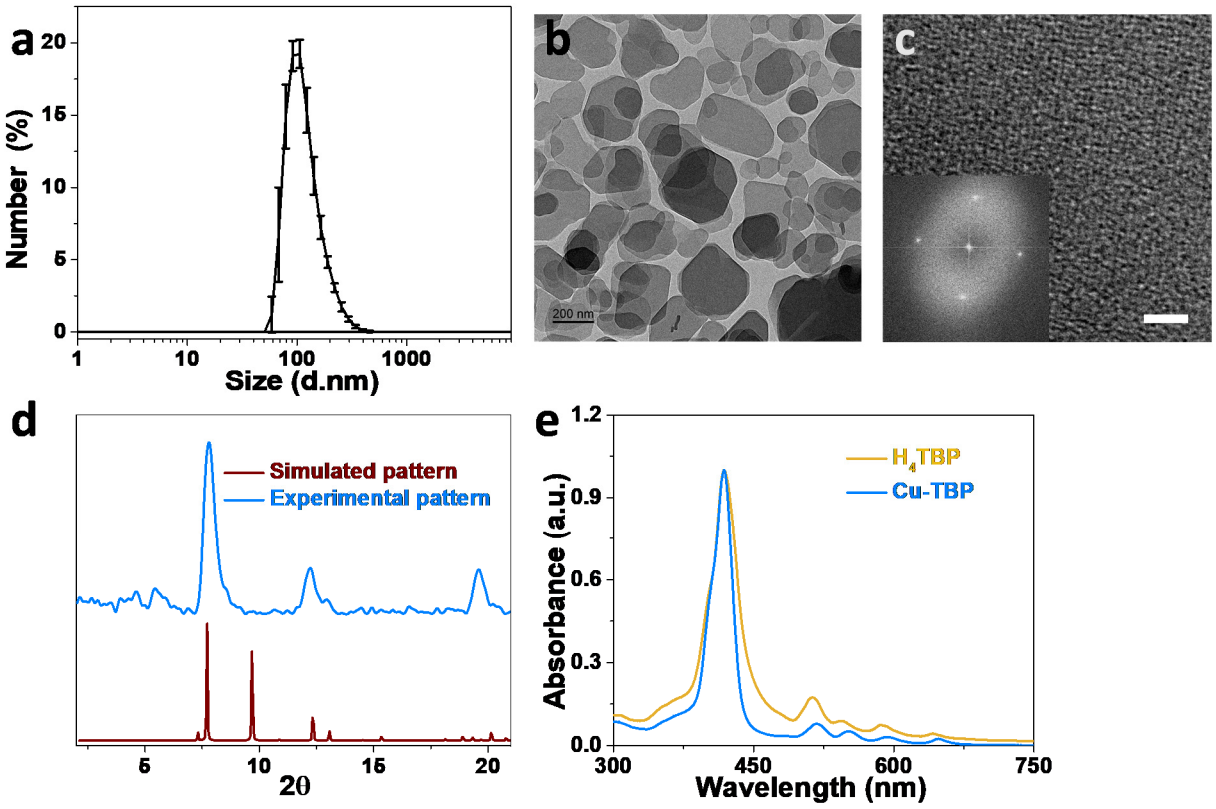

Figure 6-3 Characterization of Cu-TBP. (a) Number-averaged diameter of Cu-TBP in water by DLS measurements, n = 3. TEM (b) and HRTEM (c) image of Cu-TBP and its fast Fourier transform (FFT) pattern shown in the inset. Scale bar = 200 nm for (b) and 20 nm for (c). (d) Normalized UV-visible spectra of Cu-TBP and H_4TBP. (e) Simulated and experimental PXRD patterns of Cu-TBP. Adapted with permission from *Chem*, **2019**, *5*, 1892-1913. Copyright 2019 Elsevier Inc.

As nMOFs are endocytosed into endosomes and progressively acidic lysosomes as demonstrated in Chapters 2 and 3, we posited that Cu-TBP would only be metastable intracellularly due to the relatively weak bonding between Cu^{2+} ions and carboxylate ligands in acidic conditions, thus providing an efficient means for triggered release of Cu^{2+} ions and H_4TBP

inside cells. We analyzed the decomposition of Cu-TBP under extracellular neutral conditions as well as progressively acidic endosomal-lysosomal environments by measuring the absorbance of free H_4TBP at 402 nm in the supernatants after incubating Cu-TBP nanoplates in PBS at pH 7.4, 6.5, 5.5 and 4.5 for a pre-determined length of time.[17] Up to 80% of Cu-TBP remained intact at pH 7.4 after 24 h incubation (**Figure 6-4a**). Similarly, after 30 mins of incubation at pH 6.5, only slight decomposition of Cu-TBP was observed; however, the percent decomposition at 30 min rose to ~50% and 75% when pH level was lowered to 5.5 and 4.5 respectively, confirming the pH-triggered decomposition of Cu-TBP for the release of free Cu^{2+} and TBP ligands intracellularly. We then quantitatively compared cellular uptake of Cu-TBP and free H_4TBP ligand by UV-visible absorption spectroscopy. B16F10 cells incubated with either Cu-TBP or H4TBP at the same TBP concentration were lysed at 1, 2, 4 and 8 h time-points for TBP quantification. Cells uptook more Cu-TBP than free H_4TBP at all time-points (**Figure 6-4b**). We also determined intracellular Cu-TBP decomposition by monitoring porphyrin fluorescence of the free ligand which is completely quenched by the paramagnetic Cu^{2+} ions in intact Cu-TBP.[18] As shown in **Figure 6-4c**, the fluorescence of Cu-TBP is quenched at pH 7.4 and is recovered under acidic conditions due to the presence of free TBP from the decomposition of Cu-TBP. Both CLSM (**Figure 6-4d**) and flow cytometry (**Figure 6-4e**) studies showed that Cu-TBP treated cells exhibited more porphyrin fluorescence than H_4TBP treated cells after 2 h due to more efficient cellular internalization and rapid decomposition in acidic environment. Taken together, Cu-TBP provides an efficient nanovehicle for the delivery and release of both Cu^{2+} and H_4TBP, which are triggered by estradiol and light, respectively, to generate ROS for cell killing.

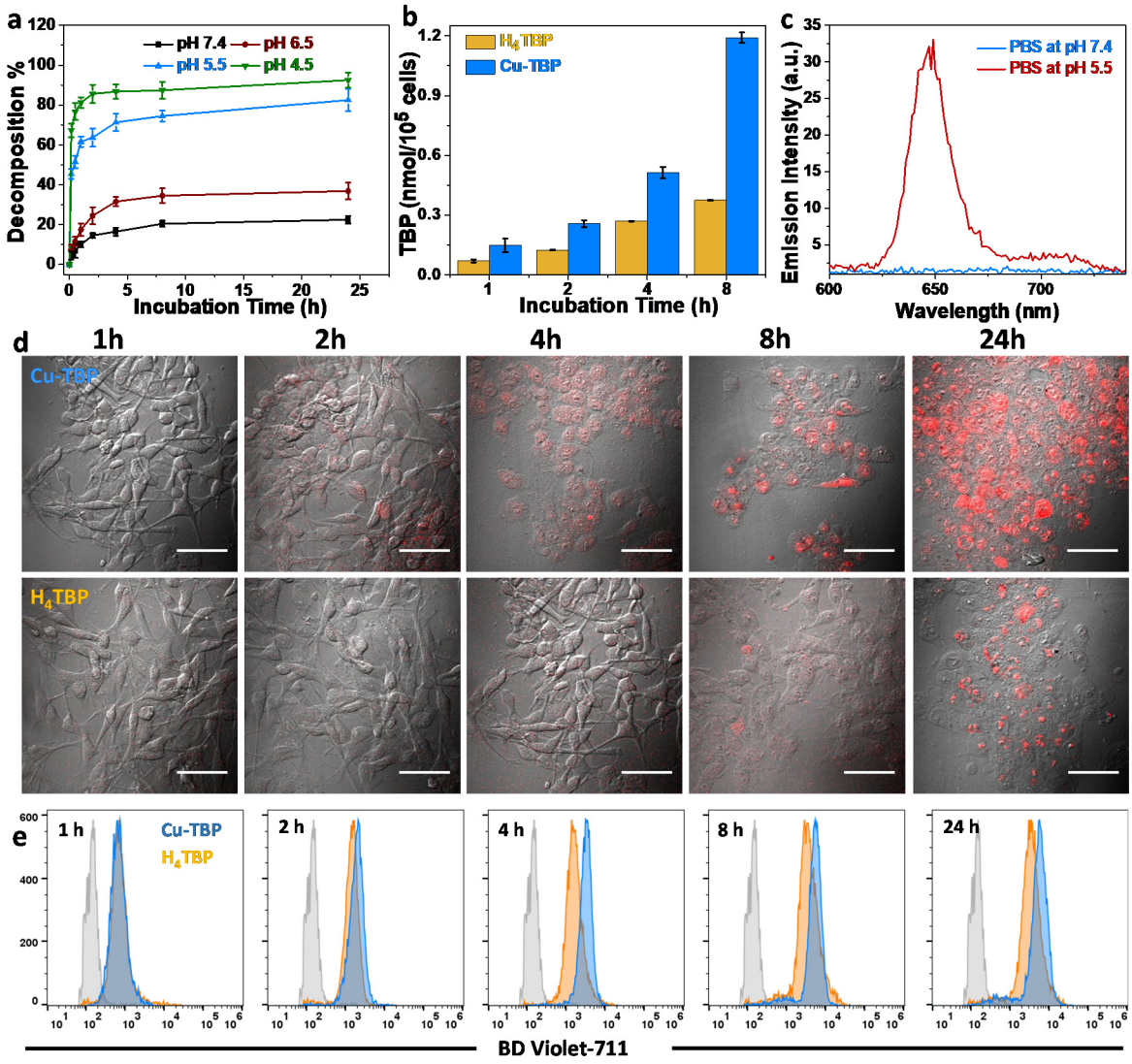

Figure 6-4 Cellular internalization and decomposition of Cu-TBP. (a) Time-dependent decomposition of Cu-TBP at pH 7.4, 6.5, 5.5 and 4.5 quantified by UV-Vis absorption of free H_4TBP, n = 3. (b) Emission spectra of Cu-TBP with 420 nm excitation at pH 5.0 or 7.0 purged with N_2. (c) Time-dependent cellular uptake of Cu-TBP or H_4TBP after 1, 2, 4 or 8 hour incubation with equivalent TBP concentrations of 20 μM. The TBP concentration was quantified by UV-Vis spectroscopy. (d) Time-dependent cellular uptake of Cu-TBP or H_4TBP after 1, 2, 4, 8 or 24 hour incubation with equivalent TBP concentrations of 20 μM monitored by confocal microscopy. Red fluorescence indicates the emission of free H_4TBP. Scale bar = 50 μm. (e) Time-dependent cellular uptake of Cu-TBP or H_4TBP after 1, 2, 4, 8 or 24 hour incubation with equivalent TBP concentrations of 20 μM detected by flow cytometry. Grey (control), blue and yellow histograms show the difference of cellular uptake level of Cu-TBP and H_4TBP in the cells, respectively. The error bars represent s.d. values. Adapted with permission from *Chem*, **2019**, *5*, 1892-1913. Copyright 2019 Elsevier Inc.

6.2.2 Hormone and light dual-triggered ROS generation

To demonstrate the feasibility of Cu^{2+}-mediated ROS generation *via* estrogen metabolic pathway, we first identified key reaction products of the pathway. As shown in **Scheme 6-1**, estradiol (E2), the major and predominant estrogen species, undergoes oxidation by cytochrome P450 to form 4-hydroxy estradiol (4-OHE2). The catechol group on 4-OHE2 can then reduce free Cu^{2+} to Cu^{+} with the concomitant formation of a semiquinone radical which subsequently transfers an electron to tissue oxygen to afford a quinone derivative and the superoxide radical (O_2^{-}). The short-lived O_2^{-} may then be reduced by superoxide dismutase (SOD) or nicotinamide adenine dinucleotide (NADH) to form stable H_2O_2, which undergoes Fenton-like reactions with Cu^{+} species to give cytotoxic $^{\bullet}OH$.[14]

Scheme 6-1 Hormone-induced Cu-mediated ROS generation process. 4-Hydroxy estradiol (4-OHE2) generated from estradiol (E2) oxidation interacts with Cu^{2+} to generate a semiquinone radical and Cu^{+}. The semiquinone radical can react with tissue O_2 to generate O_2^{-}. Intracellularly, O_2^{-} is converted to stable H_2O_2 which undergoes Cu^{+}-catalyzed Fenton-like reactions to generate $^{\bullet}OH$. Adapted with permission from *Chem*, **2019**, *5*, 1892-1913. Copyright 2019 Elsevier Inc.

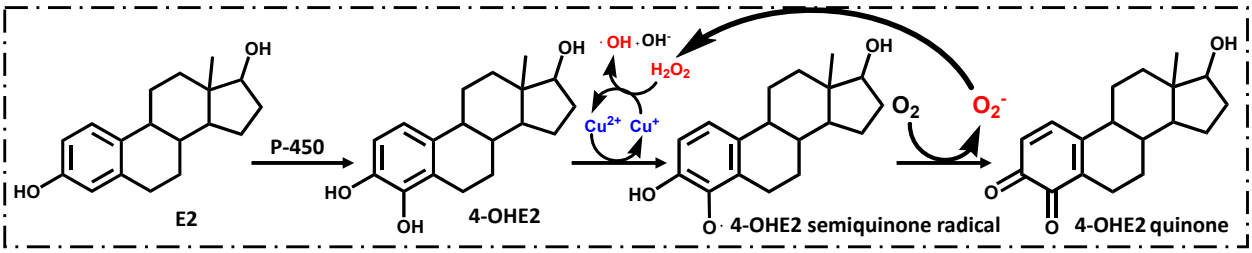

We first quantified the generation of H_2O_2 from a combination of Cu^{2+}, NADH, and 4-OHE2 using a hydrogen peroxide kit. 1 μL of hydrogen peroxide sensor solution was added to aqueous solutions of 50 μM $CuCl_2$, 100 μM NADH and/or 40 μM 4-OHE2 to give a panel of five solutions, with A, B, C, D and E representing Cu^{2+}, NADH, Cu^{2+}+4-OHE2, NADH+4-OHE2 and Cu^{2+}+NADH+4-OHE2, respectively (**Table 6-1**). The fluorescence signal at 520 nm (excitation at 490 nm) was detected and calibrated against a standard curve (**Figure 6-5a**) to quantify the

concentration of H_2O_2 generated from the Cu-estradiol redox cycle. As shown in **Figure 6-5b**, the hydrogen peroxide probe showed its fluorescence only in the presence of Cu^{2+}, NADH, and 4-OHE2, indicating that H_2O_2 can only be generated from the combination of Cu^{2+}, NADH, and 4-OHE2.

Table 6-1. Panel of five different mixtures for the generation of H_2O_2 and $^{\bullet}OH$.

Mixture	A	B	C	D	E
50 μM Cu^{2+}	√		√		√
100 μM NADH		√		√	√
40 μM 4-OHE2			√	√	√

We next confirmed the formation of $^{\bullet}OH$ using coumarin-3-carboxylic acid as the probe. In the presence of $^{\bullet}OH$, this compound is hydroxylated to form 7-hydroxycoumarin-3-carboxylic acid, which emits at 460 nm upon excitation at 380 nm. An aliquot of aqueous solution of 200 μM coumarin-3-carboxylic acid (0.1 mL) was added to a panel of five solutions, A-E, as previously described. Three independent measurements show that the coumarin probe forms its fluorescent derivative only in the presence of Cu^{2+}, NADH and 4-OHE2 (**Figure 6-5c**).

We then detected the short-lived O_2^- by electron paramagnetic resonance (EPR) spectroscopy. A nitrone spin trap, 5-tert-butoxycarbonyl 5-methyl-1-pyrroline N-oxide (BMPO), was used to form the O_2^- adduct BMPO-$^{\bullet}OOH$ which has a half-life of 23 minutes[13]. A 25mM BMPO solution served as the control. A 50 μM aqueous solution of $CuCl_2$ with or without 40 μM 4-OHE2 was added to 25 mM BMPO solution. Only the mixture containing both Cu^{2+} and 4-OHE2 showed EPR signals characteristic of the BMPO-$^{\bullet}OOH$ adduct (**Figure 6-5d**), supporting our proposed mechanistic pathways in **Scheme 6-1**.

Prior to evaluating the *in vitro* ROS generation from dual-triggered radical therapy, we determined estradiol concentrations of three human cancer cell lines with high, mid, and low estradiol concentrations.[19] Human ovarian cancer cell SKOV-3, human prostate cancer cell PC-3, and human colorectal cancer HCT-116 are reported to have estradiol concentrations of 132.33 ± 9.43, 41.94 ± 2.30 and 2.17 ± 0.13 pg/10^6 cells, respectively.[19] We determined their estradiol concentrations of 140.35 ± 13.45, 53.80 ± 9.23 and 8.30 ± 4.36 pg/10^6 cells, respectively, by Enzyme-linked immunosorbent assay (ELISA) kits (**Figure 6-6a**). We further found that the murine melanoma cell line, B16F10, exhibits a very high estradiol concentration of 124.25 ± 8.78 pg/10^6 cells (**Figure 6-6b**). We then determined cytotoxicity of dual-triggered radical therapy by 3-(4,5-dimethylthiazol-2-yl)-5-(3-carboxymethoxyphenyl)-2-(4-sulfo-phenyl)-2H-tetrazolium (MTS) assay. SKOV-3, B16F10, PC-3, and HCT-116 cells were treated with $CuCl_2$ or Cu-TBP with LED light irradiation at 0 or 90 J/cm2 (λ_{max} = 650 nm, 100 mW/cm^2, 0 or 15 min) and their cell viabilities were determined by MTS assay. Cu-TBP without light irradiation [denoted Cu-TBP(-)] has IC_{50} values of 25.68 ± 5.67, 41.33 ± 8.87, 57.23 ± 10.12 and >100 μM based on TBP concentration against SKOV-3, B16F10, PC-3 and HCT116 cells, respectively (**Figure 6-6c**). Cu-TBP with light irradiation [denoted Cu-TBP(+)] has IC_{50} values of 4.57 ± 2.45, 6.37 ± 4.26, 19.73 ± 6.78 and 34.52 ± 7.23 μM based on TBP concentration against SKOV-3, B16F10, PC-3 and HCT116 cells, respectively. These results support the Cu-estradiol redox cycle as a potential radical therapy approach and its synergy with light-triggered PDT.

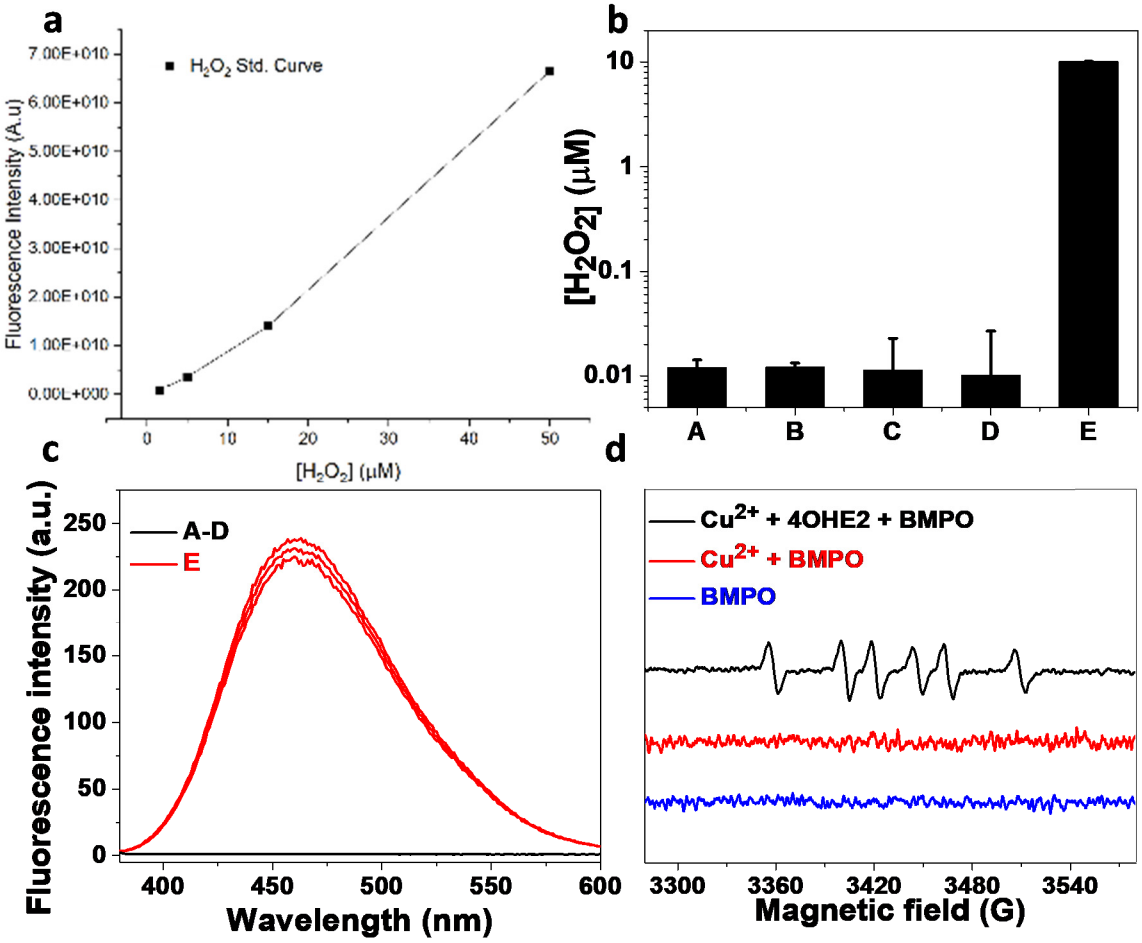

Figure 6-5 (a) Standard curve of fluorescence intensity of hydrogen peroxide probe the concentration of hydrogen peroxide. (b) Quantification of H_2O_2 generated in A-E based on the fluorescence from hydrogen peroxide kit, n = 3. (c) Quantification of $^{\bullet}OH$ generated in A-E by coumarin acid assay, n = 3. (d) EPR spectra of BMPO adduct of O_2^{-} (g = 2.006) generated from Cu^{2+} and 4-OHE2. Adapted with permission from *Chem*, **2019**, *5*, 1892-1913. Copyright 2019 Elsevier Inc.

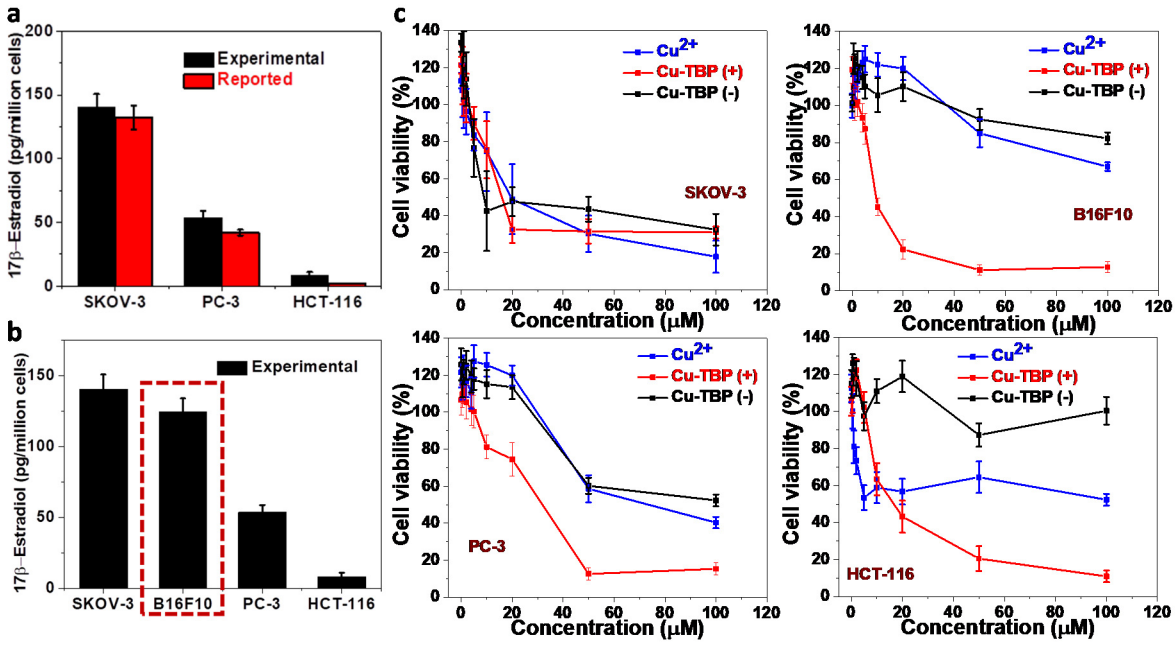

Figure 6-6 (a) Comparison of reported intracellular level of 17β-Estradiol and our results quantified with ELISA in SKOV-3, PC-3 and HCT-116, n = 3. (b) Intracellular level of 17 β-Estradiol in B16F10 quantified with ELISA kit, n = 3. (c) Cytotoxicity of $CuCl_2$ or Cu-DBP with (+) or without (-) light irradiation against SKOV-3, B16F10, PC-3, and HCT-116 cells at different TBP concentrations, n = 6. Adapted with permission from *Chem*, **2019**, *5*, 1892-1913. Copyright 2019 Elsevier Inc.

In vitro $^{\bullet}OH$ generation was then assayed with coumarin-3-carboxylic acid in B16F10 melanoma cells. The cells were incubated with $CuCl_2$, H_4TBP, or Cu-TBP at an equivalent dose of 20 μM for 4 h followed by LED irradiation and $^{\bullet}OH$ imaging by CLSM and quantification flow cytometry, respectively. Only $CuCl_2$ or Cu-TBP treated cells generated $^{\bullet}OH$ with or without light irradiation to afford blue fluorescence in CLSM images (**Figure 6-7a**) and to show strong blue mean fluorescence intensity in flow cytometry (**Figure 6-7b**). These results are consistent with our proposed $^{\bullet}OH$ generation *via* the Cu-estradiol redox cycle.

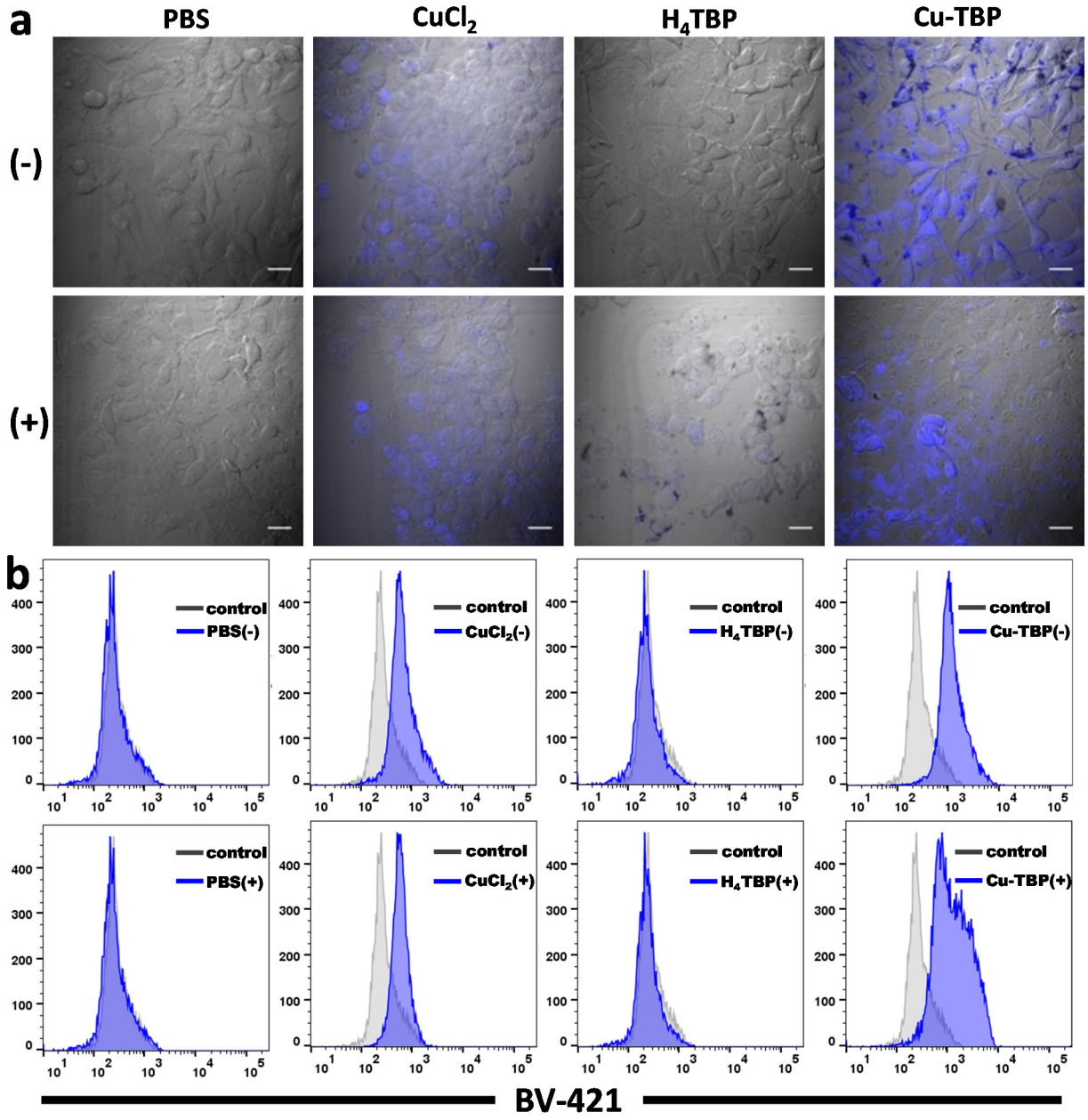

Figure 6-7 Coumarin-3-carboxylic acid assay of ˙OH observed under CLSM (a) and quantified by flow cytometry (b). The fluorescence at 460 nm comes from 7-OH coumarin-3-carboxylic. (a) Blue fluorescence indicates hydroxyl radical generation, respectively. Scale bar = 20 μm. (b) Grey histogram shows PBS control whereas blue histograms show $CuCl_2$, H_4TBP or Cu-TBP with (+) or without (-) light irradiation. Adapted with permission from *Chem*, **2019**, *5*, 1892-1913. Copyright 2019 Elsevier Inc.

In vitro $^1O_2$ and O_2^- generation in live cells were then probed by singlet oxygen sensor green (SOSG) and superoxide anion assay kit, respectively. The cells were seeded on cover slides and incubated with $CuCl_2$, H_4TBP, or Cu-TBP at an equivalent dose of 20 μM, irradiated at 0 or 90 J/cm^2, and then observed by CLSM (**Figure 6-8**). Only cells with H_4TBP and Cu-TBP incubation and light irradiation presented green fluorescence, while $CuCl_2$ and Cu-TBP groups afforded red fluorescence with or without light irradiation. The cells treated with Cu-TBP(+) showed yellow fluorescence that is merged from green and red fluorescence, indicating simultaneous $^1O_2$ and O_2^- production *via* Cu-TBP-mediated, hormone-triggered CDT and light-triggered PDT.

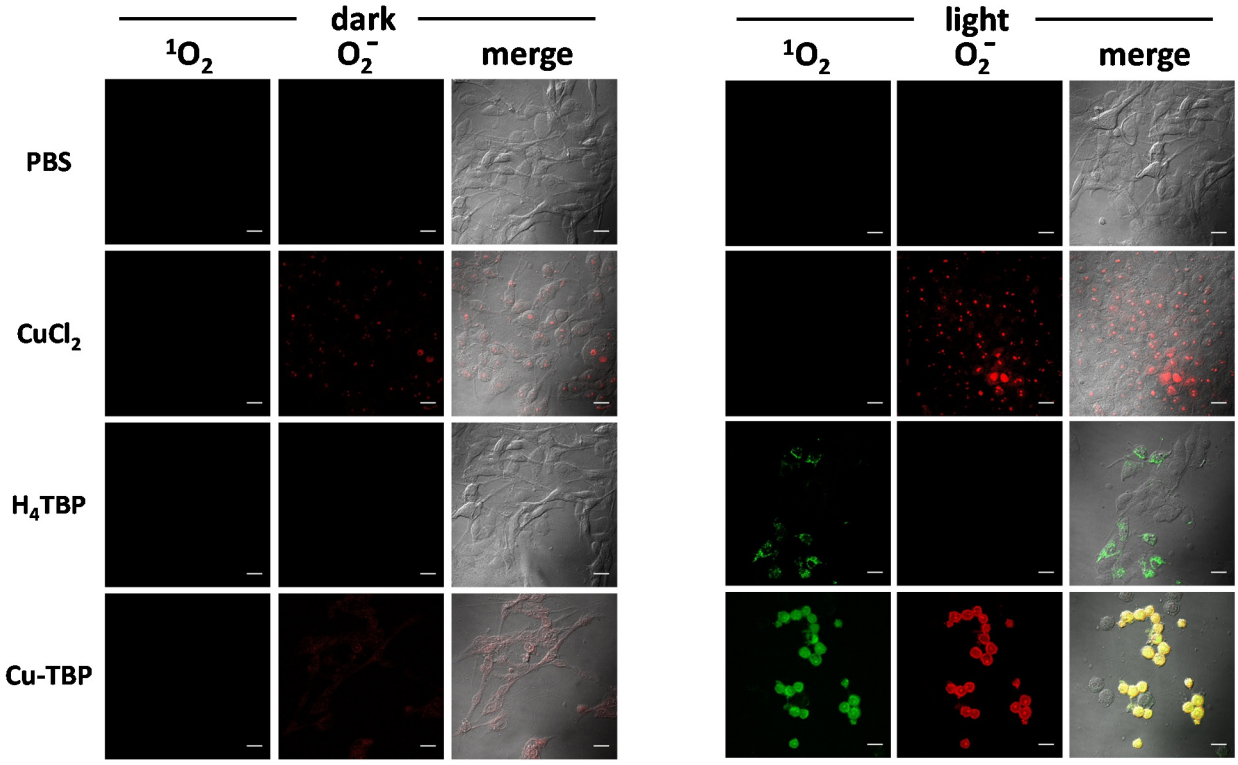

Figure 6-8 Generation of $^1O_2$ and O_2^- of cells treated with PBS, $CuCl_2$, H_4TBP or Cu-TBP with (+) or without (-) light irradiation detected with SOSG and superoxide kit. Green ($^1O_2$) and red (O_2^-) florescence merged to appear as yellow florescence. Scale bar = 20 μm**.** Adapted with permission from *Chem*, **2019**, *5*, 1892-1913. Copyright 2019 Elsevier Inc.

6.2.3 *In vitro* anti-tumor mechanism

Strong cytotoxicity of Cu-TBP(+) was demonstrated by MTS assay on B16F10 cells. Cu-TBP(-) showed moderate cytotoxicity with an IC_{50} value of 41.33 ± 8.87 μM (**Figure 6-9a**). Upon light irradiation, Cu-TBP(+) outperformed H_4TBP(+) with IC_{50} values of 6.37 ± 4.26 and 29.18 ± 3.67 μM, respectively ((**Figure 6-9b**). Optical imaging showed that Cu-TBP(+) treated cells presented severe morphological changes (**Figure 6-9c**). These results indicate that Cu-TBP(+) elicits strong anti-tumor toxicity.

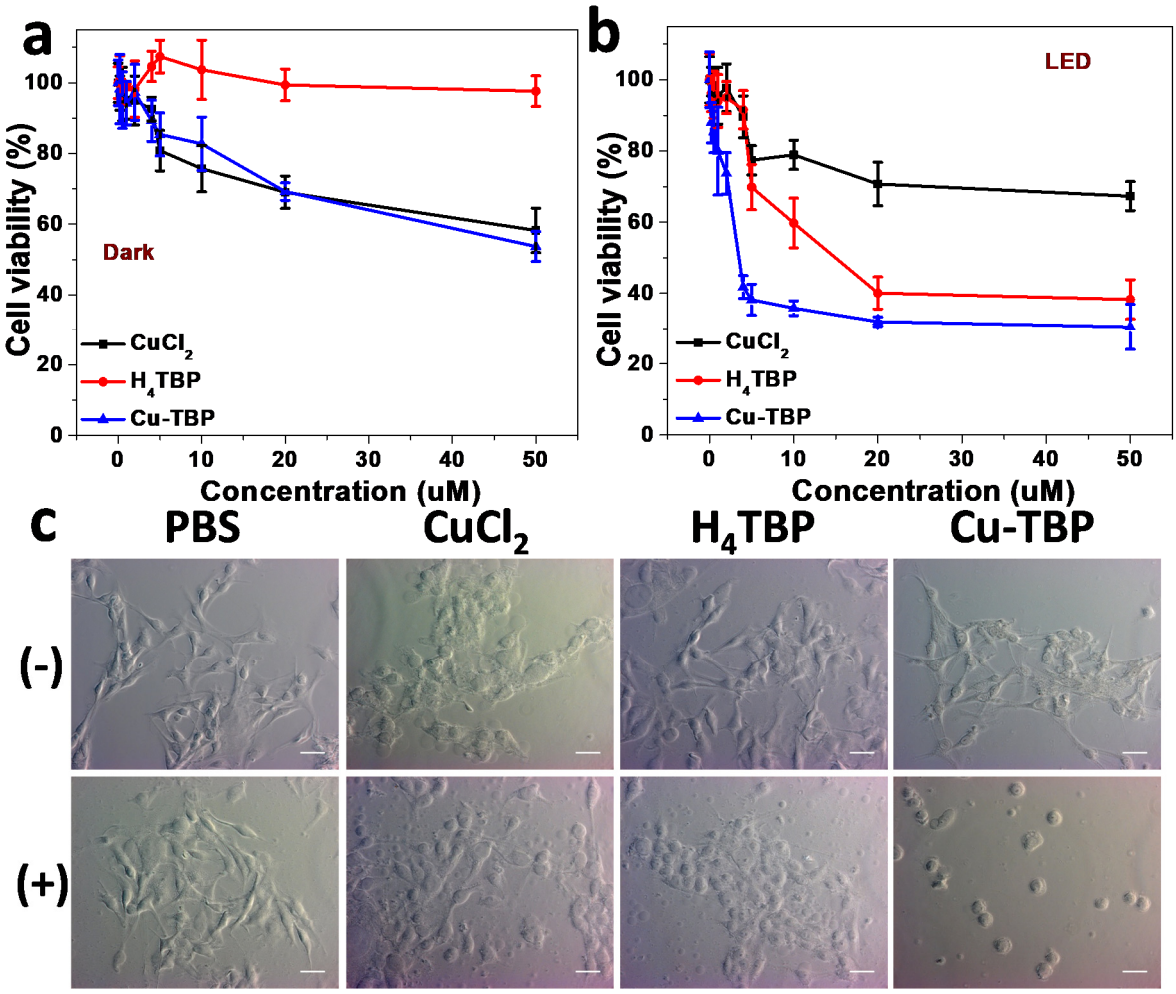

Figure 6-9 MTS assay of $CuCl_2$, H_4TBP or Cu-TBP against B16F10 cells without (a) or with light irradiation (b). (c) Optical images of B16F10 cells treated with PBS, $CuCl_2$, H_4TBP or Cu-TBP with (+) or without (-) light irradiation. Scale bar = 20 μm. Adapted with permission from *Chem*, **2019**, *5*, 1892-1913. Copyright 2019 Elsevier Inc.

The anti-tumor effects of Cu-TBP(+) were further investigated by examining cell apoptosis, DNA double strand break (DSB), and lipid peroxidation. First, B16F10 cells treated with $CuCl_2$, H_4TBP or Cu-TBP with or without light irradiation were examined by flow cytometry and confocal imaging (**Figure 6-10a**) using an Annexin V/dead cell apoptosis kit. Significant amounts of cells underwent apoptosis when treated with Cu-TBP(+) with only 19.9% healthy cells, compared to 62.7% and 70.1% healthy cells for H_4TBP(+) or $CuCl_2$(+) treatments. In dark controls, only 79.9% and 76.8% cells remain healthy in $CuCl_2$(-) and Cu-TBP(-) treatment groups, respectively, indicating the contribution of ROS generated from Cu-estradiol redox cycle to apoptotic cell death (**Figure 6-10b**).

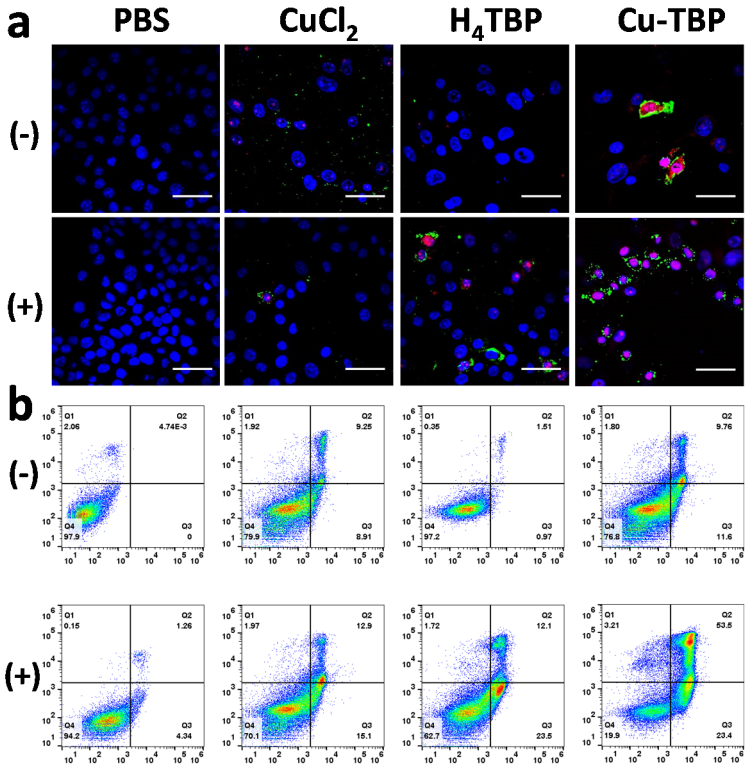

Figure 6-10 Annexin V/PI analysis of B16F10 cells observed under CLSM (a) and quantified with flow cytometry (b). Cells were incubated PBS, $CuCl_2$, H_4TBP or Cu-TBP with (+) or without (-) light irradiation. (a) Blue, red and green fluorescence represent DAPI, PI and Annexin-V-conjugated Alexa-488, respectively. Scale bar = 50 μm. (b) The quadrants from lower left to upper left (counter clockwise) represent healthy, early apoptotic, late apoptotic, and necrotic cells, respectively. The percentage of cells in each quadrant was shown on the graphs. Adapted with permission from *Chem*, **2019**, *5*, 1892-1913. Copyright 2019 Elsevier Inc.

DNA DSB was determined by γ-H2AX assay. Phosphorylated γ-H2AX was labeled to visualize and quantify in vitro DNA damage caused by •OH generated from the Cu-estradiol redox cycle. With or without light irradiation, significantly higher red γ-H2AX fluorescence was observed in the groups treated with Cu-TBP than those treated with $CuCl_2$, while no fluorescence was observed in other groups (**Figure 6-11a**). Flow cytometric analyses further showed that cells treated with Cu-TBP(+) exhibited stronger red γ-H2AX fluorescence than other treatment groups, confirming Cu-TBP(+) leads to higher •OH generation and more DNA DSB (**Figure 6-11b**).

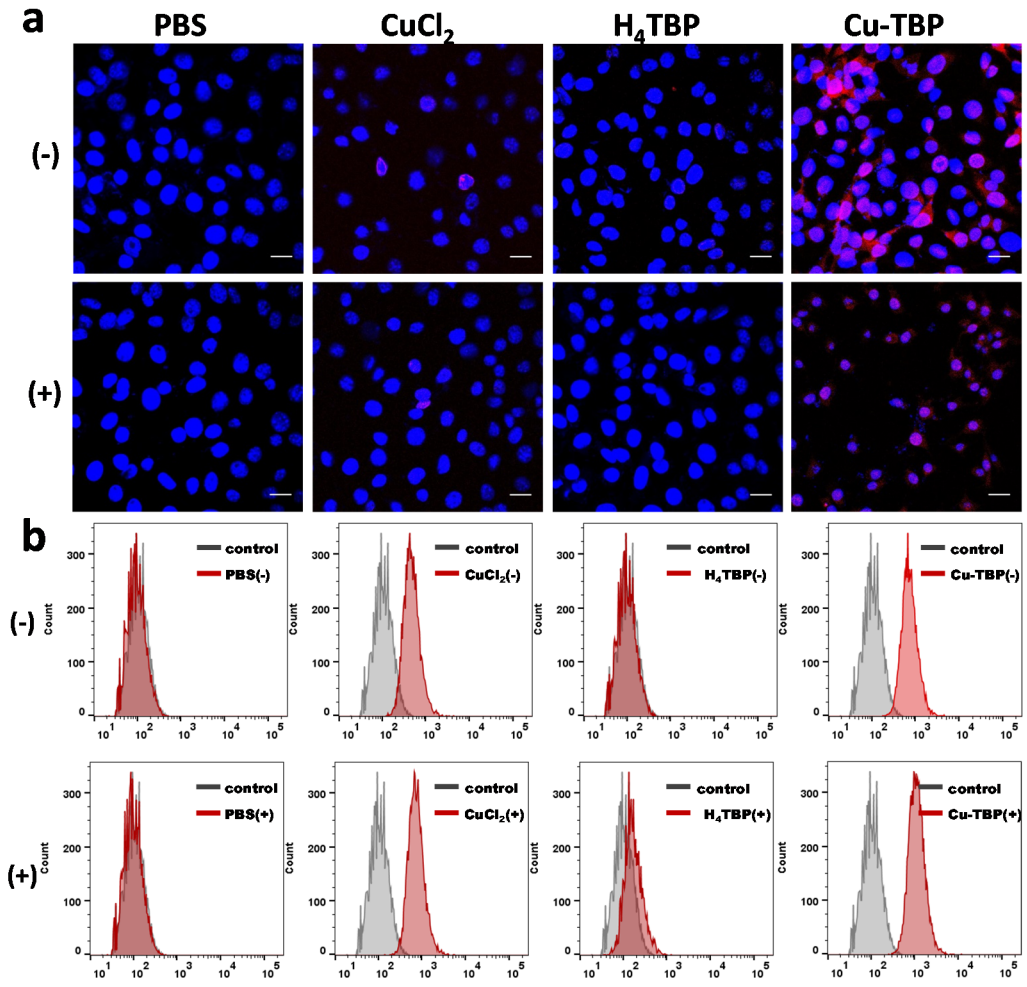

Figure 6-11 γ-H2AX immunostaining assay showing the DNA double strain breaks (DSBs) in B16F10 cells by CLSM (a) and flow cytometry (b). (a) Blue and red fluorescence show DAPI-stained nucleus and antibody-labeled γ-H2AX in the cells, respectively. Scale bar = 20 μm. (b) Grey histogram (control) and red histogram show the difference of γ-H2AX level in the cells. Adapted with permission from *Chem*, **2019**, *5*, 1892-1913. Copyright 2019 Elsevier Inc.

Lipid peroxidation was then determined by cycloxygenase 2 (COX-2) assay. Membrane COX-2, a protein responsible for membrane damage repair, is up-regulated after lipid peroxidation, providing an excellent probe for $^1O_2$ and/or O_2^- induced damage of cell membranes.[20] In dark controls, only Cu-TBP(-) or $CuCl_2$(-) treated cells showed red fluorescence of Cy5-conjugated COX-2 antibody, while cells treated with PBS(-) or H_4TBP(-) did not exhibit red fluorescence, indicating the lipid peroxidation induced by O_2^- (**Figure 6-12a**). Cells treated with H_4TBP(+) gave weak red fluorescence due to the PDT effect. Cu-TBP(+) treated cells presented strong red fluorescence, demonstrating that both $^1O_2$ and O_2^- generated in Cu-TBP(+) treatment contribute to lipid peroxidation. These results were confirmed by flow cytometry studies (**Figure 6-12b**).

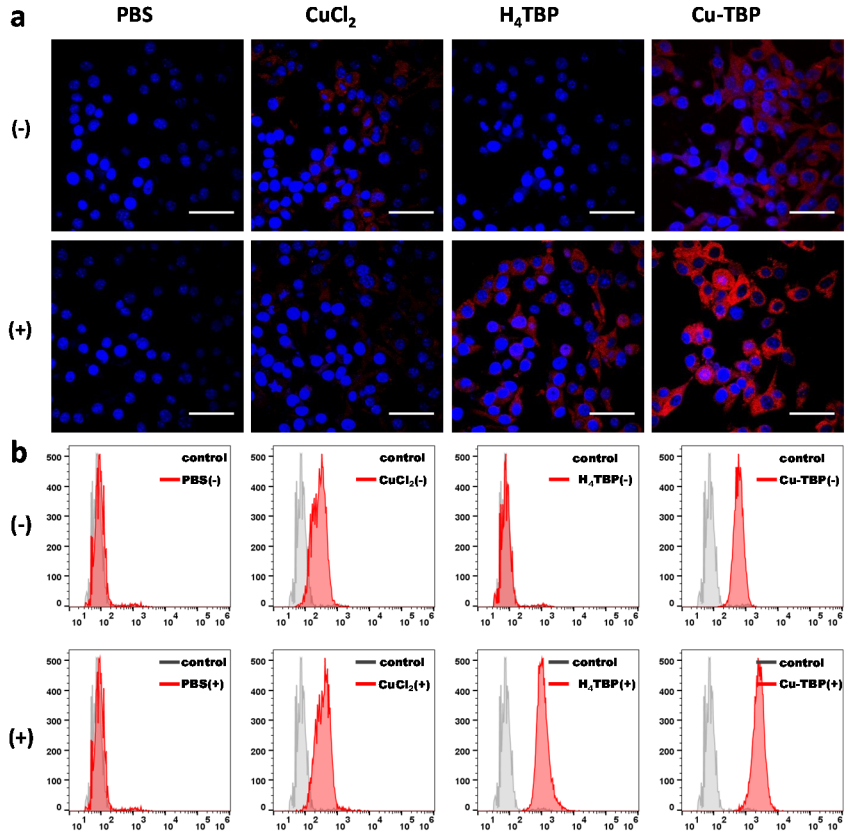

Figure 6-12 COX-2 expression of B16F10 cells treated with PBS, $CuCl_2$, H_4TBP or Cu-TBP upon light irradiation observed under CLSM (a) and quantified with flow cytometry (b). (a) Red fluorescence represents Cy5-conjugated COX-2. Scale bar = 50 μm. (b) Grey histogram (control) and red histogram show the difference of COX-2 level in the cells. Adapted with permission from *Chem*, **2019**, *5*, 1892-1913. Copyright 2019 Elsevier Inc.

6.2.4 *In vivo* anti-tumor efficacy

We carried out *in vivo* efficacy studies with mice receiving a single intratumoral injection of Cu-TBP followed by light irradiation. A melanoma mouse model of single B16F10-tumor bearing C57BL/6 mice was employed to evaluate the anti-tumor efficacy of hormone- and light-triggered radical therapies. Zn-TBP, an nMOF with a similar structure for the delivery of H_4TBP but not Cu^{2+}, was synthesized, characterized (**Figure 6-13**) and used as a control. When the tumors reached 75-100 mm^3 in volume, $CuCl_2$, H_4TBP, Zn-TBP, or Cu-TBP was injected intratumorally at equivalent doses of 0.2 μmol followed by light irradiation with a LED (λ_{max} = 650 nm, 100 mW/cm^2) for 30 mins. As shown in **Figure 6-14a**, Cu-TBP(+) treatment effectively regressed the tumors with one mouse showing complete response to the treatment, significantly slowing the tumor growth with a tumor growth inhibition index (TGI) of 96.6%. In comparison, Zn-TBP(+) and H_4TBP(+) showed only moderate anticancer efficacy with TGI values of 85.9% and 81.4%, respectively. With a TGI of 83.4%, Cu-TBP(-) also afforded comparable local outcomes as Zn-TBP(+) or H_4TBP(+), indicating a significant therapeutic contribution from Cu-catalyzed redox radical therapy. 15 days after tumor inoculation, mice were sacrificed and photographed (**Figure 6-14b**) and tumors were harvested, photographed as shown in **Figure 6-14c**, and weighted as shown in **Figure 6-14d**. Similar results were also observed on a human ovarian carcinoma model of single SKOV-3-tumor bearing athymic nude mice; SKOV-3 model was chosen for this study because of its high intracellular estradiol concentration. Treatment began when the tumors exceeded 100 mm^3 in volume. As shown in **Figure 6-14e**, Cu-TBP(-) slowed down the tumor growth with a TGI of 69.1% at a similar rate as H_4TBP(+) with a TGI of 66.7%, affirming the efficient ROS generation from the Cu-estradiol pathway. Impressively, Cu-TBP(+) treatment eradicated the tumors in all treated mice, affording a TGI of 100%.

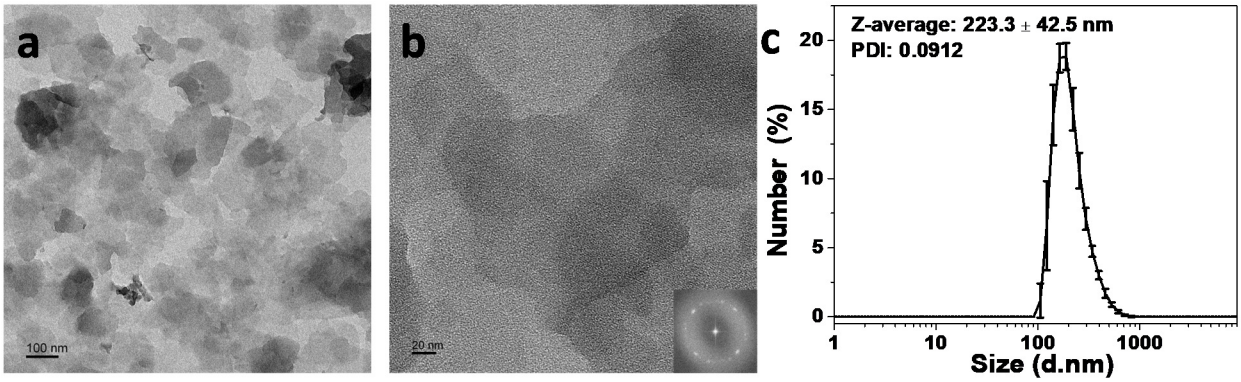

Figure 6-13 (a) Transmission electron microscopy image (TEM) and (b) High-resolution TEM image of Zn-TBP and its fast Fourier transform pattern shown in the inset. Scale bar = 100 nm for (a) and 20 nm for (b). (c) Number-averaged diameter of Zn-TBP in water by dynamic light scattering measurements, n = 3. Adapted with permission from *Chem*, **2019**, *5*, 1892-1913. Copyright 2019 Elsevier Inc.

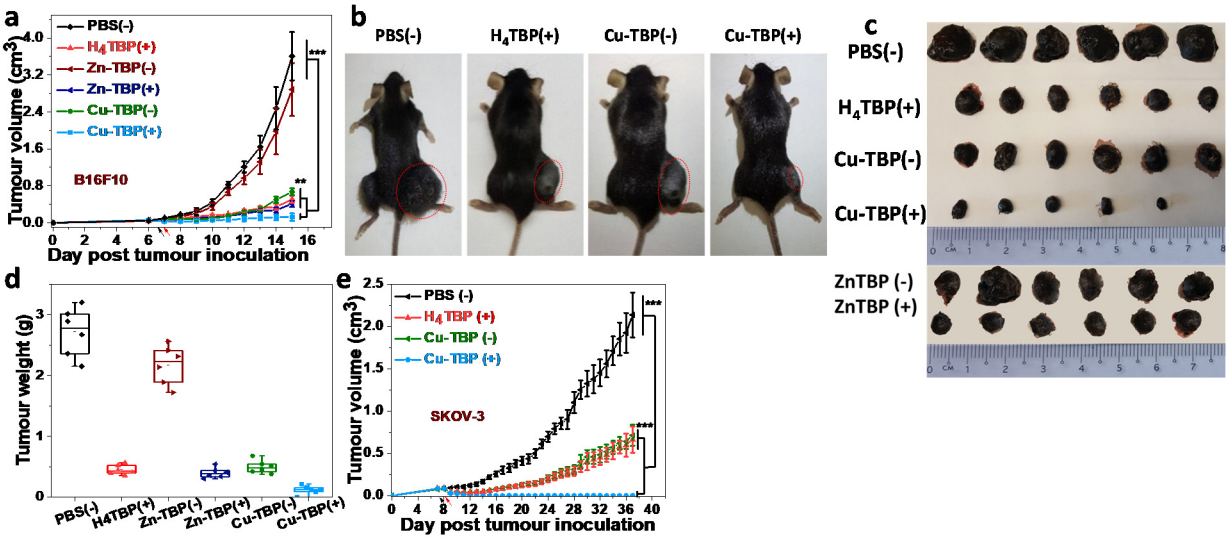

Figure 6-14 Anti-tumor efficacy of H_4TBP or Cu-TBP with (+) or without (-) light irradiation on B16F10-bearing C57BL/6 mice (a) and SKOV-3-bearing nude mice (e), n = 6. Black and red arrows refer to the times of intratumoral injections and light irradiation, respectively. (b) Photograph of as-treated B16F10 tumor-bearing C57BL/6 mice. Photographs (c) and (d) weights of excised B16F10 tumor on day 15 as treated in (a), n = 6. Adapted with permission from *Chem*, **2019**, *5*, 1892-1913. Copyright 2019 Elsevier Inc.

The estradiol concentrations in the B16F10 and SKOV-3 tumors were quantified by ELISA kits 8 and 3 days post treatment, respectively. As shown in **Figure 6-15**, in both B16F10 and SKOV-3 models, the estradiol level was significantly reduced in groups injected with Cu-TBP

with or without light irradiation, indicating that estradiol in cancer cells was consumed in Cu-catalyzed ROS generation for radical therapy.

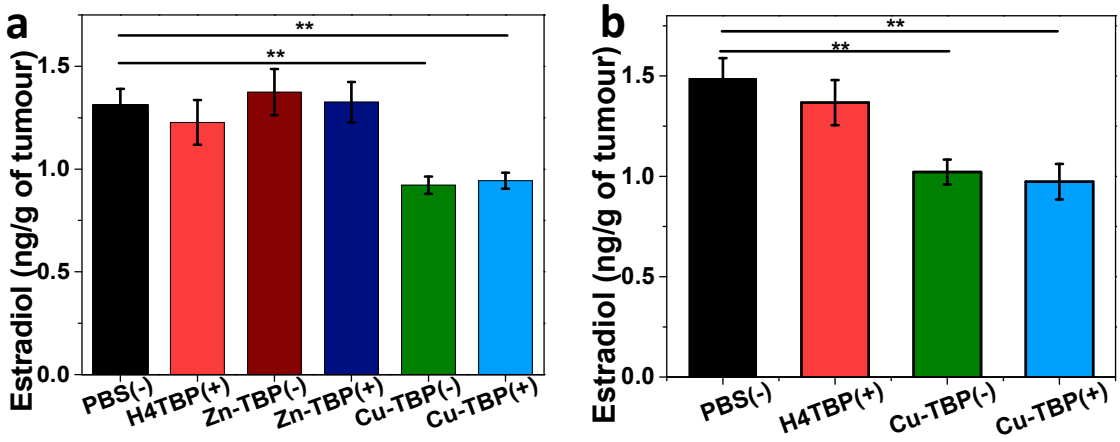

Figure 6-15 (a) Determination of intratumoral estradiol on (a) B16F10 model 8 days post treatment and (b) SKOV-3 model 3 days post treatment, n = 6. **P<0.05 from control by t-test. Adapted with permission from *Chem*, **2019**, *5*, 1892-1913. Copyright 2019 Elsevier Inc.

6.2.5 Immunogenicity

The immunogenic cell death (ICD) induced by Cu-TBP-mediated ROS generation was evaluated by detecting cell-surface expression of calreticulin (CRT) *in vitro*. As shown in **Figure 6-16a**, more green fluorescence was observed in the group treated with Cu-TBP(+) compared to other groups, indicating that ROS generated from Cu-estradiol process induced immunogenicity. Similar results were further quantitatively analyzed with flow cytometry (**Figure 6-16b**). Considerable CRT exposure appeared in $CuCl_2$(-) and Cu-TBP(-) treated groups, while Cu-TBP(+) showed much higher CRT expression on the cell-surface compared to H_4TBP(+). These results demonstrate that Cu-TBP(+) treatment induced stronger ICD over other groups due to the combination of estradiol-mediated oxidative process and light-triggered PDT process.

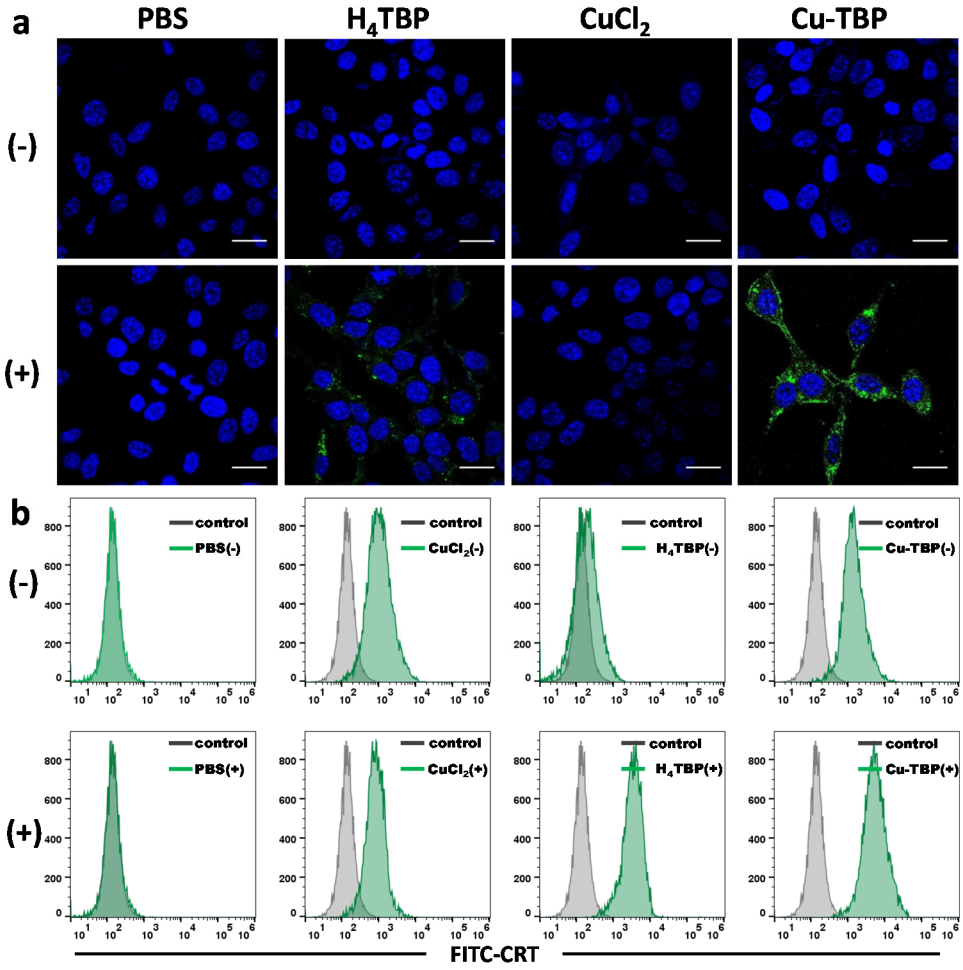

Figure 6-16 (a) CRT exposure of B16F10 was assessed after incubation with PBS, $CuCl_2$, H_4TBP or Cu-TBP with (+) or without (-) light irradiation by CLSM (a) and flow cytometry (b). (a) Blue and green fluorescence show DAPI-stained nucleus and CRT exposure on the cell surface, respectively. Scale bar = 20 μm. (b) Grey histogram (control) and blue histogram show the difference of CRT exposure level on the cell surfaces. Adapted with permission from *Chem*, **2019**, *5*, 1892-1913. Copyright 2019 Elsevier Inc.

6.2.6 Phagocytosis

As CRT-mediated phagocytosis is known to promote antigen processing and immune activation of professional antigen presenting cells (APCs), we determined whether Cu-TBP-mediated ROS generation could enhance phagocytosis of Cu-TBP(+) treated B16F10 cells. We evaluated the phagocytosis of CFSE-labeled B16F10 by both PerCP-Cy5.5-conjugated F4/80-

labeled macrophages and PE-Cy5.5-conjugated CD11c-labeled dendritic cells (DCs) with CLSM and flow cytometry. CLSM imaging showed that Cu-TBP(+) treated cells recruited more macrophages for phagocytosis (**Figure 6-17a**), which was further confirmed by flow cytometry analysis (**Figure 6-17b**).

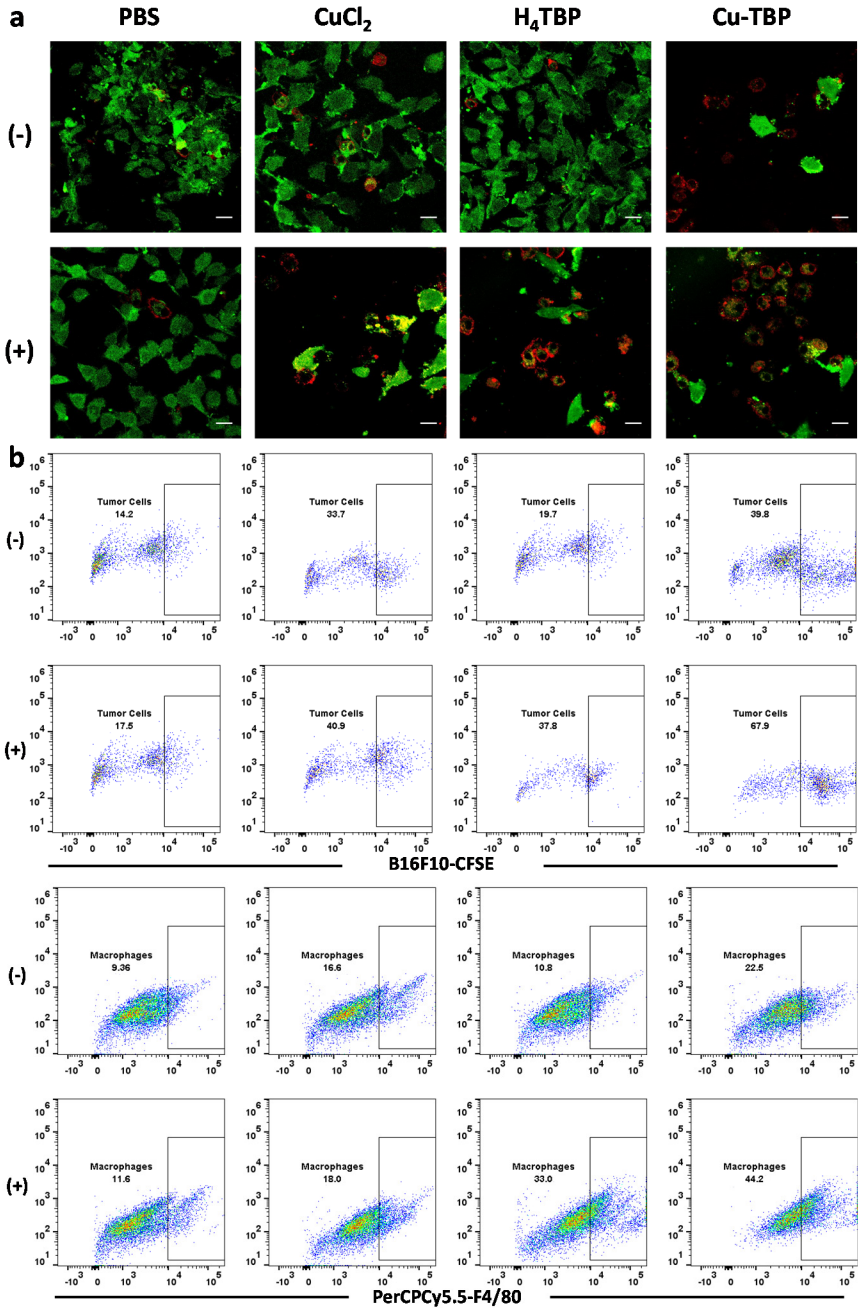

Figure 6-17 Phagocytosis of CFSE-labelled B16F10 cells by macrophages treated with PBS, $CuCl_2$, H_4TBP or Cu-TBP with (+) or without (-) light irradiation by CLSM (a) and flow cytometry

Figure 6-17, continued (b). (a) Macrophages co-cultured with treated B16F10 cells were stained with PerCP-Cy5.5-conjugated F4/80 antibody. B16F10 cells were gated on PerCP-Cy5.5-positive cells. (b) Red and green fluorescence show PerCP-Cy5.5-conjugated F4/80-labeled macrophages and CFSE-labeled B16F10 cancer cells, respectively. Scale bar = 20 μm. Adapted with permission from *Chem*, **2019**, *5*, 1892-1913. Copyright 2019 Elsevier Inc.

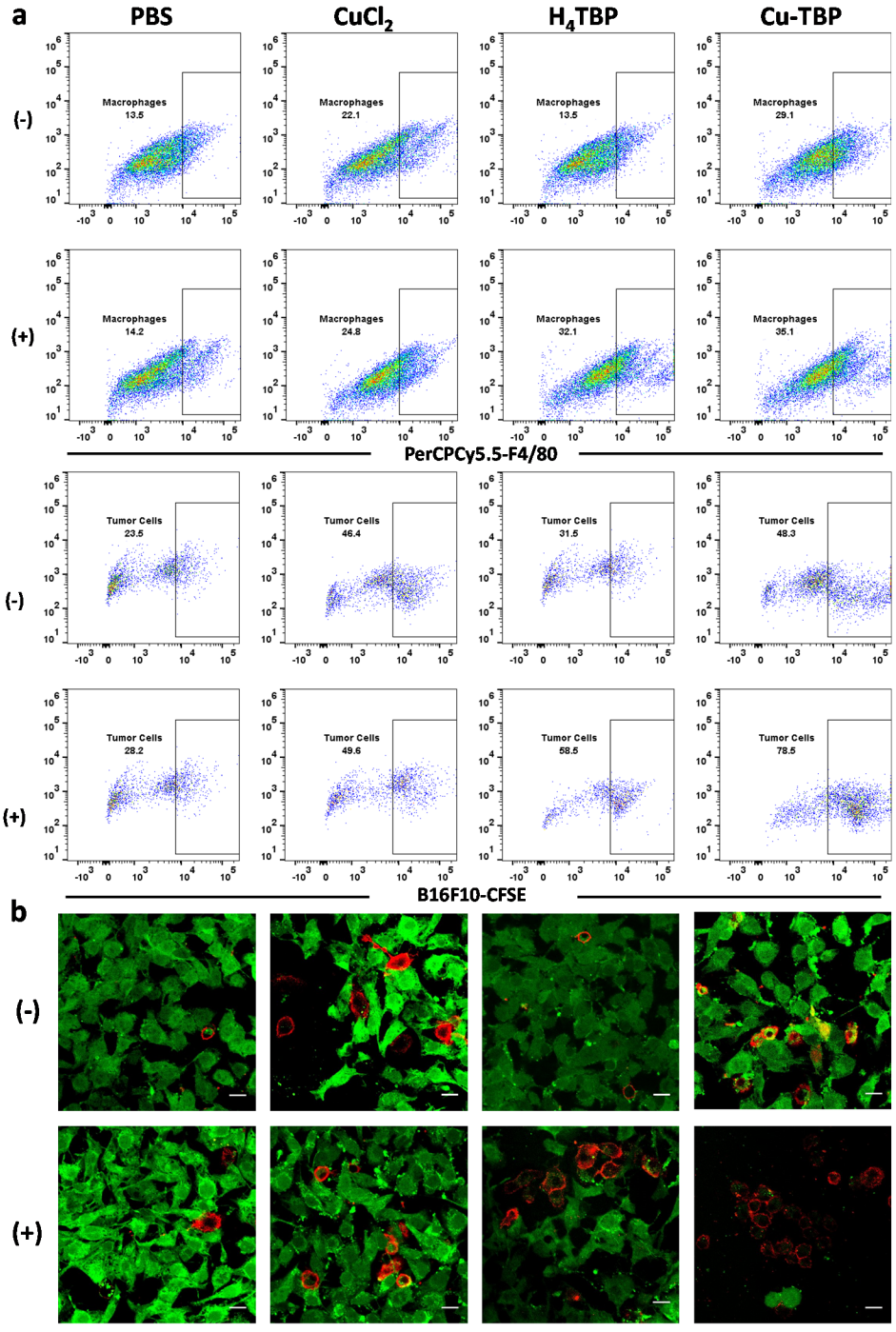

Figure 6-18 Phagocytosis of CFSE-labelled B16F10 cells by DCs treated with PBS, $CuCl_2$, H_4TBP or Cu-TBP with (+) or without (-) light irradiation by flow cytometry (a) and CLSM (b).

Figure 6-18, continued (a) DCs co-cultured with treated B16F10 cells were stained with PE-Cy5.5-conjugated CD11c antibody. B16F10 cells were gated on PE-Cy5.5-positive cells. (b) Red and green fluorescence show PE-Cy5.5-conjugated CD11c-labeled DCs and CFSE-labeled B16F10 cancer cells, respectively. Scale bar = 20 μm. Adapted with permission from *Chem*, **2019**, *5*, 1892-1913. Copyright 2019 Elsevier Inc.

For phagocytosis by DCs, the population of $CD11c^+$ cells significantly increased in cells with Cu-TBP(+) treatment (**Figure 6-18a**). Further gating of $CFSE^+$ cells from $CD11c^+$ cells afforded phagocytosed B16F10 cells in DCs. Cu-TBP(+) treated cells showed almost 80% of phagocytosis, much higher than other treatment groups. These results were confirmed by CLSM imaging (**Figure 6-18b**). Cu-TBP-mediated ROS generation thus promotes phagocytosis process, leading to enhanced antigen presentation.

6.2.7 *In vivo* anti-tumor efficacy of Cu-TBP(+) plus immune checkpoint blockade

As Cu-TBP(+) treatment is highly immunogenic and stimulates antigen presentation, we combined Cu-TBP(+) with immune checkpoint blockade to extend local therapy to systemic cancer management using a bilateral model of B16F10. When the primary tumors reached 75-100 mm^3 in volume, Cu-TBP was intratumorally injected to the primary tumors at a dose of 0.2 μmol, followed by LED irradiation (λ_{max} = 650 nm, 100 mW/cm^2) for 30 mins. 75μg of anti-PD-L1 antibody was given every three days by intraperitoneal injection. The tumor sizes were measured daily with a caliper where tumor volume equals ($width^2$ × length)/2 and plotted individually (**Figure 6-19a**). Each mouse was weighed daily to evaluate systemic toxicity. TGI values were calculated based on the tumor growth data on day 15 post-inoculation when at least one mouse in the study was sacrificed for tumor burden. Individual mice were sacrificed when total tumor burden reached 2 cm^3 and the survival curve was plotted and analyzed by the Kaplan-Meier method.

As shown in **Figure 6-19b**, Cu-TBP(+) treatment successfully regressed the local tumors with or without the combination with α-PD-L1, affording TGI values of 95.2% and 98.3% for Cu-TBP(+) and Cu-TBP(+) plus α-PD-L1, respectively. The local tumor control result is consistent with what we observed for the single tumor model (TGI = 96.6%). However, the Cu-TBP(+) treatment alone did not effectively suppress the distal tumor growth with a TGI of 64.0.

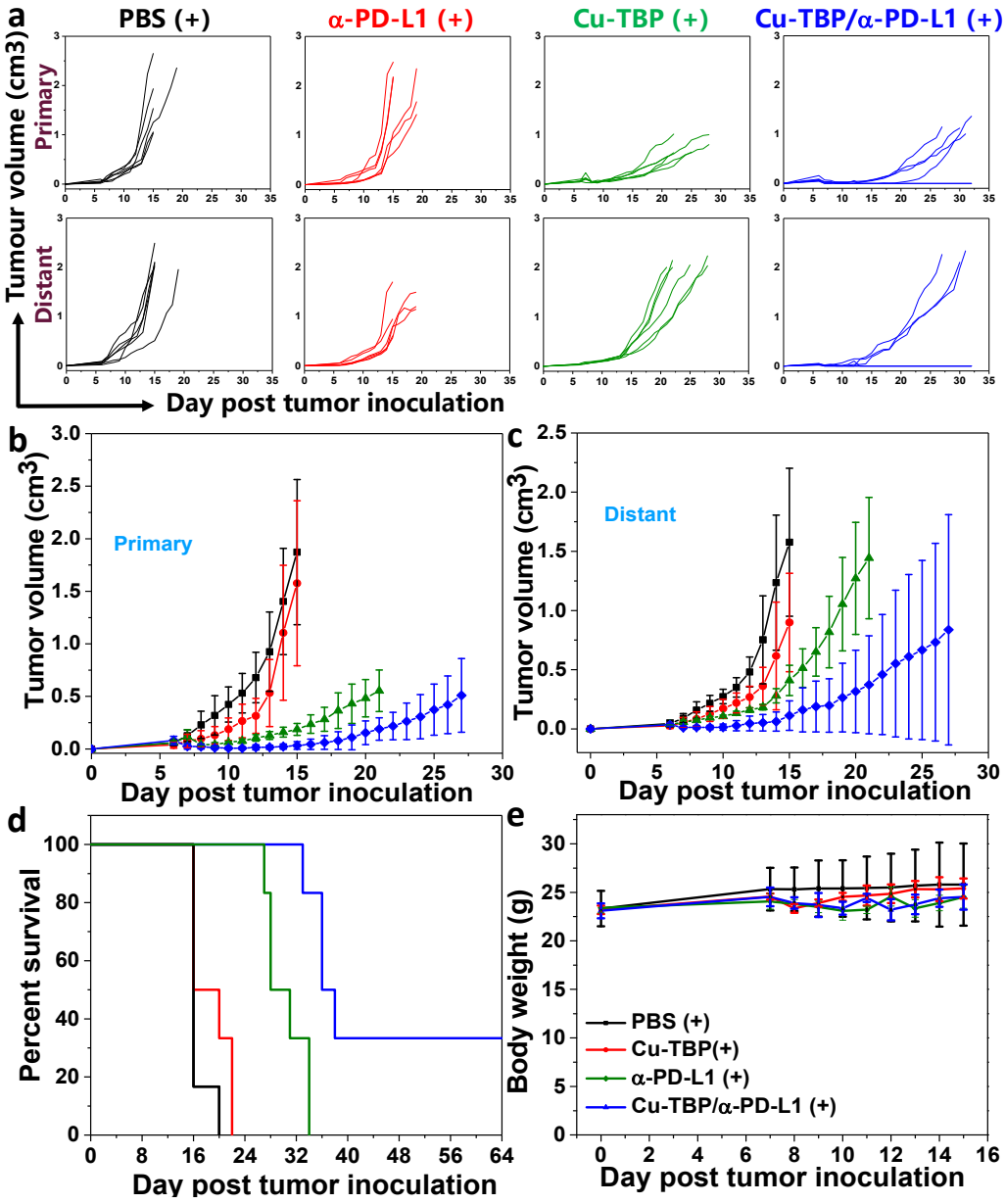

Figure 6-19 Individual tumor growth curves of B16F10 bilateral tumor-bearing mice treated with PBS, α-PD-L1, Cu-TBP or Cu-TBP plus α-PD-L1 upon light irradiation, n = 6. (a) Averaged

Figure 6-19, continued primary (b) and distant (c) tumor growth curves, survival curves (d) and body weights (e) of B16F10 bilateral tumor-bearing mice treated with PBS(+), α-PD-L1(+), Cu-TBP(+) or Cu-TBP(+) plus α-PD-L1, n = 6. Black, red, and azure arrows refer to the times of intratumoral PBS or Cu-TBP injections, light irradiation and intraperitoneal antibody administration, respectively. Central data points and error bars represent mean ± s.d. values, respectively. Adapted with permission from *Chem*, **2019**, *5*, 1892-1913. Copyright 2019 Elsevier Inc.

In contrast, the Cu-TBP(+) plus α-PD-L1 combination effectively regressed distant tumors with a TGI of 94.9% (**Figure 6-19c**). Notably, the combination therapy completely cured one-third of treated mice, indicating that the local treatment with Cu-TBP(+) synergizes with immune checkpoint blockade to induce systemic antitumor immune response. Survival analysis showed that Cu-TBP(+) plus α-PD-L1 extended the median survival time to 31 days, which is significantly longer than 10, 12 and 23.5 days for PBS, α-PD-L1 and Cu-TBP(+) treatment groups, respectively (**Figure 6-19d**). The steady body weights in all treated mice indicated that Cu-TBP(+) treatment with or without α-PD-L1 did not lead to systemic toxicity (**Figure 6-19e**). This was further confirmed by similar histologies of major organs between the Cu-TBP(+) plus α-PD-L1 group and the PBS group (**Figure 6-20**).

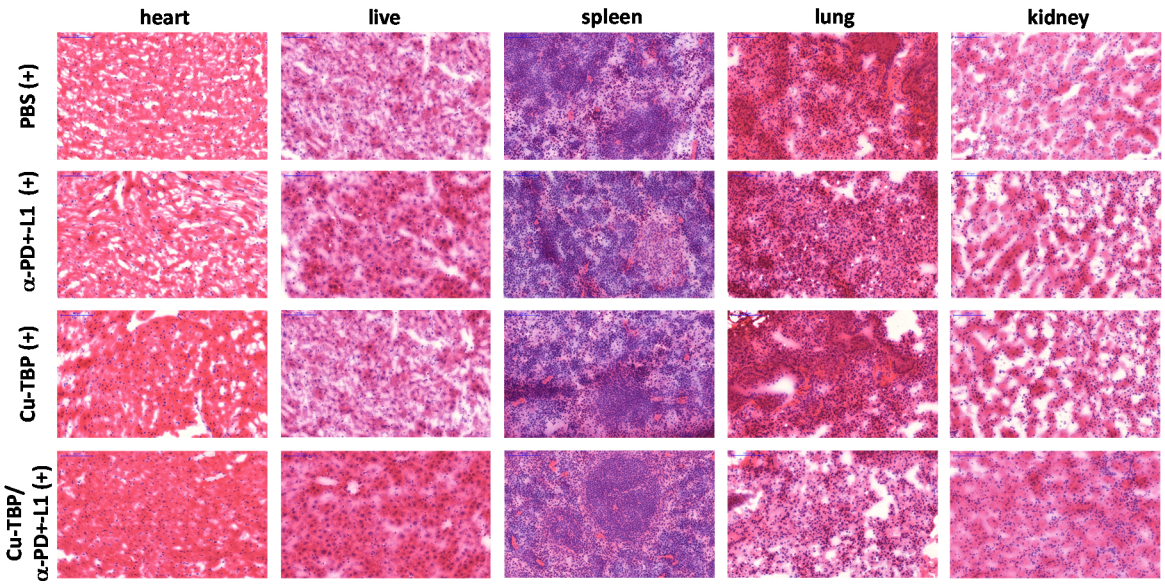

Figure 6-20 Histologies of frozen sections of as treated mice after H&E staining. Major organs of B16F10 tumor-bearing C57BL/6 mice treated with treated with PBS(+), α-PD-L1(+), Cu-TBP(+)

Figure 6-20, continued or Cu-TBP(+) plus α-PD-L1 were harvested and sectioned. From left to right: heart, liver, spleen, lung or kidney. Scale bar = 100 μm. Adapted with permission from *Chem*, **2019**, *5*, 1892-1913. Copyright 2019 Elsevier Inc.

To confirm the anti-tumor immune memory effect, we carried out a tumor rechallenge study. B16F10 tumors were established on the right flanks of mice and treated with Cu-TBP(+) plus α-PD-L1. Two out of six mice had their tumors completely eradicated after treatment, affording a cure rate of 33.3%. Tumors in the other four mice shrank to very small sizes, but regrew beginning days 26, 30, 31 and 32, respectively, post tumor inoculation. Thirty days after tumor eradication, the cured mice and naïve control mice were challenged with 1.5×10^6 B16F10 cells on the contralateral, left flank. While all naïve control mice had to be euthanized due to their tumor sizes exceeding 2.0 cm3 by day 13 post-inoculation, the cured mice remained tumor-free after tumor rechallenge (**Figure 6-21**), indicating strong anticancer immune memory effect.

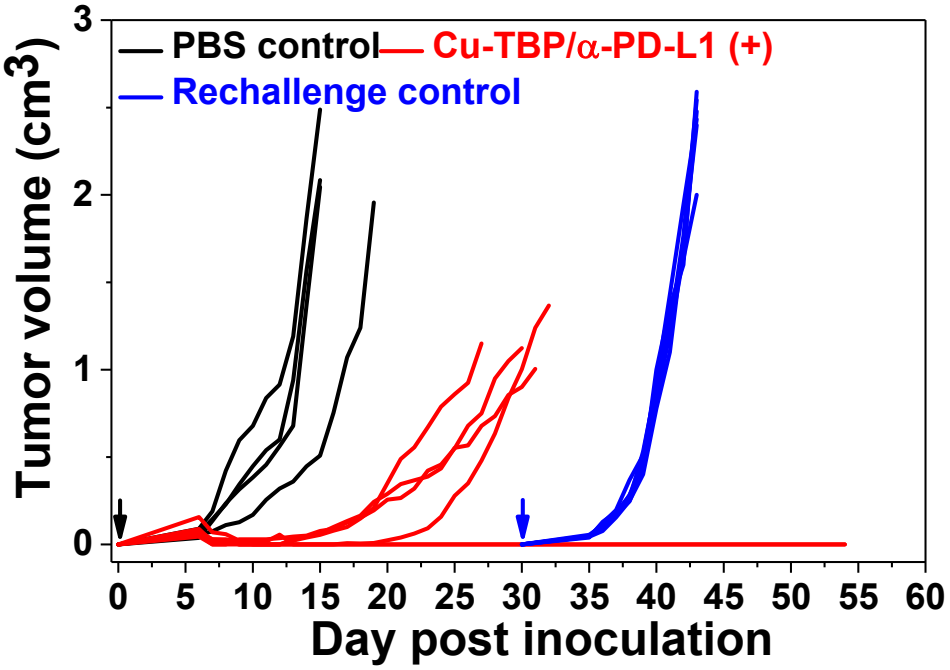

Figure 6-21 Complete tumor growth curves after the tumor rechallenge with B16F10 cells. Adapted with permission from *Chem*, **2019**, *5*, 1892-1913. Copyright 2019 Elsevier Inc.

6.2.8 Anti-tumor immunity

We then tested the anti-tumor immunity of B16F10-bearing mice treated with Cu-TBP(+) plus α-PD-L1 by Enzyme-Linked ImmunoSpot (ELISpot) and flow cytometry. We first determined the presence of tumor-antigen specific cytotoxic T cells with an IFN-γ ELISPOT assay. On day 10 after the treatment, splenocytes were harvested from B16F10-bearing mice and stimulated with SVYDFFVWL, a tumor associated antigen, for 42 hours and the IFN-γ spot forming cells were counted by Immunospot Reader. The number of antigen-specific IFN-γ producing T cells significantly increased in tumor-bearing mice treated with Cu-TBP(+) plus α-PD-L1 (109.0 ± 29.7 compared to 18.9 ± 14.9 for PBS or 53.7 ± 20.4 for α-PD-L1, **Figure 6-22**). These results show that α-PD-L1 treatment alone elicits some immunotherapeutic effects on the B16F10 model but Cu-TBP(+) treatment effectively synergizes α-PD-L1 to generate strong tumor-specific T cell response.

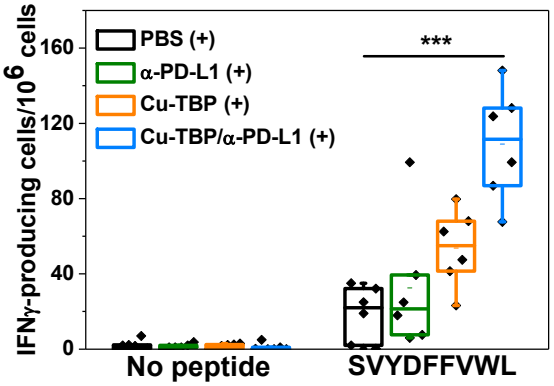

Figure 6-22 The splenocytes were harvested and stimulated with 10 μg/mL SVYDFFVWL peptide for 42 h. ELISPOT assay was performed to detect IFN-γ producing T cells. ***P<0.001 from control by t-test. Central lines, bounds of box and whiskers represent mean values, 25% to 75% of the range of data and 1.5 fold of interquartile range away from outliers, respectively. Adapted with permission from *Chem*, **2019**, *5*, 1892-1913. Copyright 2019 Elsevier Inc.

We further profiled infiltrating leukocytes in both primary and distant tumors. The representative tumor-infiltrating $CD4^+$ T cells and $CD8^+$ T cells gated on $CD45^+TCR\beta^+$ cell populations indicated that $CD4^+$ T cells and $CD8^+$ T cells infiltrated more in both primary and distant tumor sites (**Figure 6-23**). The percentage of $CD45^+$ cells in the total tumor cells significantly increased in the Cu-TBP(+) plus α-PD-L1 group in both primary and distant sites (11.72 ± 5.41 % and 8.84 ± 2.84 %, respectively) compared to the PBS control group (3.53 ± 1.25 % and 1.53 ± 0.73%, respectively). For primary tumors, the percentage of both $CD4^+$ and $CD8^+$ T cells in the total tumor cells significantly increased in Cu-TBP(+) plus α-PD-L1 group (1.60 ± 0.81% and 2.62 ± 2.35%, respectively) compared to Cu-TBP(+) group (0.18 ± 0.05 % and 0.14 ± 0.14%, respectively) and PBS control group (0.29 ± 0.15 % and 0.14 ± 0.14%, respectively). Similarly, for distant tumors, the percentage of both $CD4^+$ and $CD8^+$ T cells in the total tumor cells increased in Cu-TBP(+) plus α-PD-L1 group (0.81 ± 0.17% and 0.54 ± 0.26%, respectively) compared to PBS control group (0.20 ± 0.17 % and 0.04 ± 0.03%, respectively, **Figure 6-24a-c**).

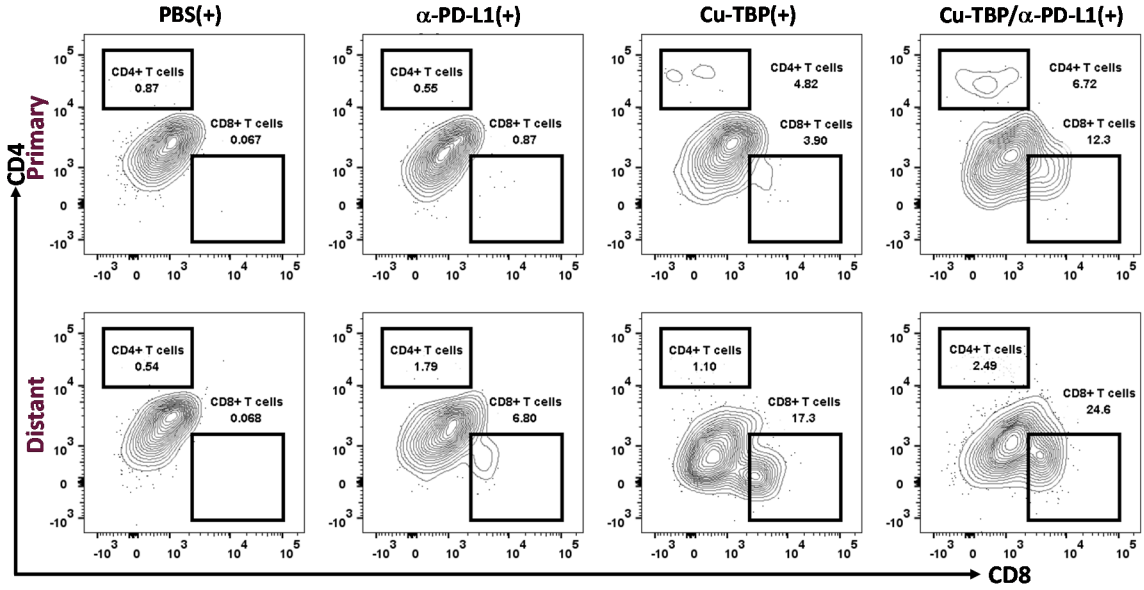

Figure 6-23 Representative quantitative analysis of T cells (gated on $CD45^+TCR\beta^+$ cells) in both primary (first row) and distant (second row) tumors analyzed by flow cytometry. Adapted with permission from *Chem*, **2019**, *5*, 1892-1913. Copyright 2019 Elsevier Inc.

In immunotherapy, the innate immune system is activated first after ICD in treated primary tumor sites. Macrophages are recruited to the tumor sites to expose tumor antigen and then dendritic cells migrate to the lymph nodes to present antigens to T cells. Cu-TBP(+) plus α-PD-L1 significantly increased the percentages of macrophages (**Figure 6-24e**) and dendritic cells (**Figure 6-24f**) in both primary and distant tumors. Moreover, the primary tumor-infiltrated neutrophils significantly increase in Cu-TBP(+) plus α-PD-L1 group compared with Cu-TBP(+) group or PBS control group (**Figure 6-24d**). These findings match well with the *in vitro* phagocytosis results, and strongly suggest that the combination of Cu-TBP(+) and α-PD-L1 not only induces innate immune response but also augments tumor-specific adaptive response in tumors.

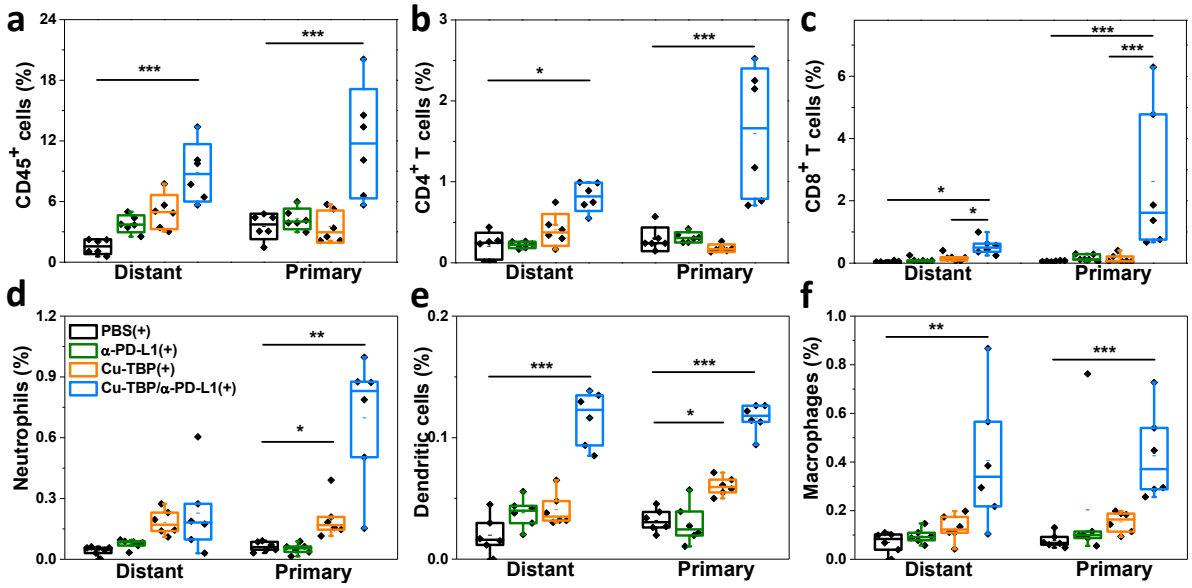

Figure 6-24 The percentage of tumor-infiltrating $CD45^+$ cells (a), $CD4^+$ T cells (b), $CD8^+$ T cells (c), macrophages (d), dendritic cells (e) and neutrophils (f) with respect to the total tumor of cells treated with PBS(+), α-PD-L1(+), Cu-TBP(+), or Cu-TBP(+) plus α-PD-L1. Data are expressed as means ± s.d., n = 6. *P<0.05 from control, **P<0.01 from control and ***P<0.001 from control by t-test. Central lines, bounds of box and whiskers represent mean values, 25% to 75% of the range of data and 1.5 fold of interquartile range away from outliers, respectively. Adapted with permission from *Chem*, **2019**, *5*, 1892-1913. Copyright 2019 Elsevier Inc.

6.3 Discussion

In CDT, metal ions as redox active pairs, usually Mn(IV)/(II), Fe(III)/(II) and Cu(II)/(I) are introduced to decompose intratumoral H_2O_2 to generate cytotoxic $^{\bullet}OH$ through Fenton and Fenton-like reactions[1,21]. With the advent of nanotechnology, strategies such as pH-responsive sequential decomposition or the use of reducing agents to tailor the TME have also been explored to expand the scope of CDT.[1,22-23] Here we demonstrate for the first time the ability to hijack the estrogen metabolic pathway to assist Cu^{2+}/Cu^{+} catalytic cycle for ROS generation through H_2O_2 decomposition. We proved this novel CDT process by detecting the generation of H_2O_2, $^{\bullet}OH$ and O_2^{-} in test tubes and in cells. Efficient internalization of both Cu^{2+} and H_4TBP was realized using Cu-TBP nMOFs as delivery vehicles. Following endocytosis, Cu-TBP decomposes in endosome/lysosome at acidic pH to release free Cu^{2+} as a CDT agent and H_4TBP as a PS

Concentration of estradiol, the predominant estrogen, has long been used as a biomarker for cancer diagnosis and prognosis[24]. For example, elevated urinary level of estradiol is linked to an increased risk of breast cancer in postmenopausal women[25]. Moreover, hormone therapy is used to treat select cancer types by blocking the production of estrogens through the use of aromatase inhibitors, antiestrogens or selective estrogen receptor modulators[11]. Our *in vivo* findings indicate efficient depletion of intratumoral estradiol with free Cu^{2+} ions released from Cu-TBP nMOFs. In support of this observation, Zn-TBP was used as a control to deliver H_4TBP for PDT but not Cu^{2+} for CDT. Mice treated with Cu-TBP displayed better tumor control over those treated with Zn-TBP with or without light irradiation. Thus, Cu-TBP-mediated radical therapy *via* Cu-estradiol catalytic cycle not only promotes efficient generation of various ROS but also induces additional therapeutic efficacy by depleting intratumoral estradiol in a fashion similar to that of conventional hormone therapy.

Checkpoint blockade immunotherapies targeting the PD-1/PD-L1 axis have provided highly effective treatments for melanoma patients. For preclinical research, B16F10 is often used to study cancer immunotherapy due to the high mutation burden of this model[26-29]. We discovered a high level of estradiol in B16F10 cell line, making it an appropriate model to study estradiol-dependent catalytic ROS generation. We found that treatment of well-established B16F10 tumors with α-PD-L1 alone was largely ineffective due to the immunosuppressive tumor microenvironment. However, the combination treatment with Cu-TBP(+) and α-PD-L1 effectively inhibited/regressed local and metastatic tumors, eradicating tumors in one-third of all treated mice. These results indicate that our proposed treatment regime can potentially expand the therapeutic scope of immune checkpoint blockade to include highly metastatic and immunosuppressive cancers.

6.4 Conclusion

In this chapter, we have synthesized Cu-TBP nMOFs to enable dual-triggered radical therapy by combining hormone-induced CDT *via* the Cu-estradiol catalytic redox cycle and light-triggered, porphyrin-based PDT. Cu-TBP-mediated CDT/PDT effectively regressed local B16F10 and SKVO-3 tumors with high estradiol levels. We further demonstrated that nMOF-mediated radical therapy potentiated α-PD-L1 CBI with strong abscopal effects on bilateral B16F10 tumor model. This synergistic combination elicits systemic antitumor immunity by boosting innate immune response and re-activating T cells in both primary and distant tumors. We have thus established the feasibility of using nMOF-mediated CDT/PDT to broaden the therapeutic effects of CBI to hormonally dysregulated tumor phenotypes.

6.5 Methods

Materials, cell lines, and animals: All of the starting chemicals were purchased from Sigma-Aldrich and Fisher (USA), unless otherwise noted, and used without further purification.

Murine melanoma cell line B16F10 was kindly provided by Dr. Ralph R. Weichselbaum at University of Chicago. Human pancreatic cancer cell PC-3 was purchased from Developmental Therapeutics Core at Northwestern University. Human colon adenocarcinoma cell, HCT-116, and the human ovarian cancer cell, SKOV-3, were purchased from the American Type Culture Collection (Rockville, MD, USA). PC-3 cells were cultured in Roswell Park Memorial Institute (RPMI) 1640 medium (GE Healthcare, USA. B16F10 cells were cultured in Dulbecco's Modified Eagle's Medium (DMEM) medium (GE Healthcare, USA). HCT-116 and SKOV-3 cells were cultured in McCoy's 5A Modified Medium. All medium was further supplemented with 100 U/mL penicillin G sodium, 100 μg/mL streptomycin sulfate and 10% fetal bovine serum (FBS, VWR, USA). Cells were cultured in a humidified atmosphere containing 5% CO_2 at 37ºC. C57BL/6 female mice (6-8 weeks) were obtained from Harlan-Envigo Laboratories, Inc (USA). The study protocol was reviewed and approved by the Institutional Animal Care and Use Committee (IACUC) at the University of Chicago.

Synthesis of Cu-TBP: To a 1 dram glass vial was added 0.43 mL of $CuCl_2$ solution (1.1 mg/mL in ethanol), 0.5 mL of the H_4TBP solution (1.9 mg/mL in ethanol), 200 μL of water, 0.74 μL of triethylamine and 10 μL of formic acid. The reaction mixture was then mixed and sonicated at room temperature for 2 h. The purple precipitate was collected by centrifugation and washed with ethanol, 5% trimethylamine/ethanol solution and ethanol.

Intracellular behavior of Cu-TBP: The cellular uptake, intracellular accumulation and decomposition of Cu-TBP were studied systemically and compared with H_4TBP. B16F10 cells were seeded on 6-well plates at 1×10^6/well overnight. Cu-TBP or H_4TBP was added to the cells at a TBP concentration of 20 μM. After incubation of 1, 2, 4, and 8 hours, cells were collected and counted with a hemocytometer then frozen and thawed repeatly for digestion. The H_4TBP was extracted with 50 μL concentrated phosphoric acid in 450 μL DMSO for UV-Vis quantification. Cells were also incubated with Cu-TBP or H_4TBP for 1, 2, 4, 8 and 24 hours for detecting fluorescence of H_4TBP under a confocal laser scanning microscope (CLSM, FV1000, Olympus, Japan) and further quantified by flow cytometry (LSRFortessa 4-15, BD, USA). The CLSM images were analyzed with ImageJ.

H_2O_2 and $^{\bullet}OH$ generation: H_2O_2 and $^{\bullet}OH$ generation was determined by the hydrogen peroxide assay kit (Sigma, USA), which reacts with H_2O_2 to give green fluorescence (excitation/emission maxima 490/520 nm) and coumarin-3-carboxylic acid, which reacts with $^{\bullet}OH$ to give blue fluorescence (excitation/emission maxima 390/465), respectively. Groups including $CuCl_2$ alone, NADH alone, $CuCl_2$+estradiol, NADH+estradiol or $CuCl_2$+NADH+estradiol were suspended in 200 μL water in the presence of 1 μL suspension of the hydrogen peroxide assay kit. The concentration of $CuCl_2$, NADH and estradiol are 50 μM, 0.1 mM and 40 μM, respectively. The fluorescence of each group was measured with a RF-5301 PC Spectrofluorophotometer (Shimadzu, Japan).

O_2^- generation: O_2^- generation was determined by the nitrone spin trap 5-tert-butoxycarbonyl 5-methyl-1-pyrroline N-oxide (BMPO), which forms distinct adducts with O_2^- (BNPO-O_2^-). $CuCl_2$ was suspended in water at a concentrations of 50 μM in the presence of 25 mM BMPO and with

or without 40μM 4-OHE2. Each suspension was added to capillary tubes and scanned on a Bruker Elexsys 500 X-band EPR spectrometer at 298 K to collect EPR signals.

Intracellular ˙OH generation: ˙OH generation in live cells was assayed with coumarin-3-carboxylic acid. B16F10 cells were cultured in 6-well plates overnight. The cells were incubated with $CuCl_2$, H_4TBP, and Cu-TBP at an equivalent dose of 20 μM for 4 h followed by LED irradiation with 0 or 90 J/cm^2 (λ_{max} = 650 nm, 100 mW/cm^2, 0 or 15 mins). Cells were stained immediately with the 20 μM coumarin-3-carboxylic acid. After incubating for 20 min, the cells were washed with PBS three times to remove excess coumarin-3-carboxylic acid. The ˙OH generated in the live cells was visualized by detecting the blue fluorescence inside the cells under CLSM and quantified by flow cytometry.

Intracellular $^1O_2$ and O_2^- generation: $^1O_2$ and O_2^- generation in live cells was detected by SOSG and superoxide anion assay kit, respectively. B16F10 cells were seeded in 6-well plates and cultured for 12 h. The culture medium was then replaced with fresh medium containing 1 μM SOSG and 1 μM superoxide anion assay kit to preload the cells with SOSG and superoxide anion assay kit. After incubating for 30 min, the cells were washed by PBS three times to remove excess SOSG and superoxide anion assay kit. The cells were incubated with $CuCl_2$, H_4TBP, and Cu-TBP at an equivalent dose of 20 μM for 4 h followed by light irradiation with 0 or 90 J/cm^2 (λ_{max} = 650 nm, 100 mW/cm^2, 0 or 15 mins). CLSM was used to visualize the $^1O_2$ and O_2^- generated in the live cells by detecting the green and red fluorescence inside the cells, respectively.

Cytotoxicity: 3-(4,5-dimethylthiazol-2-yl)-5-(3-carboxymethoxyphenyl)-2-(4-sulfo-phenyl)-2H-tetrazolium (MTS) assay (Promega, USA) was employed to evaluate cytotoxicity. B16F10 cells were seeded on 96-well plates at 1×10^4/well and further cultured for 12 h. $CuCl_2$, H_4TBP, and Cu-

TBP was added to the cells at an equivalent dose of 0, 0.5, 1, 2, 5, 10, 20, 50 μM and incubated for 4 h, followed by light irradiation with 0 or 90 J/cm^2 (λ_{max} = 650 nm, 100 mW/cm^2, 0 or 15 mins). The cells were further incubated for 72 h before determining the cell viability by MTS assay. The optical images of each group were also captured under the SZX-Zb12 stereomicroscope (Olympus, Japan).

Apoptosis/necrosis: B16f10 cells were cultured in 6-well plates overnight and incubated with $CuCl_2$, H_4TBP, and Cu-TBP at an equivalent dose of 20 μM for 4 h followed by light irradiation with 0 or 90 J/cm^2 (λ_{max} = 650 nm, 100 mW/cm^2, 0 or 15 mins). 24 h later, the cells were stained according to the AlexaFluor 488 Annexin V/dead cell apoptosis kit (Life technologies, USA), imaged by CLSM and quantified by flow cytometry.

DNA damage: B16F10 cells were cultured in a 6-well plate overnight and further incubated with $CuCl_2$, H_4TBP, and Cu-TBP at an equivalent dose of 20 μM for 4 h followed by light irradiation with 0 or 90 J/cm^2 (λ_{max} = 650 nm, 100 mW/cm^2, 0 or 15 mins). Cells were stained immediately with the HCS DNA damage kit (Life Technologies, USA) for CLSM and flow cytometry.

***In vivo* anti-tumor efficacy:** A murine melanoma model B16F10 and another human ovarian SKOV-3 were established by subcutaneously inoculating 1.5×10^6 B16F10 cells onto C57BL/6 mice or 5×10^6 SKOV-3 cells onto athymic nude mice, respectively. When the flank tumors reached 75-100 mm^3 in volume, mice were injected intratumorally with $CuCl_2$, H_4TBP, and Cu-TBP at an equivalent dose of 0.2 μmol or PBS. 4 h after injection, mice were anaesthetized with 2% (v/v) isoflurane and the primary tumors were irradiated with a LED lamp (λ_{max} = 650 nm, 100 mW/cm^2) for 30 mins. Zn-TBP with or without light irradiation treatment were added as control on B16F10 tumor-bearing mice. The tumor sizes were measured daily with a caliper where tumor volume

equals (width^2 × length)/2. Mice were sacrificed on day 15 for B16F10 model and day 38 for SKOV-3 model and the excised tumors were photographed and weighed.

Estradiol quantification: Tumors after anticancer treatment studies were harvested, weighed and homogenized to lysed cells. Intratumoral estradiol was extracted into chloroform three times and dried over vacuum. The quantification of estradiol was performed with the estradiol ELISA kit (No. 582251, Cayman, USA).

Immunogenic cell death: B16F10 cells were cultured in a 6-well plate overnight and incubated with $CuCl_2$, H_4TBP, and Cu-TBP at an equivalent dose of 20 μM for 4 h followed by light irradiation with 0 or 90 J/cm^2 (λ_{max} = 650 nm, 100 mW/cm^2, 0 or 15 mins). The cells were washed three times with PBS, fixed with 4% paraformaldehyde, incubated with AlexaFluor 488-CRT (Enzo Life Sciences, USA) with 1: 100 dilution for 2 h, stained with DAPI, and observed by CLSM. Treated cells were incubated for 4 h, collected, incubated with AlexaFluor 488-CRT antibody for 2 h, and then stained with PI for analysis by flow cytometry.

Abscopal Effect: A bilateral melanoma model was established by subcutaneously inoculating 1.5×10^6 and 7.5×10^5 B16F10 cells onto the right and left flanks of C57BL/6 mice for respective primary and secondary tumors. When the primary tumors reached 75-100 mm^3 in volume, mice were injected intratumorally with nMOFs at a dose of 0.2μmol TBP or PBS. 4 h after injection, mice were anaesthetized with 2% (v/v) isoflurane and the primary tumors were irradiated with a LED lamp (λ_{max} = 650 nm, 100 mW/cm^2) for 30 mins. Anti-PD-L1 antibody was given every three days by intraperitoneal injection at a dose of 75μg/mouse. The tumor sizes were measured daily with a caliper where tumor volume equals (width^2 × length)/2. Mice were sacrificed once the total

tumor burden attached to 2000 mm^3 in volume. Each mouse was weighed daily to evaluate toxicity. Survival percentage of each group was analyzed using the log-rank Kaplan-Meier method.

ELISpot assay: Tumor-specific immune responses to IFN-γ was measured *ex vitro* by ELISpot assay (Mouse IFN gamma ELISPOT Ready-SET-Go!®; Cat. No. 88-7384-88; eBioscience). Millipore Multiscreen HTS-IP plates was coated overnight at 4°C with anti-Mouse IFN-γ capture antibody. Single-cell suspensions of splenocytes were obtained from 4T1 tumor-carrying mice and seeded onto the antibody-coated plate at a concentration of 2×10^5 cells/well. Cells were incubated with or without SVYDFFVWL stimulation (10 mg/ml; in purity >95%; Genscript, USA) for 42 h at 37 °C and then discarded. The plate was then incubated with biotin-conjugated anti-IFN-γ detection antibody at room temperature (r.t.) for 2 h, followed by incubation with Avidin-HRP for 2 h at r.t. 3-amino-9-ethylcarbazole substrate solution (Sigma, Cat. AEC101) was added for cytokine spot detection. Spots were imaged and quantified with a CTL ImmunoSpot Analyzer (Cellular Technology Ltd, USA).

Lymphocytes profiling: Tumors were harvested, treated with 1 mg/mL collagenase I (Gibco™, USA) for 1 h, and ground by the rubber end of a syringe. Cells were filtered through nylon mesh filters with size of 40 μm and washed with PBS. tumor-draining lymph nodes were collected and directly ground through the cell strainers. The single-cell suspension was incubated with anti-CD16/32 (clone 93) to reduce nonspecific binding to FcRs. Cells were further stained with the following fluorochrome-conjugated antibodies: CD45 (30-F11), TCRβ (H57-597), CD4 (GK1.5), CD8 (53-6.7), and PI (all from eBioscience). Antibodies were used with the dilution of 1: 200. LSR Fortessa (BD Biosciences) was used for cell acquisition and data analysis was carried out with FlowJo software (Tree Star, Ashland, OR).

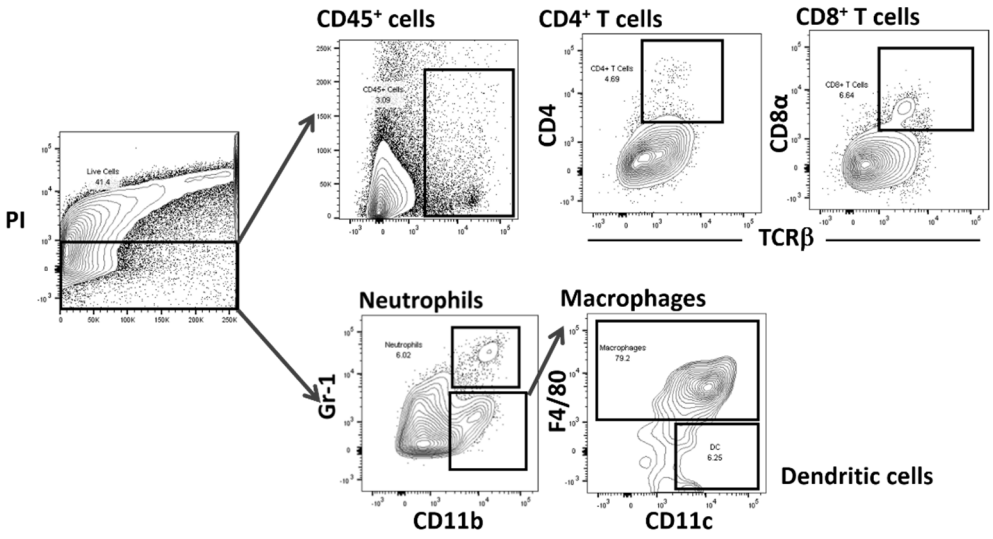

Figure 6-25 Representative gating strategies for $CD45^+$ cells, $CD4^+$ T cells, $CD8^+$ T cells, macrophages, dendritic cells, and neutrophils. Adapted with permission from *Chem*, **2019**, *5*, 1892-1913. Copyright 2019 Elsevier Inc.

6.6 References

1. Lin, L. S.; Song, J.; Song, L.; Ke, K.; Liu, Y.; Zhou, Z.; Shen, Z.; Li, J.; Yang, Z.; Tang, W., Simultaneous Fenton-like ion delivery and glutathione depletion by MnO_2-based nanoagent to enhance chemodynamic therapy. *Angewandte Chemie International Edition* **2018,** *130* (18), 4996-5000.

2. Tang, Z.; Liu, Y.; He, M.; Bu, W., Chemodynamic therapy: tumour microenvironment-mediated Fenton and Fenton-like reactions. *Angewandte Chemie International Edition* **2018**. *58* (4), 946-956.

3. Zheng, Z.-B.; Zhu, G.; Tak, H.; Joseph, E.; Eiseman, J. L.; Creighton, D. J., N-(2-hydroxypropyl) methacrylamide copolymers of a glutathione (GSH)-activated glyoxalase inhibitor and DNA alkylating agent: synthesis, reaction kinetics with GSH, and *in vitro* antitumor activities. *Bioconjugate Chemistry* **2005,** *16* (3), 598-607.

4. Kim, J.; Cho, H. R.; Jeon, H.; Kim, D.; Song, C.; Lee, N.; Choi, S. H.; Hyeon, T., Continuous O_2-evolving $MnFe_2O_4$ nanoparticle-anchored mesoporous silica nanoparticles for efficient photodynamic therapy in hypoxic cancer. *Journal of the American Chemical Society* **2017,** *139* (32), 10992-10995.

5. Fan, W.; Lu, N.; Huang, P.; Liu, Y.; Yang, Z.; Wang, S.; Yu, G.; Liu, Y.; Hu, J.; He, Q., Glucose-responsive sequential generation of hydrogen peroxide and nitric oxide for synergistic

cancer starving-like/gas therapy. *Angewandte Chemie International Edition* **2017,** *56* (5), 1229-1233.
6. Hanahan, D.; Weinberg, R. A., The hallmarks of cancer. *Cell* **2000,** *100* (1), 57-70.

7. Qin, L.-Q.; Wang, P.-Y.; Kaneko, T.; Hoshi, K.; Sato, A., Estrogen: one of the risk factors in milk for prostate cancer. *Medical Hypotheses* **2004,** *62* (1), 133-142.

8. Yager, J. D.; Davidson, N. E., Estrogen carcinogenesis in breast cancer. *New England Journal of Medicine* **2006,** *354* (3), 270-282.

9. Hall, J. M.; Couse, J. F.; Korach, K. S., The multifaceted mechanisms of estradiol and estrogen receptor signaling. *Journal of Biological Chemistry* **2001,** *276* (40), 36869-36872.

10. Revankar, C. M.; Cimino, D. F.; Sklar, L. A.; Arterburn, J. B.; Prossnitz, E. R., A transmembrane intracellular estrogen receptor mediates rapid cell signaling. *Science* **2005,** *307* (5715), 1625-1630.

11. Jordan, V. C., Selective estrogen receptor modulation: concept and consequences in cancer. *Cancer Cell* **2004,** *5* (3), 207-213.

12. Grodstein, F.; Stampfer, M. J.; Colditz, G. A.; Willett, W. C.; Manson, J. E.; Joffe, M.; Rosner, B.; Fuchs, C.; Hankinson, S. E.; Hunter, D. J., Postmenopausal hormone therapy and mortality. *New England Journal of Medicine* **1997,** *336* (25), 1769-1776.

13. Seacat, A. M.; Kuppusamy, P.; Zweier, J. L.; Yager, J. D., ESR identification of free radicals formed from the oxidation of catechol estrogens by Cu^{2+}. *Archives of Biochemistry and Biophysics* **1997,** *347* (1), 45-52.

14. Thibodeau, P. A.; Paquette, B., DNA damage induced by catecholestrogens in the presence of copper (II): generation of reactive oxygen species and enhancement by NADH. *Free Radical Biology and Medicine* **1999,** *27* (11-12), 1367-1377.

15. Rehmani, N.; Zafar, A.; Arif, H.; Hadi, S. M.; Wani, A. A., Copper-mediated DNA damage by the neurotransmitter dopamine and L-DOPA: A pro-oxidant mechanism. *Toxicology in Vitro* **2017,** *40*, 336-346.

16. Zhao, M.; Wang, Y.; Ma, Q.; Huang, Y.; Zhang, X.; Ping, J.; Zhang, Z.; Lu, Q.; Yu, Y.; Xu, H., Ultrathin 2D metal–organic framework nanosheets. *Advanced Materials* **2015,** *27* (45), 7372-7378.

17. Casey, J. R.; Grinstein, S.; Orlowski, J., Sensors and regulators of intracellular pH. *Nature Reviews Molecular Cell Biology* **2010,** *11* (1), 50-61.

18. Ma, Y.; Li, X.; Li, A.; Yang, P.; Zhang, C.; Tang, B., H_2S-activable MOF nanoparticle photosensitizer for effective photodynamic therapy against cancer with controllable singlet-oxygen release. *Angewandte Chemie International Edition* **2017,** *56* (44), 13752-13756.

19. Xu, X.; Veenstra, T. D., Concentration of endogenous estrogens and estrogen metabolites in the NCI-60 human tumor cell lines. *Genome Medicine* **2012,** *4* (4), 31.

20. Ferrario, A.; von Tiehl, K.; Wong, S.; Luna, M.; Gomer, C. J., Cyclooxygenase-2 inhibitor treatment enhances photodynamic therapy-mediated tumor response. *Cancer Research* **2002,** *62* (14), 3956-3961.

21. Ma, B.; Wang, S.; Liu, F.; Zhang, S.; Duan, J.; Li, Z.; Kong, Y.; Sang, Y.; Liu, H.; Bu, W., Self-assembled copper-amino acid nanoparticles for *in situ* glutathione "AND" H_2O_2 sequentially triggered chemodynamic therapy. *Journal of the American Chemical Society* **2018**. *141* (2), 849-857.

22. Zhang, C.; Bu, W.; Ni, D.; Zhang, S.; Li, Q.; Yao, Z.; Zhang, J.; Yao, H.; Wang, Z.; Shi, J., Synthesis of iron nanometallic glasses and their application in cancer therapy by a localized Fenton reaction. *Angewandte Chemie International Edition* **2016,** *55* (6), 2101-2106.

23. Ju, E.; Dong, K.; Chen, Z.; Liu, Z.; Liu, C.; Huang, Y.; Wang, Z.; Pu, F.; Ren, J.; Qu, X., Copper (II)–graphitic carbon nitride triggered synergy: improved ROS generation and reduced glutathione levels for enhanced photodynamic therapy. *Angewandte Chemie International Edition* **2016,** *128* (38), 11639-11643.

24. Osborne, M. P.; Bradlow, H. L.; Wong, G. Y.; Telang, N. T., Upregulation of estradiol C16α-hydroxylation in human breast tissue: a potential biomarker of breast cancer risk. *JNCI: Journal of the National Cancer Institute* **1993,** *85* (23), 1917-1920.

25. Onland-Moret, N.; Kaaks, R.; Van Noord, P.; Rinaldi, S.; Key, T.; Grobbee, D.; Peeters, P., Urinary endogenous sex hormone levels and the risk of postmenopausal breast cancer. *British Journal of Cancer* **2003,** *88* (9), 1394.

26. Ye, Y.; Wang, C.; Zhang, X.; Hu, Q.; Zhang, Y.; Liu, Q.; Wen, D.; Milligan, J.; Bellotti, A.; Huang, L., A melanin-mediated cancer immunotherapy patch. *Science. Immunology* **2017,** *2* (17), 5692.

27. Curran, M. A.; Montalvo, W.; Yagita, H.; Allison, J. P., PD-1 and CTLA-4 combination blockade expands infiltrating T cells and reduces regulatory T and myeloid cells within B16 melanoma tumors. *Proceedings of the National Academy of Sciences* **2010,** *107* (9), 4275-4280.

28. Twyman-Saint Victor, C.; Rech, A. J.; Maity, A.; Rengan, R.; Pauken, K. E.; Stelekati, E.; Benci, J. L.; Xu, B.; Dada, H.; Odorizzi, P. M., Radiation and dual checkpoint blockade activate non-redundant immune mechanisms in cancer. *Nature* **2015,** *520* (7547), 373.

29. De Henau, O.; Rausch, M.; Winkler, D.; Campesato, L. F.; Liu, C.; Cymerman, D. H.; Budhu, S.; Ghosh, A.; Pink, M.; Tchaicha, J., Overcoming resistance to checkpoint blockade therapy by targeting PI3Kγ in myeloid cells. *Nature* **2016,** *539* (7629), 443.